

Preferential and Non-Darcy Flows in the Hyporheic Zone: Surface Water-Groundwater Hydraulics and Effects on Stream Functions

Garrett Thomas Menichino

Dissertation submitted to the faculty of the Virginia Polytechnic Institute and State University in
partial fulfillment for the degree of

Doctor of Philosophy
in
Civil and Environmental Engineering

Erich T. Hester, Chair
W. Cully Hession
Durelle T. Scott
Mark A. Widdowson

October 30, 2013
Blacksburg, Virginia

Keywords: River, Hyporheic exchange, Hydraulic conductivity, Macropore, Field investigations,
Computational Fluid Dynamics

Copyright 2013, Garrett Thomas Menichino

Preferential and Non-Darcy Flows in the Hyporheic Zone: Surface Water-Groundwater Hydraulics and Effects on Stream Functions

Garrett Thomas Menichino

ABSTRACT

Surface water-groundwater interaction can provide various stream functions including temperature regulation, nutrient cycling, pollutant attenuation, and habitat creation. However previous literature is divided on the extent and conditions of these benefits. This dissertation has explored the dominance of hydraulic conductivity (K) on hyporheic hydraulics and implications to hyporheic zone functions through a series of modeling studies and field experiments.

Computational Fluid Dynamics (CFD) software was used to model the effect of varying K on weir-induced hyporheic exchange hydraulics and heat transport. Fundamental shifts in hydraulics and temperature dynamics occurred at threshold K 's. Surface water began noticeably sinking into the bed above a threshold of $K=10^{-3}$ m/s and inertial forces caused deviation from Darcy's Law. The heat transport model indicated net downstream surface water cooling from weir-induced exchange was maximized by maximizing K (flow-limited function) and thermal heterogeneity increased with K , particularly above $K=10^{-5}$ m/s. Results suggest that using CFD to predict surface water-groundwater interaction may be important to accurately predict hyporheic hydraulics and functions dependent on flow-rate or residence time.

The importance of macropores to hyporheic transport through meander bends was explored. Transport velocities, hydraulic head gradients, and solute transport rates through the meander bend were increased by macropores. Results indicate that macropores can dictate solute or pollutant transport through meander bends and in the hyporheic zone, which in turn may influence biogeochemical cycling and pollutant attenuation.

Surface-connected macropores along streams were studied as hydrologically important subsurface heterogeneities for surface water-groundwater interaction. Macropores were common geomorphic features in the Appalachian province of southwestern Virginia, and were inundated during storm events over a one-year period. Banks with macropores experienced increased hydraulic head fluctuations, temperature fluctuations, and K . Macropores increased bank storage rates and solute transport between the channel and riparian groundwater zones, which in turn may influence biogeochemical cycling, pollutant attenuation, and hyporheic habitat. Macropores may be important to hyporheic flow and solute transport in a wide range of conditions and may broaden the portion of the landscape in which hyporheic exchange is important. Future work is needed to further assess the impacts of macropores on hyporheic functions and explore new methods to map and quantify macropore geometries and inter-connectivity.

ACKNOWLEDGEMENTS

I would like to thank the Thomas F. Jeffress and Kate Miller Jeffress Memorial Trust, the Consortium of Universities for the Advancement of Hydrologic Science, Inc. (CUAHSI) Hydrogeophysics Node, the Institute for Critical Technology and Applied Science at Virginia Tech, the National Science Foundation (REU – EEC – 1062860), and the G.V. Loganathan Memorial Fellowship for support. Any opinions, findings, and conclusions or recommendations expressed in this work do not necessarily reflect the views of the above-mentioned supporters.

I would like to thank the members of my doctoral committee: Dr. Erich Hester, Dr. Cully Hession, Dr. Durelle Scott, and Dr. Mark Widdowson. Their expertise, input, and guidance have been instrumental in the development and execution of this research. I value their effort and contributions, and feel fortunate to have such a supportive committee.

I would also like to sincerely thank my advisor, Dr. Erich Hester, for his mentorship over the past four years. His patience and dedication toward my academic development, his brilliant support of my research, and his enthusiasm and encouragement throughout, have been inspirational and invaluable.

Finally, I would like to thank my family and friends for their love and support. I hope that I can repay their kindness with my own compassion and gratitude in the next years of my life.

TABLE OF CONTENTS

| | |
|---|------|
| ABSTRACT | ii |
| ACKNOWLEDGEMENTS | iii |
| TABLE OF CONTENTS | iv |
| LIST OF FIGURES | viii |
| LIST OF TABLES | xii |
| ATTRIBUTION | xiii |
| CHAPTER 1: <i>Introduction</i> | 1 |
| 1.1 BACKGROUND..... | 1 |
| 1.2 HYPORHEIC EXCHANGE AND OCCURRENCE ALONG STREAMS..... | 4 |
| 1.3 THE HYPORHEIC ZONE AND STREAM FUNCTIONS | 7 |
| 1.3.1 Pollutant attenuation and biogeochemical reactions | 7 |
| 1.3.2 In-stream peak discharge reduction and groundwater recharge | 8 |
| 1.3.3 Stream temperature buffering, cooling, regulation..... | 8 |
| 1.3.4 Habitat creation, diversity, and refugia | 9 |
| 1.4 DARCY’S LAW AND VARIABILITY OF K..... | 10 |
| 1.5 DEVIATIONS FROM DARCIAN PREDICTIONS OF HYPORHEIC EXCHANGE..... | 11 |
| 1.6 PREFERENTIAL FLOW PATHS AND MACROPORES | 12 |
| 1.7 RESEARCH OBJECTIVES | 14 |
| 1.8 ORGANIZATION OF DISSERATATION..... | 15 |
| 1.9 REFERENCES..... | 17 |
| CHAPTER 2: <i>Hydraulic and Thermal Effects of In-Stream Structure-Induced Hyporheic Exchange: Identifying Threshold Hydraulic Conductivities that Control System Response</i> | 30 |
| 2.1 ABSTRACT | 30 |
| 2.2 INTRODUCTION..... | 32 |

| | |
|--|-----------|
| 2.2.1 Hyporheic Zone Hydraulics: Processes, Theory, and Modeling | 32 |
| 2.2.2 Hyporheic Zone Temperature Dynamics: Processes, Theory, and Modeling | 33 |
| 2.2.3 Organization and Objectives of Study | 35 |
| 2.3 METHODS..... | 35 |
| 2.3.1 Hydraulics Model | 35 |
| 2.3.2 Temperature Dynamics Model | 39 |
| 2.4 RESULTS..... | 43 |
| 2.4.1 Hydraulics Model | 43 |
| 2.4.2 Temperature Dynamics Model | 44 |
| 2.5 DISCUSSION | 46 |
| 2.5.1 Hydraulics Model | 46 |
| 2.5.2 Temperature Dynamics Model | 49 |
| 2.6 CONCLUSIONS | 54 |
| 2.7 REFERENCES..... | 56 |
| CHAPTER 3: Macropores as Preferential Flow Paths in Meander Bends..... | 75 |
| 3.1 ABSTRACT | 75 |
| 3.2 INTRODUCTION..... | 77 |
| 3.3 METHODS..... | 80 |
| 3.3.1 Field Site..... | 80 |
| 3.3.2 Experimental Design | 80 |
| 3.3.3 Conventional Tracer and Hydraulics Methods..... | 81 |
| 3.3.4 Temporal Moment Analysis | 82 |
| 3.3.5 Electrical Resistivity Methods..... | 83 |
| 3.4 RESULTS..... | 85 |
| 3.4.1 Meander Bend Hydraulics | 85 |

| | |
|---|-----|
| 3.4.2 Tracer Breakthrough in Monitoring Wells | 86 |
| 3.4.3 Electrical Resistivity Imaging within the Meander Bend..... | 87 |
| 3.4.4 Hydraulic Conductivity of Meander Bend Sediments..... | 88 |
| 3.5 DISCUSSION | 89 |
| 3.5.1 Effects of Macropores on Hydrologic Processes within Meander Bends | 89 |
| 3.5.2 Potential Effects of Meander Bend Macropores on Hydrologic Processes at Larger Scales | 91 |
| 3.5.3 Methodological Advances in Quantifying Riparian Macropore Distribution and Transport..... | 93 |
| 3.6 CONCLUSIONS..... | 95 |
| 3.7 ACKNOWLEDGEMENTS | 96 |
| 3.8 REFERENCES..... | 96 |
| CHAPTER 4: <i>Macropores along Stream Channels: Abundance, Dimensions, and Effects on Surface Water-Groundwater Exchange</i> | 116 |
| 4.1 ABSTRACT | 116 |
| 4.2 INTRODUCTION..... | 118 |
| 4.3 METHODS..... | 121 |
| 4.3.1 Macropore Surveys..... | 121 |
| 4.3.2 Macropore Creation Mechanisms..... | 122 |
| 4.3.3 Macropore Hydroperiod Analysis | 122 |
| 4.3.4 Bank Storage Experiment..... | 123 |
| 4.4 RESULTS..... | 124 |
| 4.4.1 Macropore Spatial Characteristics..... | 124 |
| 4.4.2 Macropore Creation Mechanisms..... | 125 |
| 4.4.3 Macropore Hydroperiods..... | 126 |
| 4.4.4 Bank Storage Impacts..... | 126 |

| | |
|---|-----|
| 4.5 DISCUSSION | 130 |
| 4.5.1 Macropore Distribution and Abundance | 130 |
| 4.5.2 Hydrologic Implications of Macropore Characteristics | 131 |
| 4.5.3 Hydrologic Processes Affecting Bank Storage | 133 |
| 4.5.4 Water quality and ecosystem effects of macropores during bank storage | 135 |
| 4.5.5 Hydrologic impacts and water quality effects of macropores during non-storm conditions..... | 136 |
| 4.6 CONCLUSIONS..... | 137 |
| 4.7 AKNOWLEDGEMENTS..... | 138 |
| 4.8 REFERENCES..... | 138 |
| CHAPTER 5: <i>Conclusions</i> | 164 |
| 5.1 OBJECTIVES AND FINDINGS | 164 |
| 5.2 MAJOR THEMES AND CONTEXT | 166 |
| 5.3 ENGINEERING SIGNIFICANCE..... | 167 |
| 5.3.1 Implications for Stream Restoration..... | 167 |
| 5.3.2 When and where will restoring hyporheic exchange matter?..... | 169 |
| 5.4 FUTURE RESEARCH | 169 |
| 5.5 REFERENCES..... | 171 |
| APPENDIX A: <i>Supplementary Material to the Hydraulics Model in Chapter 2</i> | 175 |
| APPENDIX B: <i>Supplementary Material to the Temperature Model in Chapter 2</i> | 193 |
| APPENDIX C: <i>Testing Ground Penetrating Radar to Characterize Macropores</i> | 201 |
| APPENDIX D: <i>Testing Concrete to Cast Molds of Macropores along Stream Channels</i> | 207 |
| APPENDIX E: <i>Testing the Hydrologic Connectivity of Macropores to other Preferential Flow Paths and Measuring the Hydraulic Conductivity of Macropores</i> | 213 |
| APPENDIX F: <i>The Effect of Macropores on Transient Storage during Baseflow</i> | 219 |
| APPENDIX G: <i>Stream Gauge Locations and Rating Curve Data</i> | 228 |

LIST OF FIGURES

| | |
|---|-----|
| Figure 2-1. Panel A shows hydraulics model domain and associated boundaries in CFX. Panel B shows groundwater domain for heat transport model and associated boundaries in CFX. | 63 |
| Figure 2-2. Longitudinal water surface profiles near the weir. | 64 |
| Figure 2-3. Panel A shows geometry and mean residence time of hyporheic flow cell versus K . Panel B shows discharge through and mean residence time of hyporheic flow cell versus K for the Darcy-only model. | 65 |
| Figure 2-4. Pore scale Reynolds numbers for vertical profiles along channel center. | 66 |
| Figure 2-5. Panel A shows regions of K - i parameter space where Darcy and non-Darcy flow occur based on more than 3000 unique parameter combinations. Panel B shows differences in groundwater velocities calculated by Darcy and Darcy-Forchheimer (Ergun) models for $K=10^{-2}$ m/s (left) and $K=10^{-3}$ m/s (right) along channel center. | 67 |
| Figure 2-6. Temperature distributions along vertical slices through the groundwater domain beneath the channel centerline showing temperature distributions for $K=10^{-3}$ to 10^{-7} m/s at 16:00, June 10, 2007 and 03:00, June 11, 2007. | 68 |
| Figure 2-7. Modeled temperatures of water downwelling directly upstream of the weir and upwelling directly downstream of the weir. | 69 |
| Figure 2-8. Daily averaged cooling and buffering experienced along hyporheic flow paths and diel temperature range at upwelling location over range of K 's. | 70 |
| Figure 2-9. Panel A shows hyporheic advection and conduction versus time for $K=10^{-3}$ to 10^{-5} m/s. Panel B shows hyporheic advection and conduction versus time for $K=10^{-5}$ to 10^{-7} m/s. .. | 71 |
| Figure 2-10. Net daily advection, streambed conduction, and total thermal fluxes. | 72 |
| Figure 2-11. Thermal effect of weir-induced hyporheic advection on downstream surface water estimated by equation 8 versus time for a range of K 's. | 73 |
| Figure 2-12. Thermal effect of weir-induced hyporheic advection on downstream surface water temperatures, averaged over 96-hour modeling period. | 74 |
| Figure 3-1. Views of field site. | 108 |
| Figure 3-2. Site schematic. | 109 |
| Figure 3-3. Estimated piezometric contour map based on non-storm averaged groundwater levels collected in 8 wells for the OM treatment. | 110 |

| | |
|---|-----|
| Figure 3-4. Groundwater elevations for Well 8 (beneath channel) showing the relative timing and magnitude of storms that occurred during the experiment. | 111 |
| Figure 3-5. Breakthrough tracer curves. | 112 |
| Figure 3-6. Background (no saline tracer) ERI created for (A) the OM, and (B) the PFM. | 113 |
| Figure 3-7. Time-lapse ERI of saline tracer movement through the meander bend for the OM (left column) and the PFM (right column). | 114 |
| Figure 3-8. Profiles of K versus depth at three locations across meander bend transect for the case of the OM. | 115 |
| Figure 4-1. Schematic of field piezometer transects at Slate Branch. | 149 |
| Figure 4-2. Spatial characteristics of macropores across field sites. | 150 |
| Figure 4-3. Longitudinal distribution of macropores along each long survey reach length. | 151 |
| Figure 4-4. Relationship of median height of macropore above thalweg to average channel bankfull width. Error bars show values within a single standard deviation for each stream. ... | 152 |
| Figure 4-5. Example macropores of differing creation mechanisms. | 153 |
| Figure 4-6. Proportions of macropore creation mechanisms across sites. | 154 |
| Figure 4-7. Macropore hydroperiod analyses. | 155 |
| Figure 4-8. K 's measured from rising head field tests in wells in the M and NM transects. | 156 |
| Figure 4-9. Full year of water levels in the stream, macropore (M) transect, and non-macropore (NM) transect. | 157 |
| Figure 4-10. Water levels in the channel and transect wells during storms in summer (storm on Aug. 19), fall (storm on Nov. 13), winter (storms on Feb. 27 and Mar. 5), and spring (storms on Apr. 12, April 15, April 17, and April 20). | 158 |
| Figure 4-11. Average pre-storm water levels, average stormflow water levels, and ranges of storm water level fluctuations experienced over seasons in wells at the macropore and non-macropore transect. | 159 |
| Figure 4-12. Panel A shows temperatures experienced in channel and in wells over 1.5 months during summer. Panel B shows differences in temperature between the macropore and non-macropore transect at the 1st row and 4th row of wells for a series of storm events. | 160 |
| Figure 4-13. Water temperature ranges during storms at the 1st row, and at the 4th row of wells for the macropore and non-macropore transect. | 161 |

| | |
|--|-----|
| Figure 4-14. Conceptual model of potential hydrologic processes influencing near-channel groundwater levels during neutral baseflow conditions and storm flow conditions. | 162 |
| Figure 4-15. Thermal discharges from macropores during winter. | 163 |
| Figure A-1. Hyporheic flow cell and groundwater flow directions for Darcy-only model. | 180 |
| Figure A-2. Flow paths originating from downwelling area upstream of the weir for a range of K | 181 |
| Figure A-3. Velocity vector fields on vertical profile along channel center. | 182 |
| Figure A-4. Velocities near the weir versus K | 183 |
| Figure A-5. Differences in groundwater velocities calculated by Darcy and Darcy-Forchheimer models for $K=10^{-2}$ m/s and $K=10^{-3}$ m/s for a vertical profile aligned with channel center. | 184 |
| Figure A-6. Panel A shows criteria based thresholds of non-Darcy flow according to Re , Fo , and the empirical formula of <i>Sichardt</i> [1928]. Panel B shows differences in groundwater velocities calculated by Darcy and Darcy-Forchheimer (Ergun) models for $K=10^{-2}$ m/s and $K=10^{-3}$ m/s for 10 cm within the bed along channel center. | 185 |
| Figure A-7. Percent hyporheic flow versus K from Darcy and Darcy-Forchheimer models. .. | 187 |
| Figure A-8. Sweetspot concept for hyporheic zone functions. | 188 |
| Figure B-1. Thermal Peclet number (PeT) contour map for $K=10^{-3}$ m/s for a vertical profile along channel center in the groundwater domain. | 197 |
| Figure B-2. Spatial distribution of temperature difference between water and sediment for vertical profile along channel center for $K=10^{-3}$ m/s on 6/10/07 at 11:00. | 198 |
| Figure B-3. Hourly temperature difference between water and sediment for the downwelling location versus time. | 198 |
| Figure C-1. Site plan view schematic for macropore detection with GPR in grass field. | 203 |
| Figure C-2. Example output from post-processor from grass field experiment. | 204 |
| Figure C-3. Colored tomogram with macropores in grassy field experiment. | 204 |
| Figure C-4. Colored tomogram with macropore locations identified in field experiment. | 205 |
| Figure D-1. Apparatuses to inject concrete into macropores. | 209 |
| Figure D-2. Experimental macropore that extends 0.5 m into the bank. | 209 |

| | |
|---|-----|
| Figure D-3. Apparatus inside macropore..... | 210 |
| Figure D-4. The bank face is patched around apparatus and concrete is poured into the apparatus. | 210 |
| Figure D-5. Apparatus removed and macropore remains filled with hydraulic concrete. | 211 |
| Figure D-6. The partially excavated macropore mold after 15 minutes. | 212 |
| Figure E-1. Top panel shows tracer transport 10 seconds after rhodamine addition to apparatus installed in macropore. Bottom panel shows 30 seconds after initial addition of rhodamine. . | 215 |
| Figure E-2. Top panel shows apparatus set up inside macropore with a Leveltroll700 pressure transducer inside. Bottom panel shows the addition of water for a falling head test. | 216 |
| Figure F-1. Left panel shows injection setup and beginning of reach (0m to 5m). Right panel shows middle of reach (5m to 25m). | 222 |
| Figure F-2. Construction of macropores. | 223 |
| Figure F-3. Left panel shows post-macropore creation conditions on outside bend. Right panel shows non-macropore conditions. | 223 |
| Figure F-4. Breakthrough tracer curves (BTCs). Panels A and B show the observed BTC, the modeled BTC with exchange, and the modeled BTC without exchange at 35 m downstream for NM and M treatments, respectively. | 225 |
| Figure G-1. Stream gauge site locations near Blacksburg, VA. | 229 |

LIST OF TABLES

| | |
|--|-----|
| Table 3-1. Comparison of non-storm meander bend hydraulic gradients for both macropore treatments..... | 104 |
| Table 3-2. Temporal Moment Analysis for Wells 3-5..... | 105 |
| Table 3-3. Tracer velocities and dispersion coefficients for Wells 3-5..... | 106 |
| Table 3-4. Falling head test data during the OM treatment for each location. | 107 |
| Table 4-1. Macropore Survey Sites. | 147 |
| Table 4-2. Hydrologic processes influencing groundwater levels in near-channels wells during or shortly after storm events. | 148 |
| Table A-1. Summary of modeling scenarios. | 179 |
| Table B-1. Calibration of K to hyporheic temperatures. Observed values from <i>Hester et al.</i> [2009]..... | 195 |
| Table F-1. Stream and Transient Storage Parameters for the treatment scenarios. | 225 |
| Table G-1. Stream gauges and GPS coordinates. | 229 |
| Table G-2. Data for rating curves at sites. | 230 |

ATTRIBUTION

The contributions of the authors of the manuscripts presented in this dissertation are summarized below.

Garrett T. Menichino, E.I.T., PhD Candidate

The Charles E. Via, Jr. Department of Civil and Environmental Engineering
Virginia Polytechnic Institute and State University. Blacksburg, VA, 24061

Lead author of Chapters 2, 3, and 4. Participated in development of research design (objectives, methods, hypotheses). Performed all relevant modeling and/or field experiments. Performed data collection and analyses. Created, edited, and prepared manuscript text and figures for review and submission to peer reviewed journals.

Erich T. Hester, Ph.D., P.E. Assistant Professor

The Charles E. Via, Jr. Department of Civil and Environmental Engineering
Virginia Polytechnic Institute and State University. Blacksburg, VA, 24061

Coauthor of Chapters 2, 3, and 4. Participated in development of research design (objectives, methods, hypotheses). Reviewed data and analyses. Reviewed, revised, and provided significant contributions to the manuscripts.

Adam S. Ward, Ph.D., P.E. Assistant Professor

Department of Earth and Environmental Sciences
University of Iowa. Iowa City, IA 52242

Coauthor of Chapter 3. Participated in planning hydrogeophysical investigations at field site. Performed Electrical Resistivity Imaging (ERI) at field site during experiment. Performed data analyses of ERI data and created ERI figures. Made significant contributions to the manuscript on ERI methods and results. Participated in review and revision of complete manuscript.

CHAPTER 1: *Introduction*

1.1 BACKGROUND

Streams and rivers have classically been viewed purely as conduits for water. In the 1900s human land use increased near rivers, causing runoff to increase and flooding of rivers to become a problem. In response, engineering projects endeavored to make streams more efficient at transporting stormwater downstream. For example, in 1962 the Army Corps of Engineers straightened and dredged the Kissimmee River in Florida, shortening it from 166 km to 90 km. The result was a channelized river without any bends, which discouraged flooding of the riparian zone and floodplain, causing the floodplains and wetlands to dry out and reduced available habitat for a range of species [Koebel, 1995]. Within the channel itself, which was commonly used for largemouth bass fishing, fish populations declined. The reduction of floodplain connectivity decreased attenuation of nitrogen and phosphorus, causing increased pollutant transport downstream to Lake Okeechobee. The consequences of channelization sparked discussion to improve the water quality, habitat, and ecology of the Kissimmee River and Lake Okeechobee [Dahm *et al.*, 1995; Koebel, 1995; Toth *et al.*, 1998].

Widespread increases in urbanization and agricultural land use activities continue to increase runoff, erode and channelize streams, and pollute streams. For example, as of 2008, 55% rivers in the United States were degraded or polluted, resulting in the loss of water quality, habitat, and other ecosystem goods and services [EPA, 2013]. Problems include erosion and channelization, loss of native vegetation or riparian zone, insufficient fish passage, loss of physical aquatic habitat, high sediment loads, low dissolved oxygen levels, thermal pollution (e.g., heat pulses from urban environments), trash and debris piling, nutrient pollution (primarily nitrogen and phosphorus), trace metals (e.g., zinc, cadmium, uranium, manganese), trace contaminants (e.g., hydrocarbons, arsenic) [Allan and Castillo, 2007; Federal, 1998; Roni and Beechie, 2013].

One of the most widespread and challenging issues with stream health, particularly in developed countries, is nitrogen pollution. Nitrate-nitrogen pollution commonly enters streams and groundwater through agricultural and urban land use [Mulholland *et al.*, 2008]. The impacts of nitrogen pollution are staggering: risk of illness and methemoglobinemia (blue baby syndrome), co-occurring contaminants (e.g., pesticides or pathogens), increased water treatment

costs, and eutrophication leading to toxic algal blooms, low dissolved oxygen levels, fish kills, decreased species diversity and resiliency, and habitat loss [Gilinsky and NITG, 2009]. The United States Environmental Protection Agency (EPA) and United States Geological Survey (USGS) predict a continued rise in nitrate-nitrogen concentrations in water in the following decades [Dubrovsky and Hamilton, 2010; Gilinsky and NITG, 2009]. In response, better managing and mitigating nitrogen pollution has been deemed a Grand Engineering Challenge of the 21st century by the National Academy of Engineering [Engineering, 2010].

Another important water quality parameter is stream water temperature. Stream temperature directly affects stream ecology, chemistry, and biological function, and thus plays an important role in stream health and water quality [Allan and Castillo, 2007; Caissie, 2006]. For example, most aquatic organisms are tolerant of a narrow range of temperatures they originally experienced in their native ranges [Coutant, 1977; Hill et al., 2004; Lomolino et al., 2006], and can be negatively affected by thermal shifts [Walther et al., 2002]. Increasing temperature also decreases the solubility of dissolved oxygen in water, which can produce oxygen deficient zones [NRCS, 1998]. As a result, temperature can affect the distribution and abundance of organisms in streams [Brewer, 2011]. Temperature also influences the rates of biogeochemical reactions and nutrient cycling [Allan and Castillo, 2007; Westrich and Berner, 1988]. Stream temperatures are controlled by various factors, including land use in the watershed [Johnson, 2004; Poole and Berman, 2001]. For example, storm runoff from urban environments can transport urban heat pulses into streams that propagate downstream [Nelson and Palmer, 2007]. Cutting of riparian vegetation can increase water temperature [Johnson, 2004]. Additionally, the construction of dams on rivers or regulation of stream flow can shift the thermal regime of the river [Toffolon et al., 2010].

An important engineering question is how to mitigate for the effects of such pollution and best manage our water resources. The collection of activities performed toward return streams and rivers to pre-impacted conditions are referred to as stream restoration. Stream restoration aims to recover ecosystems, water quality, and other ecological goods and services that have been lost. Stream restoration has become a blanket buzzword associated with any type of stream project; however there are many types of projects. Stream restoration in the purest sense is the set of activities that recover the environmental health of a stream to predevelopment conditions. Full restoration is difficult to achieve in most situations because the driving forces causing the

impairment are still present in the watershed (e.g., increased runoff from urbanization). Stream rehabilitation focuses on repairing ecosystem processes, production, and services, but does not necessarily mean returning to pre-existing conditions. Stream stabilization refers to the set of activities that will control flooding, protect structures, and reduce streambank erosion in channels [Roni and Beechie, 2013].

Within streams, ecological goods and services refer to the benefits of healthy functioning ecosystems to flora, fauna, and society. These benefits include improvements to health, social, cultural, and economic conditions. Ecological goods could be clean water, aquatic habitat, or biodiversity, while ecological services could be groundwater recharge, pollutant attenuation, or providing for the fishing industry. Three common goals of stream restoration are improving water quality management, riparian zone enhancements, and in-stream habitat improvement [Bernhardt *et al.*, 2005].

Since 1990, more than \$1 billion has been spent per year on average on stream restoration projects in the United States [Bernhardt *et al.*, 2005]. The industry of stream restoration influences environmental management and policy decisions in water resources. However, there has been increasing debate as to the actual benefits of restoration projects and the scientific evidence to support its growth to such a massive industry [Lave, 2012]. This is because the majority of the restoration projects do not monitor results after completion and there is therefore little evidence of how successful or unsuccessful the projects are. For example, in the Chesapeake Bay watershed (specifically in Maryland, Pennsylvania, and Virginia) a stream restoration project has been completed on average every 16 km along streams, but only 6% of these projects included monitoring after completion [Bernhardt *et al.*, 2005]. Furthermore, the majority of these projects are performed on lengths of streams that are less than 1 km, which should make monitoring reasonably manageable. Therefore, an important direction for the future of the restoration field is increasing monitoring to provide practical data that can help better link restoration practices and resulting outcomes to ecosystem goods and services.

The stream restoration industry continues to grow, particularly because of mitigation banking, in which credits under Section 404 of the Clean Water Act can be bought or sold in order to offset impact streams or wetlands. However, even the current regulations do not have incentives to actively monitor restoration projects and success. As a result, it is perceived that

there is and will continue to be a net loss in the physical, chemical, and biological integrity of streams as a result of the mitigation banking industry [Doyle and Shields, 2012].

Problem Statement: The degraded state of streams, the potential of stream restoration to improve ecosystem goods and services, and the booming economic state of the stream restoration industry warrants collaborative efforts between practitioners and researchers to identify the most effective and sustainable designs and management strategies for restoration projects. This dissertation links the hydrologic structure of streams to resulting stream functions, focusing on surface water and groundwater interaction dynamics. Making such a connection is a critical step in mitigating existing and future water quality impacts, improving ecological functions, and sustainably managing water resources.

1.2 HYPORHEIC EXCHANGE AND OCCURRENCE ALONG STREAMS

The hyporheic zone is the region where surface water and groundwater interact in the subsurface of streams [Triska *et al.*, 1989a]. Surface water is generally high in dissolved oxygen and nutrients, while groundwater tends to be low in dissolved oxygen and high in inorganic solutes [Brunke and Gonser, 1997]. The mixing of these two water bodies creates unique and beneficial conditions that facilitate stream temperature buffering, biogeochemical cycling, and pollutant attenuation, while fostering new habitat [Boulton *et al.*, 1998; Brunke and Gonser, 1997; Dent *et al.*, 2000; Groffman *et al.*, 2005]. The value of these ecosystem services is underscored by recent recommendations that they be included among possible stream restoration goals [Boulton, 2007; Hester and Gooseff, 2010]. Previous research has shown that the extent of these functions is dependent on residence times [Brunke and Gonser, 1997; Valett *et al.*, 1996; Ward *et al.*, 2011; Zarnetske *et al.*, 2011], but the net effect of a particular hyporheic function is also dependent on the relative magnitude of surface and hyporheic flows (e.g., cooling/buffering of downstream surface water [Arrigoni *et al.*, 2008], biogeochemical processing [Findlay, 1995]). Conceptualization of hyporheic zone flow paths can be divided into two categories known as the “lung” and “gill” models, respectively [Sawyer *et al.*, 2009]. In the lung model, rapid variations in river water levels cause significant flow reversals between low and high flows, whereas in the gill model, background groundwater levels constrain flow directions to be similar during low and high flows.

There are five general mechanisms of hyporheic exchange that occur along streams: turbulent exchange, hydrostatic exchange, hydrodynamic exchange, turnover exchange, and transient exchange [Kaser *et al.*, 2009; Wondzell and Gooseff, 2013].

Turbulent exchange is the transfer of water and momentum between the surface stream and shallow subsurface [Nagaoka and Ohgaki, 1990; Packman and Bencala, 2000]. Turbulent exchange is driven by the slip velocity at the sediment interface due to the stream velocity vectors penetrating the shallow bed [Wondzell and Gooseff, 2013]. Turbulent exchange may be most important in streams with coarse porous media [Packman *et al.*, 2004] and with high gradient streams, such as mountain streams [Tonina and Buffington, 2009]. The presence of flow obstructions, such as rootwads and geomorphic steps, can increase penetration of surface water turbulence [Buffington *et al.*, 2002] thus increasing transfer momentum transfer into the subsurface and turbulent exchange.

Hydrostatic exchange occurs due to variation in water surface elevation along the stream channel. Hydrostatic exchange is driven by hydraulic head gradients between the surface stream and subsurface. Vertical hydrostatic exchange is commonly driven by geomorphic structures, where downwelling occurs upstream of the structure and upwelling after the structure. For example, hydrostatic forces drive hyporheic exchange from riffle-pool sequences [Ibrahim and Steffler, 2012; Tonina and Buffington, 2009], Weirs [Hester *et al.*, 2009], steps [Endreny *et al.*, 2011; Hester and Doyle, 2008], cross-vanes [Crispell and Endreny, 2009], J-hooks [Crispell and Endreny, 2009], and large wood [Sawyer *et al.*, 2011]. These types of geomorphic structures are frequently used in stream restoration activities and can drive both vertical and lateral exchange [Buchanan *et al.*, 2012; Radspinner *et al.*, 2010]. Lateral hydrostatic exchange commonly occurs through meander bends, where a hydraulic head differential between upstream and downstream that promotes cross-meander flow [Boano *et al.*, 2006; Cardenas, 2008; Revelli *et al.*, 2008] and additionally stream-riparian or stream-floodplain connectivity. In particular, meander bends are sometimes used as restoration tools to reestablish ecosystem function, and commonly used in restoration design to reintroduce natural sinuosity [Jacobson *et al.*, 2011].

Hydrodynamic exchange is caused by form drag behind geomorphic features and the building of velocity heads [Elliott and Brooks, 1997a; b]. Hydrodynamic exchange is an important hyporheic exchange process in dunes, some low-gradient riffle-pool sequences, and ripple beds [Buffington and Tonina, 2009; Tonina and Buffington, 2009; Wondzell and Gooseff,

2013]. In high K sediments where geomorphic features create form drag, large velocity heads may additionally cause significant hydrodynamic exchange [Salehin *et al.*, 2004]. Such cases may exist in stream restoration projects where the bed has become coarsened (i.e., naturally or by man) to avoid erosion, and channel-spanning in-stream structures are used to dissipate energy or concentrate flow (e.g., Buchanan *et al.* [2012]).

Turnover exchange is vertical exchange between the stream and shallow bed. Turnover exchange occurs when sediment is mobilized and pore space water is entrained into the water column [Elliott and Brooks, 1997b; Packman and Brooks, 2001]. Deposition of sediment can then trap water again in the subsurface. This type of hyporheic exchange is common with beds with frequent sediment transport or moving bedforms, such as sand bed streams with dunes or ripples [Buffington and Tonina, 2009]. Turnover exchange is therefore dependent on the size and frequency of the bedforms and the bedload transport within the stream [Buffington and Tonina, 2009; Tonina and Buffington, 2009].

Transient exchange is the storage of water in the bed or banks of streams due to temporal variations in water levels. When stream water levels are higher than the adjacent groundwater table, floodplains and riparian vadose zone pore spaces fill with water. Once stream water levels fall below the adjacent groundwater table, water is released from pore spaces back to the stream. During storm events, this hydrologic process is known as bank storage [Pinder and Sauer, 1971], but the concept also applies to water level fluctuations caused by daily snowmelt, evapotranspiration, hydropeaking, and tidal fluctuations [Arntzen *et al.*, 2006; Francis *et al.*, 2010; Loheide and Lundquist, 2009; Peterson and Connelly, 2001; Sawyer *et al.*, 2009; Westbrook *et al.*, 2005; Wondzell *et al.*, 2010].

The above mentioned mechanisms of hyporheic exchange occur frequently in natural streams and are achieved via common restoration practices. Additionally, these mechanisms can be augmented by increases to K . Some studies advise that increasing the K is important to increasing hyporheic exchange benefits [Kasahara and Hill, 2007]. Coarse sediments are often added in stream restoration projects to increase bed and bank stability. The addition of coarse sediments increases K , which in turn increases hyporheic flow rates. Yet upstream sources of fine sediment can later clog the interstices of such sediment placements, reducing their effectiveness in the long term [Brunke, 1999]. Also, the majority of restoration projects utilize in-stream structures (e.g. log steps, weirs, cross vanes) and landscape management techniques

(riparian enhancements) to manage water quality, storm water, the riparian zone, and floodplain connection [Bernhardt *et al.*, 2005; Buchanan *et al.*, 2012]. These implementations promote surface-groundwater exchange. However, the extent of benefits and conditions for which they perform stream functions are a focus of research. In particular, the K of the sediments where these restoration practices are placed may be the key in determining their net effects on stream functions.

1.3 THE HYPORHEIC ZONE AND STREAM FUNCTIONS

In the following paragraphs, the ecological and water quality functions of hyporheic exchange and their conditions for occurrence are described. Hyporheic functions are categorized into those that require sufficient residence times to occur (rate-limited) and those are maximized by maximizing flow rates through the hyporheic zone (flow-limited).

1.3.1 Pollutant attenuation and biogeochemical reactions

Redox gradients and entrained carbon create heterogeneous environments which can allow diverse pollutant attenuation reactions within the hyporheic zone. The hyporheic zone can either facilitate aerobic reactions and degradation or anaerobic reactions and degradation, depending on the presence of dissolved oxygen and other electron acceptors. Petroleum hydrocarbons and chlorinated solvents can sorb or bind to sediments or volatilize through the unsaturated zone [Conant *et al.*, 2004; Kim *et al.*, 1995; Landmeyer *et al.*, 2010; Smith and Lerner, 2008]. Inorganic pollutants (e.g., nitrates) and heavy metals (e.g., nickel, lead, zinc) can also be sorbed or bound to sediment [Fuller and Harvey, 2000; Gandy *et al.*, 2007; Moser *et al.*, 2003]. The hyporheic zone can also act as a sink for upwelling groundwater pollutants, such as arsenic [B V Brown *et al.*, 2007]. Sufficient residence times are important for both sorption to sediment surfaces or rate-limited reactions (e.g., anaerobic conditions for reactions), and hence attenuation of pollutants in the hyporheic zone.

The hyporheic zone can harbor diverse microbial communities due heterogeneous movement of water and nutrients [Lowell *et al.*, 2009]. These microbial communities facilitate many of reactions described earlier, such as aerobic consumption of petroleum hydrocarbons. These microbial communities can also facilitate important biogeochemical cycling of nutrients (nitrogen, phosphorus, and carbon) and also attenuate pollutants. In particular, denitrification of nitrate-polluted streams can be an important function of hyporheic exchange [Bardini *et al.*, 2012; Clement *et al.*, 2003; Zarnetske *et al.*, 2011]. Suboxic conditions are required for microbes

to convert nitrate to inert nitrogen gas via denitrification. Suboxic conditions require labile dissolved organic carbon (DOC), which in turn depends on hyporheic exchange or particulate carbon entrainment into sediments [Triska *et al.*, 1989b; Valett, 1993]. On the other hand, suboxic conditions also require sufficient hyporheic residence times to allow microbial respiration to utilize DOC and generate oxygen depletion. The overall significance of denitrification of excess nitrate migrating downstream in surface water will therefore be dependent on the balance between hyporheic exchange of water (enhanced by higher hydraulic conductivity [K]) and longer residence times (enhanced by lower K).

1.3.2 In-stream peak discharge reduction and groundwater recharge

Urban and agricultural land use practices (e.g., increasing impervious areas, removing vegetative cover) can increase surface runoff and increase peak stream flows. Higher peak flows can cause erosion of the channel banks and bed and can sweep aquatic organisms out of their habitat and downstream. For example, young fish are weaker swimmers and look for habitat with lower water velocities [Keeley and Slaney, 1996]. Bank storage influences the stream hydrograph by reducing peak flows during storm events and extending durations, and also promotes groundwater recharge [Jung *et al.*, 2004; Kondolf *et al.*, 1987]. Additionally, hydrologic fluctuations during bank storage can promote biogeochemical reactions or attenuate pollutants within the floodplain and riparian zone [Burt *et al.*, 2002; Gu *et al.*, 2012]. The K of the subsurface governs the magnitude and extent of bank storage. The functions of peak discharge reduction and groundwater recharge are limited by flow rate through the hyporheic zone. Comparatively, biogeochemical reactions and pollutant attenuation require sufficient residence times and thus are limited by residence time.

1.3.3 Stream temperature buffering, cooling, regulation

Hyporheic exchange can impact stream temperatures in the benthic layer, in deeper sediments, and in the downstream surface water column. As a result, hyporheic exchange increases thermal heterogeneity in the subsurface and can moderate surface water temperatures [Arrigoni *et al.*, 2008; Poole and Berman, 2001]. However, previous research is inconclusive to the net effect and magnitude of the impact. Arrigoni *et al.* [2008] demonstrated that cooling, buffering, and lagging all occur along hyporheic flowpaths with the potential to affect surface stream temperatures, although cooling may be insignificant. Hester *et al.* [2009] showed that hyporheic exchange under a weir increased thermal patchiness but had minimal thermal effects

on downstream surface water. Similarly, *Sawyer et al.* [2012] showed that for the case of channel spanning log structures, thermal patchiness increased around structures with minimal effect on downstream surface water temperatures. Among these publications, there are variations in flow geometry, hydrologic setting, and structure type. However, the most important variable may be the K of the porous media, which controls the mixing rate between surface water and groundwater. *Johnson* [2004] showed that stream temperatures could be buffered by 8.6°C at maximum and 3.4°C at minimum in a coarse alluvial stream where surface water-groundwater interaction occurred. Similarly, *Cardenas and Wilson* [2007c] showed that bedform-driven advection in dunes is important when K is higher than that of a coarse sand. However, for these and similar studies, the net thermal effects of hyporheic exchange (e.g., downstream surface water cooling, thermal heterogeneity) were not directly quantified.

1.3.4 Habitat creation, diversity, and refugia

The hyporheic zone is home to a range of aquatic organisms, including fungi, protozoa, invertebrates, and vertebrates [*Allan and Castillo*, 2007]. For example, stonefly nymphs, mayflies, worms, crayfish, crab are macroinvertebrates that can be found in streams and dig burrows within the hyporheic zone [*T T Brown and Brown*, 2011]. Similarly, vertebrates such as muskrats, minks, beavers, belted kingfishers and box turtles live in or near streams and make burrows within the hyporheic zone [*T T Brown and Brown*, 2011]. Additionally, a variety of migratory fish such as salmonids lay their eggs within the hyporheic zone [*Geist*, 2000; *Quinn*, 2005].

When rates of hyporheic exchange increase, the hyporheic zone can extend and habitat is created for those organisms that prefer the physiochemical properties of the hyporheic zone (e.g., low water velocities, dark, buffered temperatures, sufficient dissolved oxygen from surface water). During storm events or other times when there is increased environmental stress, organisms can seek refuge within the hyporheic zone. For example, crayfish and salamanders burrow into hyporheic sediments during periods of drought [*Boulton*, 1989]. Upwelling groundwater in the hyporheic zone can also provide ideal physiochemical conditions for aquatic organisms. For example, during winter, warmer upwelling water through the hyporheic provides thermal stability for aquatic organisms [*Curry and Noakes*, 1995; *Power et al.*, 1999]. Ecology within the hyporheic zone is influenced by flow rates and residence times, which influence interstitial velocities, organic matter content, dissolved oxygen concentration, and temperature

[Boulton, 2007; Doleolivier and Marmonier, 1992; Strayer et al., 1997]. For instance, cooler upwelling water that is not fully de-oxygenated but still nutrient laden can be preferred habitat for spawning [Baxter and Hauer, 2000; Curry and Noakes, 1995; Nielsen et al., 1994].

1.4 DARCY'S LAW AND VARIABILITY OF K

Hyporheic hydraulics are most commonly assessed using Darcy's Law to find groundwater flow rate (Q), where $Q=KiA$ (" K " is the hydraulic conductivity in m/s, " i " is the hydraulic gradient in m/m, " A " is the cross sectional flow area in m^2). i depends on stream geometry, and can be enhanced with in-stream structures (e.g., log steps) or geomorphic features [Hester and Doyle, 2008; Hester et al., 2009]. A depends on the structure of the subsurface. For example, subsurface confining layers such as bedrock or low permeability clays can decrease A [Tonina and Buffington, 2009]. Finally, K is highly variable in space and time, and it is difficult to characterize heterogeneity in the field for use in flow calculations. Instead, most groundwater flow models represent complicated heterogeneous K fields with an effective K (K_{eff}) in an effort to capture the net averaged effect of that heterogeneity at a larger scale [Lamontagne et al., 2005]. However, simplification of heterogeneity in the sediment matrix can misrepresent subsurface hydraulics by orders of magnitude [Cey et al., 2006]. As a result, the accuracy of hyporheic flow models is dependent on the estimations of K or simplifications of subsurface heterogeneity [Poole et al., 2002; Poole et al., 2006].

K has been shown to vary over 8 orders of magnitude in stream or river beds [Calver, 2001] and varies in both space and time [Genereux et al., 2008; Song et al., 2010b]. This variability is well documented; for example, K was shown to spatially range from $4.6 \cdot 10^{-6}$ to $1.2 \cdot 10^{-3}$ m/s for a single stream in Nebraska [Song et al., 2010b]. Seasonal weather patterns and flood events can promote surface runoff that carries sediment to the stream. The deposition of finer sediments in the streambed can clog the pore spaces (colmation) and restrict hydrologic exchange [Brunke, 1999]. Conversely, the deposition of coarser sediments or flushing of fines can encourage infiltration and surface-groundwater exchange. As a result, the average stream sediment K can range from $5.2 \cdot 10^{-6}$ to $2.7 \cdot 10^{-4}$ m/s over a year [Genereux et al., 2008]. Even values of K much greater than 10^{-3} m/s (corresponding to gravel) are commonly studied in hyporheic laboratory experiments [Salehin et al., 2004], hyporheic models [Endreny et al., 2011; Hester and Doyle, 2008], and observed in the hyporheic zone in nature [Kasahara and Wondzell, 2003; Poole et al., 2004; Poole et al., 2008; Wondzell et al., 2009]. Consequently, K

is a key variable in determining hyporheic flow rates [Boulton *et al.*, 2010; Findlay, 1995; Hester and Doyle, 2008; Hester and Cranmer, 2012; Valett *et al.*, 1996].

In previous studies of in-stream structures, researchers have explored the effects of structure size, channel geometry, surface stream and groundwater hydraulic conditions, channel slope, and substrate thickness [Hester and Doyle, 2008; Ibrahim and Steffler, 2012]. In contrast to K , channel geometries and structure size generally vary by less than an order of magnitude along a particular stream reach [Hester and Doyle, 2008; Kasahara and Wondzell, 2003]. Furthermore, the effect of weir height on hyporheic flow is linear and predictable [Hester and Doyle, 2008; Hester *et al.*, 2009]. While surface stream discharge changes with precipitation and with runoff, its variation generally does not exceed a few orders of magnitude, except during the largest of storms, and has little effect on hyporheic hydraulics [Hester and Doyle, 2008]. Similarly, ambient groundwater conditions can rise and fall, but water levels do not change by orders of magnitude [Hester and Doyle, 2008]. Therefore, among the various controlling variables, K can vary the most and hence has the largest impact on hyporheic hydraulics [Hester and Doyle, 2008; Sawyer *et al.*, 2012].

1.5 DEVIATIONS FROM DARCIAN PREDICTIONS OF HYPORHEIC EXCHANGE

There are several assumptions implicit in Darcy's law, including steady flow, constant temperature, laminar flow, homogenous media, and a single, incompressible fluid. The laminar flow assumption is commonly checked via the Reynolds Number (Re) and assumed valid when $Re \leq 1$. From $1 < Re < 100$ flow is considered non-Darcy, yet still laminar flow occurs, while at $Re > 100$ turbulent groundwater flow occurs [Freeze and Cherry, 1979]. In coarse sediments exhibiting high K or with high hydraulic gradients, inertial forces may become important and non-Darcy flow may become significant [Freeze and Cherry, 1979]. The tradeoff between viscous (Darcy) and inertial (non-Darcy) forces at the sediment interface has been shown to affect mass and momentum transport in porous media [Nagaoka and Ohgaki, 1990]. Non-Darcy flow layers facilitate momentum and mass transfer and act as a transition between surface water and groundwater. Non-Darcy flow layers near the bed surface have been shown to experience increased turbulent and hydrodynamic exchange, and may provide ecological and biogeochemical function [Marion *et al.*, 2008].

The most common modification to Darcy's law to account for inertial forces is Forchheimer's extension [Tonina and Buffington, 2009]. The Forchheimer extension

incorporates an inertial loss term in Darcy's law to account for form drag of porous media in regions of non-Darcy flow [Nield and Bejan, 2006]. The Forchheimer extension is mathematically a pressure drop within the Navier-Stokes momentum equation, to be used in the presence of non-Darcy flows. The Forchheimer extension has been tested and validated experimentally [Macini *et al.*, 2011; Sobieski and Trykozko, 2011] and computationally [Ahmadi *et al.*, 2010; Papathanasiou *et al.*, 2001; Thauvin and Mohanty, 1998]. However, there exists a wide range of options in calculating the Forchheimer coefficient, which makes selection difficult and often case dependent [Sobieski and Trykozko, 2011; Thauvin and Mohanty, 1998].

Computational fluid dynamics (CFD) software, such as COMSOL, Fluent, CFX, or Flow3d, can simulate hydrodynamics of surface water or groundwater, including non-Darcy flows. In addition to calculating momentum, mass, and energy transfer, CFD software is useful because it can handle complex geometries and provide higher level accuracy [Wendt, 2008]. For example, in surface water, CFX has been used to predict complex flows around in-stream structures [Shen and Diplas, 2008]. In groundwater, CFX has been used to characterize non-Darcy flow at the particle scale [Cheng *et al.*, 2008]. However, in the hyporheic zone, most models in publication to date divide hyporheic hydrodynamics into separate surface water and groundwater models and do not consider non-Darcy flows [Cardenas and Wilson, 2007a; b; c; Hester and Doyle, 2008]. Yet, fully coupled surface water-groundwater CFD models may be necessary in some cases, because simulating non-Darcy flows, turbulent exchange, and hydrodynamic exchange can be important to spatially and temporally track hyporheic flows and determining hyporheic flow rates. These hydrologic processes in turn may influence solute transport, biogeochemical reactions in the hyporheic zone, and determine downstream impacts of hyporheic exchange [Packman *et al.*, 2004].

1.6 PREFERENTIAL FLOW PATHS AND MACROPORES

Preferential flow paths are corridors of higher K that control water and solute transport through porous media. Macropores are a type of preferential flow path devoid of sediment and larger than the local pore space size of the media. Macropores in agricultural floodplains from the dry fracture of soils [Blake *et al.*, 1973], earthworm burrows [C A Edwards and Lofty, 1977; W M Edwards *et al.*, 1979], and the decay of plant roots [Aubertin, 1971; Beasley, 1976] have been shown to dominate solute transport in the subsurface. Macropores in groundwater from the fracture of bedrock have been shown to increase flow rates by orders of magnitude [Zhan *et al.*,

2011]. Macropores have not been extensively studied within the hyporheic zone, yet a growing number of studies suggest they are common [Bohlke *et al.*, 2007; Gormally *et al.*, 2011; Newman and Keim, 2013]. For instance, macropores are created by burrowing fauna, including macroinvertebrates (e.g., stonefly nymphs, mayflies, worms, crayfish, crab, mussels, clams), birds (e.g., belted kingfisher, bank swallows), mammals (e.g., mink, beaver, coypu, muskrat), and reptiles (e.g., box turtles) [Allen and Vaughn, 2009; T T Brown and Brown, 2011; Shields and Kelly, 1997; Wright *et al.*, 2011; Xin *et al.*, 2009], as well as bioturbation by benthic macroinvertebrates [DiStefano *et al.*, 2009; Mermillod-Blondin and Rosenberg, 2006; Mermillod-Blondin *et al.*, 2004; Nogaro *et al.*, 2006; Song *et al.*, 2010a].

The spatial characteristics (e.g., frequency, size, inter-connectivity) of macropores are important in determining flow rates through macropores [Matthai and Belayneh, 2004]. The spatial characteristics may vary widely with macropore creation mechanism and local stream conditions (e.g., hydrology, geology). For example, crayfish burrows can start in the surface channel, extend well into the banks and groundwater zone, and extend through the parafluvial zone [Williams *et al.*, 1974]. Soil pipes formed by subsurface erosion can connect the floodplain and hillslopes to the surface channel [Fox and Wilson, 2010; Holden, 2005; Jones, 1971; Jones and Cottrell, 2007]. Jones and Cottrell [2007] measured soil pipe interspacings from 4.75 to 15.75 m, mean diameters from 5.0 to 10.5 cm, and mean heights above thalweg from 24.2 to 56.6 cm. Noguchi *et al.* [1999] found most macropores in the unsaturated zone of a forested hillslope were 2 to 62 cm in length and mostly discontinuous. These studies provide macropore spatial dimensions but do not quantify the characteristics and distribution of all types of macropores along a range of stream channels.

The current paradigm conceives the hyporheic zone as providing appreciable benefits to the surface stream only in coarser sediments where high surface-groundwater exchange rates can occur directly through porous media itself [Boulton *et al.*, 1998; Findlay, 1995; Kasahara and Hill, 2007]. Under this rationale, coarse grained sediments must be added to or replace finer grained sediments to achieve significant hyporheic exchange [Kasahara and Hill, 2007]. The presence of preferential flow paths such as macropores can increase hyporheic exchange in finer sediments, in turn potentially enhancing functions of hyporheic exchange, yet has not been evaluated.

1.7 RESEARCH OBJECTIVES

The goal of this research was to quantify the effect of variability and heterogeneity of K on hyporheic exchange hydraulics and the implications for stream functions. The specific objectives addressed by this research are the following:

CHAPTER 2: *Hydraulic and Thermal Effects of In-Stream Structure-Induced Hyporheic Exchange: Identifying Threshold Hydraulic Conductivities that Control System Response*

- ❖ Investigate the effect of varying K on hyporheic hydraulics and stream temperature dynamics near in-stream structures by creating a fully-coupled surface water-groundwater CFD hydraulics model and a groundwater CFD temperature model

CHAPTER 3: *Macropores as Preferential Flow Paths in Meander Bends*

- ❖ Quantify the impact of macropores on hyporheic hydraulics and solute transport through meander bends by performing electrical resistivity imaging, falling head tests, and tracer injection experiments

CHAPTER 4: *Macropores along Stream Channels: Abundance, Dimensions, and Effects on Surface Water-Groundwater Exchange*

- ❖ Characterize the spatial characteristics of surface-connected macropores along streams in the Appalachian province of southwestern Virginia and quantify their impact on bank storage by conducting reach scale field surveys, hydroperiod analyses, and monitoring riparian groundwater level and temperature fluctuations during storms

1.8 ORGANIZATION OF DISSERTATION

This dissertation is comprised of three chapters that represent three separate manuscripts that are in various stages of journal submittal and acceptance. Accepted publications are reprinted here with permission from the publisher of the journal. The chapters of this dissertation are:

- ❖ Chapter 2: *Hydraulic and Thermal Effects of In-Stream Structure-Induced Hyporheic Exchange: Identifying Threshold Hydraulic Conductivities that Control System Response.* This manuscript quantifies the effect of K on hyporheic exchange hydraulics and temperature dynamics near in-stream structures and identifies threshold K 's where fundamental shifts in hydraulics and temperature dynamics occur. This manuscript has been submitted to *Water Resources Research* and is in review.
- ❖ Chapter 3: *Macropores as Preferential Flow Paths in Meander Bends.* This manuscript quantifies the importance of macropores to hyporheic transport at the scale of meander bends and discusses implications for hyporheic functions. This manuscript has been published online in *Hydrological Processes* and has been reprinted in this dissertation with permission of the publisher (license # 3241640272747). DOI: 10.1002/hyp.9573.
- ❖ Chapter 4: *Macropores along Stream Channels: Abundance, Dimensions, and Effects on Surface Water-Groundwater Exchange.* This manuscript quantifies the presence and dimensions of macropores at the reach-scale of streams, identifies their impact on bank storage, discusses implications for hyporheic functions. This manuscript is currently in preparation for submission to *Freshwater Science*.
- ❖ Appendix A: *Supplementary Material to the Hydraulics Model in Chapter 2*
- ❖ Appendix B: *Supplementary Material to the Temperature Dynamics Model in Chapter 2*
- ❖ Appendix C: *Testing Ground Penetrating Radar to Characterize Macropores*
- ❖ Appendix D: *Testing Concrete to Cast Molds of Macropores along Stream Channels*

- ❖ Appendix E: *Testing the Hydrologic Connectivity of Macropores to other Preferential Flow Paths and Measuring the Hydraulic Conductivity of Macropores*
- ❖ Appendix F: *Quantifying the Effect of Macropores on Transient Storage during Baseflow*
- ❖ Appendix G: *Stream Gauge Locations and Rating Curve Data*

1.9 REFERENCES

- Ahmadi, A., A. Arani, and D. Lasseux (2010), Numerical simulation of two-phase inertial flow in heterogeneous porous media, *Transport Porous Med*, 84(1), 177-200.
- Allan, J. D., and M. M. Castillo (2007), *Stream Ecology: Structure and Function of Running Waters*. Springer, Dordrecht, The Netherlands.
- Allen, D. C., and C. C. Vaughn (2009), Burrowing behavior of freshwater mussels in experimentally manipulated communities, *J N Am Benthol Soc*, 28(1), 93-100.
- Arntzen, E. V., D. R. Geist, and P. E. Dresel (2006), Effects of fluctuating river flow on groundwater/surface water mixing in the hyporheic zone of a regulated, large cobble bed river, *River Res Appl*, 22(8), 937-946.
- Arrigoni, A. S., G. C. Poole, L. A. K. Mertes, S. J. O'Daniel, W. W. Woessner, and S. A. Thomas (2008), Buffered, lagged, or cooled? Disentangling hyporheic influences on temperature cycles in stream channels, *Water Resour Res*, 44, W09418.
- Aubertin, G. M. (1971), *Nature and extent of macropores in forest soils and their influence on subsurface water movement*, 33 p., Northeastern Forest Experiment Station, Upper Darby, Pa.
- Bardini, L., F. Boano, M. B. Cardenas, R. Revelli, and L. Ridolfi (2012), Nutrient cycling in bedform induced hyporheic zones, *Geochim Cosmochim Acta*, 84, 47-61.
- Baxter, C. V., and F. R. Hauer (2000), Geomorphology, hyporheic exchange, and selection of spawning habitat by bull trout (*Salvelinus confluentus*), *Can J Fish Aquat Sci*, 57(7), 1470-1481.
- Beasley, R. S. (1976), Contribution of subsurface flow from the upper slopes of forested watersheds to channel flow, *Soil Sci Soc Am J*, 40(6), 955-957.
- Bernhardt, E. S., et al. (2005), Ecology - Synthesizing US river restoration efforts, *Science*, 308(5722), 636-637.
- Blake, G., E. Schlichting, and U. Zimmermann (1973), Water recharge in a soil with shrinkage cracks, *Soil Sci Soc Am J*, 37(5), 669-672.
- Boano, F., C. Camporeale, R. Revelli, and L. Ridolfi (2006), Sinuosity-driven hyporheic exchange in meandering rivers, *Geophys Res Lett*, 33, L18406.

- Bohlke, J. K., M. E. O'Connell, and K. L. Prestegard (2007), Ground water stratification and delivery of nitrate to an incised stream under varying flow conditions, *J Environ Qual*, 36(3), 664-680.
- Boulton, A. J. (1989), Over-summering refuges of aquatic macroinvertebrates in two intermittent streams in central Victoria, *Trans Roy Soc of South Austral*, 113(1), 23-34.
- Boulton, A. J. (2007), Hyporheic rehabilitation in rivers: Restoring vertical connectivity, *Freshwater Biol*, 52(4), 632-650.
- Boulton, A. J., S. Findlay, P. Marmonier, E. H. Stanley, and H. M. Valett (1998), The functional significance of the hyporheic zone in streams and rivers, *Annu Rev Ecol Syst*, 29, 59-81.
- Boulton, A. J., T. Datry, T. Kasahara, M. Mutz, and J. A. Stanford (2010), Ecology and management of the hyporheic zone: Stream-groundwater interactions of running waters and their floodplains, *J N Am Benthol Soc*, 29(1), 26-40.
- Brewer, S. K. (2011), Groundwater Influences on the Distribution and Abundance of Riverine Smallmouth Bass, *Micropterus dolomieu*, in Pasture Landscapes of the Midwestern USA, *River Res Appl*, 29 (3), 269-278.
- Brown, B. V., H. M. Valett, and E. M. Schreiber (2007), Arsenic transport in groundwater, surface water, and the hyporheic zone of a mine-influenced stream-aquifer system, *Water Resour Res*, 43, W11404.
- Brown, T. T., and S. Brown (2011), *Pocketguide to Eastern Streams*, Stackpole Books Inc.
- Brunke, M. (1999), Colmation and depth filtration within streambeds: Retention of particles in hyporheic interstices, *Int Rev Hydrobiol*, 84(2), 99-117.
- Brunke, M., and T. Gonser (1997), The ecological significance of exchange processes between rivers and groundwater, *Freshwater Biol*, 37(1), 1-33.
- Buchanan, B. P., M. T. Walter, G. N. Nagle, and R. L. Schneider (2012), Monitoring and assessment of a river restoration project in central New York, *River Res Appl*, 28(2), 216-233.
- Buffington, J. M., and D. Tonina (2009), Hyporheic exchange in mountain rivers II: Effects of channel morphology on mechanics, scales, and rates of exchange, *Geography Compass*, 3(3), 1038-1062.
- Buffington, J. M., T. E. Lisle, R. D. Woodsmith, and S. Hilton (2002), Controls on the size and occurrence of pools in coarse-grained forest rivers, *River Res Appl*, 18(6), 507-531.

- Burt, T. P., et al. (2002), Water table fluctuations in the riparian zone: comparative results from a pan-European experiment, *J Hydrol*, 265(1-4), 129-148.
- Caissie, D. (2006), The thermal regime of rivers: a review, *Freshwater Biol*, 51(8), 1389-1406.
- Calver, A. (2001), Riverbed permeabilities: Information from pooled data, *Ground Water*, 39(4), 546-553.
- Cardenas, M. B. (2008), The effect of river bend morphology on flow and timescales of surface water-groundwater exchange across pointbars, *J Hydrol*, 362(1-2), 134-141.
- Cardenas, M. B., and J. L. Wilson (2007a), Exchange across a sediment-water interface with ambient groundwater discharge, *J Hydrol*, 346(3-4), 69-80.
- Cardenas, M. B., and J. L. Wilson (2007b), Dunes, turbulent eddies, and interfacial exchange with permeable sediments, *Water Resour Res*, 43, W08412.
- Cardenas, M. B., and J. L. Wilson (2007c), Effects of current-bed form induced fluid flow on the thermal regime of sediments, *Water Resour Res*, 43, W08431.
- Cey, E., D. Rudolph, and R. Therrien (2006), Simulation of groundwater recharge dynamics in partially saturated fractured soils incorporating spatially variable fracture apertures, *Water Resour Res*, 42, W09413.
- Cheng, N. S., Z. Y. Hao, and S. K. Tan (2008), Comparison of quadratic and power law for nonlinear flow through porous media, *Exp Therm Fluid Sci*, 32(8), 1538-1547.
- Clement, J. C., L. Aquilina, O. Bour, K. Plaine, T. P. Burt, and G. Pinay (2003), Hydrological flowpaths and nitrate removal rates within a riparian floodplain along a fourth-order stream in Brittany (France), *Hydrol Process*, 17(6), 1177-1195.
- Conant, B., J. A. Cherry, and R. W. Gillham (2004), A PCE groundwater plume discharging to a river: Influence of the streambed and near-river zone on contaminant distributions, *J Cont Hyd*, 73(1-4), 249-279.
- Coutant, C. C. (1977), Compilation of temperature preference data, *Can J Fish Res Boa*, 34(5), 739-745.
- Crispell, J. K., and T. A. Endreny (2009), Hyporheic exchange flow around constructed in-channel structures and implications for restoration design, *Hydrol Process*, 23(8), 1158-1168.
- Curry, R. A., and D. L. G. Noakes (1995), Groundwater and the selection of spawning sites by brook trout (*Salvelinus-Fontinalis*), *Can J Fish Aquat Sci*, 52(8), 1733-1740.

- Dahm, C. N., K. W. Cummins, H. M. Valett, and R. L. Coleman (1995), An ecosystem view of the restoration of the Kissimmee River, *Restor Ecol*, 3(3), 225-238.
- Dent, C. L., J. D. Schade, N. B. Grimm, and S. G. Fisher (2000), Subsurface influences on surface biology, *Streams and Ground Waters*. Academic Press, San Diego, California, 381-402.
- DiStefano, R. J., D. D. Magoulick, E. M. Imhoff, and E. R. Larson (2009), Imperiled crayfishes use hyporheic zone during seasonal drying of an intermittent stream, *J N Am Benthol Soc*, 28(1), 142-152.
- Doleolivier, M. J., and P. Marmonier (1992), Patch distribution of interstitial communities - prevailing factors, *Freshwater Biol*, 27(2), 177-191.
- Doyle, M. W., and F. D. Shields (2012), Compensatory mitigation for streams under the Clean Water Act: Reassessing Science and Redirecting Policy, *J Am Water Resour As*, 48(3), 494-509.
- Dubrovsky, N. M., and P.A. Hamilton (2010), *The quality of our nation's water: Nutrients in the nation's streams and groundwater, 1992--2004*, U.S. Geological Survey, Reston, Va.
- Edwards, C., and J. Lofty (1977), Biology of earthworm, *Chaprnand and Hall, London*.
- Edwards, W. M., R. R. van der Ploeg, and W. Ehlers (1979), A Numerical Study of the Effects of Noncapillary-Sized Pores Upon Infiltration, *Soil Sci. Soc. Am. J.*, 43(5), 851-856.
- Elliott, A. H., and N. H. Brooks (1997a), Transfer of nonsorbing solutes to a streambed with bed forms: Theory, *Water Resour Res*, 33(1), 123-136.
- Elliott, A. H., and N. H. Brooks (1997b), Transfer of nonsorbing solutes to a streambed with bed forms: Laboratory experiments, *Water Resour Res*, 33(1), 137-151.
- Endreny, T., L. Lautz, and D. I. Siegel (2011), Hyporheic flow path response to hydraulic jumps at river steps: Flume and hydrodynamic models, *Water Resour Res*, 47, W02517.
- Engineering, National Academy of (2010), Grand engineering challenges. Web. 2 Feb. 2011. <<http://www.engineeringchallenges.org/cms/8996/9132.aspx>>.
- EPA, U. S. Environmental Protection Agency (2013), National rivers and streams assessment 2008–2009: a collaborative survey - Draft, edited by Office of Wetlands, Office of Research and Development EPA, Washington, DC 20460

- Federal Interagency Stream Restoration Working Group (US) (1998), *Stream corridor restoration: Principles, processes, and practices*, Federal Interagency Stream Restoration Working Group.
- Findlay, S. (1995), Importance of surface-subsurface exchange in stream ecosystems - the hyporheic zone, *Limnol Oceanogr*, 40(1), 159-164.
- Fox, G. A., and G. V. Wilson (2010), The role of subsurface flow in hillslope and stream bank Erosion: a Review, *Soil Sci Soc Am J*, 74(3), 717-733.
- Francis, B. A., L. K. Francis, and M. B. Cardenas (2010), Water table dynamics and groundwater-surface water interaction during filling and draining of a large fluvial island due to dam-induced river stage fluctuations, *Water Resour Res*, 46, W07513.
- Freeze, R. A., and J. A. Cherry (1979), *Groundwater*, Englewood Cliffs, N.J., Prentice-Hall.
- Fuller, C. C., and J. W. Harvey (2000), Reactive uptake of trace metals in the hyporheic zone of a mining-contaminated stream, Pinal Creek, Arizona, *Environ Sci Technol*, 34(7), 1150-1155.
- Gandy, C. J., J. W. N. Smith, and A. P. Jarvis (2007), Attenuation of mining-derived pollutants in the hyporheic zone: a review, *Sci Total Environ*, 373(2-3), 435-446.
- Geist, D. R. (2000), Hyporheic discharge of river water into fall chinook salmon (*Oncorhynchus tshawytscha*) spawning areas in the Hanford Reach, Columbia River, *Can J Fish Aquat Sci*, 57(8), 1647-1656.
- Genereux, D. P., S. Leahy, H. Mitsova, C. D. Kennedy, and D. R. Corbett (2008), Spatial and temporal variability of streambed hydraulic conductivity in West Bear Creek, North Carolina, USA, *J Hydrol*, 358(3-4), 332-353.
- Gilinsky, E., and NITG (2009), An urgent call to action - report of the state, EPA Nutrient Innovations Task Group (NITG). U.S. Environmental Protection Agency, Washington, D.C.
- Gormally, K. H., M. S. McIntosh, A. N. Mucciardi, and G. W. McCarty (2011), Ground penetrating radar detection and three-dimensional mapping of lateral macropores: II. riparian application, *Soil Sci Soc Am J*, 75(4), 1236-1243.
- Groffman, P. M., A. M. Dorsey, and P. M. Mayer (2005), N processing within geomorphic structures in urban streams, *J N Am Benthol Soc*, 24(3), 613-625.

- Gu, C. H., W. Anderson, and F. Maggi (2012), Riparian biogeochemical hot moments induced by stream fluctuations, *Water Resour Res*, 48, W09546.
- Hester, E. T., and M. W. Doyle (2008), In-stream geomorphic structures as drivers of hyporheic exchange, *Water Resour Res*, 44, W03417.
- Hester, E. T., and M. N. Gooseff (2010), Moving beyond the banks: Hyporheic restoration is fundamental to restoring ecological services and functions of streams, *Environ Sci Technol*, 44(5), 1521-1525.
- Hester, E. T., and E. N. Cranmer (2012), Variation of hyporheic exchange potential among urban region streams: implications for stream restoration. Environmental & Engineering Geoscience. Accepted.
- Hester, E. T., M. W. Doyle, and G. C. Poole (2009), The influence of in-stream structures on summer water temperatures via induced hyporheic exchange, *Limnol Oceanogr*, 54(1), 355-367.
- Hill, R. W., G. A. Wyse, and M. Anderson (2004), *Animal Physiology*, Sinauer Associates, Sunderland, Mass.
- Holden, J. (2005), Controls of soil pipe frequency in upland blanket peat, *J Geophys Res-Earth*, 110, F01002.
- Ibrahim, A., and P. Steffler (2012), Estimation of Hyporheic Flow in a Pool and Riffle Sequence, in *International Symposium on Ecohydraulics*. 17-21 September 2012. University of Natural Resources and Life Sciences, Vienna, Austria.
- Jacobson, R. B., T. P. Janke, and J. J. Skold (2011), Hydrologic and geomorphic considerations in restoration of river-floodplain connectivity in a highly altered river system, Lower Missouri River, USA, *Wetl Ecol Manag*, 19(4), 295-316.
- Johnson, S. L. (2004), Factors influencing stream temperatures in small streams: substrate effects and a shading experiment, *Can J Fish Aquat Sci*, 61(6), 913-923.
- Jones, J. A. A. (1971), Soil piping and stream channel initiation, *Water Resour Res*, 7(3), 602-610.
- Jones, J. A. A., and C. I. Cottrell (2007), Long-term changes in stream bank soil pipes and the effects of afforestation, *J Geophys Res-Earth*, 112, F01010.
- Jung, M., T. P. Burt, and P. D. Bates (2004), Toward a conceptual model of floodplain water table response, *Water Resour Res*, 40, W12409.

- Kasahara, T., and S. M. Wondzell (2003), Geomorphic controls on hyporheic exchange flow in mountain streams, *Water Resour Res*, 39(1), 1005.
- Kasahara, T., and A. R. Hill (2007), Instream restoration: its effects on lateral stream-subsurface water exchange in urban and agricultural streams in Southern Ontario, *River Res Appl*, 23(8), 801-814.
- Kaser, D. H., A. Binley, A. L. Heathwaite, and S. Krause (2009), Spatio-temporal variations of hyporheic flow in a riffle-step-pool sequence, *Hydrol Process*, 23(15), 2138-2149.
- Keeley, E., and P. Slaney (1996), *Quantitative measures of rearing and spawning habitat characteristics for stream-dwelling salmonids: Guidelines for habitat restoration*, Watershed Restoration Program, Ministry of Environment, Lands and Parks, British Columbia.
- Kim, H. K., H. F. Hemond, L. R. Krumholz, and B. A. Cohen (1995), In-situ biodegradation of Toluene in a contaminated stream .1. Field Studies, *Environ Sci Technol*, 29(1), 108-116.
- Koebel, J. W. (1995), An Historical-Perspective on the Kissimmee River Restoration Project, *Restor Ecol*, 3(3), 149-159.
- Kondolf, G. M., L. M. Maloney, and J. G. Williams (1987), Effects of bank storage and well pumping on base-flow, Carmel-River, Monterey-County, California, *J Hydrol*, 91(3-4), 351-369.
- Lamontagne, S., F. W. Leaney, and A. L. Herczeg (2005), Groundwater-surface water interactions in a large semi-arid floodplain: Implications for salinity management, *Hydrol Process*, 19(16), 3063-3080.
- Landmeyer, J. E., P. M. Bradley, D. A. Trego, K. G. Hale, and J. E. Haas (2010), MTBE, TBA, and TAME Attenuation in Diverse Hyporheic Zones, *Ground Water*, 48(1), 30-41.
- Lave, R. (2012), *Fields and Streams : Stream Restoration, Neoliberalism, and the Future of Environmental Science*. University of Georgia Press, Athens.
- Loheide, S. P., and J. D. Lundquist (2009), Snowmelt-induced diel fluxes through the hyporheic zone, *Water Resour Res*, 45, W07404.
- Lomolino, M. V., B. R. Riddle, and J. H. Brown (2006), *Biogeography*, Sinauer Associates, Sunderland, Mass.

- Lowell, J. L., N. Gordon, D. Engstrom, J. A. Stanford, W. E. Holben, and J. E. Gannon (2009), Habitat heterogeneity and associated microbial community structure in a small-scale floodplain hyporheic flow path, *Microb Ecol*, 58(3), 611-620.
- Macini, P., E. Mesini, and R. Viola (2011), Laboratory measurements of non-Darcy flow coefficients in natural and artificial unconsolidated porous media, *J Petrol Sci Eng*, 77(3-4), 365-374.
- Marion, A., A. I. Packman, M. Zaramella, and A. Bottacin-Busolin (2008), Hyporheic flows in stratified beds, *Water Resour Res*, 44, W09433.
- Matthai, S. K., and M. Belayneh (2004), Fluid flow partitioning between fractures and a permeable rock matrix, *Geophys Res Lett*, 31, L07602.
- Mermillod-Blondin, F., and R. Rosenberg (2006), Ecosystem engineering: the impact of bioturbation on biogeochemical processes in marine and freshwater benthic habitats, *Aquat Sci*, 68(4), 434-442.
- Mermillod-Blondin, F., R. Rosenberg, F. Francois-Carcaillet, K. Norling, and L. Mauclaire (2004), Influence of bioturbation by three benthic infaunal species on microbial communities and biogeochemical processes in marine sediment, *Aquat Microb Ecol*, 36(3), 271-284.
- Moser, D. P., J. K. Fredrickson, D. R. Geist, E. V. Arntzen, A. D. Peacock, S. M. W. Li, T. Spadoni, and J. P. McKinley (2003), Biogeochemical processes and microbial characteristics across groundwater-surface water boundaries of the Hanford Reach of the Columbia River, *Environ Sci Technol*, 37(22), 5127-5134.
- Mulholland, P. J., et al. (2008), Stream denitrification across biomes and its response to anthropogenic nitrate loading, *Nature*, 452(7184), 202-246.
- Nagaoka, H., and S. Ohgaki (1990), Mass transfer mechanism in a porous riverbed, *Water Res*, 24(4), 417-425.
- Nelson, K. C., and M. A. Palmer (2007), Stream temperature surges under urbanization and climate change: Data, models, and responses, *J Am Water Resour As*, 43(2), 440-452.
- Newman, A. E., and R. F. Keim (2013), Mesoscale connectivity through a natural levee, *Hydrol Earth Syst Sc*, 17(2), 691-704.
- Nield, D. A., and A. Bejan (2006), *Convection in porous media*, 3rd ed., 640 p., Springer, New York.

- Nielsen, J. L., T. E. Lisle, and V. Ozaki (1994), Thermally stratified pools and their use by Steelhead in northern California streams, *T Am Fish Soc*, 123(4), 613-626.
- Nogaro, G., F. Mermillod-Blondin, F. Francois-Carcaillet, J. P. Gaudet, M. Lafont, and J. Gibert (2006), Invertebrate bioturbation can reduce the clogging of sediment: an experimental study using infiltration sediment columns, *Freshwater Biol*, 51(8), 1458-1473.
- Noguchi, S., Y. Tsuboyama, R. C. Sidle, and I. Hosoda (1999), Morphological characteristics of macropores and the distribution of preferential flow pathways in a forested slope segment, *Soil Sci Soc Am J*, 63(5), 1413-1423.
- Packman, A. I., and K. E. Bencala (2000), Modeling surface-subsurface hydrological interactions, *Streams and Ground Waters*, 45-81.
- Packman, A. I., and N. H. Brooks (2001), Hyporheic exchange of solutes and colloids with moving bed forms, *Water Resour Res*, 37(10), 2591-2605.
- Packman, A. I., M. Salehin, and M. Zaramella (2004), Hyporheic exchange with gravel beds: Basic hydrodynamic interactions and bedform-induced advective flows, *J Hydraul Eng*, 130(7), 647-656.
- Papathanasiou, T. D., B. Markicevic, and E. D. Dendy (2001), A computational evaluation of the Ergun and Forchheimer equations for fibrous porous media, *Phys Fluids*, 13(10), 2795-2804.
- Peterson, R. E., and M. P. Connelly (2001), Zone of interaction between Hanford site groundwater and adjacent Columbia river, *PNNL-13674, Richland, WA*.
- Pinder, G. F., and S. P. Sauer (1971), Numerical simulation of flood wave modification due to bank storage effects, *Water Resour Res*, 7(1), 63-70.
- Poole, G. C., and C. H. Berman (2001), An ecological perspective on in-stream temperature: Natural heat dynamics and mechanisms of human-caused thermal degradation, *Environ Manage*, 27(6), 787-802.
- Poole, G. C., J. A. Stanford, C. A. Frissell, and S. W. Running (2002), Three-dimensional mapping of geomorphic controls on flood-plain hydrology and connectivity from aerial photos, *Geomorphology*, 48(4), 329-347.
- Poole, G. C., J. A. Stanford, S. W. Running, and C. A. Frissell (2006), Multiscale geomorphic drivers of groundwater flow paths: Subsurface hydrologic dynamics and hyporheic habitat diversity, *J N Am Benthol Soc*, 25(2), 288-303.

- Poole, G. C., J. A. Stanford, S. W. Running, C. A. Frissell, W. W. Woessner, and B. K. Ellis (2004), A patch hierarchy approach to modeling surface and subsurface hydrology in complex flood-plain environments, *Earth Surf Proc Land*, 29(10), 1259-1274.
- Poole, G. C., S. J. O'Daniel, K. L. Jones, W. W. Woessner, E. S. Bernhardt, A. M. Helton, J. A. Stanford, B. R. Boer, and T. J. Beechie (2008), Hydrologic spiralling: the role of multiple interactive flow paths in stream ecosystems, *River Res Appl*, 24(7), 1018-1031.
- Power, G., R. S. Brown, and J. G. Imhof (1999), Groundwater and fish—insights from northern North America. *Hydrol Process*, 13(3), 401-422.
- Quinn, T. P. (2005), *The behavior and ecology of Pacific salmon and trout*. Am Fish Soc, Bethesda, Md.
- Radspinner, R., P. Diplas, A. Lightbody, and F. Sotiropoulos (2010), River training and ecological enhancement potential using in-stream structures, *J Hydraul Eng*, 136(12), 967-980.
- Revelli, R., F. Boano, C. Camporeale, and L. Ridolfi (2008), Intra-meander hyporheic flow in alluvial rivers, *Water Resour Res*, 44, W12428.
- Roni, P., and T. J. Beechie (2013), *Stream and watershed restoration : a guide to restoring riverine processes and habitats*. John Wiley & Sons; Hoboken, NJ.
- Salehin, M., A. I. Packman, and M. Paradis (2004), Hyporheic exchange with heterogeneous streambeds: Laboratory experiments and modeling, *Water Resour Res*, 40, W11504.
- Sawyer, A. H., M. B. Cardenas, and J. Buttles (2011), Hyporheic exchange due to channel-spanning logs, *Water Resour Res*, 47, W08502.
- Sawyer, A. H., M. B. Cardenas, and J. Buttles (2012), Hyporheic temperature dynamics and heat exchange near channel-spanning logs, *Water Resour Res*, 48, W01529.
- Sawyer, A. H., M. B. Cardenas, A. Bomar, and M. Mackey (2009), Impact of dam operations on hyporheic exchange in the riparian zone of a regulated river, *Hydrol Process*, 23(15), 2129-2137.
- Shen, Y., and P. Diplas (2008), Application of two- and three-dimensional computational fluid dynamics models to complex ecological stream flows, *J Hydrol*, 348(1-2), 195-214.
- Shields, S. J., and J. F. Kelly (1997), Nest-site selection by belted kingfishers (*Ceryle alcyon*) in Colorado, *Am Midl Nat*, 137(2), 401-403.

- Smith, J. W. N., and D. N. Lerner (2008), Geomorphologic control on pollutant retardation at the groundwater–surface water interface, *Hydrol Process*, 22(24), 4679-4694.
- Sobieski, W., and A. Trykozko (2011), Sensitivity Aspects of Forchheimer's Approximation, *Transport Porous Med*, 89(2), 155-164.
- Song, J. X., X. H. Chen, and C. Cheng (2010a), Observation of bioturbation and hyporheic flux in streambeds, *Front Environ Sci En*, 4(3), 340-348.
- Song, J. X., X. H. Chen, C. Cheng, D. M. Wang, and W. K. Wang (2010b), Variability of streambed vertical hydraulic conductivity with depth along the Elkhorn River, Nebraska, USA, *Chinese Sci Bull*, 55(10), 992-999.
- Strayer, D. L., S. E. May, P. Nielsen, W. Wollheim, and S. Hausam (1997), Oxygen, organic matter, and sediment granulometry as controls on hyporheic animal communities, *Arch Hydrobiol*, 140(1), 131-144.
- Thauvin, F., and K. K. Mohanty (1998), Network modeling of non-Darcy flow through porous media, *Transport Porous Med*, 31(1), 19-37.
- Toffolon, M., A. Siviglia, and G. Zolezzi (2010), Thermal wave dynamics in rivers affected by hydropeaking, *Water Resour Res*, 46, W08536.
- Tonina, D., and J. M. Buffington (2009), Hyporheic exchange in mountain rivers I: Mechanics and environmental effects, *Geography Compass*, 3(3), 1063-1086.
- Toth, L. A., S. L. Melvin, D. A. Arrington, and J. Chamberlain (1998), Hydrologic manipulations of the channelized Kissimmee river - Implications for restoration, *Bioscience*, 48(9), 757-764.
- Triska, F. J., V. C. Kennedy, R. J. Avanzino, G. W. Zellweger, and K. E. Bencala (1989a), Retention and transport of nutrients in a 3rd-order stream in northwestern California - hyporheic processes, *Ecology*, 70(6), 1893-1905.
- Triska, F. J., V. C. Kennedy, R. J. Avanzino, G. W. Zellweger, and K. E. Bencala (1989b), Retention and transport of nutrients in a 3rd-order stream - channel processes, *Ecology*, 70(6), 1877-1892.
- Valett, H. M. (1993), Surface-hyporheic interactions in a sonoran desert stream - hydrologic exchange and diel periodicity, *Hydrobiologia*, 259(3), 133-144.

- Valett, H. M., J. A. Morrice, C. N. Dahm, and M. E. Campana (1996), Parent lithology, surface-groundwater exchange, and nitrate retention in headwater streams, *Limnol Oceanogr*, 41(2), 333-345.
- Walther, G. R., E. Post, P. Convey, A. Menzel, C. Parmesan, T. J. C. Beebee, J. M. Fromentin, O. Hoegh-Guldberg, and F. Bairlein (2002), Ecological responses to recent climate change, *Nature*, 416(6879), 389-395.
- Ward, A. S., M. N. Gooseff, and P. A. Johnson (2011), How can subsurface modifications to hydraulic conductivity be designed as stream restoration structures? Analysis of Vaux's conceptual models to enhance hyporheic exchange, *Water Resour Res*, 47, W08512.
- Wendt, J. F. (2008), *Computational fluid dynamics: an introduction*, Springer.
- Westbrook, S., J. Rayner, G. Davis, T. Clement, P. L. Bjerg, and S. Fisher (2005), Interaction between shallow groundwater, saline surface water and contaminant discharge at a seasonally and tidally forced estuarine boundary, *J Hydrol*, 302(1), 255-269.
- Westrich, J. T., and R. A. Berner (1988), The effect of temperature on rates of sulfate Reduction in marine-sediments, *Geomicrobiol J*, 6(2), 99-117.
- Williams, D. D., N. E. Williams, and H. B. N. Hynes (1974), Observations on the life history and burrow construction of the crayfish *Cambarus fodiens* (Cottle) in a temporary stream in southern Ontario, *Can J Zoo*, 52(3), 365-370.
- Wondzell, S. M., and M. N. Gooseff (2013), 9.13 Geomorphic Controls on Hyporheic Exchange Across Scales: Watersheds to Particles, in *Treatise on Geomorphology*, edited by J. F. Shroder, pp. 203-218, Academic Press, San Diego.
- Wondzell, S. M., M. N. Gooseff, and B. L. McGlynn (2010), An analysis of alternative conceptual models relating hyporheic exchange flow to diel fluctuations in discharge during baseflow recession, *Hydrol Process*, 24(6), 686-694.
- Wondzell, S. M., J. LaNier, R. Haggerty, R. D. Woodsmith, and R. T. Edwards (2009), Changes in hyporheic exchange flow following experimental wood removal in a small, low-gradient stream, *Water Resour Res*, 45, W05406.
- Wright, D. H., H. Lomeli, P. S. Hofmann, and C. Nguyen (2011), Burrow occupancy and nesting phenology of bank swallows along the Sacramento River, *Calif Fish Game*, 97(3), 138-147.
- Xin, P., G. Q. Jin, L. Li, and D. A. Barry (2009), Effects of crab burrows on pore water flows in salt marshes, *Adv Water Resour*, 32(3), 439-449.

Zarnetske, J. P., R. Haggerty, S. M. Wondzell, and M. A. Baker (2011), Dynamics of nitrate production and removal as a function of residence time in the hyporheic zone, *J Geophys Res-Biogeophys*, 116, G01025.

Zhan, H. B., J. Z. Qian, Z. Chen, and S. H. Luo (2011), Solute transport in a filled single fracture under non-Darcian flow, *Int J Rock Mech Min*, 48(1), 132-140.

CHAPTER 2: *Hydraulic and Thermal Effects of In-Stream Structure-Induced Hyporheic Exchange: Identifying Threshold Hydraulic Conductivities that Control System Response*

Garrett T. Menichino¹, Erich T. Hester¹

¹Department of Civil and Environmental Engineering, Virginia Tech, Blacksburg, VA 24061

Status: This manuscript was submitted to *Water Resources Research* in September 2013 and is in review.

2.1 ABSTRACT

In-stream structure-induced hyporheic exchange and associated thermal dynamics affect stream ecosystems, yet their importance is controlled by spatial variability of sediment hydraulic conductivity (K). We calibrated a computational fluid dynamics (CFD) model of surface and groundwater hydraulics near a channel spanning weir (represents log dams, boulder weirs) to field data and varied K from 10^{-7} to 10^{-2} m/s (silt to gravel). Surface water stopped cresting the weir and completely sunk into the bed above a $K=10^{-3}$ m/s. Non-Darcy flow was prevalent above $K=10^{-3}$ m/s, and velocity errors using non-CFD models ranged up to 32.2%. We then used CFD to analyze weir-induced heat transport during summer. As K increased from 10^{-7} to 10^{-3} m/s, weir-induced hyporheic heat advection steadily increased. Cooling and buffering along hyporheic flow paths decreased with increasing K , particularly above $K=10^{-5}$ and 10^{-4} m/s, respectively. Vertical conduction between surface water and groundwater near the weir decreased with increasing K , particularly above $K=10^{-5}$ m/s. Conduction between hyporheic flow paths and adjacent groundwater helped cool hyporheic flow. Downstream surface water cooling by hyporheic advection increased steadily with K as increases in hyporheic flow overwhelmed decreases in cooling along hyporheic flow paths. Yet such effects were small

(0.016°C) even at $K=10^{-3}$ m/s. The largest thermal effect of weir-induced exchange was therefore enhanced subsurface heterogeneity (up to ~3°C, particularly for K above 10^{-5} m/s) which increases benthic habitat diversity and may create biogeochemical hotspots. Spatial variability of weir-induced hyporheic dynamics was controlled by thresholds of $K=10^{-3}$ m/s (hydraulics) and $K=10^{-5}$ - 10^{-4} m/s (thermal).

Keywords: Surface water, Groundwater, Permeability, Computational fluid dynamics, Non-Darcy, Heat flux

Key Points

- Weir-induced hyporheic water and heat exchange vary most above threshold K 's
- Higher threshold K for hydraulics (10^{-3} m/s) than heat transfer (10^{-5} - 10^{-4} m/s)
- Largest thermal effect of exchange is increased subsurface heterogeneity

2.2 INTRODUCTION

In-stream structures are common geomorphic features in natural and restored streams. They are made of rock or wood, span part or the entire width of the channel, and obstruct flow. Structures are commonly used in restoration projects to dissipate hydraulic energy, regulate sediment transport, stabilize channels, and create habitat [Buchanan *et al.*, 2012; Radspinner *et al.*, 2010]. Structures create head drops in the surface stream, thereby inducing hydraulic head gradients in the subsurface which drive downwelling flow upstream of the structure that returns to the channel as upwelling flow downstream of the structure (i.e., hyporheic exchange) in hydrologically gaining or neutral streams. Structure types include large wood (e.g., log jams) [Briggs *et al.*, 2012], simple channel-spanning weirs [Hester and Doyle, 2008], and complex rock structures (e.g., J-hooks and cross vanes) [Crispell and Endreny, 2009]. The interaction of surface water and groundwater creates unique conditions that can facilitate stream temperature buffering, biogeochemical cycling, and pollutant attenuation, while creating unique habitat [Boulton *et al.*, 1998; Brunke and Gonser, 1997; Groffman *et al.*, 2005].

Stream temperature dynamics are particularly important because of their effect on stream ecology, chemistry, and biological function [Allan and Castillo, 2007; Caissie, 2006]. Most aquatic organisms tolerate a narrow range of temperatures [Coutant, 1977; Giller and Malmqvist, 1998; Hester and Doyle, 2011], and can be harmed by thermal shifts [Walther *et al.*, 2002]. As a result, temperature can affect the distribution and abundance of organisms in streams [Brewer, 2011]. Temperature also influences the rates of biogeochemical reactions and nutrient cycling [Allan and Castillo, 2007; Westrich and Berner, 1988]. Stream temperatures are affected by various factors such as atmospheric temperature fluctuations, groundwater seeps, riparian shading, and land use [Hester and Doyle, 2011; Johnson, 2004; Mohseni and Stefan, 1999; Poole and Berman, 2001].

2.2.1 Hyporheic Zone Hydraulics: Processes, Theory, and Modeling

Hyporheic flow rates are most commonly quantified using Darcy's Law to find groundwater flow rate (Q , L³/T), where $Q=KiA$ ("K" is the hydraulic conductivity (m/s), "i" is the hydraulic gradient (m/m), "A" is the cross sectional flow area (m²), and residence times are related to flow through velocity. K in particular varies over 8 orders of magnitude [Brassington, 2007; Calver, 2001], and is highly variable in both space [Song *et al.*, 2010b] and time [Genereux *et al.*, 2008]. Consequently, K is an important variable in determining hyporheic flow

rates [Boulton *et al.*, 2010; Findlay, 1995; Hester and Doyle, 2008; Hester and Cranmer, 2012; Valett *et al.*, 1996].

Hyporheic zones are commonly conceptualized and modeled under the premise that Darcy flow occurs everywhere (e.g., [Cardenas and Wilson, 2007b]). Darcy's law is valid when the particle Reynolds Number (Re_p , describing groundwater flow) is less than 1, indicating flow is both laminar and Darcian. From $1 < Re_p < 100$ flow is non-Darcian, yet still laminar, while at $Re_p > 100$ non-Darcy, turbulent groundwater flow occurs [Freeze and Cherry, 1979]. In coarse sediments with high K or with high i , inertial forces may become important and non-Darcy flow may become significant [Freeze and Cherry, 1979]. Non-Darcy flows occur at rates lower than those predicted by Darcy's law; therefore, applying Darcy's Law results in overestimating groundwater flow rates. This effect could be important when assessing solute/contaminant transport or hyporheic zone functions dependent on residence time. The significance of non-Darcy flows for hyporheic exchange is expected to be highly variable in space and time. For example, non-Darcy flows are expected to be more important in preferential flow areas (high K regions) or near high hydraulic head gradients (e.g., in-stream structures).

We are unaware of any studies that quantify the effect of non-Darcy flows on hyporheic hydraulics over a range of K . Computational fluid dynamics (CFD) software (e.g., Fluent, CFX, Flow3D) uses the Navier-Stokes equations and can simulate fully coupled surface water and groundwater dynamics including momentum and turbulence transfer near and across the surface water-groundwater interface [Crispell and Endreny, 2009; Endreny *et al.*, 2011a]. A fully coupled surface water-groundwater CFD is necessary to properly simulate non-Darcy flows in the hyporheic zone. However, many hyporheic models are divided into separate surface water and groundwater models [Endreny *et al.*, 2011b; Hester and Doyle, 2008; Spanoudaki *et al.*, 2009] and cannot directly simulate mass and momentum transfer between domains. Additionally, surface water dynamics drive hydrodynamic forces and turbulent diffusion, which can facilitate hyporheic exchange flows [Kaser *et al.*, 2009; Wondzell and Gooseff, 2013]. Therefore, modeling both surface water and groundwater dynamics and their interaction is critical in quantifying hyporheic exchange as well as the effect of non-Darcy flows.

2.2.2 Hyporheic Zone Temperature Dynamics: Processes, Theory, and Modeling

There is variability among the literature regarding whether bidirectional surface water-groundwater interaction (hyporheic exchange) has a significant thermal effect on surface stream

temperatures. Some studies show that it does have a significant surface water effect [Beschta *et al.*, 1987; Bilby, 1984; Johnson, 2004; Moore *et al.*, 2005]. Other studies show that weir-induced exchange increases thermal patchiness but has minimal thermal effects on downstream surface water [Hester *et al.*, 2009; Sawyer *et al.*, 2012]. One reason for the discrepancy across these studies may be the wide range of K 's investigated, which influences the proportion of surface water that cycles through the hyporheic zone. Hydraulic retention within the subsurface can lead to mixing of warmer daytime water and cooler nighttime water, causing a cooling/buffering effect along hyporheic flow paths [Arrigoni *et al.*, 2008]. Net cooling or warmer can also occur along hyporheic flowpaths in summer or winter (respectively) as surface water of seasonally varying temperature mixes with deeper groundwater of more constant temperature [Arrigoni *et al.*, 2008; Evans and Petts, 1997; Poole *et al.*, 2008; White *et al.*, 1987]. Because groundwater velocities are much less than surface water velocities, temperature trends of hyporheic flow reentering the channel can lag relative to those in surface water [Arrigoni *et al.*, 2008]. However, at the same time, the net downstream effect on surface water is dependent on the relative magnitude of surface stream flow and hyporheic flow (e.g., Arrigoni *et al.* [2008]). Therefore, increasing hyporheic flow rate (e.g., by coarsening streambeds) can increase the effects of hyporheic exchange on surface water [Findlay, 1995; Valett *et al.*, 1996].

Conduction and hyporheic heat advection can both be important heat transfer mechanisms in streambeds [Cardenas and Wilson, 2007b; Hester *et al.*, 2009]. Hyporheic heat advection is the transfer of heat between surface water and groundwater caused by movement of surface water through sediment [Story *et al.*, 2003]. Conduction is the direct transfer of heat along temperature gradients. Within the hyporheic zone, conduction can occur between sediment and porewater, between surface water and groundwater, as well as between different regions of groundwater. In this study, we focus on vertical conduction between surface water and groundwater and refer to it streambed conduction. For brevity we also refer to streambed conduction as “conduction”, unless otherwise stated.

The relative importance of hyporheic advection and conduction is controlled by K . Previous studies have found that increasing K increases hyporheic heat advection [Cardenas and Wilson, 2007b; Sawyer *et al.*, 2012]. However, these studies varied K by at most 2 orders of magnitude, and did not quantify both advection and conduction over this range. These studies thus did not quantify resultant cooling and buffering along hyporheic flow paths, and impacts of

such processes on surface water temperatures, across the wide range of K observed in streams. These studies therefore were not able to identify ranges of K when each thermal process dominates, as well as threshold K 's where cooling and buffering along hyporheic flow paths and associated thermal effects on surface and subsurface water become important.

2.2.3 Organization and Objectives of Study

We used CFD to determine the effect of varying K from silt to gravel on hyporheic hydraulics and temperature dynamics within a streambed. In our first model, we used CFD to simulate fully-coupled water column and hyporheic hydraulics over a wide range of K (>2 orders of magnitude) at a channel-spanning weir (represents log dams, boulder weirs, and similar natural and stream restoration structures) in order to determine threshold K 's and i 's when (1) weir-induced hyporheic exchange becomes large enough to affect local surface water depths and hence hyporheic gradients and flowpaths, (2) non-Darcy hyporheic flows become important including spatial patterns within hyporheic flow cells, and (3) CFD is required to properly simulate hyporheic flow. In a second model, we add heat transport processes in summer to determine threshold K 's and i 's when (4) the relative dominance of conduction and weir-induced hyporheic advection switches, cooling and buffering along weir-induced hyporheic flow paths increase more quickly, weir-induced thermal heterogeneity of the subsurface becomes important, and net downstream surface water cooling from weir-induced exchange becomes important.

2.3 METHODS

2.3.1 Hydraulics Model

2.3.1.1 Governing Equations and Background

We modeled the hydraulics of surface water-groundwater exchange near a single channel-spanning weir (representing a log dam, boulder weir, cross vane, etc.) using the three-dimensional, finite volume CFD software, ANSYS CFX. ANSYS CFX uses the Navier-Stokes equations for surface and groundwater water flow. For groundwater flow, the porous region is defined as a pressure drop in the momentum equation,

$$\frac{dp}{dx} = -\frac{\mu}{k}v - \beta\rho v^2 \quad (1)$$

where k is the permeability (m^2) and β is the inertial loss coefficient ($1/\text{m}$), also known as the non-Darcy flow coefficient or Forchheimer Coefficient. The viscous loss term uses the

permeability of the media to model Darcy flow while the inertial losses term accounts for non-Darcy flow through β .

β has been empirically calculated under a variety of conditions and depends on permeability, pore size, porosity, and tortuosity [Li and Engler, 2001; Macini *et al.*, 2011; Sobieski and Trykozko, 2011]. We calculated β from a commonly used approach, the Ergun equation,

$$\beta = \frac{a}{b^{0.5} * k^{0.5} * n^{3/2}} \quad (2)$$

where n is the porosity, k is the permeability, specifically in cm^2 , $a=1.75$, and $b=150$ [Li and Engler, 2001; Nield and Bejan, 2006]. This equation is valid for flow through porous beds of spherical particles with a wide range of inertial resistances [Andersson, 2012].

We used Reynolds Averaging of the Navier-Stokes equations for turbulence modeling, and we achieved turbulence closure with the Shear Stress Transport (SST) model in ANSYS CFX. SST combines the κ - ω model in the near-wall region with the κ - ϵ model in the free stream [Menter, 1994], including a formulated transport equation for intermittency, which triggers the regional transition of turbulence to and from laminar [ANSYS, 2011b; Menter *et al.*, 2006]. We used intermittency to identify the porous media as a laminar flow region and checked this assumption with Re during post-processing (discussed later in Methods section). We used the volume of fluid (VOF) method in ANSYS CFX to model the free surface boundary of surface water [ANSYS, 2011a].

2.3.1.2 Model Domain and Boundary Conditions

We built our model to represent the field experiment performed by Hester *et al.*, [2009] of weir-induced hyporheic exchange in Craig Creek, a 1st order stream, in Blacksburg, VA. Hester *et al.* [2009] recorded hydrostatic pressures from June 8, 2007 through June 12, 2007 in surface water, the hyporheic zone, and in floodplain groundwater for a channel spanning wooden weir that was 15.2 cm high. The channel was roughly 1.5 m wide with a baseflow discharge ranging from 0.5 to 5.0 L/s. The reach was a 10 m long riffle having a gravel substrate with an increasing percentage of sand at depth. Further details of the site, experimental setup, and data collection can be found in Hester *et al.* [2009].

The surface water portion of the model domain is a channel 1.5 m wide by 0.3 m high by 5.4 m long (Figure 2.1a). The height of the surface domain was about 35% taller than average

stream flow depth to simulate the atmosphere above the water surface and optimize VOF accuracy versus computational efficiency. A 15.2 cm tall channel-spanning weir was placed at the channel center and was 2.5 cm thick in the downstream direction. Bed slope was set to 0.008 m/m based on field survey data. Over the four days modeled (June 9, 2007 through June 12, 2007), channel discharge averaged 1.66 L/s and the maximum change in surface water levels was 2.0%, allowing us to use four-day average stream flow rate and upstream depth as the inflow boundary (surface water [SW] upstream [UPS] in Figure 2.1a). We set an outflow boundary at the downstream end of the channel (i.e., SW downstream [DS]) with hydrostatic pressure corresponding to the average observed depth of flow. CFX uses the term “wall” to refer to no flow boundaries. We used no-slip walls for the sides of the channel (walls in Figure 2-1a) and atmospheric pressure (air in Figure 2-1a) for the top. We modeled the weir (weir in Figure 2-1a) by cutting its geometry out of the surface water domain, and set the cutout as a no-slip wall. The weir did not extend into the subsurface, consistent with field conditions in *Hester et al.* [2009]. We set the bed of the channel as an interface between the surface water and groundwater domains that permitted the conservative transfer of momentum and mass (interface in Figure 2-1a). Mesh upstream and downstream of the weir consisted of rectangular prisms that were 2 cm by 4 cm (i.e., downstream length by width). The heights of these elements were 0.5 mm at the sediment interface, increased towards the free surface and transitioned to tetrahedral elements. Mesh at the nappe (i.e., water flowing over weir) consisted of 2 mm tetrahedral elements to better resolve the detailed flow at that location.

The saturated groundwater domain extended a total of 6.0 m lateral to the stream (Y direction in Figure 2-1), 2.0 m deep below the stream bottom (Z direction in Figure 2-1), and 5.4 m in the longitudinal direction (X direction in Figure 2-1). We made the sediment permeability field homogenous and isotropic [*Cardenas and Wilson, 2007a; Endreny et al., 2011a*] to isolate the impacts of changing K on hyporheic hydraulics. We used pressure inlets and outlets to represent groundwater inflow (groundwater [GW] Right, GW UPS in Figure 2-1) and outflow boundaries (i.e., GW Left, GW DS in Figure 2-1), respectively. The bottom of the groundwater domain was set as a free-slip wall (GW Bottom in Figure 2-1). Observed groundwater water levels at approximately the corners of the model domain (locations A, B, C, and D in Figure 2-1) were linearly interpolated to create hydrostatic pressure profiles for the groundwater boundaries. Similar to surface water, groundwater levels in the floodplain piezometers varied less than 2%

from the average over the four days in each well [Hester *et al.*, 2009], and we therefore kept the groundwater boundaries constant in time. Mesh in porous media consisted of rectangular prisms and tetrahedral elements with thicknesses of 0.5 mm at the sediment interface and increased with depth. Beyond 50 cm in depth, tetrahedral elements ranging from 4 to 10 cm were used. A total of over 900,000 elements were used in the mesh for both surface water and groundwater domains. Further grid refinement did not change the solution.

2.3.1.3 Parameterization of K

Hydraulic conductivity measured at the field site using falling head tests in the bed and floodplain ranged from $9.2 \cdot 10^{-4}$ to $1.8 \cdot 10^{-5}$ m/s, with a geometric mean K of $4.5 \cdot 10^{-5}$ m/s [Hester *et al.*, 2009]. We selected $K=10^{-2}$ m/s as the upper end-member case because it (along with even higher values) can be frequently found in previous field studies of naturally occurring sediments, laboratory flume studies, and modeling studies of hyporheic exchange (e.g., Calver [2001], Hester and Doyle [2008], Sawyer *et al.* [2011], Packman *et al.* [2004]). See Discussion section for more detail.

2.3.1.4 Model Output, Analyses, and Calculations

We define percent hyporheic flow as the percent of surface stream discharge that downwells upstream of the weir and returns to the surface downstream of the weir. We calculated this by dividing the hyporheic flow rate by surface water discharge,

$$Q_h = \frac{(Q_d + Q_u)/2}{Q_{ups}} \cdot 100 \quad (3)$$

where Q_h is the percent hyporheic flow rate (m^3/s), Q_d is the downwelling hyporheic flow rate upstream of the weir (m^3/s), Q_u is the upwelling hyporheic flow rate downstream of the weir (m^3/s), and Q_{ups} is the surface stream discharge upstream of the weir (m^3/s). To ensure that the flow being considered was hyporheic and not groundwater discharge/recharge, we identified the hyporheic downwelling and upwelling areas by analyzing particle traces and vector plots within the post-processor (i.e., ANSYS CFD-Post). We then used the post-processor to calculate flow rates through these areas.

We calculated the particle Reynolds number (Re_p) within the groundwater domain as,

$$Re_p = \frac{\rho D_p v}{\mu} \quad (4)$$

where D_p is the characteristic length taken to be the mean pore diameter (m). For our analyses of Darcy versus non-Darcy flow, we applied commonly used Re cutoffs (e.g., from $1 < Re < 100$ flow is non-Darcian [Freeze and Cherry, 1979]). While some of our modeled scenarios contained non-Darcy flow (see Results section), none contained turbulent flow in the groundwater domain as determined by Re always < 100 . This validated the intermittency portion of our turbulence model (i.e., subsurface was laminar) discussed earlier.

2.3.2 Temperature Dynamics Model

2.3.2.1 Domain, Governing Equations, and Boundary Conditions

In the second part of this study, we used the output of the hydraulics model as input to a model of heat transport in groundwater (Figure 2-1b). We divided the streambed interface into two model boundaries: upstream and downstream of the weir (upstream surface water [UPS SW] and downstream surface water [DS SW] in Figure 2-1b). The weir was 2.5 cm thick in the downstream direction, so the streambed at the weir was modeled as an impervious wall. Model discretization for the heat transport model was the same as in the hydraulics model.

Although we modeled surface water in the hydraulics model, we did not do so in the heat transport model because we did not have heat budget data for the surface water-air interface. Instead we used the temporally varying temperatures measured at the bottom of the surface stream water column upstream of the weir as an inlet boundary condition for our groundwater heat transport model.

For each K , we exported total pressure boundary conditions on the bed interface from the hydraulics model to act as steady-state hyporheic inflow (in downwelling areas) and hyporheic outflow (in upwelling areas) boundaries. Because we exported total pressures, which included the static and dynamic pressure, momentum transfer through the interface was preserved from the fully-coupled model. Additionally, because we imposed boundary conditions from the hydraulics model, we preserved the hyporheic flow paths, flow cells and their geometry for each K .

Thermal boundary conditions were time-varying based on data from Hester *et al.*, [2009]. The UPS SW boundary condition, which contained the hyporheic downwelling area for each K , was set to hourly stream temperatures at the bottom of the surface water column (point E in

Figure 2-1b). The DS SW thermal boundary was set as an opening, which allowed the heat from upwelling groundwater to exit, but also for conduction to occur across the streambed. We set this boundary to hourly stream temperatures in the surface channel downstream of the weir. Groundwater inflow (GW Right and GW UPS in Figure 2-1) and bottom wall (GW Bottom in Figure 2-1) thermal boundary conditions were set using hourly temperatures in the floodplain (points A, B, C, and D in Figure 2-1) and the deepest temperature probe in groundwater (point D in Figure 2-1b), respectively. Temperatures observed at point D were on average 13.5°C with little variation ($\pm 0.15^\circ\text{C}$) over the four days modeled. Thermal boundary conditions at the GW DS and GW Left were outflow boundaries that allowed the exit of heat.

The heat transport model uses heat transport equations for the fluid (i.e., water) and for the solid (i.e., sediment) [ANSYS, 2011a]. The model uses the interfacial area density (α_{fs}) between the water and sediment phases (1/m) and a heat transfer coefficient (h) to calculate heat transfer between pore water and sediment grains ($\text{W/m}^2\cdot^\circ\text{C}$) [ANSYS, 2011a; *Nield and Bejan*, 2006; *Vafai*, 2005]. We calculated α_{fs} and h from formulations proposed by *Dixon and Cresswell* [1979] and shown in *Nield and Bejan* [2006], for each K we modeled. Porosity was set to 0.3. Density and viscosities of water were held constant [*Sawyer et al.*, 2012]. Across a wide range of K , the thermal conductivity and specific heat of saturated sediment vary little [*Niswonger and Prudic*, 2003] and are often set as constant (e.g., *Cardenas and Wilson* [2007b]), so we kept these values constant (see 2.2.3 for field measurement). Furthermore, because variation in K is significantly larger than any natural variation in thermal properties we hold constant, as we expect K to have the strongest influence on heat dynamics (e.g., *Niswonger and Prudic* [2003]).

2.3.2.2 Model Calibration and Variation of Hydraulic Conductivity

We ran the heat transport model for a model time of 108 hours with transient temperature boundaries and under steady state hydraulics (representing 12:00 June 8, 2007 through 0:00 June 13, 2007). The first 12 hours of each model run was spin-up time to establish the temperature field from initializing conditions. Our calibration and subsequent analysis (Section 2.3) were therefore confined to the final 96 hours, or 0:00 June 9, 2007 through 0:00 June 13, 2007. We calibrated the model to observed temperatures in wells at 19 hyporheic zone locations in *Hester et al.* [2009] (points 1-19 in Figure 2-1b).

We used goal-driven least-squares to optimize K where modeled temperature at the 19 points best matched that observed from *Hester et al.* [2009]. Calibration was done separately at three different times, including 16:00 on June 10, 2007, 7:00 on June 11, 2006, and 0:00 on June 12, 2012, corresponding to the afternoon, morning, and midnight on three consecutive days. We used the geometric mean K of the calibrated values ($2.9 \cdot 10^{-5}$ m/s) as the basecase, which is the same order magnitude as the geometric mean ($4.5 \cdot 10^{-5}$ m/s) observed by *Hester et al.* [2009].

After calibration, the modeled K was varied from 10^{-7} to 10^{-3} m/s (silt to gravel). The upper limit of K was set to 10^{-3} m/s because that was the highest K for which our hydraulic boundary conditions were valid in the hydraulics model.

2.3.2.3 Model Output, Analyses, and Calculations

We analyzed our model results in terms of cooling (in °C) and buffering (in °C) of water temperatures along hyporheic flowpaths (i.e. upwelling hyporheic flow relative to downwelling surface water) by adapting the method of *Arrigoni et al.* [2008]. We fit the modeled upwelling hyporheic temperature time series (flow weighted average temperature of Area F in Figure 2-1b) to a sinusoidal equation, Eq. 5, using the non-linear fit function in Wolfram Mathematica to minimize standard error.

$$T_h = (0.5R) \cos((h - P) c) + M \quad (5)$$

M is the mean daily temperature, R is the diel temperature range, P is phase, T_h is the water temperature for a given hour, and c is $2\pi/24$ [*Arrigoni et al.*, 2008]. We calculated cooling as the difference in mean temperature and buffering as the difference in amplitude between downwelling (Point E in Figure 2-1b) and the fitted upwelling temperatures for each K . We calculated the subsurface diel temperature range as R in Eq. 5 for all K 's.

Hyporheic heat advection is the net heat transfer between the water column and sediments due to the movement of surface water through the subsurface. Hyporheic advective heat flux, J_a (j/s), was calculated from model output on an hourly basis using Eq. 6 [*Moore et al.*, 2005] for the range of K 's. In Eq. 6, T_d and T_u (both in °C) refer to the downwelling and upwelling temperatures and are represented by Points E and a flow weighted average over Area F in our model (Figure 2-1b), respectively. The specific heat capacity of the fluid (water), C_f , was set to 4187 J/kg·°C. The total discharge rate through the hyporheic flow cell from the hydraulics model was used for Q_h (m³/s) for each K .

$$J_a = \rho_f C_f Q_h (T_u - T_d) \quad (6)$$

Vertical conductive heat fluxes between surface water and the subsurface (i.e., streambed conduction) were calculated from model output on an hourly basis using Eq. 7 [Moore *et al.*, 2005] for the range of K 's. Streambed conduction is distinct from conduction between the hyporheic flow cell and surrounding/deeper groundwater which can influence temperatures (e.g., cool) along hyporheic flow paths. We refer to the latter process as groundwater conduction (see Results and Discussion sections). We report streambed conductive heat fluxes as the sum of conduction upstream and downstream of the weir. The conduction depth is Δz_c (m), and T_c and T_{sw} are the temperatures ($^{\circ}\text{C}$) at the conduction depth and upstream surface water, respectively. We set the conduction depth to 0.435 m and the conduction area, A_c (m^2), for downwelling (1.0 m^2) and upwelling (6.5 m^2) areas from Hester *et al.* [2009]. We measured bulk thermal conductivity λ_{fs} and bulk thermal diffusivity, α_{fs} (m^2/s), at several locations in the streambed at the field site with a Decagon KD2 Pro instrument. We observed little variation between locations and hence used average values; $\lambda_{fs}=1.95 \text{ w/m}\cdot^{\circ}\text{C}$ and $\alpha_{fs}=5.62\cdot 10^{-7} \text{ m}^2/\text{s}$. Using n , the bulk density (ρ_{fs}) and specific heat capacity (C_{fs}) were calculated as 2154 kg/m^3 and $1613 \text{ j/kg}\cdot^{\circ}\text{C}$, respectively.

$$J_c = \rho_{fs} C_{fs} A_c \alpha_{fs} \left(\frac{T_c - T_{sw}}{\Delta z_c} \right) \quad (7)$$

We calculated the effect of weir-induced hyporheic heat advection on downstream surface water temperatures using Eq. 8 [Story *et al.*, 2003]. Hyporheic heat advective flux is accounted for in the equation through Q_h and T_u . The upstream surface water temperature is T_{sw} ($^{\circ}\text{C}$). Change in downstream surface water temperatures from the mixing of hyporheic water with surface channel water, ΔT_{dssw} ($^{\circ}\text{C}$), was calculated each hour over a 24-hour period and then averaged. ΔT_{dssw} is the downstream surface water temperature change (i.e., cooling or warming) from the perspective of surface water. This temperature change is different from hyporheic cooling or buffering, which occurs along hyporheic flow paths (discussed earlier).

$$\Delta T_{dssw} = \frac{Q_h}{(Q_s - Q_h)} (T_u - T_{sw}) \quad (8)$$

Hydrodynamic dispersion, including mechanical dispersion, can affect heat transfer within the hyporheic zone and is important relative to conduction when the thermal-mechanical Peclet number (Pe_T) is 0.1 or greater [Cardenas and Wilson, 2007b]. We calculated Pe_T as,

$$Pe_T = Re \cdot Pr = \frac{nvlc_w}{\lambda_{fs}} \quad (9)$$

where l is the length scale, taken to be the longitudinal dispersivity and set to 0.01 m [Cardenas and Wilson, 2007b]. Pe_T was calculated via Eq. 9 for the highest K (10^{-3} m/s) to determine if mechanical dispersion was important to heat transfer in the models. For $K=10^{-3}$ m/s, the maximum Pe_T was $2.6 \cdot 10^{-2}$ and is localized in a region < 5 cm beneath the weir. For $K=10^{-3}$ m/s, the average Pe_T was $9.6 \cdot 10^{-4}$ and is representative of the majority of the groundwater domain. In our model, all Pe_T for the highest K were an order of magnitude or more below 0.1. As a result, mechanical dispersion was not explicitly included in the models (i.e., dispersivity was set to 0).

2.4 RESULTS

2.4.1 Hydraulics Model

2.4.1.1 Hyporheic Hydraulics and Flow Paths

The weir induced a hyporheic flow cell comprised of surface water downwelling upstream of the weir that subsequently upwelled on the downstream side of the weir. For most K 's modeled ($K \leq 10^{-3}$ m/s), surface water flowed over the top of the weir (Figure 2-2). By contrast, at $K=10^{-2}$ m/s sediment permeability was so high that no flow occurred over the weir and all surface cycled through the hyporheic flow cell beneath the weir. The percent of surface flow that cycled through the hyporheic flow cell correspondingly increased with K up to 100% for $K=10^{-2}$ m/s (Figure 2-3A).

Larger scale background groundwater head gradients in the down-valley direction produced flow diagonally across the 3D domain. This caused the upwelling hyporheic flow paths to be deflected, with some longer/deeper downwelling flow paths originating from surface water far upstream of the weir exiting through the GW Left/GW DS outlets instead of returning to the channel. We delineated the hyporheic flow cell separately for each K by filtering out just those flow paths that both downwelled from and upwelled to the channel. As K increased from 10^{-7} to 10^{-2} m/s, mean residence time predictably decreased (Figure 2-3A). At the same time, the

length and depth of the hyporheic flow cell decreased, as did the mean hyporheic flow path length and upwelling/downwelling gradients (Figure 2-3B). An obvious threshold was observed at $K \sim 10^{-3}$ m/s not only for hyporheic zone geometry, flow path lengths, and gradients (Figure 2-3B), but also for hyporheic effects on surface water (Figure 2-2).

2.4.1.2 Darcy vs. Non-Darcy Flows

We analyzed whether flow conditions were Darcian or non-Darcian by comparing the results from our default model, which used the permeability to define momentum sources in groundwater, to our non-Darcy model, which used the permeability and a quadratic loss coefficient to define momentum sources in groundwater. In the presence of large resistances (i.e., low K and low i), the groundwater flow equations used in CFX automatically reduce to a version of Darcy's law in three-dimensions [ANSYS, 2011a], and produce results analogous to commonly used groundwater transport codes such as MODFLOW. The majority of the flows encountered over the range of K and i were Darcian. At $K \leq 10^{-4}$ m/s, Darcy flow prevailed throughout the model flow domain (Figure 2-4). Non-Darcy flow existed when K and i were high. For $K = 10^{-3}$ m/s, a small patch of non-Darcy flow existed directly under the weir that extended roughly 0.08 m in the downstream direction and 0.05 m deep. At $K = 10^{-2}$ m/s, the entire flow domain was non-Darcian. So again, a hydraulic threshold existed at $K \sim 10^{-3}$. This threshold shifted with variation in i (Figure 2-5a).

Groundwater velocities and hyporheic fluxes calculated using the Darcy model overpredict those of the Darcy-Forchheimer model. This overprediction for velocities was generally very small, but increased with i to a maximum of 32.2% and 3.17% for $K = 10^{-2}$ and 10^{-3} , respectively (Figure 2-5b). Similarly, when $K \geq 10^{-3}$ m/s the hyporheic flux overprediction due to Darcy flow assumptions was significant. This overprediction was 2.2% at $K = 2.5 \cdot 10^{-3}$ m/s 10.1% at $K = 5 \cdot 10^{-3}$ m/s.

2.4.2 Temperature Dynamics Model

2.4.2.1 Hyporheic Temperature Patterns

Temperature distributions along vertical slices through the groundwater domain beneath the channel centerline for 16:00 on June 10, 2007 and 03:00 on June 11, 2007 are shown in Figure 2-6. These two times were chosen because summer surface water temperatures were near their maximum (16:00) and minimum (03:00). Streambed conduction transferred heat from

surface water into the subsurface during the day but cooled the subsurface during the night for all K 's. This is most obvious in shallow sediments, particularly for smaller K 's where the advection signal is minimal. Downwelling water upstream of the weir was warmer than upwelling water downstream of weir at 16:00, and downwelling water was cooler than upwelling water at night. This advective signal is most obvious for larger K 's (10^{-3} and 10^{-4} m/s). In particular, for $K \geq 10^{-5}$ m/s, heat transfer from surface water to hyporheic water by advection was observed as a pulse of warm water entering the model domain from surface water upstream of the weir. As K increased, this pulse of warm water became warmer and more widespread, indicated by higher temperatures throughout the hyporheic zone for $K=10^{-3}$ m/s relative to 10^{-7} m/s. For $K=10^{-5}$ m/s, this advective heat pulse (16:00) faded overnight within the hyporheic zone (03:00).

At higher K 's (10^{-4} and 10^{-3} m/s) the advective heat pulse migrated out of the hyporheic zone via the upwelling zone downstream of the weir. In particular, for $K=10^{-4}$ m/s, the heat plume observed downwelling upstream of the weir at 16:00 June 10, 2007 is stretched out over a range of upwelling flow paths 0 to 0.40 m deep by 03:00 June 11, 2007. Additionally, for $K=10^{-4}$ m/s at 16:00, there was a plume of heat about 0.80 m deep from the previous day (June 9, 2007). By 03:00 June 11, 2007, this heat plume exited the hyporheic flow cell. Finally, warm water can be seen relatively deep in the subsurface upstream of the hyporheic flow cell for $K \geq 10^{-4}$ m/s. This occurs via advection of heat originating in surface water during the day along downwelling flowpaths that do not return to the channel within the model domain. The net effect of these various thermal processes is that daily maximum thermal heterogeneity in the hyporheic zone increased with K up to $\sim 3^\circ\text{C}$ for $K > 10^{-3}$ m/s (Figure 2-6). Most of this increase occurred above a threshold K of 10^{-5} m/s.

Downwelling and upwelling temperatures exhibited cyclic diel patterns (Figure 2-7). As K increased, the amplitude of such diel cycles in upwelling water increased, and approached those in surface water. We fit the temperature profiles in Figure 2-7 to Eq. 5. Root mean square errors for parameters R and M in Eq. 5 were less than 0.15°C .

As K increased, the daily average cooling and buffering along hyporheic flowpaths decreased, while the diel amplitude at the upwelling location increased (Figure 2-8). In other words, as K increased, upwelling temperatures increasingly resembled those in surface water. Thresholds occur for buffering and cooling at $K=10^{-4}$ and 10^{-5} m/s, respectively, above which

larger decreases were observed. Similarly, daily-averaged diel temperature range increased more quickly above a threshold at $K=10^{-4}$ m/s.

2.4.2.2 Hyporheic Advection and Streambed Conduction

Hyporheic advection warmed the surface water during summer nights and early mornings, and cooled the surface water from the late mornings into early afternoons, with the magnitude of this effect varying dramatically over the range of K . Streambed conduction exhibited the same temporal trends of warming and cooling but showed less variability with K . Comparison of modeled advection and conduction results to those from *Hester et al.*, [2009] corroborate our calibrated K between 10^{-5} and 10^{-4} m/s (Section 2.2).

All daily net fluxes were cooling from the perspective of surface water (Figure 2-10). At low K ($<10^{-4}$ m/s), conduction was the dominant heat transfer mechanism. As K increased, net daily conduction decreased slightly to a threshold of $K=10^{-5}$ m/s, above which it decreased significantly. By contrast, net daily advection increased consistently with K . Total net daily heat flux (i.e., advection plus conduction) varies less than either contributing process, and was driven by conduction for $K<10^{-5}$ m/s and by the trend in advection for $K>10^{-4}$ m/s. The minimum and maximum total net daily heat fluxes are observed at $K=10^{-4}$ m/s and $K=10^{-3}$ m/s, respectively.

2.4.2.3 Downstream Surface Water Impacts of Hyporheic Advection

The estimated thermal effect of weir-induced hyporheic advection on surface water temperatures downstream of the weir exhibited diel fluctuations from weir-induced exchange, and the magnitude of the fluctuations increased with K (Figure 2-11). Temperature changes are from the perspective of the surface stream and differ from cooling or buffering that occur along hyporheic flow paths in the subsurface (i.e., Figure 2-8). For each K , downstream surface water was cooled between about 08:00 and 18:00 each day, with downstream warming the rest of the time. Downstream surface water cooling increased monotonically with K (Figure 2-12); however, downstream surface water cooling was small even at high K (e.g., 0.016°C at 10^{-3} m/s).

2.5 DISCUSSION

2.5.1 Hydraulics Model

2.5.1.1 Effect of K Variation on Hyporheic Hydraulics

The weir-induced hyporheic hydraulics we simulated fundamentally shifted at K approximately equal to 10^{-3} m/s. Surface water stopped flowing over the weir and the surface

water began noticeably sinking into the bed (Figure 2-2). This caused a decrease in surface water head gradients across the weir, which caused a decrease in downwelling and upwelling hyporheic gradients upstream and downstream of the weir (Figure 2-3B). These shifts in gradient in turn caused a reduction in the size of the hyporheic flow cell. Because we had relatively low baseflow discharge in the channel, such shifts in hydraulics may occur at higher K for higher channel discharges. Similarly, other variables, such as channel geometry, structure height, and ambient groundwater levels may influence where this shift occurs. Nevertheless, we expect the concept of a threshold would still apply. The lack of surface flow at $K > 10^{-3}$ m/s is similar to situations where streams flow into karst terrain or from glacial till (low K) to glacial outwash (high K), only to reappear even further down-stream (authors' personal observation). While surface flow disappears in intermittent or ephemeral streams as a function of time, here we discuss surface flow that disappears as a function of space due to heterogeneity of K and sometimes i . Given the high natural variability of K , quantifying the spatial and temporal variation of K is important to identifying such regions.

Another key shift in the hydraulic regime that occurred at about $K=10^{-3}$ was the advent of non-Darcy flow. Use of the Darcy model in our study resulted in maximum overestimates of groundwater velocity (and therefore hyporheic flow rate) of 32.2% at $K=10^{-2}$. While no previous hyporheic studies have calculated such errors to our knowledge, *Sobieski et al.* [2011] showed a non-linear relationship between pressures and velocities for non-Darcy flow in a column experiment. Expanding on their work, we approximated a Darcy flow model by linearly extrapolating their observed pressures and velocities at their lowest data points. We found that their observed velocities (and discharge, when flow area is the same) were more than 22% lower than a simple Darcian approximation for $K=2 \cdot 10^{-2}$ m/s. Modeling non-Darcy flow may be necessary to accurately predict flow rates in regions with high K , for instance in high gradient streams, stream restoration designs with coarse sediments, gravel streambeds [*Packman et al.*, 2004], fractured media [*Qian et al.*, 2011], and subsurface macropores [*Menichino et al.*, 2012]. These effects would be particularly important in assessing hyporheic zone functions that are dependent on residence times. We note that internal erosion is possible within sediment for certain discharges, certain head drops at the weir, and certain bed materials, but is beyond the scope of this study.

Similarly, non-Darcy flows may be important with high i , such as near geomorphic structures, including weirs or step pools [Endreny *et al.*, 2011a]. Across the range of i in our model, we showed that steep hydraulic head gradients and high hyporheic velocities near the weir can locally augment the importance of non-Darcy flow (Figures 2-4 and 2-5). This indicates that the region where the most hyporheic flow occurred had the highest inertial losses and largest deviation in velocities calculated from Darcy's law. It is therefore important to consider inertial losses and non-Darcy flows when i is high or hyporheic flow paths are concentrated. This is more likely to occur in weir or step-type structures than in dunes or riffles.

2.5.1.2 Natural Variability of K and Prevalence of High K Sediment

We focused on variation of K due to its overwhelming control on where and when hyporheic exchange has a significant effect on the surface stream. K has been shown to vary over 8 orders of magnitude [Calver, 2001] in both space and time [Genereux *et al.*, 2008; Song *et al.*, 2010b]. Our work builds on previous studies which quantified the effects of structure size, channel geometry, surface stream and groundwater hydraulic conditions, channel slope, and substrate thickness on structure-induced hyporheic exchange [Hester and Doyle, 2008; Hester *et al.*, 2009; Ibrahim and Steffler, 2012; Kasahara and Wondzell, 2003]. By contrast, previous studies on in-stream structures have quantified the effect of variation of K on structure-induced hyporheic exchange up to 2 orders of magnitude [Lautz and Siegel, 2006; Sawyer *et al.*, 2012]. Even studies of other types of geomorphic forms have only varied K up to 2 orders of magnitude [Cardenas and Wilson, 2007b; Cardenas *et al.*, 2004; Kasahara and Hill, 2008; Storey *et al.*, 2003]. One notable exception is [Hester and Doyle, 2008], which varied K over 6 orders of magnitude with in-stream structures, but did not evaluate effects on hyporheic functions like thermal processes.

Given the shift in character of hyporheic hydraulics we observed for $K > 10^{-3}$ m/s, it is important to characterize the prevalence of such coarse sediments. Such sediments are commonly studied in laboratory experiments and modeling studies. For example, Hester and Doyle [2008] modeled hyporheic exchange with a maximum K of 10^{-2} m/s. Endreny *et al.* [2011a] performed a flume experiment with a homogenous and isotropic gravel bed with a K of $3 \cdot 10^{-3}$ m/s, and afterwards modeled hyporheic exchange in the flume using CFD. Sawyer *et al.* [2011] performed a flume experiment with bed permeability of $8.5 \cdot 10^{-9}$ m², which for a temperature of 20°C is a K of $8.3 \cdot 10^{-2}$ m/s, and then modeled the subsurface with CFD.

Additionally, *Sawyer et al.* [2012] performed a hyporheic flume study with sediments of K of $3.3 \cdot 10^{-2}$ m/s, and modeled the sediments with CFD. *Cardenas and Wilson* [2007d] and *Cardenas and Wilson* [2007b] performed modeling with CFD of sediments with a maximum permeability of $5 \cdot 10^{-9}$ m² ($K=4.9 \cdot 10^{-2}$ m/s at 20°C). Finally, *Packman et al.* [2004] performed a hyporheic zone flume study of a bed K of $1.5 \cdot 10^{-1}$ m/s.

Sediments with $K > 10^{-3}$ m/s are also observed in nature. For instance, in a meta-analysis study of riverbed K 's, there were 4 studies with measured $K > 10^{-3}$ m/s and one study with measured $K > 10^{-2}$ m/s [*Calver*, 2001]. In hyporheic settings, several studies have measured $K > 10^{-3}$ m/s [*Kasahara and Wondzell*, 2003; *Poole et al.*, 2004; *Poole et al.*, 2008; *Wondzell et al.*, 2009]. *Lu et al.* [2012] measured streambed K 's up to $6.5 \cdot 10^{-3}$ m/s in streams draining from the Central Great Plains in the United States. High gradient streams in the western United States can have streambeds with K 's as high as $1.2 \cdot 10^{-1}$ m/s [*Poole et al.*, 2004]. Yet such high K 's are not confined to high gradient streams. For example, *Kasahara and Wondzell* [2003] measured K 's up to $1.5 \cdot 10^{-3}$ m/s in a 0.02 m/m gradient stream, and subsequently modeled hyporheic flows at the site with a minimum gradient of 0.005 m/m. This is consistent with the bed slope used in our modeling (0.008 m/m). Additionally, our modeling includes sediments within the adjacent floodplain and riparian zone. Regions of higher K (i.e., preferential flow paths) are frequently observed near streams [*Bridge*, 1985; *Duval and Hill*, 2006; *Fox et al.*, 2009; *Fox et al.*, 2010; *Takahashi et al.*, 2008]. For example, *Fox et al.* [2009] estimated riparian zone K 's from grain size as $7.4 \cdot 10^{-3}$ and measured K in the field as $2.7 \cdot 10^{-3}$ m/s.

2.5.2 Temperature Dynamics Model

Our work considered the thermal impacts of hyporheic exchange from three perspectives: 1) temperature changes that occur along hyporheic flow paths (i.e., cooling and buffering, Figure 2-8) the impact of such hyporheic flowpaths on subsurface thermal heterogeneity (Figure 2-6), and 3) temperature changes that occur in downstream surface water due to mixing with upwelling hyporheic flows (i.e., net daily cooling in Figure 2-12). We discuss each of these effects below.

2.5.2.1 Effects of Weir-Type In-Stream Structures on Heat Transfer across the Streambed

In our model, cooling and buffering of water traveling along hyporheic flow paths increased with hyporheic residence time and therefore decreased with K (Figure 2-8). This is consistent with *Sawyer et al.* [2012] who observed little cooling or buffering along hyporheic

flowpaths induced by a log structure where K was more than an order of magnitude higher than even our highest K ($3.3 \cdot 10^{-2}$ m/s). Similarly, *Arrigoni et al.* [2008] showed that for $K=3.5 \cdot 10^{-3}$ to $8.1 \cdot 10^{-3}$ m/s, upwelling hyporheic temperatures exhibited negligible cooling, although they were buffered 2 to 6°C. We attribute their greater buffering to their longer flow paths.

Despite this decrease in cooling along hyporheic flowpaths with increasing K , our modeling indicated that bulk cooling of downstream surface water due to mixing with weir-induced hyporheic exchange increased consistently with K (Figure 2-12). In other words, maximizing hyporheic flow rate maximized downstream surface water cooling during summer for the range of K we modeled. This means that increases in K caused increases in hyporheic flow rate that outweighed any concurrent decreases in the degree of cooling that water experienced as it travelled along hyporheic flow paths. As K increased from 10^{-7} to 10^{-3} m/s, hyporheic flow rates increased 4 orders of magnitude, whereas the average cooling of upwelling water temperatures decreased less than 1 order of magnitude.

Although few studies have explored the thermal impact of in-stream structures on surface water temperatures, our results are consistent with the small effect observed by *Sawyer et al.* [2012]. However, this effect could be increased by installing multiple weirs or similar structures, which is a common practice in stream restoration. However, such additive effects from structure sequencing would be heavily dependent on how the spacing of structures compares to distance required for thermal equilibration with atmospheric temperatures [*Hester and Gooseff*, 2011; *Mohseni and Stefan*, 1999]. Furthermore, the spacing of structures would be limited by structure height and reach slope. Depending on flow geometry and site conditions (e.g., shading and wind speed), weirs may be more important thermally as surface storage features that increase these other thermal processes (e.g., solar heating and evaporation), than by inducing hyporheic flow and associated cooling or buffering [*Sawyer and Cardenas*, 2012].

The balance of heat transfer processes between the stream water column and the subsurface in our simulations fundamentally shifted at K approximately equal to 10^{-4} m/s. Weir-induced hyporheic heat advection dominated for $K > 10^{-4}$ m/s (i.e., clean sand, gravel, and coarser), streambed conduction (computed for the same area of streambed where advection was occurring) dominated for $K < 10^{-4}$ m/s (i.e., clean sand, silt, and finer) (Figure 2-8). The increase in advection occurred due to increased hyporheic flow. The decrease in streambed conduction occurred due to concurrent decreases in temperature difference between the surface water and

hyporheic water. Because K is highly variable in space [Calver, 2001] and time [Genereux *et al.*, 2008], we expect the relative balance of hyporheic advection and streambed conduction near in-stream structures in to be highly variable. For example, streambed conduction may be the dominant hyporheic heat transfer mechanism in deep pools that have mostly fine sediments. Conversely, heat advection may be the dominant hyporheic heat transfer mechanism in riffles, which generally consist of coarser sediments.

The quantification of hyporheic heat advection and conduction over 5 orders of magnitude of K is a key result of this study. Previous studies have not simulated such a wide range of K , but nonetheless are consistent in specific ways. For example, hyporheic heat advection increased over 1.5 and 2 orders of magnitude of K , induced by dunes and channel-spanning logs, respectively [Cardenas and Wilson, 2007b; Sawyer *et al.*, 2012]. Both studies use Peclet numbers to determine the importance of advection and conduction, but do not directly quantify advective and conductive fluxes over the range of K . However, visual inspection of their results suggests a balance between advection and conduction may occur in the low range of K they modeled (i.e., $\sim 10^{-4}$ m/s in Sawyer *et al.* [2012], $\sim 10^{-3}$ m/s in Cardenas and Wilson [2007b]). Our quantification of heat fluxes over 5 orders of magnitude of K allows us to more definitively determine the K where advection equals conduction for weir-induced hyporheic exchange (estimated as $K=1.1 \cdot 10^{-4}$ m/s, Figure 2-10). We selected increments of K that were an order of magnitude apart to characterize a wide range of sediments that could likely occur in the hyporheic zone and the associated importance of advective and conductive heat transfer. Selecting smaller K increments would better resolve the trends in the results, but would not change our basic findings.

This study focuses on hyporheic advection and streambed conduction as processes that exchange heat between the surface stream and shallow groundwater in the vicinity of an in-stream structure. Nevertheless, advective heat exchange between surface water and deeper groundwater can also occur outside the hyporheic flow cell in areas of upwelling and downwelling. This is most noticeable in our results for $K \geq 10^{-4}$ m/s. For example, upstream of the hyporheic flow cell, downwelling of warmer water can be seen up to ~ 1.0 m deep (Figure 2-6). Similarly, downstream of the hyporheic flow cell, upwelling of cooler water can be seen in the shallow subsurface. K clearly has a strong effect on this background upwelling and downwelling advection as well.

2.5.2.2 Effects of Weir-Type In-Stream Structures on Hyporheic Thermal Patterns

For the lowest K where advection was significant (10^{-5} m/s), a small heat pulse entered the hyporheic zone upstream of the weir during the day (Figure 2-6, left), and faded overnight within the hyporheic zone (Figure 2-6, right), consistent with *Hester et al.* [2009]. By contrast, at higher K (10^{-4} and 10^{-3} m/s), the heat pulse seemed to migrate through the hyporheic flow cell and exit via the upwelling zone downstream of the weir. This suggests that at higher K , a coherent pulse of heat can migrate through the hyporheic zone, while at lower K the dispersive action of conduction and reduced groundwater velocities prevent formation of such a coherent migrating pulse. Thus a threshold of thermal response exists at K of $\sim 10^{-5}$ m/s. Additionally, flow paths within the hyporheic flow cell at night (right panel of Figure 2-6) at higher K (10^{-4} and 10^{-3} m/s) have already flushed the thermal pulse through the hyporheic zone, whereas deeper and longer flow paths depict lingering warmer temperatures. This is consistent with the presence of multiple flow paths layered on top of each other, each with different velocities and residence times.

Our results indicate that structure-induced hyporheic flow enhanced subsurface thermal heterogeneity both temporally (diel cycle) and spatially during summer by up to 3 °C (Figure 2-6). This effect was most pronounced above a threshold of $K=10^{-5}$ m/s (Figure 2-8). This is consistent with previous studies that showed hyporheic exchange can induce significant thermal patchiness in sediments [*Cardenas and Wilson*, 2007b; *Lautz and Fanelli*, 2008; *Sawyer et al.*, 2012]. Given the minimal thermal effects of structure-induced hyporheic advection on surface water that we observed even at high K , increased subsurface thermal heterogeneity seems to be the primary thermal signature of structure-induced hyporheic exchange. Such subsurface thermal effects can be important because they affect biodiversity by creating habitat or refuges for aquatic organisms [*Ebersole et al.*, 2003] and determines rates of biogeochemical reactions and microbial processes [*Lautz and Fanelli*, 2008]. Furthermore, the coupling of higher hyporheic thermal heterogeneity with oxygen and nutrients from surface water can create biogeochemical hotspots [*Doll et al.*, 1999; *Lautz and Fanelli*, 2008].

2.5.2.3 Effects of Weir-Type In-Stream Structures on Heat Transfer within the Streambed

In addition to heat conduction between groundwater and the surface stream (streambed conduction), conduction can also occur *within* the subsurface, and this can have important effects on advection. Our model simulated advection of hyporheic water along hyporheic flow paths,

but the heat advected along those flowpaths is affected by conduction with adjacent groundwater (outside of the hyporheic flow cell). For example, for $K=10^{-3}$ m/s at 16:00, water outside the hyporheic flow cell is cooler than water inside. This thermal gradient induces conduction that cools water that is moving along hyporheic flow paths. Although we do not independently quantify such conduction between the hyporheic flow cell and adjacent groundwater, it is simulated in the model, and therefore accounted for in our calculations of cooling and buffering along hyporheic flow paths (Eq. 6). This type of conduction is the likely reason we see a net cooling effect along hyporheic flowpaths rather than just buffering. Numerous prior studies have found similar cooling or warming along hyporheic flow paths, but they are inconclusive regarding the relative importance and magnitude of such effects. For example, some studies show that hyporheic exchange under a weir can increase subsurface thermal heterogeneity but with minimal thermal effects on downstream surface water [Hester *et al.*, 2009; Sawyer *et al.*, 2012]. Other studies show surface water-groundwater interaction can have a significant thermal effect on surface water temperatures [Johnson, 2004; Moore *et al.*, 2005; Story *et al.*, 2003].

Conduction can also occur within streambeds at smaller scales between sediment grains and porewater. When there is rapid heat advection through porous media, local thermal equilibrium (LTE) may not be achieved between the water and sediment phases at the pore scale [Haji-Sheikh and Minkowycz, 2008]. In such a non-local thermal equilibrium (NLTE) case, water and sediment are at different temperatures, and the heat transport equation must be explicitly solved for both sediment and water. Studies assessing the validity of assuming LTE have proposed guidelines for modeling [Amiri and Vafai, 1994; Vafai and Sozen, 1990]. For instance, Vafai and Sozen [1990] suggest that the suitability of the LTE model is based on the discrepancy between water and sediment temperatures (expressed in Kelvin), and is as follows; >15% is very poor, 10-15% is poor, 5-10% is fair, 1-5% is good, <1% is very good. Our model showed <0.01% change for $K=10^{-3}$ m/s, which falls in the “very good” range, suggesting that NLTE was not necessary to accurately characterize heat transport from weir-induced hyporheic exchange, and fluid-sediment heat transfer was unimportant relative to streambed conduction occurring at larger scales or to advection. Nevertheless, NLTE may be important in regions experiencing higher transport rates or greater variation of input temperatures than we modeled here; for example preferential flow paths that are directly connected to the surface stream [Menichino and Hester, 2013].

2.5.2.4 Methodological Insights and Limitations

We idealized the subsurface as homogeneous and isotropic consistent with prior hyporheic zone CFD models of hydraulics and temperature dynamics [Endreny *et al.*, 2011a; Sawyer *et al.*, 2011; 2012]. We assumed a homogenous matrix because our focus was how variation in K affected temperatures along hyporheic flow paths and in downstream surface water. In natural systems, K can be highly heterogeneous, and future studies should explore the use of heterogeneous K fields to better match real sediment conditions. For instance, in stream restoration, the streambed may be lined with coarse sediments to promote bed stability. Such layering of coarse sediments would promote increased shallow hyporheic exchange. Additionally, anisotropy is common in sediments, and vertical K is commonly assumed to be 0.1 times that of horizontal K [Duwelius, 1996; Salehin *et al.*, 2004]. Adding anisotropy would compress the vertical infiltration of heat into the subsurface. This would cause less advective heat transfer for each K , which would influence cooling and buffering along hyporheic flow paths, as well as downstream surface water impacts.

2.6 CONCLUSIONS

In the first part of this study, we present a fully coupled model of surface water-groundwater exchange induced by an in-stream structure (weir-type representing large wood, a log dam, or similar structure) using computational fluid dynamics (CFD). As hydraulic conductivity (K) increased from 10^{-7} to 10^{-2} m/s, weir-induced hyporheic hydraulics change little until a threshold K of approximately 10^{-3} m/s, when surface water stopped flowing over the weir, the entire surface discharge infiltrated the bed, and re-emerged on the downstream side of the weir. This triggered reduction in water levels upstream of the weir, decreased hydraulic gradients upstream and downstream, and reduced the size of the hyporheic flow cell.

Another important shift in the hydraulic regime was the introduction of non-Darcy flow above about $K=10^{-3}$ m/s. Use of the Darcy model resulted in overestimates of groundwater velocity (and therefore hyporheic flow rate) up to 32.2% relative to the Darcy-Forchheimer model at $K=10^{-2}$ m/s. Hyporheic fluxes, inertial losses and deviation from Darcy's law were all strongest right below the weir due to high gradients (i). Accounting for inertial losses and non-Darcy flows in CFD is important when $K>10^{-3}$ m/s and or i is high. High i and associated concentrated flow paths are more likely to occur in weir or step type structures than in dunes or riffles.

In the second part of this study, we modeled hyporheic zone hydraulics and heat transport near the weir to quantify thermal dynamics of weir-induced hyporheic exchange during summer. Cooling and buffering along weir-induced hyporheic flow paths respectively decreased from 0.20 to 0.097°C and 0.86 to 0.40°C as K increased from 10^{-7} to 10^{-3} m/s due to an associated decrease in average hyporheic residence times from 14500 to 1.39 hours. Both trends steepened above thresholds of $K=10^{-5}$ and 10^{-4} m/s, respectively. By contrast, weir-induced hyporheic exchange simultaneously increased from 0.0016% to 15.9% of surface stream discharge, greatly increasing weir-induced hyporheic advection.

The dominant heat transfer mechanism between the surface stream and the hyporheic zone was dependent on K . When $K > 10^{-4}$ m/s, hyporheic advection was dominant and when $K < 10^{-4}$ m/s, streambed conduction (vertical heat transfer between the surface stream and groundwater) was dominant. This is primarily due to decreases in conduction above a threshold of $K=10^{-5}$ m/s. Because K is highly variable in space and time, the dominant heat transfer mechanism should be highly variable along streams. Also inherent in our calculations of cooling and buffering along hyporheic flow paths was conduction between the hyporheic flow cell and adjacent groundwater (i.e., groundwater conduction). Our results suggest that such groundwater conduction is important in cooling and buffering water along hyporheic flow paths.

Average weir-induced hyporheic cooling of surface water during summer increased monotonically from $1.9 \cdot 10^{-6}$ to 0.016°C over the range of K . This trend is a net result of greater increases in hyporheic flow rate than decreases in cooling of along hyporheic flow paths. These results suggest that in natural systems, downstream surface water cooling during summer from weir-induced hyporheic exchange is maximized by maximizing hyporheic flow rates. Nevertheless, cooling of the bulk surface water column at even the maximum K in our study was small (0.016 °C). In the context of stream restoration, multiple in-stream weirs could potentially have additive thermal benefits, yet may be limited by air-stream thermal equilibration.

Perhaps the most important thermal function of weir-induced hyporheic exchange was enhanced spatial and temporal thermal heterogeneity. This heterogeneity increased with K , particularly above a thresholds of $K=10^{-5}$ and 10^{-4} m/s, respectively. The average diel temperature range increased to 2.13°C and the maximum thermal heterogeneity increased to ~3°C as K increased from 10^{-7} to 10^{-3} m/s. These temperature changes can be important to both benthic organisms and biogeochemical reaction rates.

2.7 REFERENCES

- Allan, J. D., and M. M. Castillo (2007), *Stream Ecology: Structure and Function of Running Waters*, Springer, Dordrecht, The Netherlands.
- Amiri, A., and K. Vafai (1994), Analysis of dispersion effects and nonthermal equilibrium, non-darcian, variable porosity incompressible-flow through porous-media, *Int J Heat Mass Tran*, 37(6), 939-954.
- Andersson, B. (2012), *Computational Fluid Dynamics for Engineers*, xi, 189 p. pp., Cambridge University Press, Cambridge ; New York.
- ANSYS, Inc. (2011a), *Ansys CFX-Solver Modeling Guide*, ANSYS, Inc., PA.
- ANSYS, Inc. (2011b), *Ansys CFX-Solver Theory Guide*, ANSYS, Inc., PA.
- Arrigoni, A. S., G. C. Poole, L. A. K. Mertes, S. J. O'Daniel, W. W. Woessner, and S. A. Thomas (2008), Buffered, lagged, or cooled? Disentangling hyporheic influences on temperature cycles in stream channels, *Water Resour Res*, 44, W09418.
- Beschta, R. L., R. E. Bilby, G. W. Brown, L. B. Holtby, and T. D. Hofstra (1987), Stream temperature and aquatic habitat: Fisheries and forestry interactions, in *Streamside Management: Forestry and Fishery Interactions*, edited by E. O. Salo and T. W. Cundy, pp. 191-232, University of Washington, Seattle, WA.
- Bilby, R. E. (1984), Characteristics and frequency of cool-water areas in a western washington stream, *J Freshwater Ecol*, 2(6), 593-602.
- Boulton, A. J., S. Findlay, P. Marmonier, E. H. Stanley, and H. M. Valett (1998), The functional significance of the hyporheic zone in streams and rivers, *Annu Rev Ecol Syst*, 29, 59-81.
- Boulton, A. J., T. Datry, T. Kasahara, M. Mutz, and J. A. Stanford (2010), Ecology and management of the hyporheic zone: stream-groundwater interactions of running waters and their floodplains, *J N Am Benthol Soc*, 29(1), 26-40.
- Brassington R. 2007. *Field Hydrogeology*. John Wiley: Chichester, England ; Hoboken, NJ.
- Brewer, S. K. (2011), Groundwater Influences on the Distribution and Abundance of Riverine Smallmouth Bass, *Micropterus dolomieu*, in Pasture Landscapes of the Midwestern USA, *River Res Appl*, 29(3), 269-278.
- Bridge, J. S. (1985), Paleochannel patterns inferred from alluvial deposits - a critical-evaluation, *J Sediment Petrol*, 55(4), 579-589.

- Briggs, M. A., L. K. Lautz, J. M. McKenzie, R. P. Gordon, and D. K. Hare (2012), Using high-resolution distributed temperature sensing to quantify spatial and temporal variability in vertical hyporheic flux, *Water Resour. Res.*, 48, W02527.
- Brunke, M., and T. Gonser (1997), The ecological significance of exchange processes between rivers and groundwater, *Freshwater Biol*, 37(1), 1-33.
- Buchanan, B. P., M. T. Walter, G. N. Nagle, and R. L. Schneider (2012), Monitoring and assessment of a river restoration project in central New York, *River Res Appl*, 28(2), 216-233.
- Caissie, D. (2006), The thermal regime of rivers: a review, *Freshwater Biol*, 51(8), 1389-1406.
- Calver, A. (2001), Riverbed permeabilities: Information from pooled data, *Ground Water*, 39(4), 546-553.
- Cardenas, M. B., and J. L. Wilson (2007a), Thermal regime of dune-covered sediments under gaining and losing water bodies, *J Geophys Res-Bioge*, 112, G04013.
- Cardenas, M. B., and J. L. Wilson (2007b), Dunes, turbulent eddies, and interfacial exchange with permeable sediments, *Water Resour Res*, 43, W08412.
- Cardenas, M. B., and J. L. Wilson (2007c), Effects of current-bed form induced fluid flow on the thermal regime of sediments, *Water Resour Res*, 43, W08431.
- Cardenas, M. B., J. L. Wilson, and V. A. Zlotnik (2004), Impact of heterogeneity, bed forms, and stream curvature on subchannel hyporheic exchange, *Water Resour Res*, 40, W08307.
- Coutant, C. C. (1977), Compilation of Temperature Preference Data, *Can J Fish Res Bo*, 34(5), 739-745.
- Crispell, J. K., and T. A. Endreny (2009), Hyporheic exchange flow around constructed in-channel structures and implications for restoration design, *Hydrol Process*, 23(8), 1158-1168.
- Dixon, A. G., and D. L. Cresswell (1979), Theoretical prediction of effective heat-transfer parameters in packed-beds, *Aiche J*, 25(4), 663-676.
- Doll, B. A., N. C. S. R. Institute, and N. C. S. G. C. Program (1999), *Stream Restoration: A Natural Channel Design Handbook*, North Carolina Stream Restoration Institute.
- Duval, T. P., and A. R. Hill (2006), Influence of stream bank seepage during low-flow conditions on riparian zone hydrology, *Water Resour Res*, 42, W10425.

- Duwelius, R. F. (1996), *Hydraulic Conductivity of the Streambed, East Branch Grand Calumet River, Northern Lake County, Indiana*, US Department of the Interior, US Geological Survey.
- Ebersole, J. L., W. J. Liss, and C. A. Frissell (2003), Thermal heterogeneity, stream channel morphology, and salmonid abundance in northeastern Oregon streams, *Can J Fish Aquat Sci*, 60(10), 1266-1280.
- Endreny, T., L. Lautz, and D. I. Siegel (2011a), Hyporheic flow path response to hydraulic jumps at river steps: Flume and hydrodynamic models, *Water Resour Res*, 47, W02517.
- Endreny, T., L. Lautz, and D. Siegel (2011b), Hyporheic flow path response to hydraulic jumps at river steps: Hydrostatic model simulations, *Water Resour Res*, 47, W02518.
- Evans, E. C., and G. E. Petts (1997), Hyporheic temperature patterns within riffles, *Hydrolog Sci J*, 42(2), 199-213.
- Findlay, S. (1995), Importance of surface-subsurface exchange in stream ecosystems - the hyporheic zone, *Limnol Oceanogr*, 40(1), 159-164.
- Fox, G. A., J. W. Fuchs, D. E. Storm, C. J. Penn, and G. O. Brown (2009), Subsurface transport of phosphorus in riparian floodplains: influence of preferential flow paths, *J Environ Qual*, 38(2), 473-484.
- Fox, G. A., D. M. Heeren, R. B. Miller, D. E. Storm, T. Halihan, and C. J. Penn (2010), Preferential flow effects on subsurface contaminant transport in alluvial floodplains, *T ASABE*, 53(1), 127-136.
- Freeze, R. A., and J. A. Cherry (1979), *Groundwater*, Prentice-Hall, Englewood Cliffs, N.J.
- Genereux, D. P., S. Leahy, H. Mitasova, C. D. Kennedy, and D. R. Corbett (2008), Spatial and temporal variability of streambed hydraulic conductivity in West Bear Creek, North Carolina, USA, *J Hydrol*, 358(3-4), 332-353.
- Giller, P. S., and B. Malmqvist (1998), *The Biology of Streams and Rivers*, Oxford University Press.
- Groffman, P. M., A. M. Dorsey, and P. M. Mayer (2005), N processing within geomorphic structures in urban streams, *J N Am Benthol Soc*, 24(3), 613-625.
- Haji-Sheikh, A., and W. J. Minkowycz (2008), Heat transfer analysis under local thermal non-equilibrium conditions. *Emerging Topics in Heat and Mass Transfer in Porous Media*, edited by P. Vadász, pp. 39-62, Springer, Netherlands.

- Hester, E. T., and M. W. Doyle (2008), In-stream geomorphic structures as drivers of hyporheic exchange, *Water Resour Res*, 44, W03417.
- Hester, E. T., and M. N. Gooseff (2011), Hyporheic Restoration in Streams and Rivers, in *Stream Restoration in Dynamic Fluvial Systems: Scientific Approaches, Analyses, and Tools*, pp. 167-187, AGU, Washington, DC.
- Hester, E. T., and M. W. Doyle (2011), Human Impacts to River Temperature and Their Effects on Biological Processes: A Quantitative Synthesis, *J Am Water Resour As*, 47(3), 571-587.
- Hester, E. T., and E. N. Cranmer (2012), Variation of hyporheic exchange potential among urban streams and implications for stream restoration. *Environmental & Engineering Geoscience*. Accepted.
- Hester, E. T., M. W. Doyle, and G. C. Poole (2009), The influence of in-stream structures on summer water temperatures via induced hyporheic exchange, *Limnol Oceanogr*, 54(1), 355-367.
- Ibrahim, A., and P. Steffler (2012), Estimation of Hyporheic Flow in a Pool and Riffle Sequence, in *International Symposium on Ecohydraulics*. 17-21 September 2012. University of Natural Resources and Life Sciences, Vienna, Austria.
- Johnson, S. L. (2004), Factors influencing stream temperatures in small streams: substrate effects and a shading experiment, *Can J Fish Aquat Sci*, 61(6), 913-923.
- Kasahara, T., and S. M. Wondzell (2003), Geomorphic controls on hyporheic exchange flow in mountain streams, *Water Resour Res*, 39(1), 1005.
- Kasahara, T., and A. R. Hill (2008), Modeling the effects of lowland stream restoration projects on stream-subsurface water exchange, *Ecol Eng*, 32(4), 310-319.
- Kaser, D. H., A. Binley, A. L. Heathwaite, and S. Krause (2009), Spatio-temporal variations of hyporheic flow in a riffle-step-pool sequence, *Hydrol Process*, 23(15), 2138-2149.
- Lautz, L., and R. Fanelli (2008), Seasonal biogeochemical hotspots in the streambed around restoration structures, *Biogeochemistry*, 91(1), 85-104.
- Lautz, L. K., and D. I. Siegel (2006), Modeling surface and ground water mixing in the hyporheic zone using MODFLOW and MT3D, *Adv Water Resour*, 29(11), 1618-1633.

- Li, D., and T. Engler (2001), Literature Review on Correlations of the Non-Darcy Coefficient, paper presented at SPE Permian Basin Oil and Gas Recovery Conference, Society of Petroleum Engineers, Midland, Texas, 15-17 May 2001.
- Lu, C. P., X. H. Chen, C. Cheng, G. X. Ou, and L. C. Shu (2012), Horizontal hydraulic conductivity of shallow streambed sediments and comparison with the grain-size analysis results, *Hydrol Process*, 26(3), 454-466.
- Macini, P., E. Mesini, and R. Viola (2011), Laboratory measurements of non-Darcy flow coefficients in natural and artificial unconsolidated porous media, *J Petrol Sci Eng*, 77(3-4), 365-374.
- Menichino, G. T., and E. T. Hester (2013), Macropores along Stream Channels: Abundance, Dimensions, and Effects on Surface Water-Groundwater Exchange, unpublished.
- Menichino, G. T., A. S. Ward, and E. T. Hester (2012), Macropores as preferential flow paths in meander bends, *Hydrol Process*, Published online 16 Nov 2012. DOI: 10.1002/hyp.9573.
- Menter, F. R. (1994), 2-Equation Eddy-Viscosity Turbulence Models for Engineering Applications, *Aiaa J*, 32(8), 1598-1605.
- Menter, F. R., R. Langtry, and S. Volker (2006), Transition modelling for general purpose CFD codes, *Flow Turbul Combust*, 77(1-4), 277-303.
- Mohseni, O., and H. G. Stefan (1999), Stream temperature air temperature relationship: a physical interpretation, *J Hydrol*, 218(3-4), 128-141.
- Moore, R. D., P. Sutherland, T. Gomi, and A. Dhakal (2005), Thermal regime of a headwater stream within a clear-cut, coastal British Columbia, Canada, *Hydrol Process*, 19(13), 2591-2608.
- Nield, D. A., and A. Bejan (2006), *Convection in porous media*, Springer, New York.
- Niswonger, R., and D. Prudic (2003), Modeling heat as a tracer to estimate streambed seepage and hydraulic conductivity, *Heat as a tool for studying the movement of ground water near streams*, 81-89.
- Packman, A., M. Salehin, and M. Zaramella (2004), Hyporheic Exchange with Gravel Beds: Basic Hydrodynamic Interactions and Bedform-Induced Advective Flows, *J Hydraul Eng*, 130(7), 647-656.

- Poole, G. C., and C. H. Berman (2001), An ecological perspective on in-stream temperature: Natural heat dynamics and mechanisms of human-caused thermal degradation, *Environ Manage*, 27(6), 787-802.
- Poole, G. C., J. A. Stanford, S. W. Running, C. A. Frissell, W. W. Woessner, and B. K. Ellis (2004), A patch hierarchy approach to modeling surface and subsurface hydrology in complex flood-plain environments, *Earth Surf Proc Land*, 29(10), 1259-1274.
- Poole, G. C., S. J. O'Daniel, K. L. Jones, W. W. Woessner, E. S. Bernhardt, A. M. Helton, J. A. Stanford, B. R. Boer, and T. J. Beechie (2008), Hydrologic spiralling: The role of multiple interactive flow paths in stream ecosystems, *River Res Appl*, 24(7), 1018-1031.
- Qian, J. Z., H. B. Zhan, Z. Chen, and H. Ye (2011), Experimental study of solute transport under non-Darcian flow in a single fracture, *J Hydrol*, 399(3-4), 246-254.
- Radspinner, R., P. Diplas, A. Lightbody, and F. Sotiropoulos (2010), River Training and Ecological Enhancement Potential Using In-Stream Structures, *J Hydraul Eng*, 136(12), 967-980.
- Salehin, M., A. I. Packman, and M. Paradis (2004), Hyporheic exchange with heterogeneous streambeds: Laboratory experiments and modeling, *Water Resour Res*, 40, W11504.
- Sawyer, A. H., and M. B. Cardenas (2012), Effect of experimental wood addition on hyporheic exchange and thermal dynamics in a losing meadow stream, *Water Resour Res*, 48, W10537.
- Sawyer, A. H., M. B. Cardenas, and J. Buttles (2011), Hyporheic exchange due to channel-spanning logs, *Water Resour Res*, 47, W08502.
- Sawyer, A. H., M. B. Cardenas, and J. Buttles (2012), Hyporheic temperature dynamics and heat exchange near channel-spanning logs, *Water Resour Res*, 48, W01529.
- Sobieski, W., and A. Trykozko (2011), Sensitivity Aspects of Forchheimer's Approximation, *Transport Porous Med*, 89(2), 155-164.
- Song, J. X., X. H. Chen, C. Cheng, D. M. Wang, and W. K. Wang (2010), Variability of streambed vertical hydraulic conductivity with depth along the Elkhorn River, Nebraska, USA, *Chinese Sci Bull*, 55(10), 992-999.
- Spanoudaki, K., A. I. Stamou, and A. Nanou-Giannarou (2009), Development and verification of a 3-D integrated surface water-groundwater model, *J Hydrol*, 375(3-4), 410-427.

- Storey, R. G., K. W. F. Howard, and D. D. Williams (2003), Factors controlling riffle-scale hyporheic exchange flows and their seasonal changes in a gaining stream: A three-dimensional groundwater flow model, *Water Resour Res*, 39(2).
- Story, A., R. D. Moore, and J. S. Macdonald (2003), Stream temperatures in two shaded reaches below cutblocks and logging roads: downstream cooling linked to subsurface hydrology, *Can J Forest Res*, 33(8), 1383-1396.
- Takahashi, G., T. Gomi, and K. Sasa (2008), Hyporheic flow as a potential geomorphic agent in the evolution of channel morphology in a gravel-bed river, *Catena*, 73(3), 239-248.
- Vafai, K. (2005), *Handbook of porous media*, Taylor & Francis, Boca Raton.
- Vafai, K., and M. Sozen (1990), Analysis of Energy and Momentum Transport for Fluid-Flow through a Porous Bed, *J Heat Trans-T Asme*, 112(3), 690-699.
- Valett, H. M., J. A. Morrice, C. N. Dahm, and M. E. Campana (1996), Parent lithology, surface-groundwater exchange, and nitrate retention in headwater streams, *Limnol Oceanogr*, 41(2), 333-345.
- Walther, G. R., E. Post, P. Convey, A. Menzel, C. Parmesan, T. J. C. Beebee, J. M. Fromentin, O. Hoegh-Guldberg, and F. Bairlein (2002), Ecological responses to recent climate change, *Nature*, 416(6879), 389-395.
- Westrich, J. T., and R. A. Berner (1988), The Effect of Temperature on Rates of Sulfate Reduction in Marine-Sediments, *Geomicrobiol J*, 6(2), 99-117.
- White, D. S., C. H. Elzinga, and S. P. Hendricks (1987), Temperature Patterns within the Hyporheic Zone of a Northern Michigan River, *J N Am Benthol Soc*, 6(2), 85-91.
- Wondzell, S. M., and M. N. Gooseff (2013), 9.13 Geomorphic Controls on Hyporheic Exchange Across Scales: Watersheds to Particles, in *Treatise on Geomorphology*, edited by J. F. Shroder, pp. 203-218, Academic Press, San Diego.
- Wondzell, S. M., J. LaNier, R. Haggerty, R. D. Woodsmith, and R. T. Edwards (2009), Changes in hyporheic exchange flow following experimental wood removal in a small, low-gradient stream, *Water Resour Res*, 45(05).

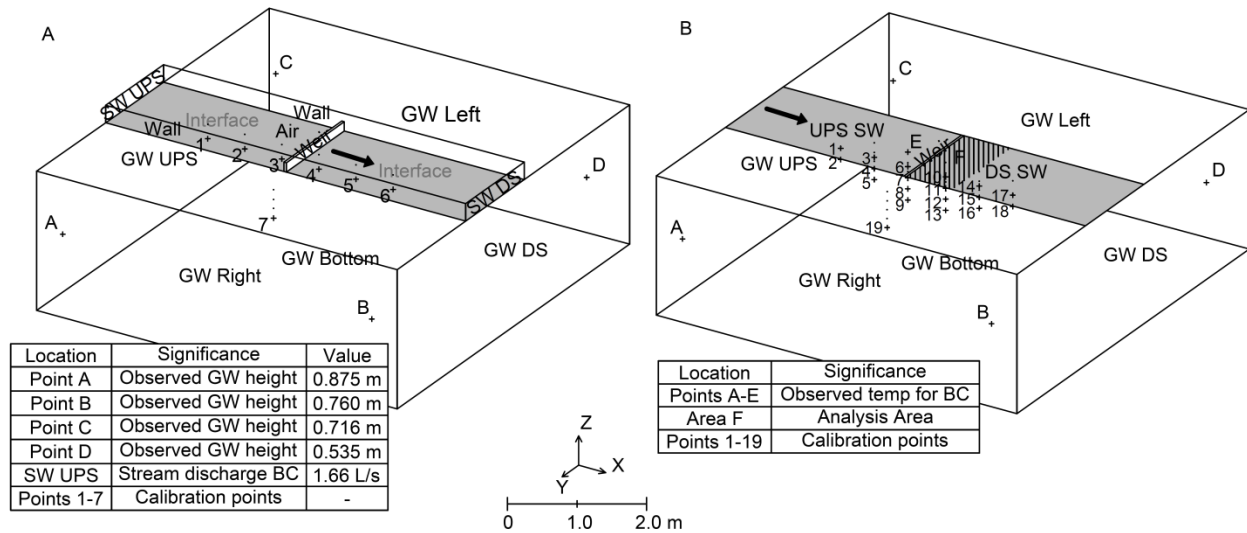


Figure 2-1. Panel A shows hydraulics model domain and associated boundaries in CFX. Observed pressures at points 1-7 are used for calibration. Calibration points 1-6 were 0.2 to 0.4 m below the streambed near the channel centerline. Point 7 is offset 1 m from channel center and 0.6 m below the channel bed. Arrow shows surface water flow direction. Points A through D refer to groundwater observation wells at different elevations in the floodplain. Panel B shows groundwater domain for heat transport model and associated boundaries in CFX. Point E is located on the sediment interface, just upstream of the weir and characterizes downwelling surface water temperatures. Area F is used for analyzing upwelling temperatures for heat flux, cooling, buffering, and diel temperature range calculations; the downstream length of this area is variable with K (1.24 to 1.15 m as K increased in hydraulics model). Temperatures observed at Points 1-19 are used for calibration. Points 1-18 are spaced on average 0.5 m longitudinally near channel center. The shallowest calibration points are located on average 0.15 m below the top of the sediment, with vertical spacing of 0.15 to 0.25 m beneath that. Point 19 is a calibration point offset 1.2 meter from channel center and 0.6 m beneath the channel bed. “BC” is boundary condition.

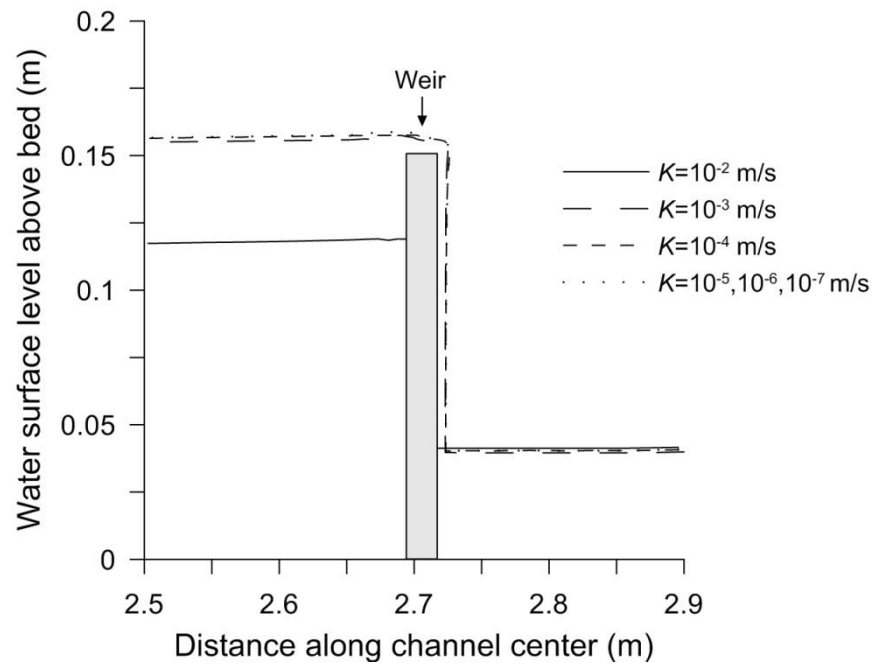


Figure 2-2. Longitudinal water surface profiles near the weir. Water surface levels for K 's of 10^{-5} , 10^{-6} , and 10^{-7} m/s were essentially identical and hence plotted together.

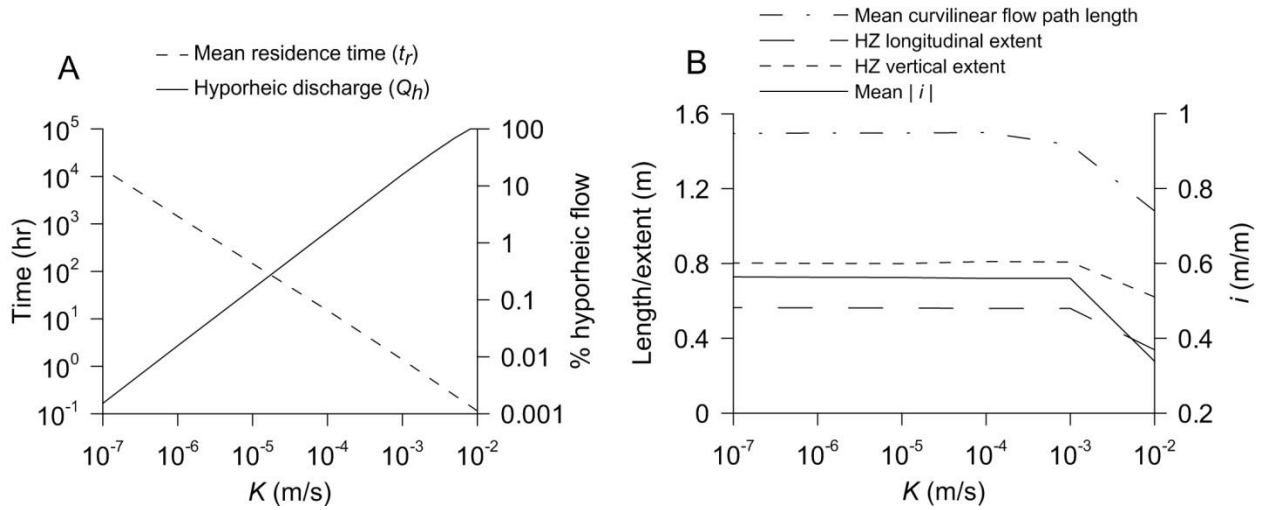


Figure 2-3. Panel A shows geometry and mean residence time of hyporheic flow cell versus K . Panel B shows discharge through and mean residence time of hyporheic flow cell versus K for the Darcy-only model. Mean i is mean of the absolute value of vertical gradients calculated between points on the streambed and 10 cm deep along the channel center both upstream and downstream of the weir.

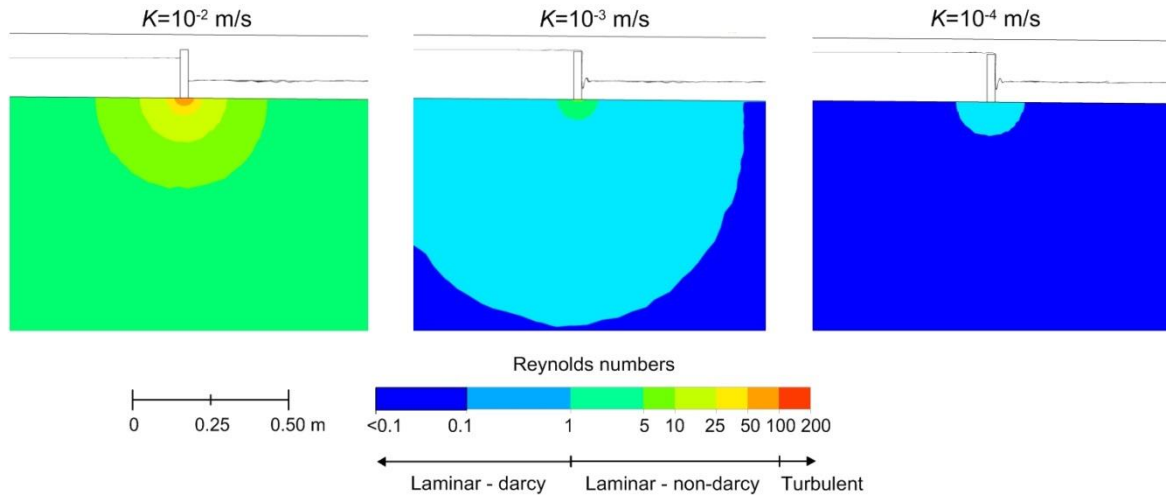


Figure 2-4. Pore scale Reynolds numbers for vertical profiles along channel center in the porous domain with water surface shown. Groundwater domain of figure is cropped. The scale shown applies to both the x and y directions.

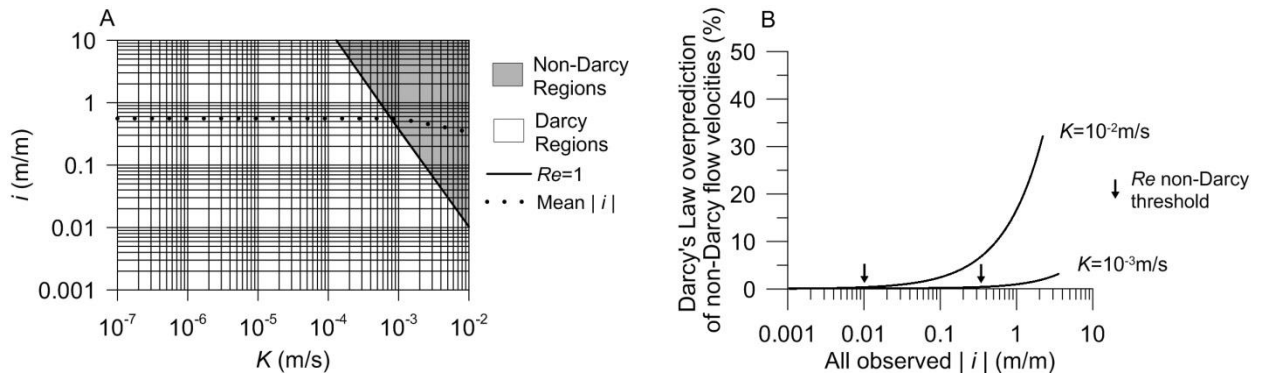


Figure 2-5. Panel A shows regions of K - i parameter space where Darcy and non-Darcy flow occur based on more than 3000 unique parameter combinations. Dotted line shows the mean $|i|$ between the bed and 10 cm into the subsurface along channel center (repeated from Figure 2-3B). Panel B shows differences in groundwater velocities calculated by Darcy and Darcy-Forchheimer (Ergun) models for $K=10^{-2}$ m/s (left) and $K=10^{-3}$ m/s (right) along channel center. Panel B includes i 's between the bed and 0.01 to 2 m within the subsurface.

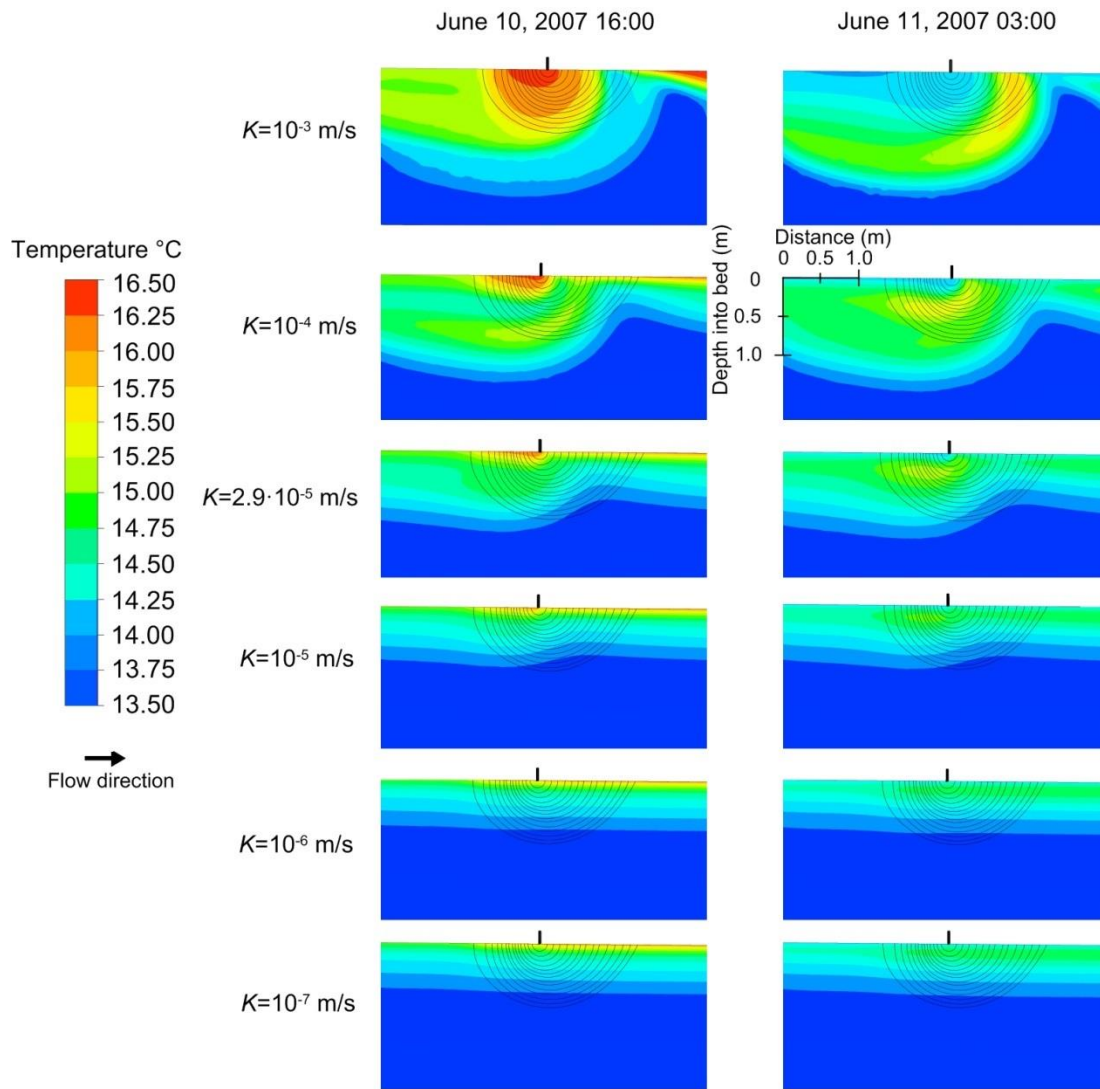


Figure 2-6. Temperature distributions along vertical slices through the groundwater domain beneath the channel centerline showing temperature distributions for $K=10^{-3}$ to 10^{-7} m/s at 16:00, June 10, 2007 and 03:00, June 11, 2007. Hyporheic flow paths are shown as black lines. The position of the weir is shown by a small black bar above each temperature map. The basecase is $K=2.9 \cdot 10^{-5}$ m/s.

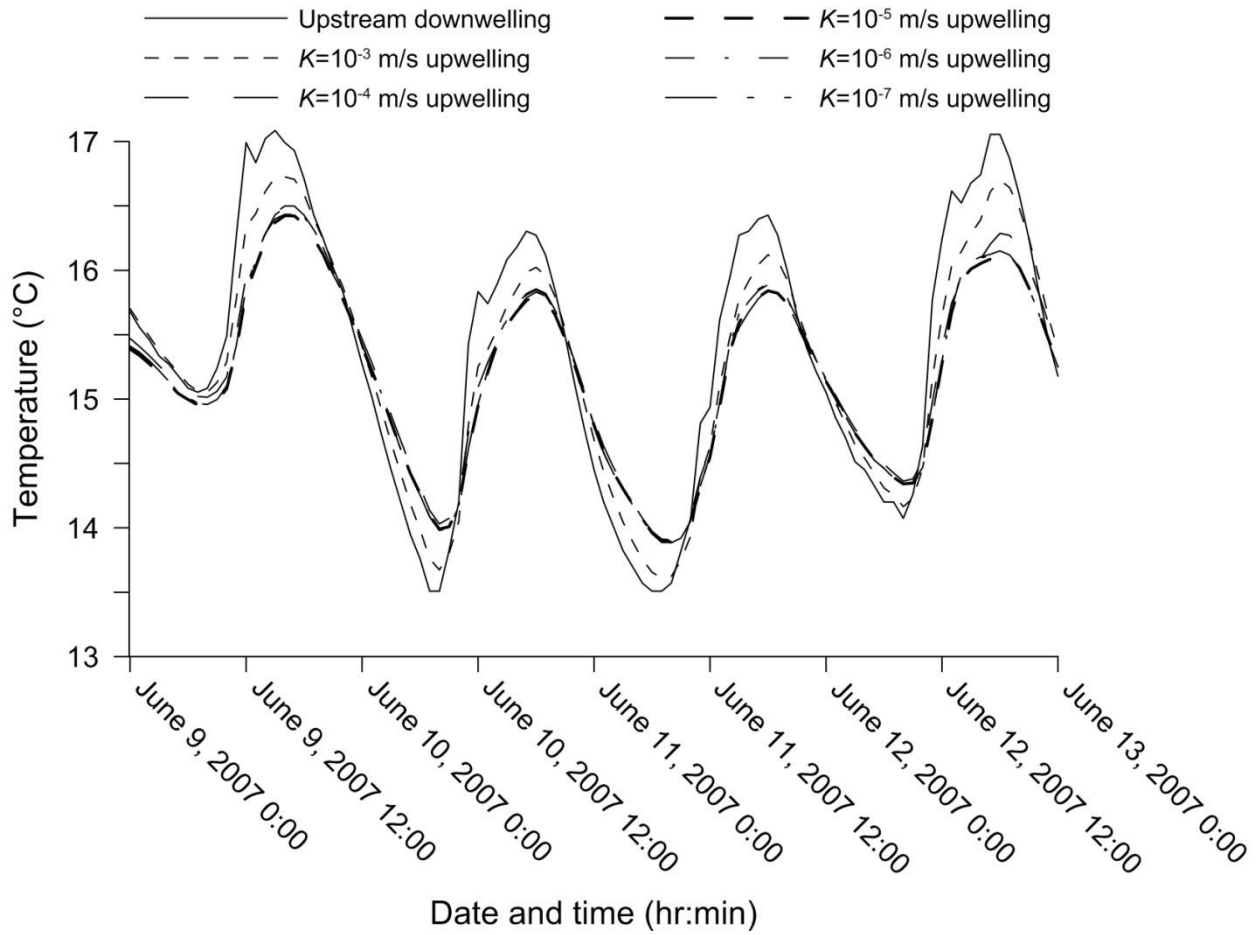


Figure 2-7. Modeled temperatures of water downwelling directly upstream of the weir (point E in Figure 2-1b) and upwelling directly downstream of the weir (flow weighted average over Area F in Figure 2-1b) over time.

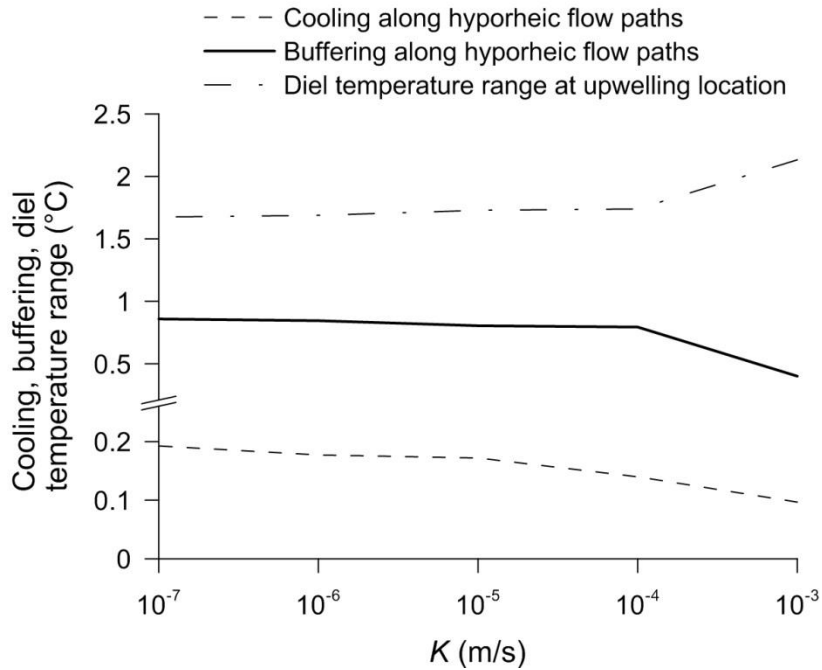


Figure 2-8. Daily averaged cooling and buffering experienced along hyporheic flow paths and diel temperature range at upwelling location over range of K 's. Cooling and buffering are calculated from differences between downwelling and the upwelling sinusoidal fits of temperature profiles. Diel temperature ranges are calculated as the amplitude of the upwelling sinusoidal fits of temperature profiles.

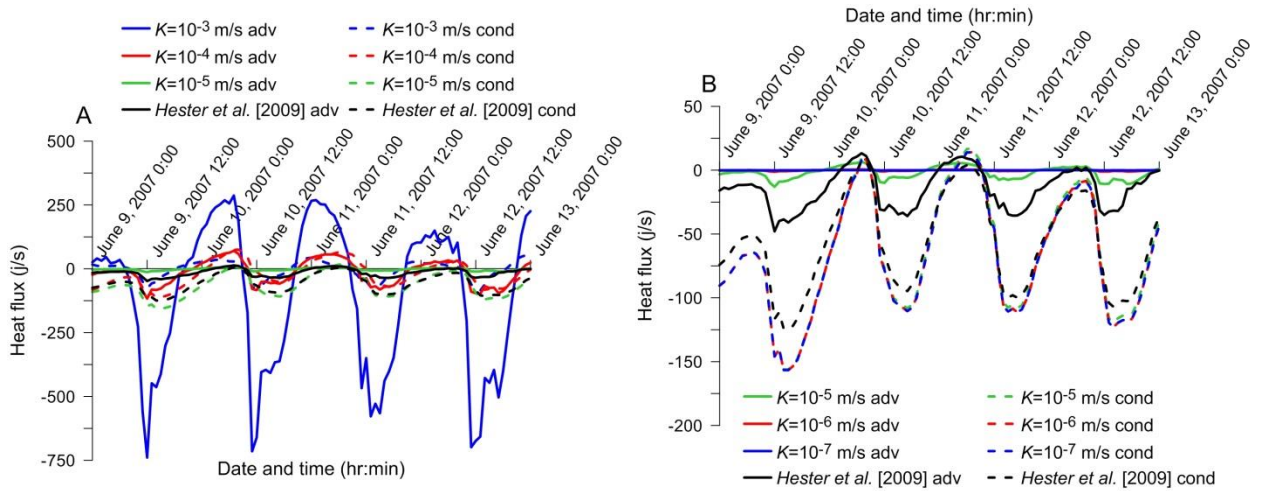


Figure 2-9. Panel A shows hyporheic advection and conduction versus time for $K=10^{-3}$ to 10^{-5} m/s. Panel B shows hyporheic advection and conduction versus time for $K=10^{-5}$ to 10^{-7} m/s. $K=10^{-5}$ m/s is repeated between panels for reference.

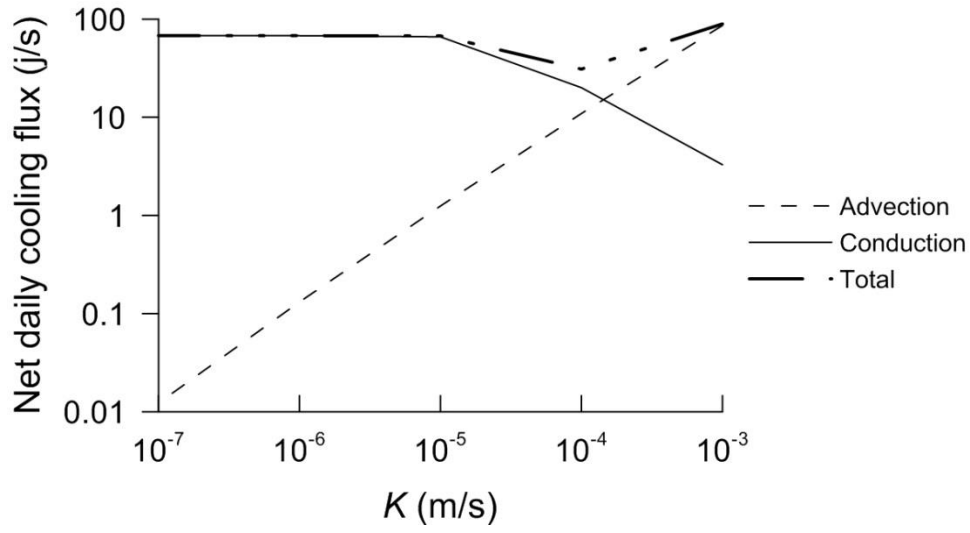


Figure 2-10. Net daily advection, streambed conduction, and total thermal fluxes calculated from hourly data.

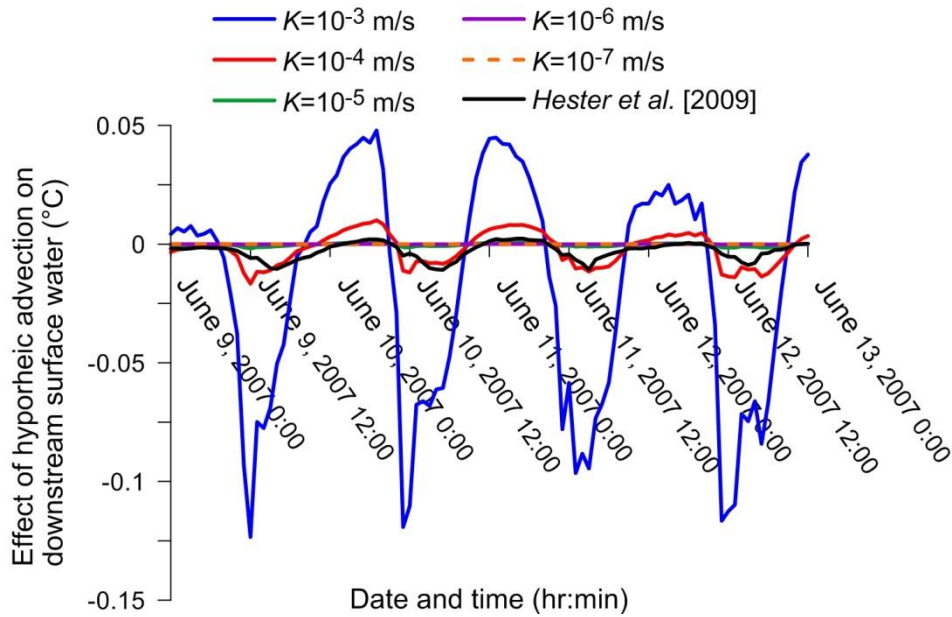


Figure 2-11. Thermal effect of weir-induced hyporheic advection on downstream surface water estimated by equation 8 versus time for a range of K 's. Positive and negative temperatures indicate warming and cooling of surface water, respectively.

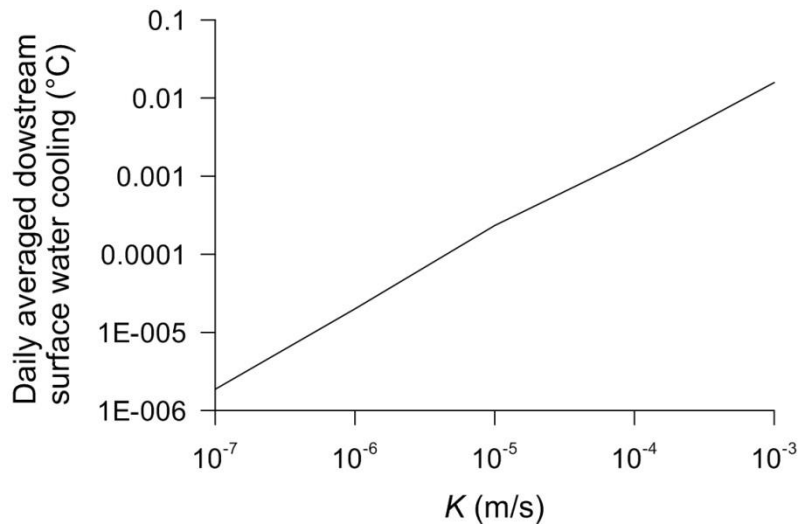


Figure 2-12. Thermal effect of weir-induced hyporheic advection on downstream surface water temperatures, averaged over 96-hour modeling period.

CHAPTER 3: *Macropores as Preferential Flow Paths in Meander Bends*

Garrett T. Menichino¹, Adam S. Ward², Erich T. Hester¹

¹Department of Civil and Environmental Engineering, Virginia Tech, Blacksburg, VA 24060

²Department of Geoscience, University of Iowa, Iowa City, IA 52242.

Status: This manuscript was submitted to *Hydrological Processes* in March 2012 and was accepted in October 2012. This manuscript is copyrighted by *Hydrological Processes* has been reprinted here with permission (license # 3241640272747). DOI: 10.1002/hyp.9573.

3.1 ABSTRACT

Macropores are subsurface connected void spaces caused by processes such as fracture of soils, micro-erosion, and fauna burrows. They are common near streams (e.g., hyporheic and riparian zones), and may act as preferential flow paths between surface water and groundwater, affecting hydrologic and biogeochemical processes. We tested the hydrologic function of macropores by constructing an artificial macropore within the saturated zone of a meander bend (open macropore, “OM”) and later filling its upstream end (partially filled macropore, “PFM”). For each treatment we injected saline tracer at an upgradient monitoring well within the meander, and monitored downgradient hydraulics and tracer transport. Pressure transducers in monitoring wells indicated hydraulic gradients within the meander were 32% higher perpendicular to and 6% higher parallel to the macropore for the OM than for the PFM. Additionally, hydraulic conductivities measured via falling head tests were 29 to 550 times higher along the macropore than in nearby sediment. We used electrical conductivity probes in wells and electrical resistivity imaging to track solute transport. Transport velocities through the meander were on average 9 and 21% higher (per temporal moment analysis and observed tracer peak, respectively) for the OM than for the PFM. Furthermore, temporal moments of tracer breakthrough analysis indicated downgradient longitudinal dispersion and breakthrough tracer curve tailing were on

average 234% and 182% higher for the OM, respectively. This suggests the OM enabled solute transport at overall shorter timescales than the matrix but also increased tailing. Our results demonstrate the importance of macropores to meander bend hydrology and solute transport.

Keywords: Stream, Connectivity, Hyporheic zone, Riparian zone, Electrical Resistivity, Hydraulics

3.2 INTRODUCTION

Floodplains, including riparian zones, are unique ecotones between terrestrial and aquatic environments [Thoms, 2003] that facilitate groundwater transport to and from the stream channel [Jung *et al.*, 2004]. Near-channel floodplains can deliver the majority of new water to streams, providing important sources of organic carbon and nutrients to aquatic organisms [McGlynn and McDonnell, 2003]. Floodplains can also function as sinks for common groundwater pollutants such as nitrate [Groffman *et al.*, 2002]. Meanders are a common geomorphic feature at the intersection of the stream channel, floodplain, and riparian zones. They experience a hydraulic head differential between upstream and downstream that promotes cross-meander flow [Boano *et al.*, 2006; Cardenas, 2008; Revelli *et al.*, 2008] and hence stream-riparian or stream-floodplain connectivity. The resulting mixing of surface water and groundwater establishes hydrologic and biogeochemical gradients in the hyporheic zone [Brunke and Gonser, 1997] that can facilitate stream temperature buffering, biogeochemical cycling, and pollutant attenuation, while fostering habitat [Boulton *et al.*, 1998; Brunke and Gonser, 1997; Groffman *et al.*, 2005]. For example, meander bends can buffer in-stream nutrient concentrations by denitrifying surface waters high in nitrate or supplying nitrogen when in-stream nitrogen concentrations are low [Van der Hoven *et al.*, 2008]. The value of these ecosystem services is underscored by recent recommendations that they be included among possible stream restoration goals [Boulton, 2007; Hester and Gooseff, 2010]. In particular, meander bends and stream-floodplain connection are sometimes used as restoration tools to reestablish ecosystem function [Jacobson *et al.*, 2011]. The extent of these benefits is dependent on flow rates and residence times through the hyporheic zone, beneath the riparian zone, and beneath the floodplain [Sabo *et al.*, 1999; Valett *et al.*, 1990].

The spatial extent of and exchange rates within the hyporheic zone depend on stream hydraulics, stream morphology, and alluvial depth, among other factors [Cardenas *et al.*, 2004; Gooseff *et al.*, 2006; Marzadri *et al.*, 2010; D. Tonina and Buffington, 2011; Zarnetske *et al.*, 2008]. One of the most important factors is the hydraulic conductivity (K) of the porous media, which spans 8 orders of magnitude and is highly variable in space and time [Brassington, 2007; Calver, 2001; Cardenas *et al.*, 2004]. Regions of higher K act as preferential flow paths by dominating water and solute transport through porous media [Fox *et al.*, 2009; Fox *et al.*, 2010]. In particular, coarse sediment layering may result from sediment transport and streambed coarsening at small [Bretschko, 2002; Cardenas *et al.*, 2004; C Chen *et al.*, 2010; Sawyer and

Cardenas, 2009] and large [*Bridge*, 1985; *Duval and Hill*, 2006; *Fox et al.*, 2009; *Fox et al.*, 2010; *Takahashi et al.*, 2008] scales.

Macropores are a type of preferential flow path that are devoid of sediment grains and greater than 3 millimeters in cross-section [*Beven and Germann*, 1982]. Macropores existing as fractured rock have been shown to increase groundwater discharge rates by orders of magnitude in deep groundwater applications [*Zhan et al.*, 2011]. Similarly, macropores have been studied in unsaturated floodplains and agricultural settings where plant roots [*Aubertin*, 1971; *Beasley*, 1976b; *Mosley*, 1982], earthworms burrows [*Bretschko*, 2002; *C A Edwards and Lofty*, 1977a], and the dry fracture of soils [*Blake*, 1973] dictate transport. While macropores may be widely distributed in the subsurface, they have not been extensively studied in the context of the hyporheic zone, with the exception of a few bioturbation studies about macropores created by benthic macro-invertebrates [*Mermillod-Blondin and Rosenberg*, 2006; *Mermillod-Blondin et al.*, 2004; *Nogaro et al.*, 2006; *Song et al.*, 2010a]. Additionally, these bioturbation studies have focused on sediment-scale hydraulics and have not determined the impact of macropores on hyporheic function or solute transport at the meander bend scale. Other research suggests macropores increase solute transport between the riparian zone and surface stream [*Angier and McCarty*, 2008; *Gormally et al.*, 2011b]; however solute transport in macropores has not been disentangled from and compared to matrix transport. By contrast, most hyporheic zone and floodplain groundwater studies assume a homogenous sediment matrix and K [*Bates et al.*, 2000; *Hester and Doyle*, 2008; *Lamontagne et al.*, 2005], ignoring the presence of macropores and other preferential flow paths. More recently, heterogeneity of K fields has been shown to control hyporheic zone and floodplain groundwater flow and transport at a range of scales [*Cardenas et al.*, 2004; *Heeren et al.*, 2010; *Heeren et al.*, 2011; *Poole et al.*, 2006; *Sawyer and Cardenas*, 2009]. However, to our knowledge, no published studies have investigated the effect of macropores on hydraulics and solute transport within hyporheic, riparian, or floodplain settings in a spatially explicit fashion that allows separation of the contributions of macropores and surrounding sediment matrix. We attribute this to the following issues: First, macropores are generally not visible except where they intersect the channel. Second, macropores can be interconnected in complex ways, which may affect flow direction and magnitude. Third, given their high K , even small macropores have the potential to significantly impact flow, and

macropore flow velocities may be high, so high spatial and temporal resolution will often be necessary.

Understanding the impacts of macropores on hydrological processes such as solute transport at both the meander bend and stream corridor scales is dependent on accurately mapping macropore frequency, size, orientation, and connection to other macropores. The difficulty of such mapping contributes to the paucity of hyporheic macropore studies. Within the vadose zone there is a diverse range of options for classifying and mapping macropores in the subsurface, including trenching and photography, latex, resins, smoke injection, X-rays, and MRI in the unsaturated vadose zone [Abou Najm *et al.*, 2010; Allaire *et al.*, 2009; Lin *et al.*, 2008; Shipitalo and Protz, 1987; Simpson *et al.*, 2007]. However, these methods are often highly invasive and require excavating or destroying the macropore. Options in deeper aquifers are more limited; generally employing either tracers or geophysical techniques such as seismic reflection, ground penetrating radar (GPR), and electrical resistivity imaging (ERI) [Baines *et al.*, 2002; Beres and Haeni, 1991; Fradelizio *et al.*, 2008]. However, limited spatial and temporal resolution along with high expense and difficult implementation has hindered their application. As a result of these limitations, while traditional hyporheic zone studies quantify the hydrologic function of any macropores that happen to be present (e.g., with wells and conventional tracer tests), they generally do not map the physical structure of the macropore, or even acknowledge its presence.

GPR in particular was used in one recent study to map macropores in riparian wetlands [Gormally *et al.*, 2011b], but it was unclear whether these macropores were in the saturated zone, which would be the most applicable to the hyporheic zone. Additionally, GPR is limited in its ability to spatially resolve an electrically conductive (e.g., saline) tracer, making tracking solute transport difficult. By contrast, ERI has been successfully applied to hyporheic zone settings [Crook *et al.*, 2008] and has shown promise in tracking the movement of saline tracers to image hyporheic flow near streams [Ward *et al.*, 2010; Ward *et al.*, 2012]. ERI uses direct or low-frequency alternating current to estimate the distribution of electrical resistance in the subsurface.

Here we present the results of a field experiment that investigated the hydrologic importance of hyporheic macropores at the scale of a meander bend. Our specific objectives were to experimentally manipulate macropores in a meander bend to (1) quantify the effect of

macropores on solute transport in the meander bend via temporal and spatial analysis of tracer breakthrough curves, (2) quantify the effect of macropores on meander bend hydraulics via impacts to hydraulic gradients and K fields, and (3) investigate the ability of ERI to map macropores and the effect of macropores on solute transport in the hyporheic zone.

3.3 METHODS

3.3.1 Field Site

We conducted field studies in a meander bend (Figure 3-1) along a tributary to Tom's Creek in Heritage Park near Blacksburg, VA. The stream is first-order, and averages 60 cm wide and 20 cm deep with 0.025 m/m channel slope set in a wide valley at the foot of the Jefferson National Forest. Velocity-area measurements conducted 6/16/2011 (3 days after the final experiments described below) estimated baseflow discharge at 10 L/s. The banks are mostly comprised of fine sand, with coarse sand and pebbles in the bed. The surrounding floodplains are seasonal wetlands with grasses, sedges, shrubs, and sparse trees. Nine polyvinyl chloride monitoring wells, 3.18 cm in diameter, were installed as shown in Figure 3-2. The soils removed in installing the wells suggest floodplain soils are generally finer than the channel sediment, and exhibit a majority of silt and clay. The meander bend measures 7 meters in the downstream direction and 4 meters laterally (Figure 3-2).

3.3.2 Experimental Design

We conducted two experimental treatments to quantify the hydrologic function of a macropore in a meander bend. The first treatment was performed from 6/9/2011 to 6/11/2011, immediately followed by the second treatment, performed from 6/11/2011 to 6/13/2011. In the first treatment, ("open macropore", hereafter OM), a 3 m long macropore was constructed by driving a 2.75 cm diameter pipe horizontally into the saturated upstream end of the meander bend (Figure 3-1). The pipe was hollow in order to remove the sediment with minimal compaction to macropore walls. The pipe was then removed to allow interaction between the macropore and substrate. The macropore was driven through cohesive sediment (fine sand to clay) which stabilized the macropore and allowed the removal of the pipe without collapsing the macropore. For the second treatment, clay from the downstream channel was used to manually fill and compact the upstream half of the macropore, creating a partially filled macropore (PFM) (Figure 3-2). A weir was installed across the channel at the upstream end of the meander bend

several days prior to the first experimental treatment in order to raise the upstream channel water levels by 0.3 m. This enhanced water flow through the meander bend and ensured that the macropore was below the water table (i.e., in the hyporheic zone rather than the vadose zone). In addition, an existing 1.5 cm diameter natural macropore was discovered and was left unchanged during the experiments. The natural macropore was at the same elevation as the treatment macropore and about 0.75 m closer to the point of the meander (to the left in Figure 3-1, left panel).

3.3.3 Conventional Tracer and Hydraulics Methods

A saline solution (NaCl mixed with stream water to a concentration of 39 g/L) was injected into Well 9 at a constant rate of 34 mL/min for 6.5 hr for each experimental treatment. The injection well was located at the upstream end of the meander bend and upgradient of the macropores (Figure 3-2). The saline tracer caused a decrease in electrical resistivity in the subsurface along subsurface flow paths intersecting the well that can be visualized with ERI [Ward *et al.*, 2010]. LTC loggers (Solinst, Inc.) recorded tracer presence in Wells 1-5 through electrical conductivity measurements. We periodically took manual measurements of in-stream specific electrical conductivity throughout the experiments using an YSI EC300 (Yellow Springs Instruments) handheld probe. We calculated transport velocity between the injection well and each downgradient well (Wells 3-5) by subtracting the time of peak arrival at the given downgradient well from the time at the start of drip and dividing by the surveyed distances between the two wells.

Water levels were collected every minute at Wells 1-5 using LTC loggers and at Wells 6-8 using Hobo pressure transducers (Onset, Inc.). Observed groundwater levels in Wells 1-8 prior to each injection allowed the estimation of background piezometric contour maps for the OM and PFM treatments (Figure 3-3) by creating triangular irregular networks in AutoCAD, Civil3D [Autodesk, 2011]. We calculated hydraulic head gradients from groundwater levels in the well network for both the OM and the PFM.

We conducted falling head tests in vertical profiles at three different locations across the floodplain (Figure 3-2) to resolve spatial variation in K . These tests used a Solinst drivepoint piezometer consisting of a metal drive-point with 8 cm well screen attached to a 1.27 cm-diameter 2.50 m-long metal pipe. The piezometer was driven to the observation depths using a drive hammer. Falling head tests were performed by filling the piezometer to the top with water

and using a LevelTroll 700 pressure transducer (In-situ, Inc.) to determine water levels at 0.25/sec intervals. We performed tests repeatedly as the piezometer was driven downward at intervals of 0.5-1.0 times the well screen length of 8 cm. As a result, the vertical interval of the well screen for adjacent test depths sometimes overlapped. A total number of 45 falling head tests were performed, with 15 tests at each location. The well screen inlet on the drivepoint was slightly recessed from the main body, which prevented fine sediment from smearing along or clogging the well screen during consecutive falling head tests. We visually checked and confirmed that the well screen was clear after removing the piezometer at each location. After completing all of the falling head tests, we re-inserted the 2.75 cm diameter pipe along the length of OM. At location B, a second pipe was inserted vertically downward until it rested upon the first pipe, confirming the macropore was 0.8 m below the ground surface. We estimated K from the falling head data using Hvorslev's method [Hvorslev, 1951].

3.3.4 Temporal Moment Analysis

Absolute temporal moments were calculated from electrical conductivity time-series data from each monitoring well using Eq. (1), where a_k is the k^{th} absolute temporal moment, t^k is the observation time after injection start to the k^{th} order (hr), $C(t)$ is the observed conductivity from background ($\mu\text{s}/\text{cm}$) at time t , and dt is the time step [Schmid, 2003]. For our logged conductivity data, dt was 1 minute. Eq. (2) was used to calculate the normalized moments, where n_k is the k^{th} normalized moment, by using $c(t)$, which is observed electrical conductivity normalized to the total area under the breakthrough tracer curve at time t . Higher order (i.e., 2nd and 3rd) central moments, where μ_k is the k^{th} central moment, were calculated using Eq. (3) by taking the moment normalized about the centroid in time [Schmid, 2003].

$$a_k = \int_0^{\infty} t^k \cdot C(t) dt \quad (1)$$

$$n_k = \int_0^{\infty} t^k \cdot c(t) dt \quad (2)$$

$$\mu_k = \int_0^{\infty} (t - n_1)^k \cdot c(t) dt \quad (3)$$

The 0th absolute moment (a_0) describes the total area under the breakthrough tracer curve ($\mu\text{s/cm}$) and is related to the total mass of NaCl transported to a well. The 0th normalized moment (n_0) is by definition unity. The 1st normalized moment (n_1) describes the time required for 50% of the solute to reach a well (mean arrival time, hr). The 2nd central moment (μ_2) describes the temporal spread of solute as it passed a well (variance of arrival times, hr^2), which is a function of diffusion and dispersion. The 3rd central moment (μ_3) describes the deviation of the temporal distribution of solute from a Gaussian (symmetric) distribution (hr^3), where negative and positive values are related to skew to earlier and later times, respectively [Doyle and Shields, 2012; Govindaraju and Das, 2007]. We calculated each of the above temporal moments and values related to skewness for Wells 3-5 as well as the percent change between the OM and PFM experiments.

The effective (mean) velocity (V , m/s) of subsurface transport was calculated from the 1st normalized moment of the breakthrough tracer data using Eq. (4) [Vereecken, 2006]. We calculated mean velocities for wells demonstrating breakthrough curves (Wells 3-5) by using x , the surveyed distance between the injection and observation wells.

$$V = \frac{x}{n_1} \quad (4)$$

Effective dispersion is the summation of molecular diffusion and hydrodynamic dispersion, and is used in the advection-dispersion equation. The effective dispersion coefficient (D , m^2) can be calculated from the 1st and 2nd normalized moments of the breakthrough tracer data using Eq. (5) [Vereecken, 2006]. We calculated effective dispersion coefficients for Wells 3-5 by using V , the mean velocities calculated via Eq. (4).

$$D = \frac{\mu_2 * x * V^3}{2x} \quad (5)$$

3.3.5 Electrical Resistivity Methods

We installed an ERI transect across the meander bend (including the macropore) comprised of 12 electrodes (1 cm diameter stainless steel, driven approximately to 15 cm depth) at 0.2 m spacing and centered on the macropore (laterally) and the meander bend (longitudinally, Figure 3-2). We developed a data collection scheme for the expected anomaly at the macropore location using forward modeling via the R2 Generalized Inversion Code [A. Binley, 2010]. A

number of collection schemes were tested to balance rapid temporal resolution, necessary for monitoring the transport of solute through the macropore, with characterization of the macropore's location in the subsurface (i.e., a collection scheme that provided high spatial resolution at the macropore). The chosen scheme consisted of 118 quadripoles (i.e., measurements including a current pair and potential pair), including dipole-dipole and Wenner measurements, and allowed collecting an electrical resistivity data set in approximately 5 minutes using a SyscalPro ten-channel meter (IRIS Instruments, Orleans, France). Reciprocal data were not collected, to maximize temporal resolution. We stacked (i.e., averaged) two measurements for each quadripole, and added a third measurement if the standard deviation as a percent of the mean was greater than 3%. Background data were collected prior to each solute tracer experiment, and data were collected continuously during the injections. A tarp was installed over the site to minimize infiltration of rainwater during storm events.

The research code R2 Generalized 2-D Inversion of Resistivity Data (v2.6, Binley, 2010) was used to invert resistivity data for each set of observations. Data collected during each set of 118 observations were assigned to a single time step. Temporal smearing within individual data sets was assumed to be minimal given the speed of our collection scheme. The algorithm for the collection scheme was based on an Occam's inversion [Andrew Binley and Kemna, 2005]. Inversion was completed for a grid of 5 cm by 5 cm pixels, with no surface topography represented at the site and treating the current and potential electrodes as point sources located at the surface. We assumed an error model of 0.001 Ω absolute error in field data, and a relative error of 0.2% of the observed resistance. Data were equally weighted initially, and weights were adjusted iteratively by the inversion code. Background data were inverted to create a background resistivity model for both the OM and PFM cases; this was used as a starting model for inversion of data collected during and after each solute injection. To isolate changes caused by the presence of solute tracer, the background resistivity image was subtracted from each of the images collected at the independent time steps throughout each solute tracer experiment [Ward *et al.*, 2010; Ward *et al.*, 2012]. Regularization to previous data sets and inversion of differences in resistance from the starting model could be used to improve inversions in future studies. We calculated the percent change for each pixel, with solute tracer presence indicated by a negative change in electrical resistivity from background. We emphasize here that the 2-D imaging completed in this study must be interpreted within the context of limitations of the

method. The images resulting from the inversion are solutions to an ill-posed (i.e., non-unique solutions exist given the inherent assumptions of the inversion process) and ill-conditioned problem (i.e., small errors in the data may lead to large model errors) [Ward *et al.*, 2010; Ward *et al.*, 2012]. Additionally, 2-D inversion compresses the 3-D electrical field generated during the measurements onto a 2-D plane. Images are subject to out-of-plane effects, meaning that the image may initially sense the solute plume before it actually passes the transect and may be sensitive to the plume even after it has moved downstream of the transect.

3.4 RESULTS

3.4.1 Meander Bend Hydraulics

A storm event occurred during the course of each macropore treatment. Non-storm conditions (i.e., 0-5 hours from the start of each drip) show similar patterns between the two treatments in piezometric elevations in Wells 1-8 (Figure 3-3). In particular, contours within the meander bend indicate groundwater transport in the downstream direction (down-valley, parallel to macropore) as well as slightly towards the stream (cross-valley, perpendicular to macropore). The slightly gaining condition is indicated by comparing groundwater levels in Wells 6 and 7 in Figure 3-3. The storm event that occurred during each treatment increased water levels in the surface channel, but did not overtop the meander bend. Groundwater elevations observed in a well beneath the channel (Well 8) were used to quantify the relative timing and magnitude of the resulting storm waves past the study site (Figure 3-4). Storm events affected groundwater elevations in Well 8 from 5 to 11 hours after each drip began. The magnitude and the timing of the storm within the duration of the injection were similar between treatments, allowing comparison of the meander bend behavior during each treatment. Both flood durations were approximately 5 hours, and peak changes in groundwater elevation were 0.15 and 0.26 m in Well 8 (for OM and PFM, respectively). Times to peak from drip start in Well 8 were 7.1 and 8.2 hours for the OM and PFM, respectively. Storm events similarly affected hydraulic heads in all observation wells from approximately 5 to 10 hours after drip began; the maximum head change was 0.27 m for the OM and 0.18 m for the PFM across all wells.

We calculated hydraulic head gradients in or near the macropore, specifically between Wells 2 and 1 (cross-valley) and Wells 2 and 4 (down-valley) (Figure 3-4). Our calculated hydraulic head gradients were averaged over the duration when hydraulic heads in the floodplain and beneath the channel (via Well 7 and 8) were not affected by stormflow (i.e., non-storm

conditions, 0-5 hours) to allow comparison between the two treatments (Table 3-1). Results describe the influence of the macropore treatments on meander bend hydraulic head gradients. The macropore cross-valley hydraulic head gradient was 32% percent higher for the OM than for the PFM during non-storm conditions. Similarly, the magnitude of the macropore down-valley head gradient was 6% higher for the OM than for the PFM. In contrast, larger scale non-storm head gradients (i.e., across the entire field site) both longitudinally downstream through the meander (i.e., Well 8 to 4) and laterally from the floodplain toward the stream (i.e., Well 7 to 4) remained essentially the same during the experiment (Figure 3-3 and Table 3-1), changing by only 0.0% and 0.2% respectively.

3.4.2 Tracer Breakthrough in Monitoring Wells

In-stream measurements of specific conductivity upstream of Well 8 were 630 and 600 $\mu\text{S}/\text{cm}$ for the OM and the PFM at background (i.e., pre-injection). These values decreased over the storm event by 120 and 50 $\mu\text{S}/\text{cm}$ for the OM and PFM respectively (Figure 3-5A). Wells 1 and 2 (at the upgradient end of the macropore) did not exhibit well-defined saline tracer breakthroughs, but instead exhibited perturbations that coincided with peak groundwater levels for the two storm events (Figures 3-5B, 3-5C and 3-4). In contrast, Wells 3-5 (downgradient of macropore) exhibited distinct tracer breakthroughs with peak specific conductivities on average 7.0 hours and 8.4 hours after drip start for the OM and PFM respectively (Figures 3-5D, 3-5E, 3-5F). Because background conductivities varied among the wells, background conductivities observed in loggers were subtracted from tracer time-series for Wells 3-5 and plotted as change from background to isolate tracer behavior [Hauer and Lamberti, 2006]. However, conductivities in Wells 1 and 2, and background in-stream conductivities were not plotted as change from background to avoid confusion with what is interpreted as tracer breakthrough. Peak electrical conductivity in Well 4 was 47% lower (11900 versus 8080 $\mu\text{S}/\text{cm}$ above background) for the PFM than for the OM (Figure 3-5D). Comparatively, peak conductivities in Well 3 were 105% higher (289 versus 137 $\mu\text{S}/\text{cm}$ above background) for the PFM than for the OM (Figure 3-5E), and peak conductivities in Well 5 were 8% lower (103 versus 107 $\mu\text{S}/\text{cm}$ above background) for the PFM than for the OM (Figure 3-5F). Additionally, the saline tracer plume at Wells 3 and 4 was more spread out in time for the PFM than for the OM. Finally, for Wells 3 and 4, arrival of peak conductivities occurred about two hours later for PFM than for the OM.

The temporal moments calculated for Wells 3-5 are shown in Table 3-2 and include the 0th absolute moments (a_0), the 1st moments normalized to the total area under the breakthrough tracer curve (n_1), and the 2nd and 3rd central normalized moments (μ_2, μ_3). In Table 3-2, the percent change for the OM relative to the PFM for each temporal moment is important in assessing the impact of the macropore on solute transport. The total area under the breakthrough tracer curve (a_0) in Wells 3 and 4 was 60% lower and 109% higher respectively for the OM than for the PFM. The mean arrival times (n_1) in Wells 3-5 were 14%, 9%, and 2% lower for the OM than for the PFM. Using n_1 for Wells 3-5 and equation (4), we calculated the mean velocity to each well for the PFM and OM treatments (Table 3-3). In Table 3-3, the percent change for the OM relative to the PFM is important in assessing the impact of the macropore on transport rates. Estimated mean velocities to Wells 3-5 were 21%, 16%, and 26% higher for the OM than for the PFM, consistent with lower mean arrival times in Table 3-2. Peak velocities in Table 3-3 were calculated based on time of peak electrical conductivity from breakthrough tracer curves, and similarly to mean velocities, all are higher for the OM than for the PFM. Such velocities assume transport along a straight line from injection well to observation well; true flow paths are likely more tortuous such that actual velocities are likely higher. The saline tracer spread over time (μ_2) in Wells 3-5 was 20%, 136%, and 373% higher for the OM than for the PFM. Using the 1st and 2nd temporal moments for each well and equation (5), we estimated the dispersion coefficients from the PFM and OM treatments (Table 3-3). The dispersion coefficients in Wells 3-5 were 90%, 209%, and 404% higher for the OM than for the PFM, which are consistent with the increased spread of tracer over time (μ_2). The values of μ_3 are related to skewness of the tracer distribution in Wells 3-5 and were 109%, 268%, and 170% higher for the OM than for the PFM.

3.4.3 Electrical Resistivity Imaging within the Meander Bend

Electrical resistance measurements had an average stacking error (standard deviation as a fraction of the mean value) in the pre-tracer data of 0.042% and 0.044% for the OM and PFM cases, respectively, with background inversions converging to a root mean square error of 1.13% and 1.00%. These measurement and inversion errors are representative of the order of magnitude for the collection and inversion of data during and after each tracer injection. Background ERI (pre-tracer, Figure 3-6) was spatially similar between treatments, with regions of lower resistivity near the macropore (approximately $X = 0$ m, $Z = -0.4$ m). The location of

maximum change in background resistivity between the experiments was shallower than the macropore ($X = -1.0$ to -0.5 m, $Z = -0.2$ to 0.0 m). We interpreted this as a location that was relatively dry when first imaged (Panel A), was saturated by rain events, and held additional water as soil moisture when imaged later (Panel B).

Saline tracer movement through the meander bend appears as a decrease in electrical resistivity in time-lapse ERI (Figure 3-7). For the OM, this drop in resistivity occurred only in a region centered around approximately $X=-0.1$ m $Z=-0.5$ m (Figure 3-7, left). This area of resistivity reached a minimum at 7 hours, consistent with the stop of the injection at 6.5 hours. Beyond 9 hours, resistivity increased as the saline tracer flushed through the meander bend. The region maintained a well-defined shape whose size tracked drops in resistivity, extending from $-0.3 < X < 0.3$ and $-0.4 < Z < -0.9$ at the maximum percent change.

For the PFM with saline tracer, ERI depicted near-minimum values in resistivity within the first hour of injection at multiple regions within the domain (e.g., $-0.3 < X < -0.1$ and $-0.3 < Z < -0.6$). Unlike for the OM, none of these regions steadily increased in size over the course of the 6.5-hour injection. At 9 hours, a region of low resistivity appeared at $0 < X < 0.6$ and $-0.5 < Z < -0.9$ that is similar to the OM in shape, size, and percent change in resistivity. We hypothesize that this region represents the unfilled portion of the PFM.

3.4.4 Hydraulic Conductivity of Meander Bend Sediments

A large variation in K was observed with depth at each of the three falling head test locations (Figures 3-2, 3-8). The three highest values of K across all three locations ($4.4 \text{ E-}04$, $4.8 \text{ E-}04$, $4.5 \text{ E-}04$ m/s) were measured at location B at the depth where the 8 cm well screen intersected the elevation of the macropore. Additionally, there were areas of relatively high K at the other two locations (A and C), which indicate preferential flow paths that would dominate advective transport in their respective locations. To quantitatively compare K measurements at each of these preferential flow path locations to those elsewhere in the sediment matrix, we divided all K 's at each location into two sets of values: those at or above the 90th percentile for that location (representing preferential flow paths) and those below (representing non-preferential flow paths). This division was chosen because the well screen was believed to intersect the OM on about 10% of the falling head tests conducted at location B. We calculated the geometric mean of K separately for those values above and those values below the 90th percentile cutoff for each location (resulting in 6 averages, Table 3-4). Finally, we calculated the

ratio of the mean above the 90th percentile to the mean below the 90th percentile, in order to quantify the degree to which a given preferential flow path would dominate flow at that location. This ratio was 29.1 at location B (where the macropore was located) relative to 8.19 and 11.0 at locations A and C, respectively. To compare preferential flow in the macropore to nearby matrix flow, we calculated ratios of the mean above 90th percentile at location B and the mean below 90th percentile at the other locations. The maximum ratio indicates 550 times higher K in the macropore in location B than the matrix in location C.

3.5 DISCUSSION

3.5.1 Effects of Macropores on Hydrologic Processes within Meander Bends

Our results show that macropores in a meander bend act as preferential flow paths by increasing advective transport rates through the meander bend (Table 3-3). This trend agrees with previous findings from deeper groundwater that fractures can have flow rates that are orders of magnitude higher than the adjacent matrix [Elci and Molz, 2009; Geiger et al., 2010; Qian et al., 2011]. However, the magnitude of the effect on velocities in our data is less (roughly 1 order of magnitude, Table 3-3) than in many of these other studies. Part of this discrepancy is likely because we compared the OM to a PFM rather than undisturbed soil, such that the effect of the OM on meander bend transport is likely greater than we report. Another possible explanation for reduced effect of the OM in our study is the limited connectivity of the macropore. In particular, prior work confirms that increasing macropore connectivity with other preferential flow paths, in addition to increasing macropore dimensions (i.e., aperture, depth) will increase the discharge in macropores [Matthai and Belayneh, 2004]. Contributions to reduced connectivity in our study include a lack of connection of the OM to the stream at its downgradient end as well as compaction of the macropore walls during construction. In contrast, the nearby natural macropore appears to have had higher connectivity than the artificial macropore, as shown by differences in tracer breakthrough. Specifically, the natural macropore experienced near minimum resistivity during the 1st hour after drip started during the PFM treatment, while it took the artificial macropore until the 7th hour of the OM treatment to achieve minimum resistivity (Figure 3-7, right column). This suggests that the natural macropore allowed faster transport than the OM and potentially had higher connectivity with other nearby preferential flow paths that were not detected explicitly by our measurements or with surface water itself.

The confounding effects of connectivity can be eliminated by analyzing potential for flow, as quantified by permeability. In particular, fracture studies in groundwater have shown that preferential flow paths strongly influence transport rates when the ratio of the permeability of the preferential flow path to the sediment matrix is greater than 100 [Matthai and Belayneh, 2004]. Since the ratio of permeability is identical to the ratio of K , we can compare this to our study where the top 10% of K at location B (i.e., macropore K) was 29.1 times higher than the bottom 90% at location B (i.e., matrix K). However, the literature bases matrix K on flow only in a homogenous sediment matrix, while we estimated matrix K from field measurements at locations adjacent to and likely influenced by the OM. Therefore, a more accurate comparison to the literature might be drawn by selecting a K representative of the flow in the sediment matrix, rather than flow adjacent to the OM. For example, the top 10% of K at location B (i.e., macropore K) is 550 times higher than the bottom 90% of K at location C (i.e., matrix K), which would indicate a strong influence of the OM on transport rates in the meander. This agrees with wetland studies that have shown lateral macropore flow to have 150 times higher K than the matrix [Elci and Molz, 2009].

Our results show that macropore flow dominates solute flux through the meander by diverting solute from other flow paths and focusing solute transport downgradient. The OM and the unfilled portion of the artificial macropore in the PFM case allowed tracer transport through the same 2.75 cm in diameter cross sectional area. However, the area under the breakthrough tracer curve (a_0) was 109% higher for the OM than for the PFM, indicating greater tracer flux to Well 4 (immediately downgradient of the macropore) during the OM than the PFM treatment. The tracer in the OM case is correspondingly less spatially dispersed (i.e., occupies fewer flow paths) laterally across the meander, as indicated by Well 3 exhibiting 60% less total area under the breakthrough tracer curve (a_0) for OM than for PFM. This is consistent with the ERI results (Figure 3-7, right column) where the PFM scenario showed tracer transport not only to the macropore ($X = -0.1$, $Z = -0.5$ m), but also to a shorter natural macropore (centered near $X = 1.0$ m, $Z = -0.5$ m) and deeper into the subsurface. Conversely, the natural macropore did not show a change in resistivity during the OM treatment (Figure 3-7, left column) because the OM dominated solute transport in the down-valley direction and solute did not reach the natural macropore. The low resistivity ring around the PFM in Figure 3-7 ($X = 0$ to 1 m) is a result of diffused transport around the filled macropore and the inversion of ER measurements (discussed

later). Our results agree with previous research which found solute transport to be more spatially disperse in situations with non-preferential flow than preferential flow [Weiler and Fluhler, 2004]. Dispersion of the tracer that occurred during the PFM treatment can be thought of as a form of hydrodynamic macrodispersion [Cirpka and Kitanidis, 2000; Gelhar and Axness, 1983] driven by advection of solute in diverging macropores (or preferential flow paths more generally).

Our results show that solute transport in macropores occurs at substantially shorter timescales than in the sediment matrix, enhancing longitudinal spread of solute over time when the flow domain (e.g., meander bend) is viewed as a whole. The existence of these different flow domains impacts both residence times and transient storage in the meander. At the 9th hour of the PFM treatment as shown by ERI (Figure 3-7), saline tracer penetrates the section of the artificial macropore that we did not fill ($0 < X < 0.6$ and $-0.5 < Z < -0.9$). At the 15th hour, ERI shows the flushing of tracer from the macropore earlier than other regions, contributing to enhanced longitudinal dispersion. This is consistent with temporal moment analysis, where local dispersion coefficients and breakthrough curve skew toward longer times were greater in Wells 3-5 for the OM than for the PFM (Table 3-2). Specifically at Well 5, the percent change in μ_2 was greater than the percent change in μ_3 , and the percent change in dispersion coefficients was greatest, indicating the importance of transport processes other than advection, such as dispersion. Particularly telling is that a 209% increase in dispersion and 268% increase in μ_3 were observed for Well 4, immediately downgradient of the macropore. These results indicate that the OM facilitated transport within the meander at overall shorter timescales than the sediment matrix yet also exhibited longer tails, consistent with previous simulations of open fractures [Bauget and Fourar, 2008; Qian et al., 2011].

3.5.2 Potential Effects of Meander Bend Macropores on Hydrologic Processes at Larger Scales

Macropores can be categorized by their hydrologic connection with the surface stream as either surface-connected or non-surface-connected. Our experimental manipulation, and therefore our discussion here, focuses on surface-connected macropores because they are easily identifiable and interact directly with the surface stream. Surface-connected macropores in theory could affect two broad categories of solute transport at larger scales. First, they could affect solute transport downstream through stream corridors by (1) creating surface dead zone storage and (2) enhancing bidirectional exchange with the hyporheic zone. This suggests that

surface-connected macropores should increase transient storage at the reach scale [Aumen, 1990; Bencala and Walters, 1983]. Depending on the magnitude of this effect, macropores may significantly affect reach scale stream hydrology and solute transport. Future studies should focus on scaling variables such as transient storage parameters [Runkel, 1998] including F_{med} , the ratio of the transport time incorporating transient storage versus pure downstream transport in the main channel [Runkel, 2002].

The second broad category of solute transport at larger scales is how macropores may affect the connection between surface water in the stream channel and groundwater aquifers of various kinds (e.g., shallow floodplain aquifers, deeper aquifers). In our experiments, macropore flow was directed from the channel toward the floodplain because of the macropore's spatial relationship to hydraulic gradients within the channel and meander bend. The first aspect of this is the orientation of the macropore itself, which in our case is down-valley across the meander at the location where it intersects the channel. Although we are not aware of studies that survey macropore orientation in stream systems, our expectation is that this orientation could vary considerably. For example, hyporheic macroinvertebrate burrows are often perpendicular in the vertical direction [Mermillod-Blondin *et al.*, 2002]. Alternatively, root casts and erosional macropores can extend horizontally into the banks and provide baseflow to the stream [Bohlke *et al.*, 2007].

The second aspect of the spatial relationship between a macropore and the hydraulic gradient it experiences is the orientation of the gradient itself. In our study, the hydraulic gradient in the meander bend was down-valley across the meander, similar to the macropore. The installation of the weir increased the magnitude of the head gradients and may have affected the direction of those gradients [Cardenas, 2009a]. Since the direction and magnitude of such gradients can vary widely along the length of a channel with alternating losing (e.g., down-welling, out-welling, lower groundwater table) and gaining reaches (e.g., up-welling, in-welling, higher groundwater table) on multiple scales [Cardenas, 2009b; Gooseff *et al.*, 2006; Payn *et al.*, 2009], macropore impacts to stream hydrology and solute transport should be highly heterogeneous. For instance, in a hydrologically losing stream, macropores may augment stream losses beyond what may be anticipated from stream-to-floodplain or stream-to-aquifer head gradients. Conversely, in a hydrologically gaining stream, macropores enhance stream gains

from groundwater. Either of these affects would then alter stream baseflow conditions by increasing water levels, stream velocities, and sediment transport.

In both cases macropores would have important implications for stream water quality, particularly when allowing the surface stream to bypass low permeability zones or connecting the surface stream to buried layers of high permeability [Bohlke *et al.*, 2007]. Additionally, macropores could potentially allow upwelling contaminants, for example perchloroethene discharge into a river [Conant *et al.*, 2004], to bypass the attenuative capacity of the hyporheic zone. For example, groundwater nitrate in agricultural areas that upwells through macropores could create concentrated hotspots of nitrate and hence microbial or algal metabolism within the surface stream [Angier and McCarty, 2008; Bohlke *et al.*, 2007; Gu *et al.*, 2008]. The significance of both hydrological and water quality effects would depend on how much flow is carried by macropores, which would depend on a variety of factors, including head gradient, macropore diameter, and macropore connectivity.

3.5.3 Methodological Advances in Quantifying Riparian Macropore Distribution and Transport

Limitations in spatial and temporal resolution of mapping technologies, high equipment costs, and lengthy time requirements are explanations why preferential flow paths are usually left unmapped and unidentified [Allaire *et al.*, 2009; A Newman, 2010]. For example, resin impregnation and skeletisation has been performed on macropores in floodplains [Abou Najm *et al.*, 2010; Allaire *et al.*, 2009; Golabi *et al.*, 1995] but these require non-saturated conditions and long setup and drying times [Allaire *et al.*, 2009]. Dye tracers have been used in shallow groundwater applications because they are relatively easy to use and identify different preferential flow paths but they require the destruction of the matrix [Nobles *et al.*, 2004]. Our study represents progress in such characterization methods in a variety of ways, including both ERI and falling head tests.

ERI has been used in prior studies in hydrogeophysical characterization of shallow subsurface flow and transport in relatively coarse porous media within floodplains [Fox *et al.*, 2010] and beneath the stream channel [Ward *et al.*, 2010; Ward *et al.*, 2012]. However, macropores are devoid of sediments, suggesting that unobstructed transport can potentially be at such high rates that characterizing tracer breakthrough in macropores is difficult. To quantify potentially high flow velocities in the macropore, we used an ERI data collection scheme designed to achieve high temporal resolution, particularly in the area of the treatment macropore.

The resulting scheme allowed us to successfully image solute transport through the meander bend. We acknowledge that our high temporal resolution did not turn out to be necessary for characterizing flow in the artificial macropore, probably due to its lack of connectivity to other preferential flow paths at the downgradient end (as discussed earlier), yet such resolution may be necessary in situations with higher connectivity. For example, the natural macropore showed considerably faster response to the tracer, yet we successfully characterized the breakthrough curve there as well.

Conventional falling head tests generally result in values of K for sediments in the vicinity of a small number of discrete well screens. Here we adapted that method to allow resolution of K 's at a greater number of closely spaced depths. Unlike falling head tests conducted in conventional floodplain wells, we did not use a borehole larger than the diameter of the piezometer and we therefore avoided the associated modifications of the condition and structure of the tested soil. Instead, the use of a screened metal drivepoint allowed us to select a series of test depths with reasonably high vertical spatial resolution while minimally disturbing the media adjacent to and below the piezometer. This drivepoint method has been used at a small number of depths in streambeds, but to our knowledge it has not been applied at such a large number of closely spaced vertical intervals either in the floodplain or streambed. This method will prove most useful in sediment with large vertical variations in K yet without large clasts (e.g., boulders), logs, etc., that would impede the drivepoint.

Tandem use of falling head tests and ERI of a saline tracer complement each other. As implemented, ERI provided two-dimensional spatially contiguous mapping capabilities and tracer breakthrough times, but did not measure any hydrologic parameters. By contrast, falling head tests provide direct measurement of hydraulic parameters but have comparatively poorer spatial extent and resolution. Nevertheless, we acknowledge that use of ERI in our study was simplified by prior knowledge of the location of the artificially constructed macropore. Because macropores represent highly concentrated and directed flow, if the locations and orientations of macropores were not known ahead of time, success in locating and identifying the macropores with ERI would depend on the relative positions of the macropore, the saline injection, and the ERI transects. As a result, characterizing field macropores may require adaptive management and consecutive experiments. Nevertheless, we did characterize transport in the natural

macropore reasonably well, even though we were not aware of its existence prior to conducting the experiments.

We note there were some discrepancies between the two techniques in terms of the vertical coordinates where the macropore was observed. For example, ERI shown in Figures 3-6 and 7 suggest the macropore is at an elevation ranging from -0.4 m to -0.6 m relative to the ground surface. Falling head tests (Figure 3-8) depict the macropore at an elevation of -0.8 m relative to the ground surface. There are several potential causes that contribute to this discrepancy. First, the macropore was driven into the bank at a downward angle (roughly 5-10°) to ensure that it would remain completely saturated along its entire length. Using observed distances and this slope, we estimate the macropore was 0.15 -0.25 m deeper at the location of the falling head tests than at the ERI transect, which would explain much of the discrepancy and why the solute plume seems to sink with time. Nevertheless, we hypothesize that three methodological issues also contributed: (1) we represented ERI electrodes in the inversion model as point features located along the surface, while they were actually driven to shallow depths; (2) to achieve high temporal resolution in geophysical imaging, we sacrificed the collection of additional observations which may have improved spatial resolution of the ER images; and (3) ERI inversion results are non-unique and non-exact. The regularization and smoothing that occurs in the inversion process, coupled with the small spatial scale of the macropore relative to inversion pixels, may also help explain the minor discrepancy in macropore depth between ER results and physical measurements of the macropore location.

3.6 CONCLUSIONS

This study serves as a preliminary investigation of the hydrologic importance of macropores in the hyporheic zone at the scale of meander bends. Results from electrical resistivity imaging (ERI), breakthrough tracer analysis, falling head tests, and monitoring hydraulic heads at a meander field site agree that the primary hydrologic function of the macropore is to preferentially transport water at higher flow velocities along hydraulic head gradients. In particular, an artificially created macropore (“open macropore,” or OM) exhibited 29 to 550 times higher hydraulic conductivities than the nearby sediment matrix. Hydraulic gradients perpendicular and parallel to the macropore were respectively 32% and 6% higher for the OM than the partially filled macropore (PFM) case. Results show on average 9% higher mean transport velocities according to temporal moment analysis and 21% higher velocity of the

tracer breakthrough peak for the OM than for the PFM. This indicates that macropores enable solute transport at significantly shorter timescales than matrix transport. Nevertheless, temporal moment analysis also showed that the longitudinal dispersion and tailing of the breakthrough tracer curves were on average 234% and 182% higher for the OM than PFM, respectively. So macropores increase transport velocities but also increase tracer tailing. While a single artificial macropore facilitated such local dispersion in the OM case, the remnant of the artificial macropore in conjunction with pre-existing natural preferential flow paths facilitated macrodispersion within the meander (where tracer spread out considerably in space) during the PFM case. These results may have implications at larger scales. For example, macropores may affect downstream transport and stream-aquifer connectivity by enabling both (1) surface dead zone storage and (2) enhanced bidirectional exchange with the hyporheic zone. Finally, our results indicate that use of time-lapse ERI coupled with saline tracers can be used to characterize transport through macropores, to identify the presence or absence of preferential flow paths through meander bends, and to identify macropore locations within a spatial tolerance. This study can serve as starting point for future investigations of the importance of macropores and other preferential flow paths at various scales (i.e., geomorphic form, reach, watershed) and in determining hyporheic zone, riparian zone, and floodplain function.

3.7 ACKNOWLEDGEMENTS

The authors thank the Thomas F. Jeffress and Kate Miller Jeffress Memorial Trust, the Consortium of Universities for the Advancement of Hydrologic Science, Inc. (CUAHSI) Hydrogeophysics Node, the Institute for Critical Technology and Applied Science at Virginia Tech, and the National Science Foundation (REU - *EEC-1062860*) for support. The authors thank Victoria Sicking for field assistance. The authors thank Audrey Sawyer and an additional anonymous reviewer for helpful comments on this manuscript.

3.8 REFERENCES

- Abou Najm MR, Jabro JD, Iversen WM, Mohtar RH, Evans RG. 2010. New method for the characterization of three-dimensional preferential flow paths in the field. *Water Resour Res* 46, W02503.
- Allaire SE, Roulier S, Cessna AJ. 2009. Quantifying preferential flow in soils: A review of different techniques. *Journal of Hydrology* 378: 179-204.

- Angier JT, McCarty GW. 2008. Variations in base-flow nitrate flux in a first-order stream and riparian zone. *Journal of the American Water Resources Association* 44: 367-380.
- Aubertin, G. M. 1971. Nature and extent of macropores in forest soils and their influence on subsurface water movement. Northeastern Forest Experiment Station, Upper Darby, Pa.
- Aumen NG. 1990. Concepts and methods for assessing solute dynamics in stream ecosystems. *J N Am Benth Soc* 9: 95-119.
- Autodesk. 2011. AutoCAD Civil3D 2011.
- Baines D, Smith DG, Froese DG, Bauman P, Nimeck G. 2002. Electrical resistivity ground imaging (ERGI): a new tool for mapping the lithology and geometry of channel-belts and valley-fills. *Sedimentology* 49: 441-449.
- Bates PD, Stewart MD, Desitter A, Anderson MG, Renaud JP, Smith JA. 2000. Numerical simulation of floodplain hydrology. *Water Resour Res* 36: 2517-2529.
- Bauget F, Fourar M. 2008. Non-Fickian dispersion in a single fracture. *J Cont Hyd* 100: 137-148.
- Beasley, R. S. 1976. Contribution of Subsurface Flow from the Upper Slopes of Forested Watersheds to Channel Flow. *Soil Sci Soc Am J* 40: 955-957.
- Bencala KE, Walters RA. 1983. Simulation of solute transport in a mountain pool and riffle stream - a transient storage model. *Water Resour Res* 19: 718-724.
- Beres M, Haeni FP. 1991. Application of ground penetrating radar methods in hydrogeologic studies. *Ground Water* 29: 375-386.
- Beven K, Germann P. 1982. Macropores and water-flow in soils. *Water Resour Res* 18(5): 1311-1325.
- Binley A. 2010. Resistivity Freeware. Andrew Binley. Accessed 11/28/2010: Retrieved from <http://www.es.lancs.ac.uk/people/amb/Freeware/freeware.htm>.
- Binley A, Kemna A. 2005. DC resistivity and induced polarization methods. In *Hydrogeophysics*, Rubin Y, Hubbard SS (eds). Springer, Netherlands; 129-156.
- Blake, G. 1973. Water Recharge in a Soil with Shrinkage Cracks. *Soil Sci Soc Am* 37: 669.
- Boano, F., C. Camporeale, R. Revelli, and L. Ridolfi (2006), Sinuosity-driven hyporheic exchange in meandering rivers, *Geophys Res Lett*, 33, L18406.

- Bohlke JK, O'Connell ME, Prestegard KL. 2007. Ground water stratification and delivery of nitrate to an incised stream under varying flow conditions. *J Env Qual* 36: 664-680.
- Boulton AJ. 2007. Hyporheic rehabilitation in rivers: restoring vertical connectivity. *Freshwater Bio* 52: 632-650.
- Boulton AJ, Findlay S, Marmonier P, Stanley EH, Valett HM. 1998. The functional significance of the hyporheic zone in streams and rivers. *Annual Review of Ecology and Systematics* 29: 59-81.
- Brassington R. 2007. *Field hydrogeology*. John Wiley: Chichester, England ; Hoboken, NJ.
- Bretschko G. 2002. Interstitial flow through preferential flow paths in the hyporheic zone of the Oberer Seebach, Austria. *Aquatic Sci* 64: 307-316.
- Bridge JS. 1985. Paleochannel Patterns Inferred from Alluvial Deposits; a Critical Evaluation. *J Sed Petro* 55: 579-589.
- Brunke M, Gonser T. 1997. The ecological significance of exchange processes between rivers and groundwater. *Freshwater Bio* 37: 1-33.
- Calver A. 2001. Riverbed permeabilities: Information from pooled data. *Ground Water* 39: 546-553.
- Cardenas MB. 2008. The effect of river bend morphology on flow and timescales of surface water-groundwater exchange across pointbars. *J Hydro* 362: 134-141.
- Cardenas MB. 2009a. Direct simulation of pore level Fickian dispersion scale for transport through dense cubic packed spheres with vortices. *Geochem Geophys Geosys* 10.
- Cardenas MB. 2009b. A model for lateral hyporheic flow based on valley slope and channel sinuosity. *Water Resour Res* 45, W01501.
- Cardenas MB. 2009c. Stream-aquifer interactions and hyporheic exchange in gaining and losing sinuous streams. *Water Resources Research* 45, W06429.
- Cardenas MB, Wilson JL, Zlotnik VA. 2004. Impact of heterogeneity, bed forms, and stream curvature on subchannel hyporheic exchange. *Water Resour Res* 40, W08307.
- Chen C, Packman AI, Zhang DX, Gaillard JF. 2010. A multi-scale investigation of interfacial transport, pore fluid flow, and fine particle deposition in a sediment bed. *Water Resour Res* 46, W11560.

- Cirpka OA, Kitanidis PK. 2000. Characterization of mixing and dilution in heterogeneous aquifers by means of local temporal moments. *Water Resour Res* 36(5): 1221-1236.
- Conant B, Cherry JA, Gillham RW. 2004. A PCE groundwater plume discharging to a river: influence of the streambed and near-river zone on contaminant distributions. *J Cont Hyd* 73: 249-279.
- Crook N, Binley A, Knight R, Robinson DA, Zarnetske J, Haggerty R. 2008. Electrical resistivity imaging of the architecture of substream sediments. *Water Resour Res* 44, W00D13.
- Duval TP, Hill AR. 2006. Influence of stream bank seepage during low-flow conditions on riparian zone hydrology. *Water Resour Res* 42, W10425.
- Edwards, C. A. and J. R. Lofty. 1977. *Biology of earthworms*. Chapman and Hall ; Wiley, London.
- Edwards, W. M. 1979. Numerical Study of the Effects of Noncapillary-Sized Pores Upon Infiltration. *Soil Sci Soc Am J* 43: 851-856.
- Elci A, Molz FJ. 2009. Identification of Lateral Macropore Flow in a Forested Riparian Wetland through Numerical Simulation of a Subsurface Tracer Experiment. *Water Air and Soil Poll* 197: 149-164.
- Fox GA, Fuchs JW, Storm DE, Penn CJ, Brown GO. 2009. Subsurface transport of phosphorus in riparian floodplains: influence of preferential flow paths. *J Env Qual* 38: 473-484.
- Fox GA, Heeren DM, Miller RB, Storm DE, Halihan T, Penn CJ. 2010. Preferential flow effects on subsurface contaminant transport in alluvial floodplains. *T ASABE* 53: 127-136.
- Fradelizio GL, Levander A, Zelt CA. 2008. Three-dimensional seismic-reflection imaging of a shallow buried paleochannel. *Geophysics* 73: B85-B98.
- Geiger S, Cortis A, Birkholzer JT. 2010. Upscaling solute transport in naturally fractured porous media with the continuous time random walk method. *Water Resour Res* 46, W12530.
- Gelhar LW, Axness CL. 1983. 3-dimensional stochastic analysis of macrodispersion in aquifers. *Water Resour Res* 19(1): 161-180.
- Golabi MH, Radcliffe DE, Hargrove WL, Tollner EW. 1995. Macropore effects in conventional tillage and no-tillage soils. *J Soil Water Conserv* 50: 205-210.

- Gooseff MN, Anderson JK, Wondzell S, LaNier J, Haggerty R. 2006. A modeling study of hyporheic exchange pattern and the sequence, size, and spacing of stream bedforms in mountain stream networks, Oregon, USA (Retraction of vol 19, 2005). *Hydrol Process* 20: 2443-2457.
- Gormally KH, McIntosh MS, Mucciardi AN, McCarty GW. 2011. Ground penetrating radar detection and three-dimensional mapping of lateral macropores: II. riparian application. *Soil Sci Soc Am J* 75: 1236-1243.
- Govindaraju RS, Das BS. 2007. *Moment analysis for subsurface hydrologic applications*. Springer, London.
- Groffman PM, Boulware NJ, Zipperer WC, Pouyat RV, Band LE, Colosimo MF. 2002. Soil nitrogen cycle processes in urban Riparian zones. *Env Sci Tech* 36: 4547-4552.
- Groffman PM, Dorsey AM, Mayer PM. 2005. N processing within geomorphic structures in urban streams. *J N Am Benth Soc* 24: 613-625.
- Gu CH, Hornberger GM, Herman JS, Mills AL. 2008. Influence of stream-groundwater interactions in the streambed sediments on nitrate flux to a low-relief coastal stream. *Water Resour Res* 44, W11432.
- Hauer FR, Lamberti GA. 2006. *Methods in Stream Ecology*. Academic Press/Elsevier: San Diego, CA.
- Heeren DM, Fox GA, Miller RB, Storm DE, Fox AK, Penn CJ, Halihan T, Mittelstet AR. 2011. Stage-dependent transient storage of phosphorus in alluvial floodplains. *Hydrol Process* 25: 3230-3243.
- Heeren DM, Miller RB, Fox GA, Storm DE, Halihan T, Penn CJ. 2010. Preferential flow effects on subsurface contaminant transport in alluvial floodplains. *T ASABE* 53: 127-136.
- Hester, E. T., and M. W. Doyle (2008), In-stream geomorphic structures as drivers of hyporheic exchange, *Water Resour Res*, 44, W03417.
- Hester ET, Gooseff MN. 2010. Moving beyond the banks: hyporheic restoration is fundamental to restoring ecological services and functions of streams. *Env Sci Tech* 44: 1521-1525.
- Hvorslev MJ. 1951. *Time lag and soil permeability in ground-water observations*. U.S. Waterways Experiment Station: Vicksburg, Miss.; 50 p.

- Jacobson R.B., Janke T.P., Skold J.J. 2011. Hydrologic and geomorphic considerations in restoration of river-floodplain connectivity in a highly altered river system, Lower Missouri River, USA. *Wetl Ecol Manag* 19: 295-316.
- Jung, M., T. P. Burt, and P. D. Bates (2004), Toward a conceptual model of floodplain water table response, *Water Resour Res*, 40, W12409.
- Koestel, J, Vanderborght J, Javaux M, Kemna A, Binley A, Vereecken H. Non-invasive 3-D transport characterization in a sandy soil using ERT: 1. Investigation the validity of ERT-derived transport parameters. *Vadose Zone J.*, 8(3), 711-722.
- Lamontagne S, Leaney FW, Herczeg AL. 2005. Groundwater-surface water interactions in a large semi-arid floodplain: implications for salinity management. *Hydrol Process* 19: 3063-3080.
- Lin H, Luo LF, Halleck P. 2008. Quantifying soil structure and preferential flow in intact soil using x-ray computed tomography. *Soil Sci Soc of Am J*, 72: 1058-1069.
- Marzadri A, Tonina D, Bellin A, Vignoli G, Tubino M. 2010. Semianalytical analysis of hyporheic flow induced by alternate bars. *Water Resour Res* 46, W07531.
- Matthai, S. K., and M. Belayneh (2004), Fluid flow partitioning between fractures and a permeable rock matrix, *Geophys Res Lett*, 31, L07602.
- McGlynn B. L., McDonnell J. J. (2003). Quantifying the relative contributions of riparian and hillslope zones to catchment runoff. *Water Resour Res* 39, 1390: 11.
- Mermillod-Blondin F, Gerino M, des Chatelliers MC, Degrange V. 2002. Functional diversity among 3 detritivorous hyporheic invertebrates: an experimental study in microcosms. *Journal of the North American Benthological Society* 21: 132-149.
- Mermillod-Blondin F, Rosenberg R (2006). Ecosystem engineering: the impact of bioturbation on biogeochemical processes in marine and freshwater benthic habitats. *Aquatic Sci* 68(4): 434-442.
- Mermillod-Blondin F, Rosenberg R, Francois-Carcaillet F, Norling K, Mauclair L. (2004). Influence of bioturbation by three benthic infaunal species on microbial communities and biogeochemical processes in marine sediment. *Aquat Microb Ecol* 36(3): 271-284.
- Newman A. 2010. Water and solute transport in the shallow subsurface of a riverine wetland natural levee. M.S. thesis Louisiana State University: Baton Rouge, LA. Dissertations and Theses. Web. 10 Nov 2011.

- Nobles MM, Wilding LP, McInnes KJ. 2004. Pathways of dye tracer movement through structured soils on a macroscopic scale. *Soil Sci* 169: 229-242.
- Nogaro G, Mermillod-Blondin F, Francois-Carcaillet F, Gaudet JP, Lafont M, Gibert J. 2006. Invertebrate bioturbation can reduce the clogging of sediment: an experimental study using infiltration sediment columns. *Freshwater Bio* 51: 1458-1473.
- Payn RA, Gooseff MN, McGlynn BL, Bencala KE, Wondzell SM. 2009. Channel water balance and exchange with subsurface flow along a mountain headwater stream in Montana, United States. *Water Resour Res* 45, W11427.
- Poole GC, Stanford JA, Running SW, Frissell CA. 2006. Multiscale geomorphic drivers of groundwater flow paths: subsurface hydrologic dynamics and hyporheic habitat diversity. *J N Am Benth Soc* 25: 288-303.
- Qian JZ, Zhan HB, Chen Z, Ye H. 2011. Experimental study of solute transport under non-Darcian flow in a single fracture. *J Hydro* 399: 246-254.
- Revelli, R., F. Boano, C. Camporeale, and L. Ridolfi (2008), Intra-meander hyporheic flow in alluvial rivers, *Water Resour Res*, 44, W12428.
- Runkel RL. 1998. *One-dimensional transport with inflow and storage (OTIS) : a solute transport model for streams and rivers*. U.S. Dept. of the Interior: Denver, CO.
- Runkel RL. 2002. A new metric for determining the importance of transient storage. *Journal of the North American Benthological Society* 21: 529-543.
- Sabo MJ, Bryan CF, Kelso WE, Rutherford A. 1999. Hydrology and aquatic habitat characteristics of a riverine swamp: I. Influence of flow on water temperature and chemistry. *Reg Riv-Res & Manag* 15: 505-523.
- Sawyer AH, Cardenas MB. 2009. Hyporheic flow and residence time distributions in heterogeneous cross-bedded sediment. *Water Resour Res* 45, W08406.
- Schmid BH. 2003. Temporal moments routing in streams and rivers with transient storage. *Advances in Water Resources* 26: 1021-1027.
- Shipitalo MJ, Protz R. 1987. Comparison of morphology and porosity of a soil under conventional and zero tillage. *Can J Soil Sci* 67: 445-456.
- Simpson MJ, Simpson AJ, Gross D, Spraul M, Kingery WL. 2007. H-1 and F-19 nuclear magnetic resonance microimaging of water and chemical distribution in soil columns. *Env Toxic Chem* 26: 1340-1348.

- Song JX, Chen XH, Cheng C. 2010. Observation of bioturbation and hyporheic flux in streambeds. *Fron of Env Sci Eng China* 4: 340-348.
- Storey R, Schachtman DP, Thomas MR. 2003. Root structure and cellular chloride, sodium and potassium distribution in salinized grapevines. *Plant, Cell & Environment* 26: 789-800.
- Su, GW, Geller JT, Pruess K, Hunt JR. 2001. Solute transport along preferential flow paths in unsaturated fractures. *Water Resour Res* 37(10): 2481– 2491.
- Tonina D, Buffington JM. 2011. Effects of stream discharge, alluvial depth and bar amplitude on hyporheic flow in pool-riffle channels. *Water Resour Res* 47, W08508.
- Valett HM, Fisher SG, Stanley EH. 1990. Physical and chemical characteristics of the hyporheic zone of a sonoran desert stream. *J N Am Benth Soc* 9: 201-215.
- Van der Hoven SJ, Fromm NJ, Peterson EW. 2008. Quantifying nitrogen cycling beneath a meander of a low gradient, N-impacted, agricultural stream using tracers and numerical modelling. *Hydrol Process* 22: 1206-1215.
- Vereecken H. 2006. *Applied hydrogeophysics*. Springer, Dordrecht, The Netherlands.
- Ward AS, Gooseff MN, Singha K. 2010. Imaging hyporheic zone solute transport using electrical resistivity. *Hydrol Process* 24: 948-953.
- Ward AS, Gooseff MN, Singha K. 2012. How does subsurface characterization affect simulations of hyporheic exchange? *Ground Water*, 51: 14-28.
- Ward, AS, Fitzgerald M, Gooseff MN, Voltz TJ, Binley AM, Singha K. 2012b. Hydrologic and geomorphic controls on hyporheic exchange during base flow recession in a headwater mountain stream. *Water Resour Res* 48, W04513.
- Weiler M, Fluhler H. 2004. Inferring flow types from dye patterns in macroporous soils. *Geoderma* 120: 137-153.
- Zarnetske JP, Gooseff MN, Bowden WB, Greenwald MJ, Brosten TR, Bradford JH, McNamara JP. 2008. Influence of morphology and permafrost dynamics on hyporheic exchange in arctic headwater streams under warming climate conditions. *Geophys Res* 35, L02501.
- Zhan HB, Qian JZ, Chen Z, Luo SH. 2011. Solute transport in a filled single fracture under non-Darcian flow. *Int J Rock Mech Min Sci* 48:132-140.

Table 3-1. Comparison of non-storm meander bend hydraulic gradients for both macropore treatments.

| Hydraulic Gradient Scale | Hydraulic Gradient Direction | Wells | PFM Gradient (m/m) from 0-5 Hours | OM Gradient (m/m) from 0-5 Hours | Percent Change (%) from PFM to OM treatment |
|--------------------------|------------------------------|-------------|-----------------------------------|----------------------------------|---|
| In or near macropore | Cross-Valley | Well 2 to 1 | 0.0448 | 0.0593 | 32.4 |
| | Down-Valley | Well 2 to 4 | 0.0962 | 0.1022 | 6.2 |
| Across entire field site | Cross-Valley | Well 7 to 6 | 0.0144 | 0.0144 | 0.0 |
| | Down-Valley | Well 8 to 3 | 0.0871 | 0.0873 | 0.2 |

Table 3-2. Temporal Moment Analysis for Wells 3-5.

| | Describes | Well 3 | | | Well 4 | | | Well 5 | | |
|------------|--|----------|----------|--------------|----------|----------|--------------|----------|----------|--------------|
| | | PFM | OM | % Δ^1 | PFM | OM | % Δ^1 | PFM | OM | % Δ^1 |
| α_0 | Area under BTC ² ($\mu\text{s}/\text{cm}$) | 24.0 | 9.51 | -60.3 | 807. | 1680 | 109. | 13.0 | 35.7 | 176. |
| n_1 | Mean arrival (hr) | 0.369 | 0.317 | -14.2 | 0.370 | 0.338 | -8.64 | 0.402 | 0.369 | -2.07 |
| μ_2 | Variance (hr ²) | 1.06E-03 | 1.27E-03 | 19.9 | 1.20E-03 | 2.83E-03 | 136. | 2.49E-03 | 1.18E-02 | 373. |
| μ_3 | Value related to skewness (hr ³) | 2.21E-05 | 4.61E-05 | 109. | 3.00E-05 | 1.10E-04 | 268. | 1.27E-04 | 3.43E-04 | 170. |

¹ “% Δ ” is the percent change for the OM relative to the PFM.

² “BTC” is the breakthrough tracer curve for the electrical conductivity data.

Table 3-3. Tracer velocities and dispersion coefficients for Wells 3-5.

| Based on | Variable | Well 3 | | | Well 4 | | | Well 5 | | |
|-------------------|--------------------------------|--------|------|--------------|--------|------|--------------|--------|------|--------------|
| | | PFM | OM | % Δ^1 | PFM | OM | % Δ^1 | PFM | OM | % Δ^1 |
| BTCs ² | Velocity of peak (m/d) | 9.60 | 11.6 | 20.8 | 9.08 | 10.5 | 15.6 | 8.08 | 10.2 | 26.2 |
| n_1 | Mean velocity (m/d) | 8.90 | 10.4 | 16.6 | 8.24 | 9.01 | 9.43 | 7.36 | 7.52 | 2.12 |
| n_1, μ_2 | Dispersion (m ² /d) | 0.37 | 0.71 | 90.0 | 0.37 | 1.0 | 209. | 0.50 | 2.5 | 404. |

¹ “% Δ ” is the percent change for the OM relative to the PFM.

² “BTC” is the breakthrough tracer curve for the electrical conductivity data.

Table 3-4. Falling head test data during the OM treatment for each location.

| Parameter | Meander (A) | Macropore (B) | Floodplain (C) |
|---|-------------|---------------|----------------|
| Maximum K (m/s) | 1.41E-04 | 4.76E-04 | 9.51E-06 |
| Geometric mean of top 10% of K 's (m/s) | 1.31E-04 | 4.57E-04 | 9.16E-06 |
| Geometric mean of bottom 90% of K 's (m/s) | 1.60E-05 | 1.63E-05 | 8.31E-07 |
| Ratio of top 10% and bottom 90% | 8.2 | 29.1 | 11.0 |
| Ratio of top 10% at location B and bottom 90% | 28.6 | 29.1 | 550. |
| Standard deviation of all K 's (m/s) | 4.88E-05 | 1.76E-04 | 3.09E-06 |



Figure 3-1. Views of field site. Left panel is looking downstream towards site and monitoring well configuration. Right panel shows macropore being constructed by driving a 2.75 cm diameter hollow pipe into the upstream end of the meander bend at the bottom of the channel.

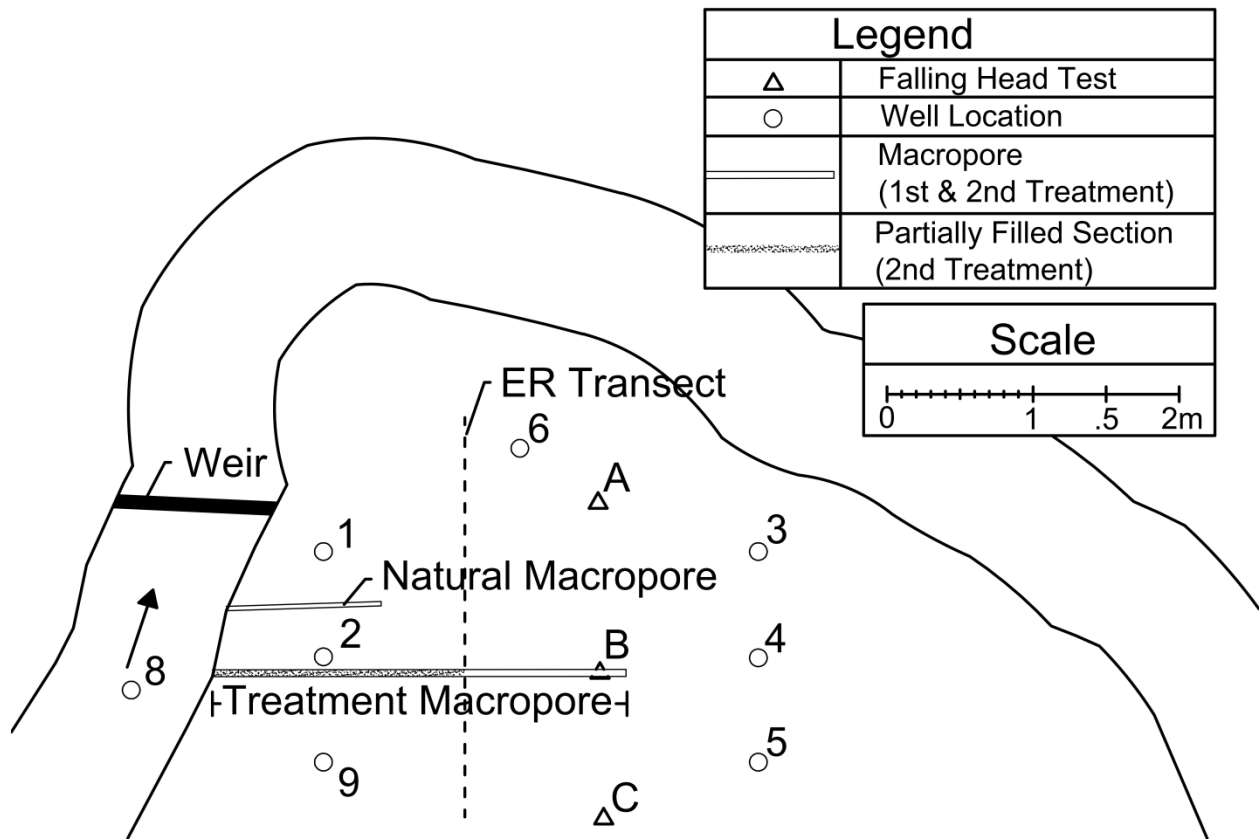


Figure 3-2. Site schematic. Water in the channel flows from left to right around the meander bend. Shown are the surveyed locations of monitoring wells, the location of the treatment macropore and the naturally occurring macropore, the ERI transect consisting of 12 electrodes, and the locations of the falling head tests. Well 7 was located in the floodplain (not shown, see Figure 3-3). Well 9 was the injection well.

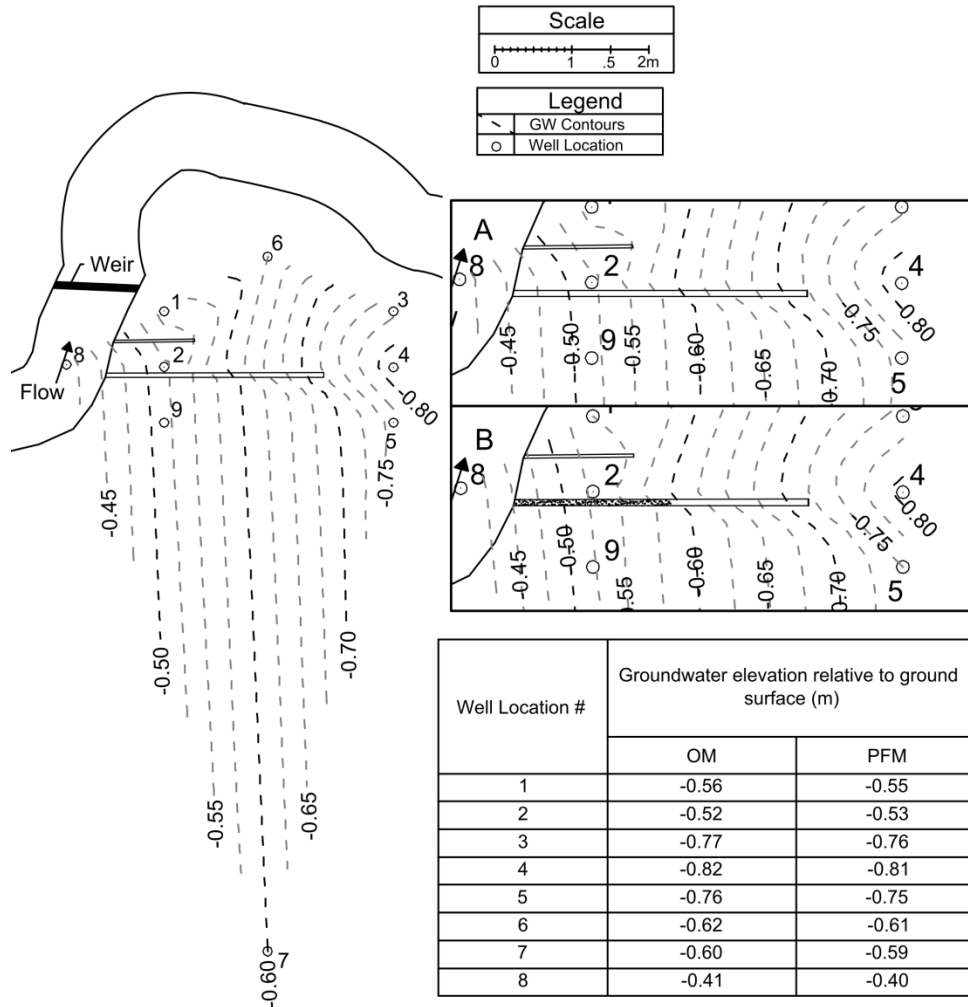


Figure 3-3. Estimated piezometric contour map based on non-storm averaged groundwater levels collected in 8 wells for the OM treatment. Arrows indicate surface stream flow direction.

Contours at the meander-scale show little change between the OM (inset A) and PFM (inset B) scenarios, even immediately adjacent to the macropore. The presented results are averaged data from 1:30-6:30 pm on 6-9-2011 for the OM and from 12:00-5:00 pm on 6-11-2011 for the PFM (0-5 hours from start of drip). Contours were generated with triangular irregular networks in AutoCAD, Civil3D. The contours adjacent to both macropore treatments are concave; however this is likely caused by the interpolation scheme used to create the contours. The ground surface elevation at Well 2 was selected as an arbitrary datum for comparing and analyzing piezometric elevations, ERI, and hydraulic conductivity measurements.

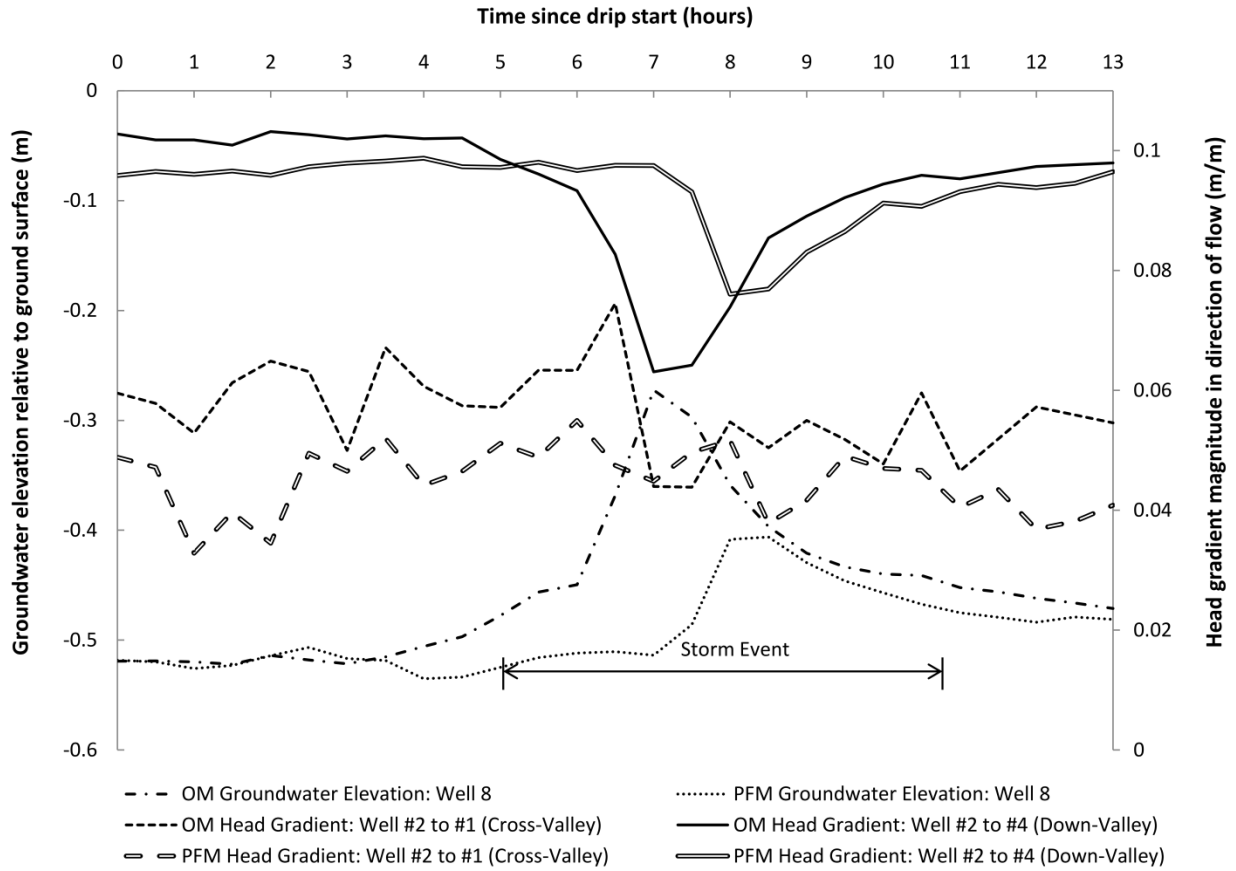


Figure 3-4. Groundwater elevations for Well 8 (beneath channel) showing the relative timing and magnitude of storms that occurred during the experiment (left y-axis). Elevations are relative to ground surface at Well 2. Also shown are cross-valley and down-valley head gradient magnitudes in or near the macropore and across the entire field site (right y-axis).

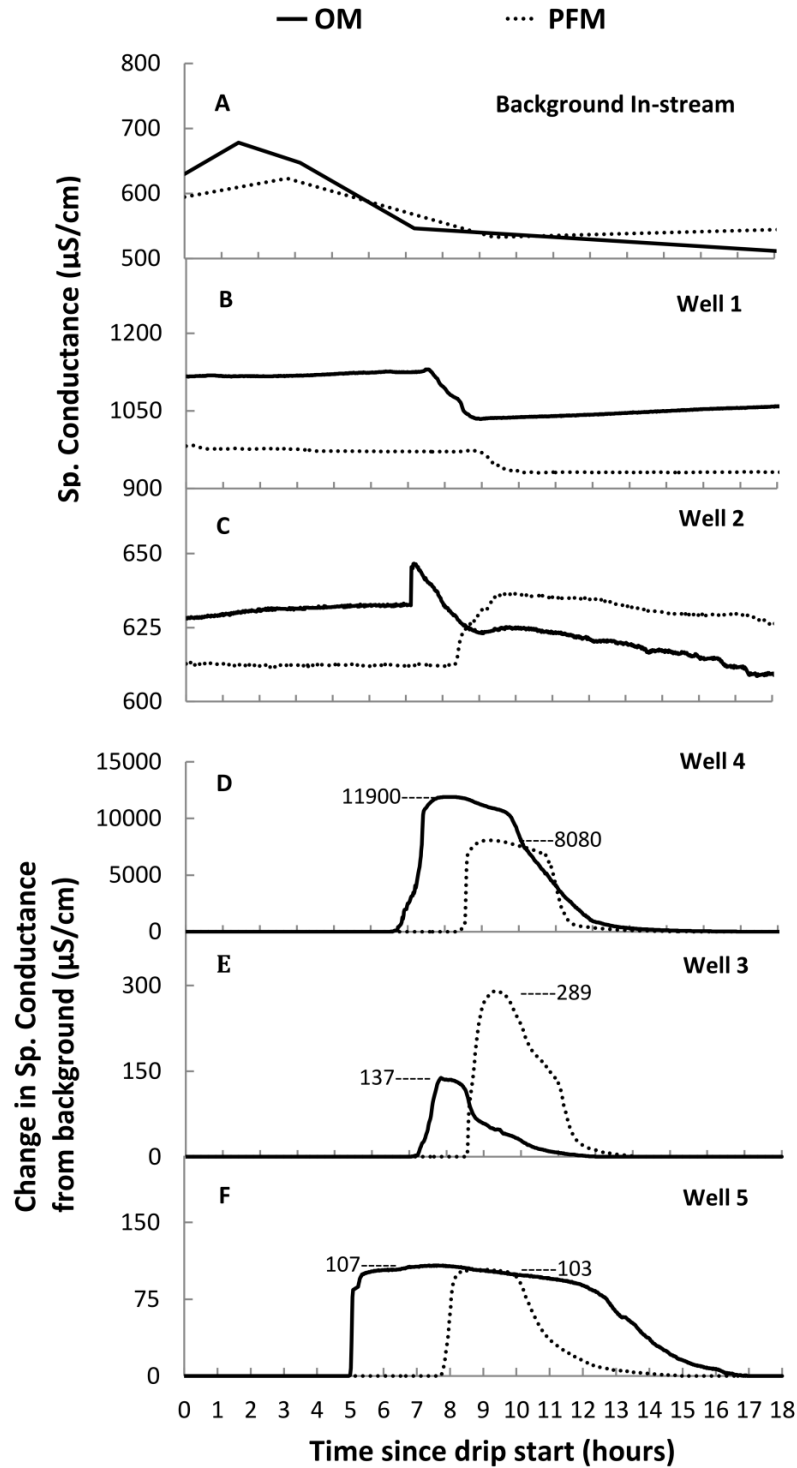


Figure 3-5. Breakthrough tracer curves. Panel A shows in-stream specific conductivity readings ($\mu\text{S}/\text{cm}$). Panels B-C show specific conductivity readings ($\mu\text{S}/\text{cm}$) while Panels D-F show change in specific conductivity readings ($\mu\text{S}/\text{cm}$) from background. Peak values are labeled for Panels D-F.

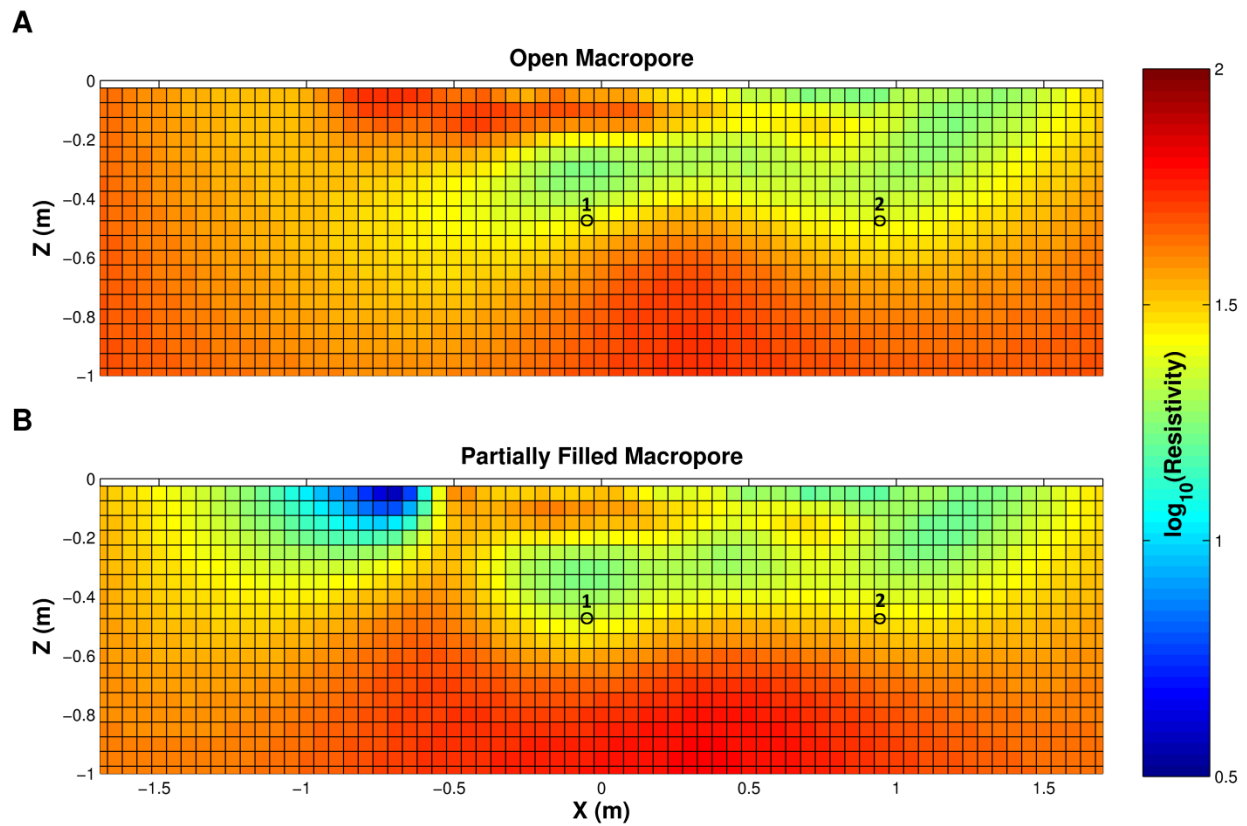


Figure 3-6. Background (no saline tracer) ERI created for (A) the OM, and (B) the PFM. Images are cross sections of the meander bend looking upstream (i.e., the surface stream is on the right-hand side of each subplot, see Figure 3-2). Elevations are relative to ground surface at Well 2. Approximate macropore locations are shown for the treatment macropore (1) and natural macropore (2).

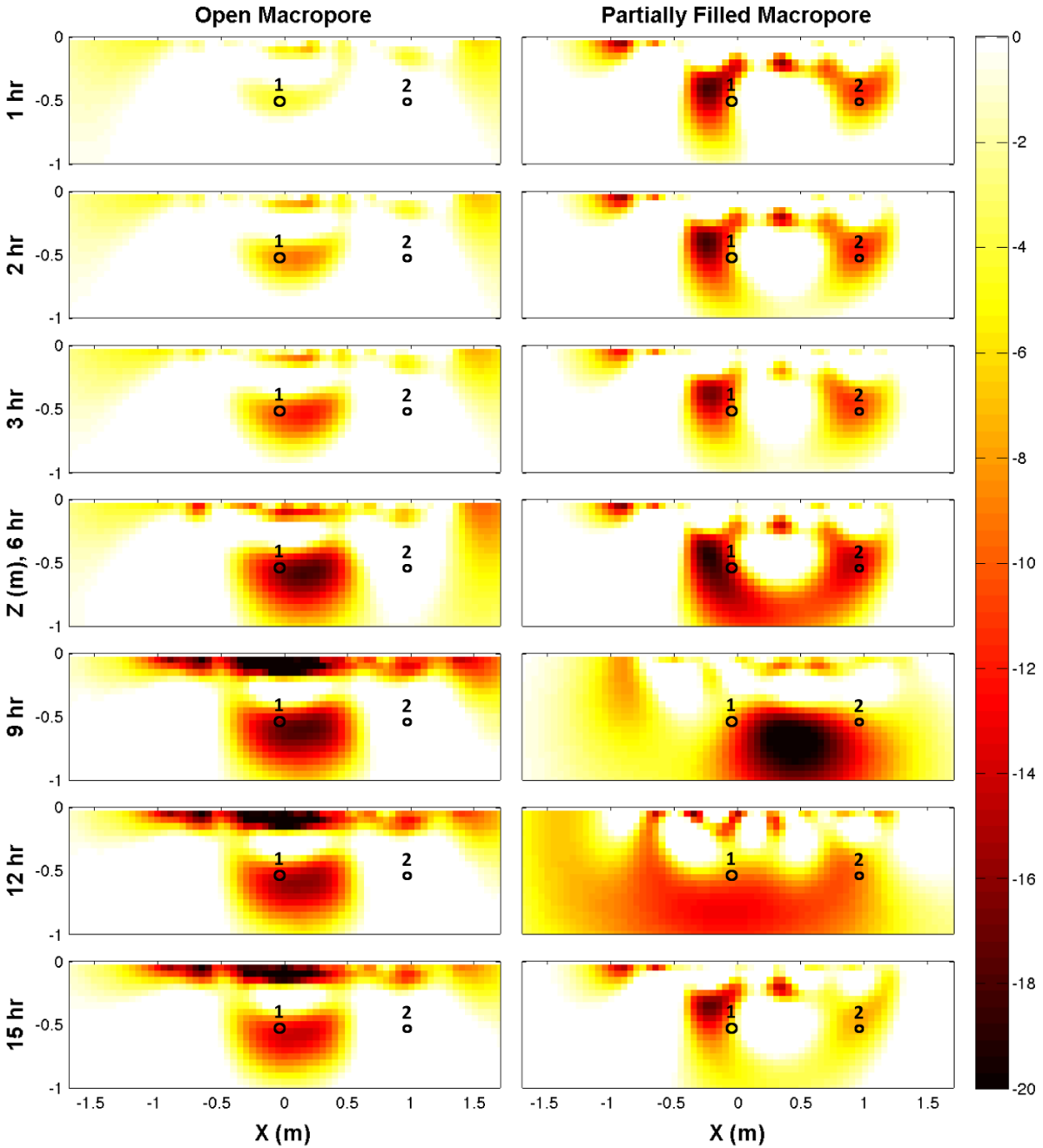


Figure 3-7. Time-lapse ERI of saline tracer movement through the meander bend for the OM (left column) and the PFM (right column). Images are looking upstream (same orientation as Figure 3-6). Color indicates the decrease in electrical resistivity in the subsurface due to tracer (as percent change from background). Each row of the plot is for a different total time elapsed from the start of the tracer drip. Elevations are relative to ground surface at Well 2. Approximate macropore locations are shown for the treatment macropore (1) and natural macropore (2).

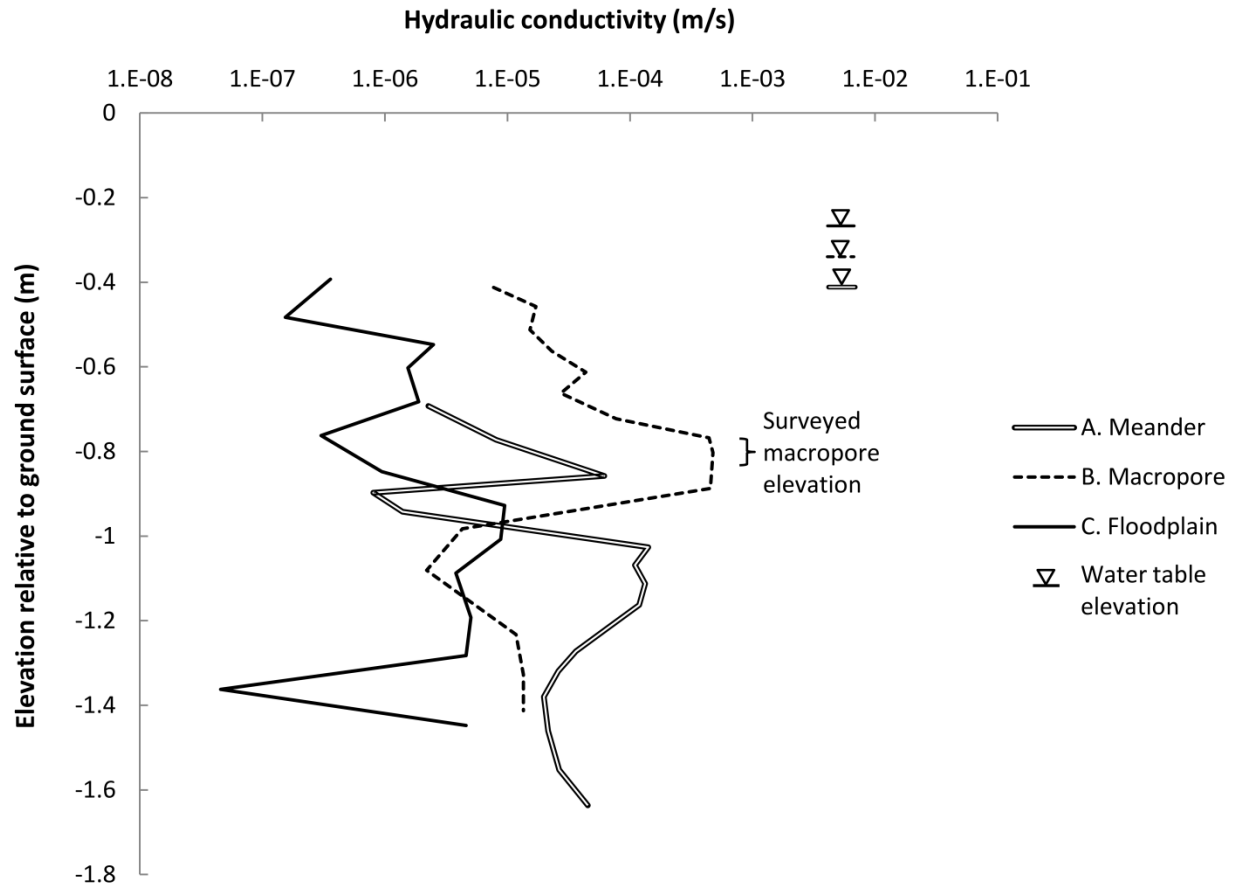


Figure 3-8. Profiles of K versus depth at three locations across meander bend transect for the case of the OM (locations in Figure 3-2). The macropore spanned the elevation from -0.79 to -0.81 m at location B. Elevations are relative to ground surface at Well 2.

CHAPTER 4: *Macropores along Stream Channels: Abundance, Dimensions, and Effects on Surface Water-Groundwater Exchange*

Garrett T. Menichino¹, Erich T. Hester¹

¹Department of Civil and Environmental Engineering, Virginia Tech, Blacksburg, VA 24061

Status: This material is currently in preparation for submission to *Freshwater Science*.

4.1 ABSTRACT

Macropores are connected void spaces in the subsurface and can act as preferential flow paths for groundwater transport. Macropores connected to stream channels have been documented, yet their dimensions and distribution patterns have not been well characterized. We performed field surveys across five streams of a variety of sizes, gradients, and watershed land uses in the Appalachian Mountains of Southwest Virginia, and found that surface-connected macropores are nearly ubiquitous. We attribute the creation of macropores in this region to a variety of mechanisms, including soil piping, tree root decay, erosion around hardened structures, macroinvertebrate burrows, and invertebrate burrows. The diverse range of such formation mechanisms and the presence of fine sediment in all five streams suggest that macropores may also be common outside these mountainous settings. Macropores openings were slightly wider than tall, with median cross-sectional widths and heights of 3.5 cm and 3.0 cm, respectively. The median and maximum macropore lengths to first bend were 15.0 cm and 120.5 cm into the bank, respectively. Yet true (tortuous) macropore lengths are likely often greater, and developing methods to accurately map macropores is recommended. The median interspacing of macropores across all streams was 0.38 m while the mean interspacing was 1.12 m, indicating macropores were clustered in space. These interspacings are likely underestimates as we did not record macropores whose openings were less than 1 cm in diameter. Macropores are inundated at different times due to differences in their heights on the stream bank, channel

geometry, and precipitation. Our HEC-RAS modeling of channel hydraulics in the five streams indicates that only 1-32% of macropores were inundated by channel water at baseflow while up to 97% were inundated during the largest storms. Because most macropores were inundated during storm events, we quantified the effect of macropores on hyporheic exchange by installing a transect of wells perpendicular to a bank with macropores at the face (M transect), to a transect of wells at a bank face without macropores (NM transect). Four wells were installed at each transect, with A and B existing 0.5m and 1.0m into the bank, respectively. We demonstrated the effect of macropores on bank storage in two ways: first, by the overall differences between the two transects in hydraulic head fluctuations, temperature fluctuations, and K measurements; and second, by the observation of the greatest response in the macropore transect for hydraulic head fluctuation is not at the well closest to the stream. Water level fluctuations during storms over a one year period at M-A and M-B were on average 139% higher than water level fluctuations at NM-A and NM-B, suggesting that macropores acted as preferential flow paths and increased bank storage during these storm events. Both M-A and M-B closely tracked in-stream levels during the rising limb, but quickly drew down at the tail end of the storm flow, because the macropores quickly emptied their entire volume of water when stream water levels receded. Similarly, during a year of storm events, macropores increased temperature fluctuations 0.5m into the bank along the M transect by an average 29% over the NM transect. Rising head tests show that K at M-A and M-B was 60.5 and 139 times higher than NM-A and NM-B, respectively. Hydraulic head fluctuations, temperature fluctuations, and K measurements agree that macropores act as preferential flow paths and increase bank storage, which in turn may influence hyporheic functions; hyporheic habitat, pollutant attenuation, biogeochemical cycling. Surface water infiltration was the hydrologic process responsible for bank storage and was augmented by macropores. Pressure wave propagation caused groundwater levels to increase throughout the bank and riparian zone almost concurrently with channel water level rise during storms over the year.

Keywords: Connected void spaces, Hydraulic conductivity, Field survey, Matrix flow, Hyporheic exchange, Bank storage

4.2 INTRODUCTION

The hyporheic zone is the region where surface water and groundwater interact beneath and adjacent to stream channels [Triska *et al.*, 1989b]. Hyporheic flow paths can extend vertically (e.g., weir-induced hyporheic exchange), laterally (e.g., intra-meander flow), or longitudinally (e.g., along paleochannels, through mid-channel bars) along the stream channel depending on stream morphology and hydrologic conditions [Burkholder *et al.*, 2008; Hester and Doyle, 2008; Poole *et al.*, 2006; Revelli *et al.*, 2008]. Surface water is generally high in dissolved oxygen and nutrients, while groundwater is generally low in dissolved oxygen, high in inorganic solutes, and has low velocities relative to surface water [Brunke and Gonser, 1997; Triska *et al.*, 1989]. The interaction of these two water bodies creates unique conditions that can provide various functions for the surface stream including temperature regulation, nutrient cycling, pollutant buffering, and habitat creation [Brunke and Gonser, 1997].

Floodplains and riparian zones can supply groundwater to streams, providing aquatic organisms with organic carbon and nutrients [McGlynn and McDonnell, 2003], and acting as a sink for common surface water pollutants, such as nitrate [Groffman *et al.*, 2002; P Vidon *et al.*, 2010]. When stream water levels are higher than the adjacent groundwater table, floodplains and riparian vadose zone pore spaces can fill with water. Once stream water levels fall below the adjacent groundwater table, water is released from pore spaces back to the stream. During storm events, this hydrologic process is known as bank storage [Pinder and Sauer, 1971], but the concept also applies to water level fluctuations caused by daily snowmelt, evapotranspiration, hydropeaking, and tidal fluctuations [Arntzen *et al.*, 2006; Francis *et al.*, 2010; Loheide and Lundquist, 2009; Peterson and Connelly, 2001; Sawyer *et al.*, 2009; Westbrook *et al.*, 2005; Wondzell *et al.*, 2010]. Hyporheic zone flow paths can be divided loosely into two categories known as the “gill” and “lung” models, respectively [Sawyer *et al.*, 2009]. In the gill model, flow directions are similar during low flow and high flow conditions because of constraining background groundwater levels, whereas in the lung model, flow directions have notable reversals based on relatively rapid variations in river water levels.

Bank storage reduces peak channel flows during storm events and promotes groundwater recharge [Jung *et al.*, 2004; Kondolf *et al.*, 1987]. Bank storage can also intercept and hold pulses of water quality constituents being transported downstream [X Chen and Chen, 2003]. Pollutants can enter banks during storm events and be slowly released at baseflow [Squillace *et*

al., 1993]. These constituents can remain at elevated levels in riparian groundwater for months or years [McCallum *et al.*, 2010]. Peter *et al.* [2012] found >50% decline in nitrate in storm water that entered riparian groundwater. Bank storage is increasingly recognized as important to the overall heat and solute budget of streams. For example, bank storage can alter the stream heat budget by storing heat or acting as a thermal sink in urban areas [Anderson *et al.*, 2011] and dam regulated rivers [Gerecht *et al.*, 2011]. Anderson *et al.* [2011] found that banks could store 72% of the heat stored within the stream. Bank storage can facilitate biogeochemical conditions for hotspots of microbial activity in the floodplain/riparian zone [Burt *et al.*, 2002; Gu *et al.*, 2012]. Gu *et al.* [2012] found a median nitrate removal rate by denitrification in bank storage of 2.1 g/d per m of stream length (max of 140 g/d/m) corresponding to a median nitrate uptake velocity of $2.7 \cdot 10^{-5}$ m/min, suggesting the importance of bank storage for nutrient budgets at the ecosystem level.

Rates of hyporheic exchange are commonly assessed with Darcy's Law to find groundwater flow rate (Q , L³/T), where $Q=KiA$ ("K" is the hydraulic conductivity (m/s), "i" is the hydraulic gradient (m/m), "A" is the cross-sectional flow area (m²), and residence times are related to flow through velocity. K varies over 8 orders of magnitude [Brassington, 2007; Calver, 2001], and is highly variable in both space and time [Genereux *et al.*, 2008; Song *et al.*, 2010b]. Consequently, K is a key variable in determining hyporheic flow rates [Boulton *et al.*, 2010; Findlay, 1995; Hester and Doyle, 2008; Hester and Cranmer, 2012; Valett *et al.*, 1996]. Regions of relatively high K act as preferential flow paths for groundwater flow and have been shown to dominate water and solute transport through porous media near streams [Fox *et al.*, 2009; Fox *et al.*, 2010] and control bank storage [Kondolf *et al.*, 1987].

Macropores are a type of preferential flow path devoid of sediment and larger than the local pore space size of the media. Macropores in agricultural floodplains created by the dry fracture of soils [Blake *et al.*, 1973], earthworm burrows [C A Edwards and Lofty, 1977b; W M Edwards *et al.*, 1979], and the decay of plant roots [Aubertin, 1971; Beasley, 1976a] have been shown to dominate solute transport in the subsurface. Bedrock fractures have been shown to increase flow rates by orders of magnitude in groundwater [Zhan *et al.*, 2011]. Macropores have not been extensively studied within the hyporheic zone, yet a growing number of studies suggest they are common [Bohlke *et al.*, 2007; Gormally *et al.*, 2011b; A E Newman and Keim, 2013]. For instance, macropores are created by burrowing fauna, including macroinvertebrates (e.g.,

stonefly nymphs, mayflies, worms, crayfish, crab, mussels, clams), birds (e.g., belted kingfisher, bank swallows), mammals (e.g., mink, beaver, coypu, muskrat), and reptiles (e.g., box turtles) [Allen and Vaughn, 2009; T T Brown and Brown, 2011; Shields and Kelly, 1997; Wright et al., 2011; Xin et al., 2009], as well as bioturbation by benthic macro-invertebrates [DiStefano et al., 2009; Mermillod-Blondin and Rosenberg, 2006; Mermillod-Blondin et al., 2004; Nogaro et al., 2006; Song et al., 2010a]. Yet no studies have systematically evaluated macropores of all formation mechanisms along example streams or rivers. As such, the density and distribution of such habitat features are generally unknown. Furthermore, no studies have quantified how frequently such macropores are inundated, so their temporal hydrologic characteristics are likewise poorly understood.

The spatial characteristics (e.g., frequency, size, inter-connectivity) of macropores are important in determining flow rates through macropores [Matthai and Belayneh, 2004]. The spatial characteristics may vary widely with macropore creation mechanism and local stream conditions (e.g., hydrology, geology). For example, crayfish burrows can start in the surface channel, extend well into the banks and groundwater zone, and extend through the parafluvial zone [Williams et al., 1974]. Soil pipes formed by subsurface erosion can connect the floodplain and hillslopes to the surface channel [Fox and Wilson, 2010; Holden, 2005; Jones, 1971; Jones and Cottrell, 2007]. Jones and Cottrell [2007] measured soil pipe interspacings from 4.75 to 15.75 m, mean diameters from 5.0 to 10.5 cm, and mean heights above thalweg from 24.2 to 56.6 cm. Noguchi et al. [1999] found most macropores in the unsaturated zone of a forested hillslope were 2 to 62 cm in length and mostly discontinuous. These studies provide spatial dimensions for certain types of macropores but do not quantify the characteristics and distribution of all types of macropores along a range of stream channels.

Macropores (soil pipes) can facilitate flow from hillslopes toward streams, providing a significant portion of flow to streams during storms [J A A Jones and Crane, 1984]. Recent research shows that surface-connected macropores within a meander bend can substantially increase hyporheic flow rates and exchange with surface water [Menichino et al., 2012]. Such macropores may increase solute transport between the stream and riparian zone [Angier and McCarty, 2008; Gormally et al., 2011; Newman and Keim, 2013]. Macropores exist at various heights along stream channels, and we expect that most will be inundated mainly during events, with their greatest hydrologic significance thus being to increase bank storage. However, we are

unaware of studies that demonstrate the capacity of macropores to increase bidirectional exchange between stream channel and riparian/floodplain groundwater zones.

Here we present a field study of the spatial characteristics of surface-connected macropores in stream banks and their impact on bank storage. Our objectives were to (1) survey and quantify reach scale macropore abundance and dimensions (i.e., diameter, depth, elevation within the channel) across five streams, (2) determine reach scale macropore hydroperiods (i.e., temporal variation of macropore saturation) at these five streams for one year, and (3) quantify macropores impact on stream channel-floodplain groundwater connectivity by quantifying bank storage rates and hyporheic zone size.

4.3 METHODS

4.3.1 Macropore Surveys

We surveyed surface-connected macropores in five streams in the Appalachian Mountains near Blacksburg, Virginia. The streams vary in channel size, sediment type, and land use (Table 4-1). For each macropore encountered, we measured cross-sectional height and width at the opening, length (into bank) to first bend, height of opening above the thalweg, and longitudinal distance along the reach. We only surveyed macropores that were 1 cm or greater in opening height or width, because smaller macropores were difficult to locate. For each stream channel we delineated two reach lengths for survey data collection: one reach that was 20 times bankfull widths in length (“short reach”) and a second that was 60 times the bankfull width (“long reach”). The short reaches were nested at the center of the long reaches. We determined the spatial dimensions of all macropores in the short reaches. A dowel rod with metric graduation was used to determine length (into bank) to first bend of macropores. Macropore dimensions were measured to the nearest 0.5 cm, such that the greatest error in a single measurement was 0.25 cm. We determined the longitudinal positions of each macropore and macropore frequencies in the long reaches. We chose a large reach survey for our frequency analysis to more accurately characterize widespread macropore abundance along streams. Bankfull dimensions described in this study pertain to the bankfull discharge, which is a surrogate for the discharges responsible for forming and maintaining the channel [*Leopold and Dunne, 1978*]. Bankfull width and height was measured at several riffles based on accepted bankfull indicators [*Harrelson et al., 1994; McCandless, 2003; Rosgen, 1996*] and averaged along each short reach. We also surveyed channel geometry at every major morphological

feature longitudinally along the channel (e.g., break in slope, riffle to pool transition) to use as channel geometry in HEC-RAS models of stream hydraulics (see hydroperiod analysis).

4.3.2 Macropore Creation Mechanisms

We categorized each macropore in each short reach (Table 4-1) according to likely creation mechanism based on approaches found in the literature. We assigned groundwater-driven erosion (i.e., soil pipe) when water was consistently discharging from the macropore at baseflow [Fox and Wilson, 2010; Jones and Cottrell, 2007]. We assigned root decay/erosion when there was a root observed within the macropore or the macropore was within the root zone (i.e., high on banks) and surrounded by roots protruding from the banks [Ghestem et al., 2011]. We designated bank erosion/undercutting when macropores existed where surface water undercut the banks or where bank sloughing occurred from wetting and drying of banks. This classification could also include seepage erosion that occurred low on the banks [Fox and Wilson, 2010]. We designated macroinvertebrate burrows when the macropore was near the baseflow water level and macroinvertebrates were observed near or within the macropore, or there was evidence of digging at the base of the macropore (e.g., chimney around macropore [Williams et al., 1974]). Macroinvertebrate burrows along streams can be created by organisms such as stonefly nymphs, mayflies, worms, crayfish, crab [T T Brown and Brown, 2011; Xin et al., 2009]. We assigned vertebrate burrows when the macropore was within the unsaturated zone at baseflow, were larger than 5 cm in cross-section (i.e., upper limit of crayfish burrow per Helfrich et al. [2009]), and no flowing water or roots were present. This criterion was used because crayfish are one of the largest and common macroinvertebrates in streams [Momot, 1995], but are still smaller than most vertebrates that generally burrow in the unsaturated zone [T T Brown and Brown, 2011]. Vertebrate burrows along streams can be created by organisms such as muskrats, minks, beavers, belted kingfishers and box turtles [T T Brown and Brown, 2011]. We assigned fractured rock when the macropore existed in solid rock (e.g., bedrock). We designated erosion around rock when the macropore wrapped around a large rock or other hardened flow-diverging feature. We assigned an ambiguous creation mechanism when the macropores fit several or none of the aforementioned criteria (a small minority of the time).

4.3.3 Macropore Hydroperiod Analysis

Macropore hydroperiods refer to the time periods when macropore openings were inundated and therefore hydraulically connected to the stream. We installed stage gauges

midway along each short reach and recorded water levels at 15-minute intervals for one year. Water levels were recorded using Onset Hobo or Solinst Levellogger Junior pressure transducers. Barometric pressure was recorded every 15 minutes at Stroubles Creek (within a 16 km radius of all sites). We developed rating curves for each stream by calculating a variety of discharges via the velocity area method using a Marsh-McBirney FlowMate velocimeter. We created unsteady flow HEC-RAS stream hydraulics models of each short reach [Brunner, 1995; 2001] and modeled stream discharge at 15-minute intervals for our year of data. Model channel geometries were created from short reach survey data at each site. Bed and bank Manning's n values were back-calculated from discharge measurements using Manning's equation for at least five storms at each stream reach. We averaged n values from the largest recorded discharge, the smallest recorded discharge, and a mid-range discharge and used this for the n of the main channel. Average n 's were 0.058, 0.072, 0.057, 0.054, 0.061 for Stroubles Creek, Poverty Creek, Tom's Creek Tributary, Craig Creek, and Slate Branch, respectively. We set overbank n values based on Brunner [1995] and visual observation, ranging from 0.08 to 0.11 across sites. The upstream boundary conditions were time-varying discharges over the year, computed from water levels from the stream gauges and the rating curves. The downstream boundary conditions were normal depth using average channel slope. We exported time-varying water surface elevations at each cross-section from HEC-RAS and used Excel macros to compare these to macropore elevations along the reach. If the modeled water level equaled or exceeded the elevation of the bottom of the macropore opening, we considered the macropore inundated.

4.3.4 Bank Storage Experiment

At Slate Branch, we installed two rows of groundwater wells in the floodplain perpendicular to the stream channel at locations with ("M") and without surface-connected macropores ("NM") (Figure 4-1). We installed the stage gauge (mentioned earlier) in between the two transects. At the M transect, 6 naturally existing macropores were present along 0.41 m of stream at a 0.70 m tall bank face. These macropores ranged from 2 to 6 cm (average of 4.2 cm) in both opening height and width, 9 to 51 cm (average of 29.7 cm) in length (into bank) to first bend, and 14 to 28 cm (average of 18.7cm) above thalweg. We monitored water levels and temperatures at 15-minute intervals at the groundwater wells and stage gauge. Wells 0.5 m into the bank (row "A") and 4.0 m into the bank (row D, hereafter "D") of both transects housed Solinst Levellogger Juniors. Wells 1.0 and 2.0 m into the bank (rows B and C, hereafter "B", and

“C”) housed Onset Hobo Pressure Transducers. M transect groundwater wells had 60 cm well screens that were centered at the average macropore elevation at the M transect bank face. This screen elevation was selected to maximize the signal from the macropores. The NM transect groundwater wells had 60 cm well screens that were centered at the same height above thalweg as the M transect for comparability. The stream gauge housed a Solinst Levellogger Junior and the barometric pressure was logged offsite (discussed above in the Hydroperiod Analysis section).

We analyzed temporal trends on two timescales: seasonal variations in water levels, and storm-induced fluctuations. To determine impacts to bank storage, we calculated the range of the water levels in each well for each storm event as a fraction of the in-stream range and then averaged these ranges over each season. After collecting a year of data, rising head tests were performed in each groundwater well to measure the K using Hvorslev’s method as described in *Fetter* [2001]. Briefly, we pumped the wells dry using a peristaltic pump and logged the increase in water levels to background conditions. We used an Insitu LevelTroll 700 for the M-A and M-B wells with 250 millisecond logging rate. We used Onset Hobo pressure transducers for the other wells and logging intervals ranging from 1 to 5 minutes. To avoid rising head tests influencing nearby wells, we only performed one rising head test within a transect at a time and waited for water levels reach background before testing a new well in that transect.

Temperature data were simultaneously recorded at each Hobo and LTC. Hobo temperature sensors have a 90% thermal response time of 3.5 minutes and an accuracy of $\pm 0.37^{\circ}\text{C}$ at 20°C . Levelloggers have a temperature sensor accuracy of $\pm 0.1^{\circ}\text{C}$ and instantaneous thermal response. Due to their higher accuracy and fast response time, we only used data from locations with Levelloggers (i.e., stream gauge, M-A, M-D, NM-A, NM-D) for temperature analyses. To determine impacts to bank storage, we calculated the range of temperatures in each of the Levellogger wells as a fraction of the in-stream temperature range for each storm event and then averaged these ranges over each season.

4.4 RESULTS

4.4.1 Macropore Spatial Characteristics

A total of 474 macropores were characterized in the short reaches, with 112, 111, 106, 107, and 38 macropores found at Slate Branch, Stroubles Creek, Craig Creek, Poverty Creek, and Tom’s Creek tributary, respectively. Figure 4-2 shows macropore opening height and width

(Panel A and B, respectively), length into bank to first bend (Panel C), height above thalweg (Panel D) and interspacing (Panel E). Figure 4-3 shows the longitudinal distribution of macropores along the long survey reaches. Macropore openings were slightly wider than tall, with median cross-sectional widths and heights of 3.5 cm and 3.0 cm, respectively. The median macropore length (into bank) to first bend was 15.0 cm. The median interspacing of macropores across all streams was 0.38 m while the mean interspacing was 1.12 m, indicating macropores were not evenly spaced but instead clustered, with stretches in between clusters without macropores. Macropores were common above the average bank height at Craig Creek and Poverty Creek. This was the result of large range of bank heights at these sites. For example, at Craig Creek one bank was consistently higher than the other. At other sites, nearly all macropores existed below bankfull elevation, with only occasional outliers above the bankfull elevation. Median elevation of macropores above thalweg increases with bankfull width with an R^2 of 0.72 (Figure 4-4). We found no significant correlations between other variables (i.e., $R^2 < 0.20$), such as macropore length to first bend and macropore height on banks or macropore opening average diameter and macropore height on banks.

4.4.2 Macropore Creation Mechanisms

Figure 4-5 shows example macropores observed along stream channels at our five survey reaches as well as other streams. Crayfish were observed in the macropores in Figure 4-5A. A mink was spotted near the large macropore in Figure 4-5B. Figure 4-5C shows a location where several creation mechanisms are present, including root decay/erosion, bank erosion, and macroinvertebrate burrows. Macropores existed in a range of sediments types, even when gravel was present in the sediment matrix (Figure 4-5D). However, a cohesive quality due to at least some fine sediment was observed for most matrices surrounding macropores, enabling the macropore to hold its shape.

The dominant creation mechanism varied among streams (Figure 4-6). Macroinvertebrate burrows were the dominant type of macropore at Tom's Creek tributary. Across all the sites, most macroinvertebrate burrows we attributed to crayfish because crayfish were observed in or near the macropores. Bank erosion/undercutting, evidenced by macropores created in the middle or base of banks and the sloughing or undercutting of banks, was the dominant mechanism at Stroubles Creek, which drains an urban watershed. Macroinvertebrate burrows and root decay/erosion together accounted for over 50% all macropores identified at

each site, with the exception of Poverty Creek. The dominant creation mechanism identified at Poverty Creek was root decay/erosion. No clear trends emerge when comparing stream characteristics (e.g., land use, gradient, stream order) to a particular formation mechanism.

4.4.3 Macropore Hydroperiods

Macropore hydroperiods refer to the time periods when macropore openings are inundated and therefore hydraulically connected to the stream. We used the variation of macropore opening inundation throughout the year with HEC-RAS hydraulics modeling to calculate the fraction of macropores inundated versus discharge at each site (Figure 4-7, macropore activation curve). We also calculated the probability of exceeding various discharges using stage and flow data (Figure 4-7, flow duration curve). Baseflow discharges were calculated by averaging non-storm water levels and using rating curves to determine a baseflow mean annual discharge at each site. 1 to 32% of macropores were inundated at baseflow across sites, but nearly all macropores were inundated during the largest storms. Up to 97% of the macropores across all sites were inundated at some point during the year. Macropore activation plots also identify the probability that a particular percentage of macropores become inundated. For example, at Stroubles Creek, a Q of $0.2 \text{ m}^3/\text{s}$ or greater occurred 18% of the time over the course of the year, and during this time at least 36% of the total macropores were inundated.

The slope of the macropore activation curve is a function of macropore height on the banks, channel geometry, and stream hydrology. Steep macropore activation curves at low discharges indicate that many macropores were low on the banks or that channel geometry was narrow and deep (i.e., small increases in discharge caused a large water level rise). On the other hand, flatter macropore activation curves indicate that fewer macropores were located within a given height on the banks or that channel geometry was wide (i.e., small increases in discharge caused a small water level rise). Activation curves for Craig Creek level off at lower values, when about 40% of the total macropores become inundated. This occurs because the channel has one bank that is lower than the other, so macropores above the shorter bank height require significantly higher discharges to become inundated.

4.4.4 Bank Storage Impacts

Rising head tests showed that the highest K 's were measured at M-A and M-B and were $7.92 \cdot 10^{-5} \text{ m/s}$ and $1.15 \cdot 10^{-4} \text{ m/s}$, respectively (Figure 4-8). At the NM Transect, K decreases with

distance into the bank, with $K=1.3 \cdot 10^{-6}$ m/s at NM-A and $K=3.3 \cdot 10^{-7}$ m/s at NM-D. Comparison of K 's between transects indicated M-A was 61.5 times higher than NM-A and M-B was 140. times higher than NM-B. This indicates that up to 1 meter into the bank, the average K was 101.8 times higher at M than at NM. Small differences were observed between measured K 's at the M and NM transects for the C and D wells. In particular, NM-C was 20.7 times higher than M-C and M-D was 1.24 times higher than NM-D. The lowest K was observed at M-C and was $1.86 \cdot 10^{-8}$ m/s. We additionally note that our estimates of K at M-A and M-B are likely underestimated because we used standard well construction techniques. As a result, our well borehole was slightly larger than our piezometer and we used filter sand to fill the void. Therefore, the K we measured is limited by the K of the filter sand and underestimates the higher K of the macropores connected to the surface channel.

In Figure 4-9 we show the full year of water level fluctuations in all wells at the Slate Branch field site. Summer 2012 water levels decreased with distance from the stream, indicating the stream was hydrologically losing. We note that several wells in the non-macropore transect went dry for parts of the summer (i.e., NM-A and NM-B). For example, NM-A water levels drop below wells NM-B, NM-C from Aug. 18, 2012 to Sept. 17, 2012. Fall 2012 water levels slightly decreased with distance from the stream, indicating hydrologic conditions were more neutral but still slightly hydrologically losing. Winter water levels in the floodplain are consistently higher than the stream channel, indicating the stream was hydrologically gaining. In particular, the stream switched to hydrologically gaining sooner for the macropore (Nov. 16, 2012) than non-macropore (Dec. 19, 2012) locations. A substantially greater amount of precipitation during late spring and summer 2013 relative to the previous year caused the stream to remain hydrologically gaining throughout the remainder of our data collection. In fact, the months of May-July 2013 saw 27.8 cm more rain at the Blacksburg Airport than during the same period in 2012. 2012 precipitation patterns were more typical for the region than 2013 [NOAA, 2013].

We compared water levels in the M and NM transects for storm events that occurred in summer, fall, winter, and spring (Figure 4-10). Overall, M-A and M-B experienced greater rates of bank storage than the other wells, and the M transect had higher connectivity with the surface channel than the NM transect.

During the summer storm event, M-B experienced the greatest fluctuation among the wells and most closely tracked in-stream water levels during the rising and falling limbs of the storm (Figure 4-10B). This indicates that macropores and other PFPs were aligned in such a way that M-B had high connectivity with the stream channel during storm flows. In comparison, M-A experienced less fluctuation, a delayed peak, and slower drawdown, indicating less connectivity with the channel than at M-B. This occurred despite M-A being only half as far as M-B from the stream bank, likely indicating less preferential flow between M-A and the channel. M-C and M-D showed little water level variation over the storm event, consistent with their greater distance from the channel. NM-A and NM-B wells also experienced lower water levels and less fluctuation over the summer storm than M-A and M-B.

The response to the fall storm event was similar to the summer, with water levels at M-A and M-B closely tracking in-stream water levels (Figure 4-10D). In fact, M-A tracked the channel water levels more closely than during the summer. Comparatively, M-C and M-D experienced little water level variation during the storm. Figure 4-10C shows that the NM transect experienced less water level fluctuation than the M transect, although the response in some wells (e.g., NM-B and NM-C) was greater than in the summer (Figure 4-10A). Unlike the M transect, NM-A more closely tracked in-stream water levels than NM-B.

The response during winter was significantly different than during summer or fall. During each storm event every groundwater well in both transects exhibited a spike in water levels similar to the stream. Both M-A and M-B closely tracked observed in-stream levels and experienced sharp water level drawdowns on the falling limb of storm events (Figure 4-10F). In comparison, the rest of the wells in both the M and NM transects (Panels E and F) experienced slower drawdowns (longer tails). This difference in water level drawdown is particularly recognizable when comparing M-A and M-B to NM-A and NM-B. The same response can be seen in the spring in Panels G and H as during the winter with Panels E and F, respectively. This different response mode continued into summer 2013.

We compared average storm and non-storm water levels for each season (Figure 4-11). Storm events were identified by an increase in stream water levels that was greater than the median diel water level fluctuation for each season. We used median diel water level fluctuations because these are the most common fluctuations (i.e., non-storm) for each season. The storm water level fluctuation is the storm water level minus the pre-storm water level

averaged over each storm event in a season, and normalized to the in-stream storm water level fluctuation. This quantifies the typical water level fluctuations at that location due to storm events. This storm water level fluctuation range in M-A and M-B was on average 139% greater than NM-A and NM-B (Panels K through O). The average storm water level fluctuation during late summer indicated M-B was 892% higher than NM-B (Panel K), an average raw water level difference of 0.574 m. The average storm water level range is higher during winter, spring and early summer 2013 (Panels M, N, and O) than summer 2012 and fall (Panels K and L) because of larger storm events. During late summer 2012, M-B had a higher range of storm water levels than M-A and even in-stream (Panel K). This is because at baseflow the macropores weren't hydraulically connected to the stream and the stream was losing (i.e., water levels decreased with distance into bank). During storm events, the macropores became hydraulically connected to the stream and preferentially transported water to the wells, such that M-A and M-B tracked in-stream water levels.

We also evaluated water temperatures measured in the channel and in the transect wells throughout the year. We first examined time-series over a 1.5 month period during the summer (Figure 4-11A). Channel temperatures fluctuated at multiple temporal scales. Diel variations in processes such as solar radiation and sensible heat transfer from the air caused in-stream water temperature differences between day and night. Meteorological events, such as periods of cooler weather (i.e., Aug. 13 to Aug. 29) caused temperature trends at the timescale of days to weeks. Seasonal changes in stream temperatures caused temperature changes at the timescale of months. Storm events caused temperature changes at the timescale of hours.

During most storm events throughout the year, in-stream water temperatures reached local maxima. Slate Branch is in an urban watershed, and similar responses have been observed in other streams draining urban watersheds during storms [*Hester and Bauman, 2013b; K. C. Nelson and M. A. Palmer, 2007*]. These channel temperatures in turn perturbed groundwater temperatures, and for several storm events (e.g., Sept. 2, 3, 7), small peaks (<1.0°C) in groundwater temperature were observed at M-A. Comparatively, local maxima were not observed for NM-A. Temperatures in well water and temperature perturbations during storms decreased with distance into the bank; NM-D and M-D experienced lower, more constant groundwater temperatures than NM-A and M-A. Instead, NM-D and M-D temperatures varied

with the larger time scale changes (non-storm related such as weather shifts) to temperature, following the average channel water temperature.

To highlight the groundwater temperature fluctuation during each storm, we calculated the temperature difference between the M and NM transects (i.e. M minus NM) for wells A and D (Figure 4-12B) over 1.5 months during summer. We selected M minus NM because channel water temperatures increase during summer storm events and we wanted to keep the same sign for groundwater temperature fluctuation. Such temperatures differences exhibited peaks during larger storms for the A wells but not the D wells. Such peaks did not occur for A wells for smaller storm events (e.g., Aug. 7, 10) because the water level did not reach the macropores at M-A.

The storm water temperature fluctuation range is the water temperature during storms minus the water temperature immediately before the storm (i.e., pre-storm) conditions. We calculated the storm temperature fluctuation ranges experienced in each well for each storms during the year, normalized them by the in-stream temperature fluctuation range for each storm, and averaged them over each season (Figure 4-13). The resulting value quantifies the fraction of in-stream temperature change that is experienced during storms at a given location. This fraction of in-stream temperatures at M-A was 62%, 16%, 1.4%, 26%, and 40% higher than NM-A during the late summer 2012 (Panel A), fall 2012 (Panel B), winter 2012 (Panel C), spring 2013 (Panel D), and early summer 2013 (Panel E), respectively. Averaged over the entire year, the fraction of in-stream temperatures at M-A was 29% higher than at NM-A. Observed temperature ranges in all wells (i.e., X=0.5, 4m) were small relative to channel ranges (i.e., X=0m) because temperature signals from surface water were dampened via conductive and/or advective heat transfer with groundwater, sediment, and unsaturated zone. For each season, the fraction of in-stream temperatures for the two transects (i.e. the red and blue lines in Figure 4-13) converge at row D (X=4 m), indicating the macropore did not much effect temperatures at that location.

4.5 DISCUSSION

4.5.1 Macropore Distribution and Abundance

Our results demonstrate that surface-connected macropores are widespread and common, at least within the Valley and Ridge physiographic province of the Appalachian Mountains in Southwest Virginia (Figures 4-2 and 4-3). We found such macropores throughout the long reach of each of the five streams, despite variation in sediment texture, land use, stream size, and

gradient. Thus the presence of surface-connected macropores appears to be typical rather than anomalous. The presence of at least some fines within the sediment matrix of all five streams indicates that macropores are likely common in non-mountainous regions as well, although this bears further study. We expect that the fines provide a cohesive quality to the sediment matrix to hold the shape of the macropore. The diverse range of macropore creation mechanisms we observed (Figure 4-6), and the fact that most such mechanisms are not specific to our five streams, further strengthens the expectation that surface-connected macropores are common beyond our geographic scope. The prevalence of macropores in our study suggests an important dimension of aquatic habitat, in addition to the hydrologic effects discussed later in this Discussion section.

4.5.2 Hydrologic Implications of Macropore Characteristics

The hydrologic significance of a macropore is not only a function of macropore dimensions, but also of the connectivity with other preferential flow paths. Such interconnectivity has been studied in groundwater fractures where the better-connected the system of fractures, the higher the flow rate through the system [*Matthai and Belayneh, 2004*]. Additionally, *Noguchi et al. [1999]* showed that short macropores within forested hillslopes were often connected into larger systems of preferential flow paths and could strongly influence hillslope hydrology. In our study, M-B had higher water level ranges and tracked in-stream water levels closer than M-A. This was unexpected because M-A was closest to the bank face. The longest macropore length (into bank) to first bend we measured of the six natural surface-connected macropores was 51 cm. In order for M-B to exhibit a higher connectivity with the surface channel, the macropores were either tortuous, extending beyond what we measured and reaching M-B (1m into the bank), or well-connected with other preferential flow paths that reached M-B. We measured the length (into bank) to first bend of macropores because it was an efficient method of characterizing large numbers of macropores with minimal impact to their natural state. However, our estimation of macropore length to first bend is a useful starting point in assessing how important macropores may be, but likely underestimates of macropore hydraulic significance or connectivity with other preferential flow paths. Macropores can be quite tortuous, such as the case for macropores created by crayfish or mitten crabs [*Helfrich et al., 2009; USGS, 2012; Williams et al., 1974*]. In particular, mitten crab burrows along the Sacramento River have been cast in resin and shown to extend horizontally 87 cm, before

dipping down at 30 degree angle, and extending another 105 cm [USGS, 2012]. We suggest future studies explore innovative methods to detect macropores and more accurately quantify spatial dimensions, such as tortuous depth. For example, electrical resistivity imaging has been successfully used to identify macropores in a meander bend [Menichino *et al.*, 2012], GPR was used in the riparian zone to detect macropores [Gormally *et al.*, 2011b; Holden, 2005], and liquid latex has been used to map diverse networks of macropores in the unsaturated zone [Abou Najm *et al.*, 2010]. Accurately quantifying the full spatial characteristics of macropores is key in determining their hydrologic value.

Our data demonstrate the substantial effect of macropores on bank storage through differences in storm response 1) between the two transects and 2) between the different wells in the macropore transect. In case 1, hydraulic head fluctuations, temperature fluctuations, and K measurements were higher in the two wells of macropore transect closest to the channel than in the corresponding wells in the non-macropore transect (Figures 4-11, 4-12, and 4-13). This result agrees with previous research that found that soil with macropores to have high K . For instance, in wetlands, lateral macropore flow was shown to increase K by 150 times relative to the nearby matrix [Elci and Molz, 2009]. Similarly, in meander bends, macropores have been shown to cause up to 550 times higher K than the nearby sediment matrix and have a strong influence on solute transport within hyporheic zone [Menichino *et al.*, 2012]. The use of water level fluctuations, temperature fluctuations, and K measurements together demonstrate surface-connected macropores increase bank storage, act as preferential flow paths, and increase the size of the lung model hyporheic zone during storms. In case 2, the greatest response in hydraulic head is in M-B, which is not the closest well to the channel. This suggests that M-B is better connected with the channel through tortuous macropores than M-A (Figures 4-10 and 4-11). However, moving from M-B to M-C, water level fluctuations, temperature fluctuations, and K measurements all substantially decrease, suggesting that macropores did not influence transport much more than 1 m into the floodplain/riparian groundwater zone. Spatial variation in hydraulic conductivity, due to tortuous preferential flow paths such as macropores, has been shown to dictate solute transport and subsurface transport rates [A E Newman and Keim, 2013].

It is common in bank storage and riparian groundwater studies to assume a homogenous sediment matrix [Hantush *et al.*, 2002; Pinder and Sauer, 1971; Sawyer *et al.*, 2009], thereby ignoring the presence of preferential flow paths such as macropores. Consequently, a frequent

assumption is that floodplain/riparian zones with finer sediments low flow rates with little bank storage. Similarly, in meander bends it has been suggested that coarse grained sediments must be added to or replace finer grained sediments to achieve significant hyporheic exchange [Kasahara and Hill, 2007]. We assert that complex networks of macropores and connectivity with other preferential flow paths (e.g., coarse sediment veins, paleochannels) can allow for higher flows to be transported into the banks and riparian groundwater zone without altering the matrix. Ultimately, conceptual models of bank storage and riparian groundwater hydrology should consider the importance of macropores, particularly in finer sediments, when quantifying flow rates and associated functions.

There are some methodological limitations in our hydroperiod analysis that may influence the spatial and temporal accuracy of our macropore activation curves (Figure 6), which should be borne in mind. First, we present the macropore activation curves for one year to provide a general understanding of how macropore variation can vary over discharge. If data was collected for several more years, the stream hydrology would change between years and flow-duration curves would vary as well, in turn influencing which macropores were saturated. Also, because storm flows are not evenly distributed over a year, there may be seasonal variation of macropore importance. For example, winter experienced the highest number of storms in the streams we studied and therefore macropore activation was highest during winter. A second limitation is that our HEC-RAS models of stream hydraulics did not include obstructions or in-stream structures within the channel, which can locally influence water levels. As a result, macropores upstream of flow obstructions may be activated at lower discharges than we predict. Thirdly, we calculate Manning's n from observed discharges for several storm events and apply this Manning's n to the entire main channel. However, Manning's n can change with local conditions within the channel, such as vegetation and sediment texture. For example, sections of the channel with higher Manning's n will experience higher water levels and higher levels of macropore activation. Although these considerations can increase the complexity of the macropore activation curve, our work nevertheless demonstrates the concepts and presents useful preliminary data on how macropore inundation varies with flow and among streams.

4.5.3 Hydrologic Processes Affecting Bank Storage

Any of five hydrologic processes could have contributed to elevated water levels in our groundwater wells during or shortly after storm events : channel water infiltration through the

matrix or preferential flow paths, rainfall infiltration, hillslope contributions, and pressure wave propagation [P Vidon, 2012]. These processes are illustrated in Figure 4-14 and can be differentiated by looking at the timing of the response in floodplain groundwater wells and any water quality response (e.g., temperature) in the well (Table 4-2). Channel water infiltration is a component of bank storage and is the only process that can be considered a form of hyporheic exchange (lung model). Pressure wave propagation occurs when channel water levels increase rapidly, subjecting the shallow subsurface groundwater near the channel to high pressures, causing concurrent increases in floodplain water levels (Figure 4-14). These increases in groundwater levels occur at rates that would be orders of magnitude above Darcy flows if the source water was the surface channel [Jung et al., 2004]. Although channel water infiltration and pressure wave propagation can both be concurrent with an in-stream water level rise, the distinction is that the source water in pressure waves is local groundwater in the floodplain (Table 4-2). As a result, channel water infiltration should show larger water quality perturbations in the well, assuming channel water and local groundwater are measurably different in quality. Rainfall infiltration may or may not be concurrent with the channel water level fluctuation, and water quality perturbations will trend toward characteristics of rainfall (e.g., drop in electrical conductivity). Groundwater from hillslopes similarly may or may not be concurrent and water quality perturbations will trend toward characteristics of hillslope groundwater. Overbank flow infiltration occurs when stream stages are high enough that water spills out into the floodplain and infiltrates into the subsurface. Increases in groundwater levels are generally not concurrent with stream water increases. At our field site, water levels indicated that overbank flow occurred a few times during the year of monitoring (Figure 4-9).

M-A and M-B tracked channel water levels during storms (Figure 4-10), and the well water had the thermal properties of channel water during summer 2012 (Figure 4-13A), indicating that surface water infiltration through preferential flow paths were the dominant hydrologic process. Wells further away from the channel in both transects during summer 2012 show indicate little connectivity to channel both hydraulically and thermally. However, during winter, spring, and summer 2013, water level fluctuations at every well, including the NM transect, exhibited peaks that coincided with channel peaks (Figure 4-10, panels E through H). A similar response to storms was observed by P Vidon [2012], where pressure waves caused groundwater levels up to 100 m into the floodplain initially rose and reached peaks at the same

times as groundwater much closer to the channel. Likewise, *Kaser et al.* [2009] found that pressure waves caused groundwater levels 40 m into a floodplain to peak in sync with channel storm peaks. We attribute this behavior in our wells during 2013 to pressure wave propagation, except at M-A and M-B, where macropores acted as preferential flow paths to transport channel water into the bank. Overall then, infiltration from the channel (i.e., bank storage) was substantial in summer 2012 due to generally losing gradients. Such bank storage was much smaller in 2013 because gradients had become generally gaining. The effects of macropores on such bank storage are accordingly greatest in summer 2012 in the presence of losing gradients. The latter is consistent with macropores that discharge floodplain water and provide a significant portion of streamflow to the channel during storm events [*Jones, 1987; Jones and Crane, 1984*]. Pressure waves were an important mechanism by which head fluctuations in the channel could propagate into the floodplain in 2013. Even in summer 2012, strong head fluctuations similar to the rest of the year can be seen in several wells (Figure 4-9), suggesting the presence of pressure waves, except at a couple wells we believe may have gone dry. Several storm events during 2013 resulted in overbank flow (Figure 4-9), which means that transport into the bank could have occurred from infiltration from the surface.

4.5.4 Water quality and ecosystem effects of macropores during bank storage

Our results suggest that macropores can substantially increase transport of surface water into the riparian/floodplain aquifer and therefore may provide several important stream functions: (1) Reach-scale increases to bank storage from macropores may attenuate downstream peak discharges. The capacity of bank storage to attenuate stormflows is well documented, for instance [*Pinder and Sauer, 1971*] modeled a ~30 m wide river and found an approximate 80% decrease in peak discharge ~43 km downstream. This effect increases with K [*Hantush et al., 2002; Pinder and Sauer, 1971*], and macropores effectively act as an increase in K . (2) Macropores may enhance biogeochemical hotspots or pollutant attenuation. For example, bank storage has been shown to induce median denitrification rates of 2.1 g/d [*Gu et al., 2012*]. Such nitrate removal furthermore correlates with flowpath length within riparian zones [*P G F Vidon and Hill, 2004*]. Because macropores increase bank storage rates, they push surface water farther into the floodplain, increasing flow path lengths and potentially increasing the extent of biogeochemical reactions such as denitrification. (3) Macropores may enhance stream temperature regulation. For example, *Anderson et al.* [2011] observed mean subsurface

temperature increases of 2.39°C during storms and calculated that banks can store 72% as much heat as in the stream itself, suggesting bank storage can act as a thermal sink. Because macropores increase bank storage, they may transport and store heat, which can significantly alter stream heat budgets. (4) Macropores may provide refugia for aquatic organisms during storms. Aquatic organisms can be swept downstream by strong flows [Brunke and Gonser, 1997]. In particular, young fish are weaker swimmers and look for refugia with lower water velocities [Keeley and Slaney, 1996]. Macropores are shielded from higher velocities of the main channel providing refugia for aquatic organisms.

4.5.5 Hydrologic impacts and water quality effects of macropores during non-storm conditions

Macropores act as preferential flow paths and therefore may increase rates of transport from the floodplain/riparian zone to streams during baseflow. For example, Bohlke *et al.* [2007] showed that macropores provide the majority of baseflow to their stream. We expect that seasonal changes in water table elevation will change the number of macropores that are active during baseflow and the direction of transport will depend on applied head gradients. For example, Figure 4-15A shows a macropore discharging into Slate Branch during baseflow in winter, yet this macropore was did not discharge during baseflow in late summer 2012.

Macropores discharging to the stream may affect stream water quality. For example, macropore discharge that is substantially warmer or cooler than channel discharge can impact channel water temperature. This can be seen in Figure 4-15 where macropores are discharging water that is 1.7°C colder (Figure 4-15B) and 1.6 °C warmer (Figure 4-15D) than channel discharge. Whether baseflow warmed or cooled the surface stream was dependent on the daily stream temperature, which fluctuated with ambient air temperature. The average daily air temperature in Figure 4-15A and 4-15B was 4.4°C (23/2/2013) while Figure 4-15C and 4-15D was -0.56°C (25/2/2013). The average temperature in February was 0.72°C. While the individual macropore may not cause a substantial change in bulk downstream water temperatures, local effects may be significant. Such local effects may influence rates of local biogeochemical reactions or provide unique habitat for aquatic organisms. Discharging macropores may also be significant for biogeochemistry. For example, macropores in hillslopes or floodplains can rapidly transport un-attenuated runoff to the stream that is high in nutrients, bypassing denitrification hotspots in the sediment matrix [Bohlke *et al.*, 2007]. Similarly, in the mid-western United States, tile drainage can transport pollutants to streams and control baseflow

discharge [Hallberg, 1987; Schilling *et al.*, 2012]. In such situations, macropores are actively bypassing the attenuative capacity of the hyporheic zone. Whether discharging macropores have a beneficial or adverse impact on water quality and stream functions will depend on hydrologic conditions, spatial characteristics of macropores, and physiochemical properties of surface water and groundwater.

4.6 CONCLUSIONS

Our field surveys of five streams across a range of sizes, gradients, and watershed land uses indicate that surface-connected macropores are nearly ubiquitous geomorphic features, at least in the Valley and Ridge province of the Appalachian Mountains of Southwest Virginia. We attribute the creation of macropores in this region to a variety of mechanisms, including soil piping, tree root decay, erosion around hardened structures, macroinvertebrate burrows, and invertebrate burrows. The diverse range of such formation mechanisms and the presence of fine sediment in all five streams suggest that macropores may also be common outside these mountainous settings, and their wider distribution bears further study.

Macropores openings were slightly wider than tall, with median cross-sectional widths and heights of 3.5 cm and 3.0 cm, respectively. Maximum macropore widths and heights were similarly proportioned at 30.0 cm and 27.5 cm, respectively. The median and maximum macropore lengths to first bend were 15.0 cm and 120.5 cm into the bank, respectively. Yet true (tortuous) macropore lengths are likely often greater and developing methods to accurately map macropores is recommended. The median interspacing of macropores across all streams was 0.38 m while the mean interspacing was 1.12 m, indicating macropores were clustered in space. These interspacings are likely underestimates as we did not record macropores whose openings were less than 1 cm in diameter.

Macropores were inundated by channel water at different times due to differences in their heights on the stream bank, channel geometry, and precipitation. We modeled a year of streamflows in HEC-RAS at each of the five survey sites and computed flow duration curves versus the number of macropores active (i.e., inundated). Results indicated that only 1-32% of macropores were inundated by channel water at baseflow while up to 97% were inundated during the largest storms.

We demonstrated the hydrologic significance of macropores by comparing response to storms over the course of a year in two transects of wells (one with surface-connected

macropores [M transect] and one without [NM transect]) perpendicular to the bank in one of the five streams. The M transect experienced 139% higher hydraulic head fluctuations up to 1 m into the bank during storms than the NM transect. Similarly, the M transect experienced temperature fluctuations 0.5 m into the bank that were 29% higher of storms than the NM transect. Falling head tests confirmed that the well 1 m into the bank at the M transect had a higher K than the well 0.5m into the bank. Averaged together, the M transect had 101.8% higher K in the first 1 m into the bank than the NM transect. These results suggest that macropores enhance connection between the channel and riparian groundwater including “lung model” hyporheic exchange. These hydraulic effects in turn can affect hyporheic habitat and presence or rates of biogeochemical processes. Where bank macropores are present, conceptual models of hyporheic and groundwater flow should account for their effects.

Lastly, we observed that some macropores discharged groundwater at baseflow. This flow has the potential to bypass important riparian processes that can affect water quality. For example, discharging macropores often contributed groundwater of measurably different temperature than the channel (Figure 4-15). This has potential to alter stream temperatures, particularly in the immediate vicinity of the macropore.

4.7 ACKNOWLEDGEMENTS

The authors thank the Thomas F. Jeffress and Kate Miller Jeffress Memorial Trust and the Institute for Critical Technology and Applied Science at Virginia Tech. We acknowledge the support of the National Science Foundation through NSF/REU Site Grant EEC-1062860. Any opinions, findings, and conclusions or recommendations expressed in this paper are those of the author(s) and do not necessarily reflect the views of the National Science Foundation. The authors thank Kate Aulenbach for field assistance.

4.8 REFERENCES

- Abou Najm, M. R., J. D. Jabro, W. M. Iversen, R. H. Mohtar, and R. G. Evans (2010), New method for the characterization of three-dimensional preferential flow paths in the field, *Water Resour Res*, 46.
- Allen, D. C., and C. C. Vaughn (2009), Burrowing behavior of freshwater mussels in experimentally manipulated communities, *J N Am Benthol Soc*, 28(1), 93-100.
- Anderson, W. P., R. E. Storniolo, and J. S. Rice (2011), Bank thermal storage as a sink of temperature surges in urbanized streams, *J Hydrol*, 409(1-2), 525-537.

- Angier, J. T., and G. W. McCarty (2008), Variations in base-flow nitrate flux in a first-order stream and riparian zone, *J Am Water Resour As*, 44(2), 367-380.
- Arntzen, E. V., D. R. Geist, and P. E. Dresel (2006), Effects of fluctuating river flow on groundwater/surface water mixing in the hyporheic zone of a regulated, large cobble bed river, *River Res Appl*, 22(8), 937-946.
- Aubertin, G. M. (1971), *Nature and extent of macropores in forest soils and their influence on subsurface water movement*, Northeastern Forest Experiment Station, Upper Darby, Pa.
- Beasley, R. S. (1976), Contribution of Subsurface Flow from the Upper Slopes of Forested Watersheds to Channel Flow, *Soil Sci. Soc. Am. J.*, 40(6), 955-957.
- Blake, G., E. Schlichting, and U. Zimmermann (1973), Water Recharge in a Soil with Shrinkage Cracks, *Soil Sci. Soc. Am. J.*, 37(5), 669-672.
- Bohlke, J. K., M. E. O'Connell, and K. L. Prestegard (2007), Ground water stratification and delivery of nitrate to an incised stream under varying flow conditions, *J Environ Qual*, 36(3), 664-680.
- Boulton, A. J., T. Datry, T. Kasahara, M. Mutz, and J. A. Stanford (2010), Ecology and management of the hyporheic zone: stream-groundwater interactions of running waters and their floodplains, *J N Am Benthol Soc*, 29(1), 26-40.
- Brassington R. 2007. *Field hydrogeology*. John Wiley: Chichester, England ; Hoboken, NJ.
- Brown, T. T., and S. Brown (2011), *Pocketguide to Eastern streams*, Stackpole Books, Mechanicsburg, PA.
- Brunke, M., and T. Gonser (1997), The ecological significance of exchange processes between rivers and groundwater, *Freshwater Biol*, 37(1), 1-33.
- Brunner, G. W. (1995), HEC-RAS River Analysis System. Hydraulic Reference Manual. Version 1.0, DTIC Document.
- Brunner, G. W. (2001), *HEC-RAS River Analysis System: User's Manual*, US Army Corps of Engineers, Institute for Water Resources, Hydrologic Engineering Center.
- Burkholder, B. K., G. E. Grant, R. Haggerty, T. Khangaonkar, and P. J. Wampler (2008), Influence of hyporheic flow and geomorphology on temperature of a large, gravel-bed river, Clackamas River, Oregon, USA, *Hydrol Process*, 22(7), 941-953.
- Burt, T. P., et al. (2002), Water table fluctuations in the riparian zone: comparative results from a pan-European experiment, *J Hydrol*, 265(1-4), 129-148.

- Calver, A. (2001), Riverbed permeabilities: Information from pooled data, *Ground Water*, 39(4), 546-553.
- Chen, X., and X. Chen (2003), Stream water infiltration, bank storage, and storage zone changes due to stream-stage fluctuations, *J Hydrol*, 280(1), 246-264.
- DiStefano, R. J., D. D. Magoulick, E. M. Imhoff, and E. R. Larson (2009), Imperiled crayfishes use hyporheic zone during seasonal drying of an intermittent stream, *J N Am Benthol Soc*, 28(1), 142-152.
- Edwards, C. A., and J. R. Lofty (1977), *Biology of earthworms*, Chapman and Hall; Wiley, London.
- Edwards, W. M., R. R. van der Ploeg, and W. Ehlers (1979), A Numerical Study of the Effects of Noncapillary-Sized Pores Upon Infiltration¹, *Soil Sci. Soc. Am. J.*, 43(5), 851-856.
- Elci, A., and F. J. Molz (2009), Identification of Lateral Macropore Flow in a Forested Riparian Wetland through Numerical Simulation of a Subsurface Tracer Experiment, *Water Air Soil Poll*, 197(1-4), 149-164.
- Fetter, C. W. (2001), *Applied hydrogeology*. Prentice Hall, Upper Saddle River, N.J.
- Findlay, S. (1995), Importance of Surface-Subsurface Exchange in Stream Ecosystems - the Hyporheic Zone, *Limnol Oceanogr*, 40(1), 159-164.
- Fox, G. A., and G. V. Wilson (2010), The Role of Subsurface Flow in Hillslope and Stream Bank Erosion: A Review, *Soil Sci Soc Am J*, 74(3), 717-733.
- Fox, G. A., J. W. Fuchs, D. E. Storm, C. J. Penn, and G. O. Brown (2009), Subsurface transport of phosphorus in riparian floodplains: influence of preferential flow paths, *J Environ Qual*, 38(2), 473-484.
- Fox, G. A., D. M. Heeren, R. B. Miller, D. E. Storm, T. Halihan, and C. J. Penn (2010), Preferential flow effects on subsurface contaminant transport in alluvial floodplains, *T ASABE*, 53(1), 127-136.
- Francis, B. A., L. K. Francis, and M. B. Cardenas (2010), Water table dynamics and groundwater–surface water interaction during filling and draining of a large fluvial island due to dam-induced river stage fluctuations, *Water Resour Res*, 46, W07513.
- Genereux, D. P., S. Leahy, H. Mitsova, C. D. Kennedy, and D. R. Corbett (2008), Spatial and temporal variability of streambed hydraulic conductivity in West Bear Creek, North Carolina, USA, *J Hydrol*, 358(3-4), 332-353.

- Gerecht, K. E., M. B. Cardenas, A. J. Guswa, A. H. Sawyer, J. D. Nowinski, and T. E. Swanson (2011), Dynamics of hyporheic flow and heat transport across a bed-to-bank continuum in a large regulated river, *Water Resour Res*, 47, W03524.
- Ghestem, M., R. C. Sidle, and A. Stokes (2011), The Influence of Plant Root Systems on Subsurface Flow: Implications for Slope Stability, *Biosci*, 61(11), 869-879.
- Gormally, K. H., M. S. McIntosh, A. N. Mucciardi, and G. W. McCarty (2011), Ground penetrating radar detection and three-dimensional mapping of lateral macropores: II. riparian application, *Soil Sci Soc Am J*, 75(4), 1236-1243.
- Groffman, P. M., N. J. Boulware, W. C. Zipperer, R. V. Pouyat, L. E. Band, and M. F. Colosimo (2002), Soil nitrogen cycle processes in urban Riparian zones, *Environ Sci Technol*, 36(21), 4547-4552.
- Gu, C. H., W. Anderson, and F. Maggi (2012), Riparian biogeochemical hot moments induced by stream fluctuations, *Water Resour Res*, 48.
- Hallberg, G. R. (1987), Nitrates in Iowa groundwater. Lewis Publishers, Michigan.
- Hantush, M. M., M. Harada, and M. A. Marino (2002), Hydraulics of stream flow routing with bank storage, *J Hydrol Eng*, 7(1), 76-89.
- Harrelson, C. C., C. L. Rawlins, J. P. Potyondy, R. M. Forest, and R. E. Station (1994), *Stream channel reference sites: an illustrated guide to field technique*, U.S. Dept. of Agriculture, Forest Service, Rocky Mountain Forest and Range Experiment Station.
- Helfrich, L. A., J. Parkhurst, and R. Neves (2009), The Control of Burrowing Crayfish in Ponds, edited by V. C. Extension, College of Agriculture and Life Sciences, Virginia Tech, Blacksburg, Va.
- Hester, E. T., and M. W. Doyle (2008), In-stream geomorphic structures as drivers of hyporheic exchange, *Water Resour Res*, 44, W03417.
- Hester, E. T., and E. N. Cranmer (2012), Variation of hyporheic exchange potential among urban region streams: implications for stream restoration. *Environmental & Engineering Geoscience*. Accepted.
- Hester, E. T., and K. S. Bauman (2013), Stream and retention pond thermal response to heated summer runoff from urban impervious surfaces, *JAWRA J Am Water Res Assoc*, 49: 328-342.

- Holden, J. (2005), Controls of soil pipe frequency in upland blanket peat, *J Geophys Res-Earth*, 110, F01002.
- Jones, A. (1971), Soil piping and stream channel initiation, *Water Resour Res*, 7(3), 602-610.
- Jones, J. A. A. (1987), The effects of soil piping on contributing areas and erosion patterns, *Earth Surf Proc Land*, 12(3), 229-248.
- Jones, J. A. A., and F. G. Crane (1984), Pipeflow and pipe erosion in the Maesnant experimental catchment, *Catchment Experiments in Fluvial Geomorphology*. Geo Books, Norwich England. 1984. p 55-72.
- Jones, J. A. A., and C. I. Cottrell (2007), Long-term changes in stream bank soil pipes and the effects of afforestation, *J Geophys Res-Earth*, 112, F01010.
- Jung, M., T. P. Burt, and P. D. Bates (2004), Toward a conceptual model of floodplain water table response, *Water Resour Res*, 40, W12409.
- Kasahara, T., and A. R. Hill (2007), Lateral hyporheic zone chemistry in an artificially constructed gravel bar and a re-meandered stream channel, southern Ontario, Canada, *J Am Water Resour As*, 43(5), 1257-1269.
- Kaser, D. H., A. Binley, A. L. Heathwaite, and S. Krause (2009), Spatio-temporal variations of hyporheic flow in a riffle-step-pool sequence, *Hydrol Process*, 23(15), 2138-2149.
- Keeley, E., and P. Slaney (1996), *Quantitative measures of rearing and spawning habitat characteristics for stream-dwelling salmonids: Guidelines for habitat restoration*, Watershed Restoration Program, Ministry of Environment, Lands and Parks, British Columbia.
- Kondolf, G. M., L. M. Maloney, and J. G. Williams (1987), Effects of Bank Storage and Well Pumping on Base-Flow, Carmel-River, Monterey-County, California, *J Hydrol*, 91(3-4), 351-369.
- Leopold, L. B., and J. Dunne (1978), Water in environmental planning, *New York*, 818p.
- Loheide, S. P., and J. D. Lundquist (2009), Snowmelt-induced diel fluxes through the hyporheic zone, *Water Resour Res*, 45, W07404.
- Matthai, S. K., and M. Belayneh (2004), Fluid flow partitioning between fractures and a permeable rock matrix, *Geophys Res Lett*, 31, L07602.

- McCallum, J. L., P. G. Cook, P. Brunner, and D. Berhane (2010), Solute dynamics during bank storage flows and implications for chemical base flow separation, *Water Resour Res*, 46, W07541.
- McCandless, T. (2003), Maryland Stream Survey: Bankfull Discharge and Channel Characteristics of Streams in the Coastal Plain Hydrologic Region, US Fish and Wildlife Service, Chesapeake Bay Field Office *Rep.*, CBFO-S03-02.
- McGlynn, B. L., and J. J. McDonnell (2003), Quantifying the relative contributions of riparian and hillslope zones to catchment runoff, *Water Resour Res*, 39(11).
- Menichino, G. T., A. S. Ward, and E. T. Hester (2012), Macropores as preferential flow paths in meander bends, *Hydrol Process*, Published online 16 Nov 2012. DOI: 10.1002/hyp.9573.
- Mermillod-Blondin, F., and R. Rosenberg (2006), Ecosystem engineering: the impact of bioturbation on biogeochemical processes in marine and freshwater benthic habitats, *Aquat Sci*, 68(4), 434-442.
- Mermillod-Blondin, F., R. Rosenberg, F. Francois-Carcaillet, K. Norling, and L. Mauclaire (2004), Influence of bioturbation by three benthic infaunal species on microbial communities and biogeochemical processes in marine sediment, *Aquat Microb Ecol*, 36(3), 271-284.
- Momot, W. T. (1995), Redefining the role of crayfish in aquatic ecosystems, *Rev Fish Sci*, 3(1), 33-63.
- Nelson, K. C., and M. A. Palmer (2007), Stream temperature surges under urbanization and climate change: Data, models, and responses, *J Am Water Resour Assoc*, 43(2), 440-452.
- Newman, A. E., and R. F. Keim (2013), Mesoscale connectivity through a natural levee, *Hydrol Earth Syst Sc*, 17(2), 691-704.
- NOAA, National Oceanic and Atmospheric Administration (2013), National Oceanic and Atmospheric Administration's National Weather Source. <<http://www.noaa.gov/>>.
- Nogaro, G., F. Mermillod-Blondin, F. Francois-Carcaillet, J. P. Gaudet, M. Lafont, and J. Gibert (2006), Invertebrate bioturbation can reduce the clogging of sediment: an experimental study using infiltration sediment columns, *Freshwater Biol*, 51(8), 1458-1473.
- Noguchi, S., Y. Tsuboyama, R. C. Sidle, and I. Hosoda (1999), Morphological characteristics of macropores and the distribution of preferential flow pathways in a forested slope segment, *Soil Sci Soc Am J*, 63(5), 1413-1423.

- Peter, S., R. Rechsteiner, M. F. Lehmann, R. Brankatschk, T. Vogt, S. Diem, B. Wehrli, K. Tockner, and E. Durisch-Kaiser (2012), Nitrate removal in a restored riparian groundwater system: functioning and importance of individual riparian zones, *Biogeosciences*, 9(11), 4295-4307.
- Peterson, R. E., and M. P. Connelly (2001), Zone of interaction between Hanford site groundwater and adjacent Columbia river, *PNNL-13674, Richland, WA*.
- Pinder, G. F., and S. P. Sauer (1971), Numerical simulation of flood wave modification due to bank storage effects, *Water Resour Res*, 7(1), 63-70.
- Poole, G. C., J. A. Stanford, S. W. Running, and C. A. Frissell (2006), Multiscale geomorphic drivers of groundwater flow paths: subsurface hydrologic dynamics and hyporheic habitat diversity, *J N Am Benthol Soc*, 25(2), 288-303.
- Revelli, R., F. Boano, C. Camporeale, and L. Ridolfi (2008), Intra-meander hyporheic flow in alluvial rivers, *Water Resour Res*, 44, W12428.
- Rosgen, D. L. (1996), *Applied River Morphology*, Wildland Hydrology, Pagosa Springs, Colo.
- Sawyer, A. H., M. B. Cardenas, A. Bomar, and M. Mackey (2009), Impact of dam operations on hyporheic exchange in the riparian zone of a regulated river, *Hydrol Process*, 23(15), 2129-2137.
- Schilling, K. E., P. Jindal, N. B. Basu, and M. J. Helmers (2012), Impact of artificial subsurface drainage on groundwater travel times and baseflow discharge in an agricultural watershed, Iowa (USA), *Hydrol Process*, 26(20), 3092-3100.
- Shields, S. J., and J. F. Kelly (1997), Nest-site selection by belted kingfishers (*Ceryle alcyon*) in Colorado, *Am Midl Nat*, 137(2), 401-403.
- Song, J. X., X. H. Chen, and C. Cheng (2010a), Observation of bioturbation and hyporheic flux in streambeds, *Front Environ Sci En*, 4(3), 340-348.
- Song, J. X., X. H. Chen, C. Cheng, D. M. Wang, and W. K. Wang (2010b), Variability of streambed vertical hydraulic conductivity with depth along the Elkhorn River, Nebraska, USA, *Chinese Sci Bull*, 55(10), 992-999.
- Squillace, P. J., E. Thurman, and E. T. Furlong (1993), Groundwater as a nonpoint source of atrazine and deethylatrazine in a river during base flow conditions, *Water Resour Res*, 29(6), 1719-1729.

- Strahler, A. N. (1952), Hypsometric (area-altitude) analysis of erosional topography, *Geol Soc Am Bull*, 63(11), 1117-1142.
- Triska, F. J., V. C. Kennedy, R. J. Avanzino, G. W. Zellweger, and K. E. Bencala (1989), Retention and Transport of Nutrients in a 3rd-Order Stream in Northwestern California - Hyporheic Processes, *Ecology*, 70(6), 1893-1905.
- USGS, United States Geological Survey (2012), Chinese Mitten Crabs Burrows. Web. 10 Jan. 2013. < http://bard.wr.usgs.gov/sfcreek_main/sfq_mitten_burrowing.html>.
- Valett, H. M., J. A. Morrice, C. N. Dahm, and M. E. Campana (1996), Parent lithology, surface groundwater exchange, and nitrate retention in headwater streams, *Limnol Oceanogr*, 41(2), 333-345.
- Vidon, P. (2012), Towards a better understanding of riparian zone water table response to precipitation: surface water infiltration, hillslope contribution or pressure wave processes, *Hydrol Process*, 26(21), 3207-3215.
- Vidon, P., C. Allan, D. Burns, T. P. Duval, N. Gurwick, S. Inamdar, R. Lowrance, J. Okay, D. Scott, and S. Sebestyen (2010), Hot spots and hot moments in riparian zones: Potential for improved water quality management, *JAWRA J Am Water Resour Assoc*, 46(2), 278-298.
- Vidon, P. G. F., and A. R. Hill (2004), Landscape controls on nitrate removal in stream riparian zones, *Water Resour Res*, 40, W03201.
- Westbrook, S., J. Rayner, G. Davis, T. Clement, P. L. Bjerg, and S. Fisher (2005), Interaction between shallow groundwater, saline surface water and contaminant discharge at a seasonally and tidally forced estuarine boundary, *J Hydrol*, 302(1), 255-269.
- Williams, D. D., N. E. Williams, and H. B. N. Hynes (1974), Observations on the life history and burrow construction of the crayfish *Cambarus fodiens* (Cottle) in a temporary stream in southern Ontario, *Can J Zoo*, 52(3), 365-370.
- Wondzell, S. M., M. N. Gooseff, and B. L. McGlynn (2010), An analysis of alternative conceptual models relating hyporheic exchange flow to diel fluctuations in discharge during baseflow recession, *Hydrol Process*, 24(6), 686-694.
- Wright, D. H., H. Lomeli, P. S. Hofmann, and C. Nguyen (2011), Burrow occupancy and nesting phenology of bank swallows along the Sacramento River, *Calif Fish Game*, 97(3), 138-147.

Xin, P., G. Q. Jin, L. Li, and D. A. Barry (2009), Effects of crab burrows on pore water flows in salt marshes, *Adv Water Resour*, 32(3), 439-449.

Zhan, H. B., J. Z. Qian, Z. Chen, and S. H. Luo (2011), Solute transport in a filled single fracture under non- Darcian flow, *Int J Rock Mech Min*, 48(1), 132-140.

Table 4-1. Macropore Survey Sites.

| Stream name | Land use¹ | Stream Order² | Short Survey Reach Length (m) | Long Survey Reach Length (m) | Average bankfull width (m) | Average bankfull height (m) | Typical bank sediment type | Reach gradient (m/m) |
|------------------------------|-----------------------------|---------------------------------|--------------------------------------|-------------------------------------|-----------------------------------|------------------------------------|--|-----------------------------|
| Slate Branch | Urban | 2 | 104 | 312 | 5.2 | 0.69 | Sandy loam | 0.0098 |
| Stroubles Creek | Urban/Ag | 2 | 114 | 342 | 5.7 | 0.72 | Silt loam | 0.0093 |
| Craig Creek | Forest | 3 | 164 | 492 | 8.2 | 0.76 | Sand and silt with bedrock and cobbles | 0.0092 |
| Poverty Creek | Forest | 2 | 106 | 318 | 5.3 | 0.68 | Sandy loam | 0.0129 |
| Tom's Creek Tributary | Forest/Ag | 1 | 36 | 108 | 1.8 | 0.43 | Silt and clay | 0.0023 |

¹Watershed land use was determined by delineating stream watersheds from topographic maps and inspecting aerial photographs.

²Stream order was determined using the Strahler method [Strahler, 1952].

Table 4-2. Hydrologic processes influencing groundwater levels in near-channels wells during or shortly after storm events.

| <u>Hydrologic Process causes groundwater level increase</u> | <u>Observed timing of water level change in well relative to timing of in-stream water level change</u> | <u>Source water (determines observed water quality change in well)</u> |
|---|---|--|
| Infiltration from channel via matrix or PFP (bank storage) | Concurrent or delayed, depending on K | Surface water |
| Pressure wave propagation from channel | Concurrent | Local groundwater |
| Overbank flow infiltration | Generally not concurrent | Surface water |
| Rainwater infiltration | Generally not concurrent | Rainfall |
| Groundwater from hillslopes | Generally not concurrent | Hillslope groundwater |

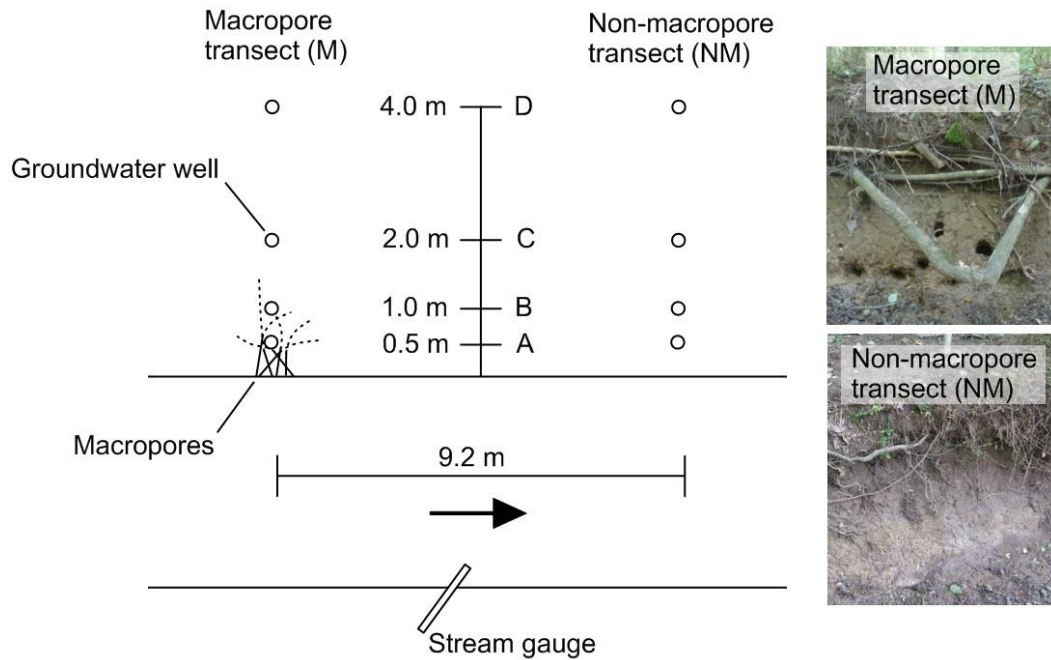


Figure 4-1. Schematic of field piezometer transects at Slate Branch. Six natural macropores exist at the bank face of the macropore (M) transect. No macropores exist at the bank face of the non-macropore (NM) transect. Arrow denotes surface stream flow direction. Macropores are shown in diagram based on the length (into bank) to first bend (i.e., solid lines) and possible additional tortuous depth (i.e., dashed lines).

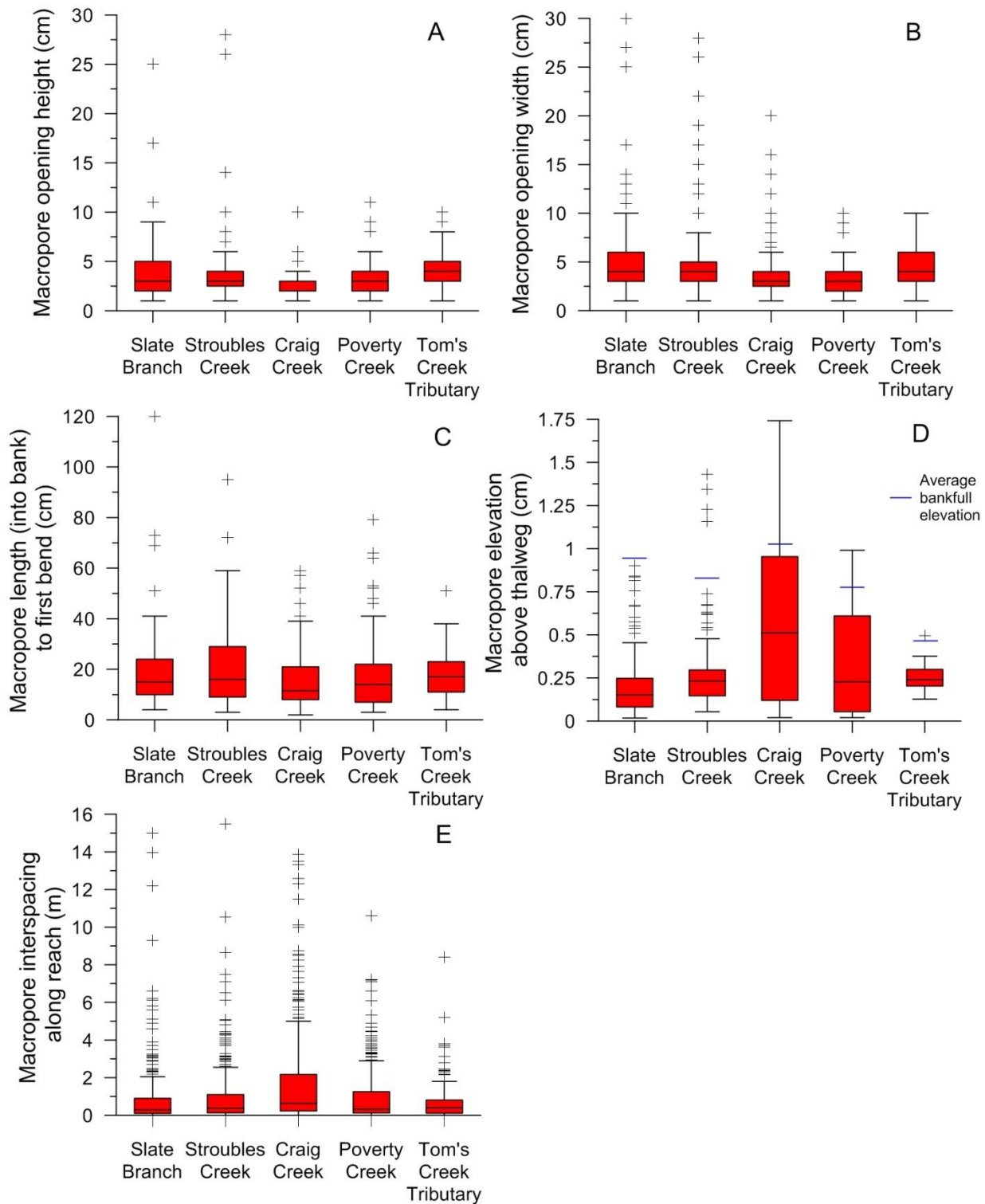


Figure 4-2. Spatial characteristics of macropores across field sites: Macropore opening height and width (Panel A and B, respectively), length into bank to first bend (Panel C), height above thalweg (Panel D) and interspacing (Panel E). Values outside of the middle 50% of the distribution by 1.5 times the interquartile range are presented as outliers.

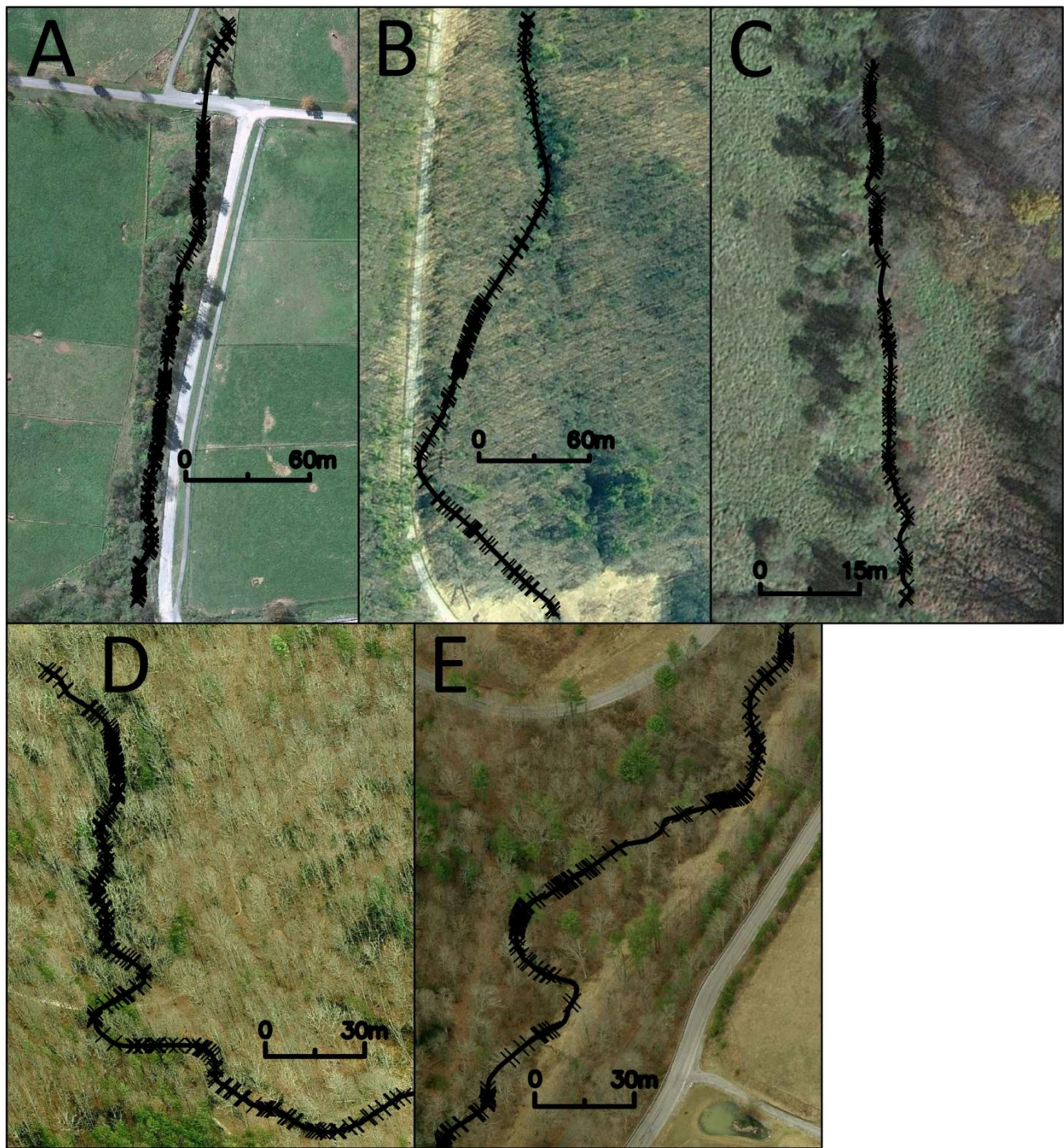


Figure 4-3. Longitudinal distribution of macropores along each long survey reach length. Panel A, B, C, D, E, F refer to Stroubles Creek, Craig Creek, Toms Creek Tributary, Poverty Creek, and Slate Branch, respectively. Panels created using aerial photos from Google Maps and AutoCAD 2011.

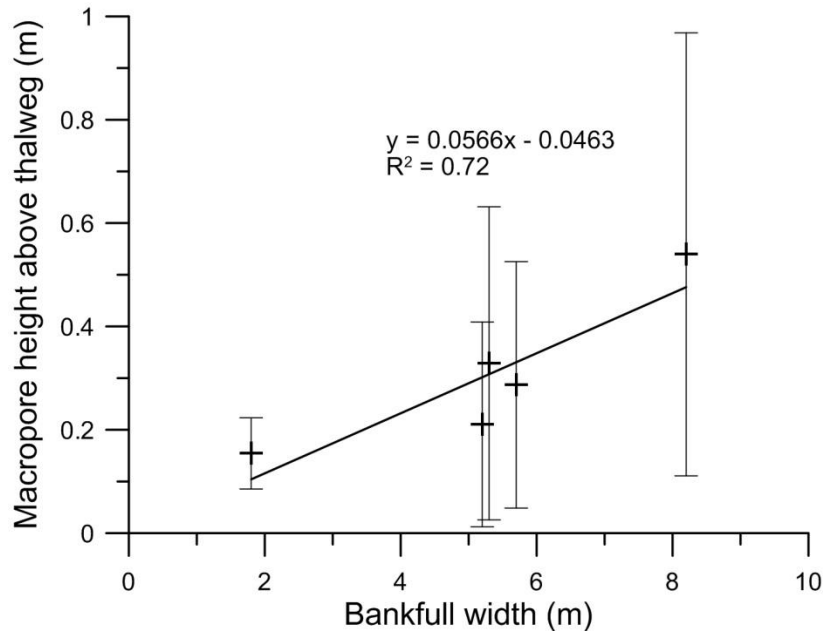


Figure 4-4. Relationship of median height of macropore above thalweg to average channel bankfull width. Error bars show values within a single standard deviation for each stream.

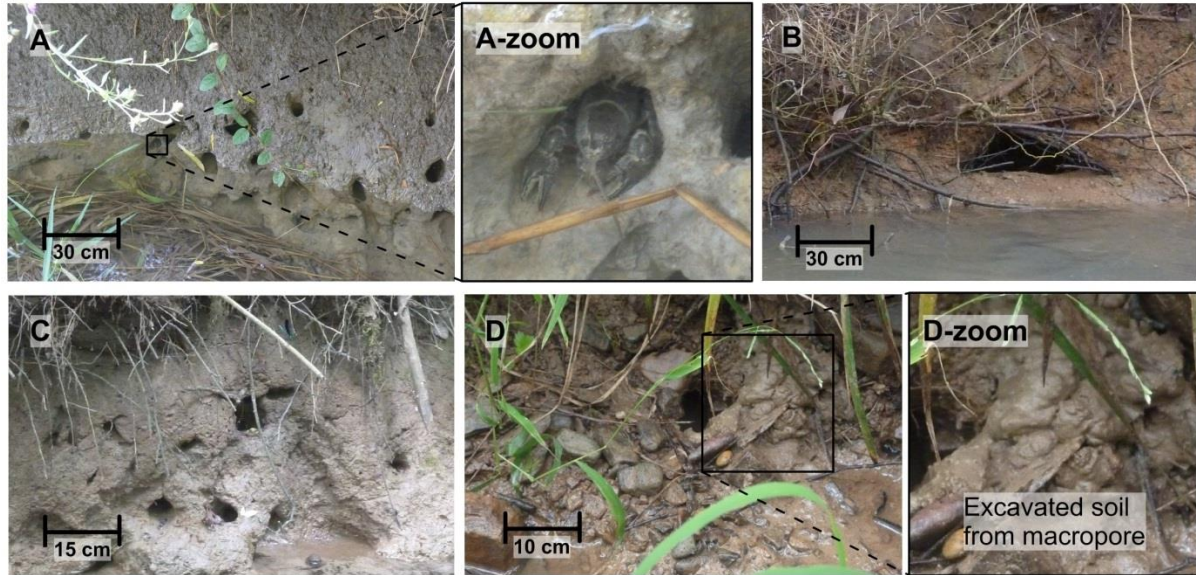


Figure 4-5. Example macropores of differing creation mechanisms, including a) macroinvertebrates (crayfish, shown in inset) on the outside of a meander bend, b) vertebrates (e.g., mink) on the banks at a pool, c) root decay/erosion (upper macropores), bank erosion (middle/lower non-inundated macropores), and macroinvertebrates (inundated macropores) on banks at a riffle, and d) macroinvertebrates in a sediment matrix containing gravel at a riffle. Panel D-zoom shows recently unearthed soil from the saturated zone (likely by crayfish) around macropore opening, whereas other nearby soil is more consolidated and drier.

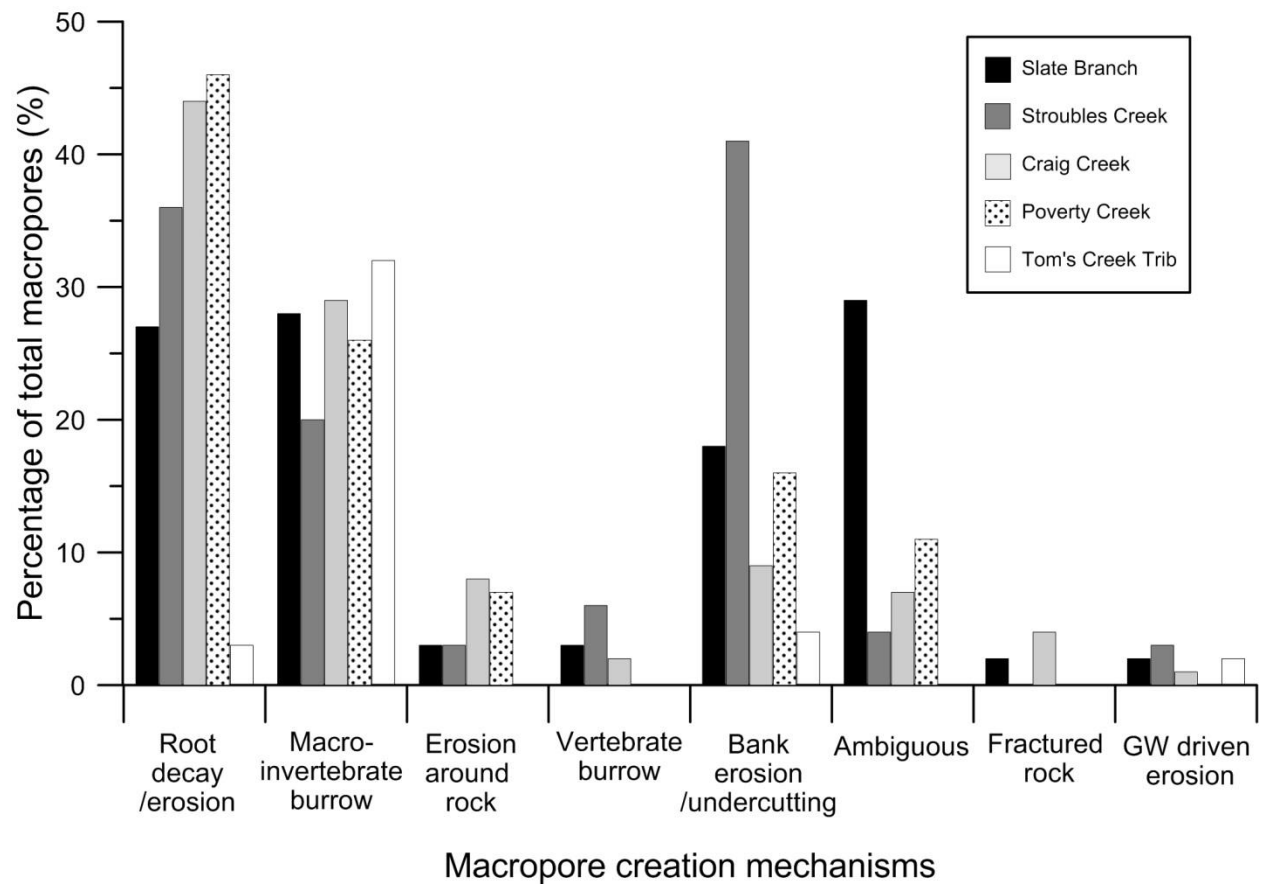


Figure 4-6. Proportions of macropore creation mechanisms across sites.

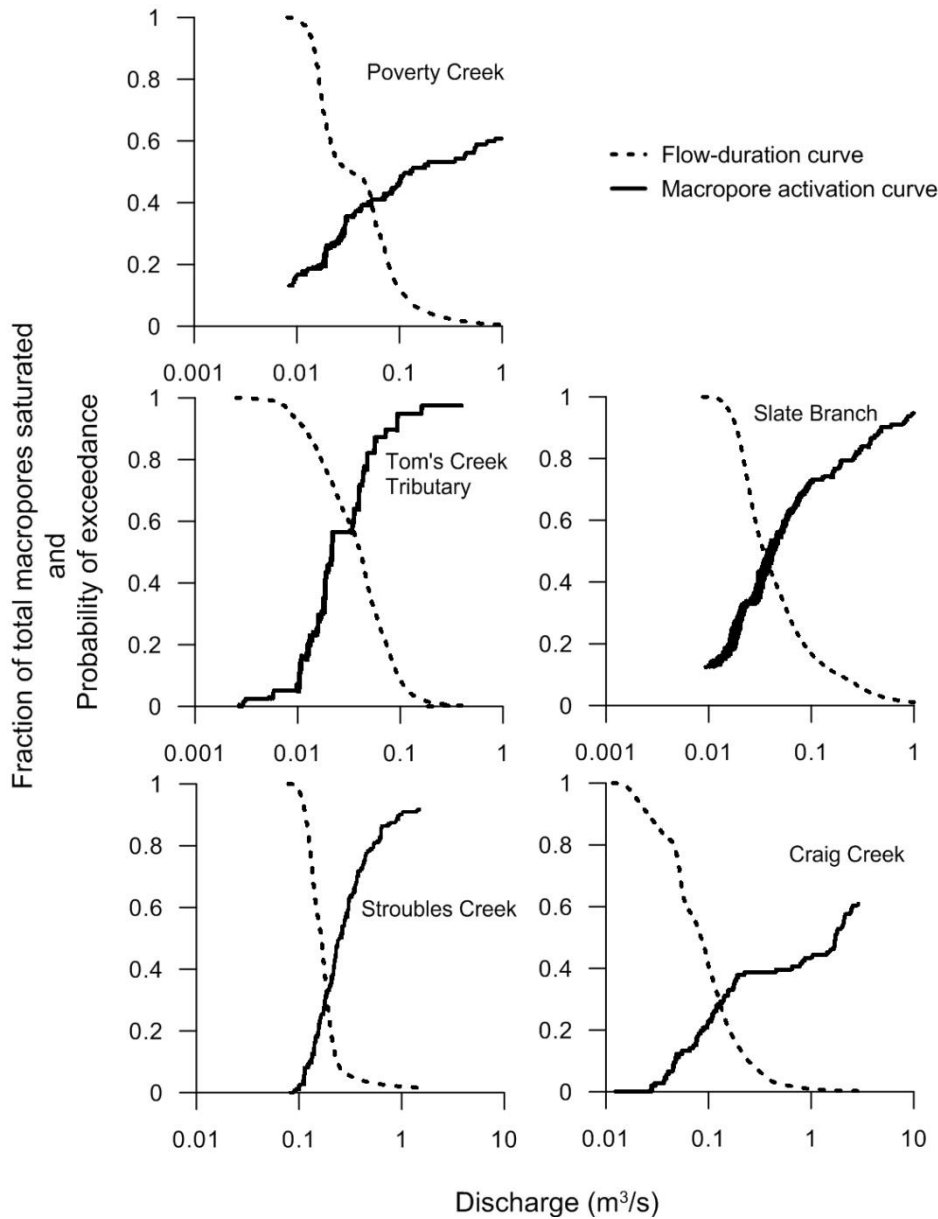


Figure 4-7. Macropore hydroperiod analyses. Maximum discharges shown are less than 2 times the maximum discharge measured with the velocity-area method. This is done to avoid extrapolating higher discharges from rating curves and to show macropore activation curve trends at lower discharges in more detail. Macropore activation curves are based on the moving average of macropore inundation over time.

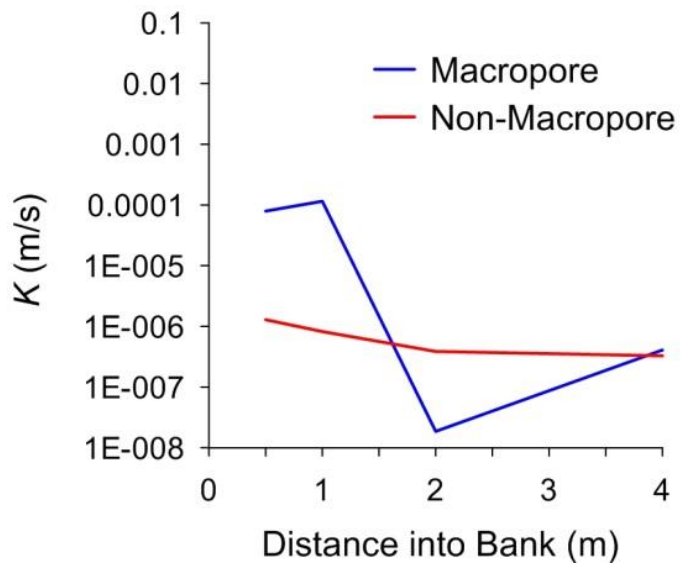


Figure 4-8. K 's measured from rising head field tests in wells in the M and NM transects.

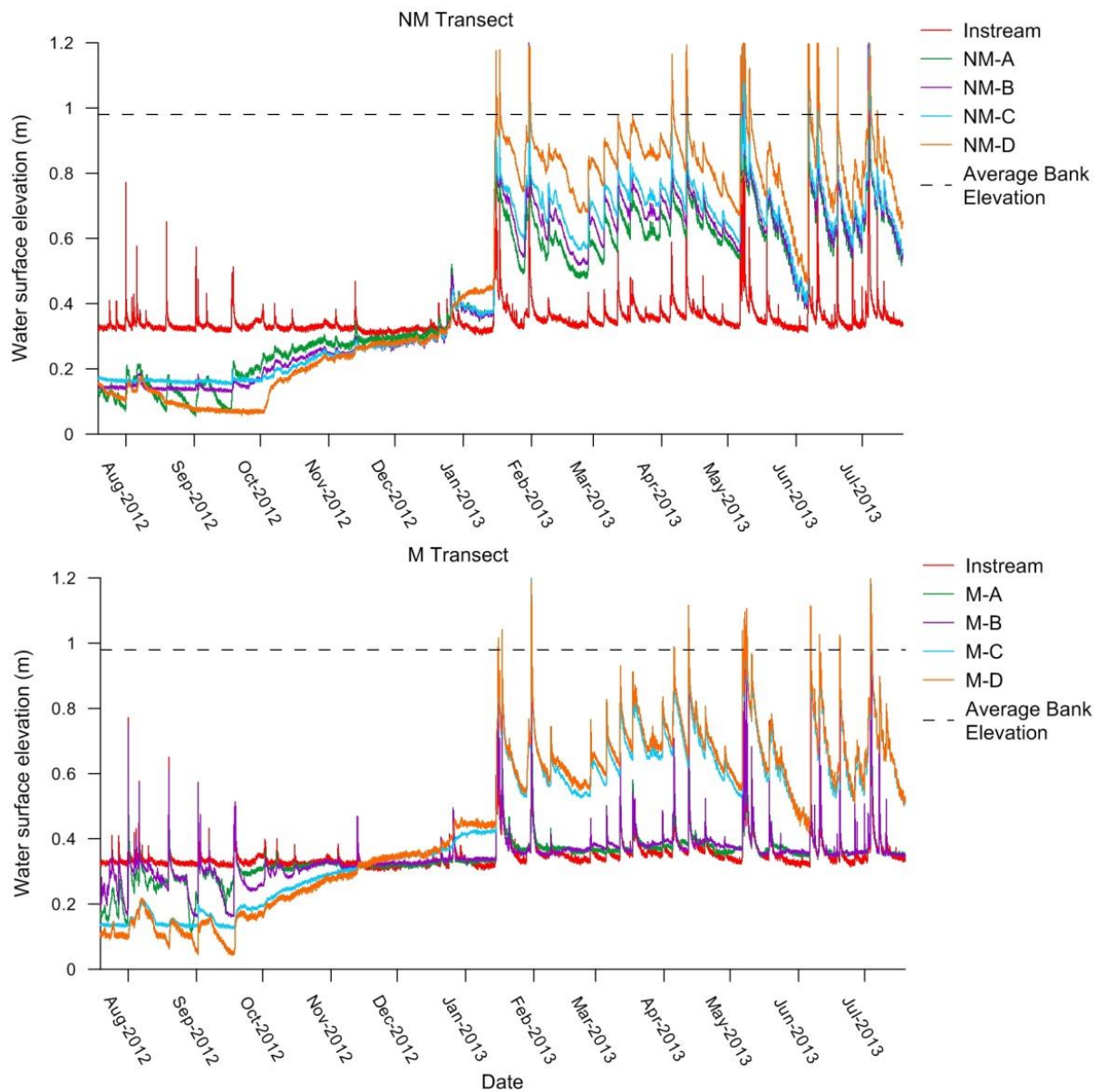


Figure 4-9. Full year of water levels in the stream, macropore (M) transect, and non-macropore (NM) transect. See Figure 4-1 for well locations.

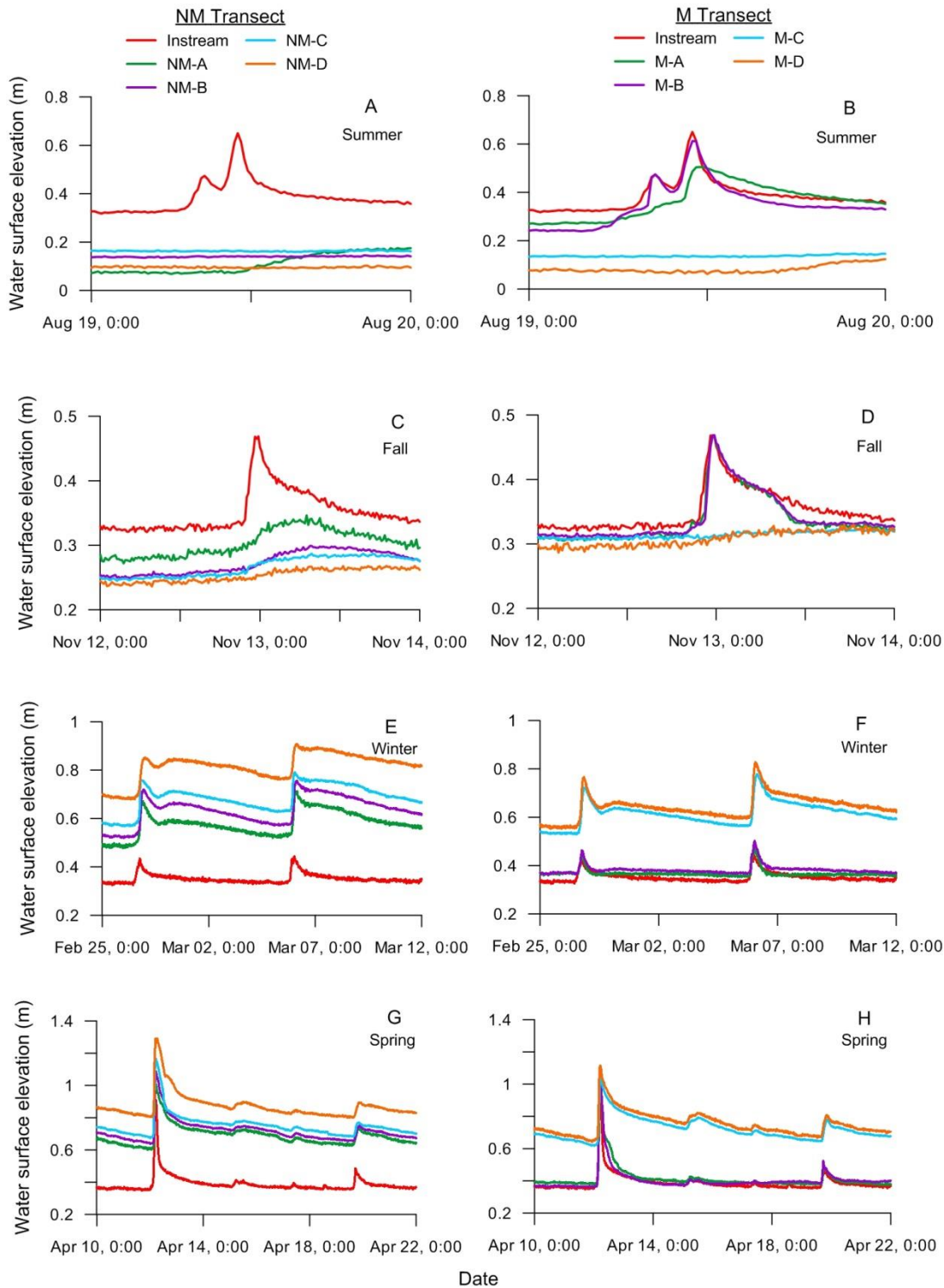


Figure 4-10. Water levels in the channel and transect wells during storms in summer (storm on Aug. 19), fall (storm on Nov. 13), winter (storms on Feb. 27 and Mar. 5), and spring (storms on Apr. 12, April 15, April 17, and April 20). The average elevation of the channel bank at the transects is 0.96 m. Note differences in Y-axis scale among plots.

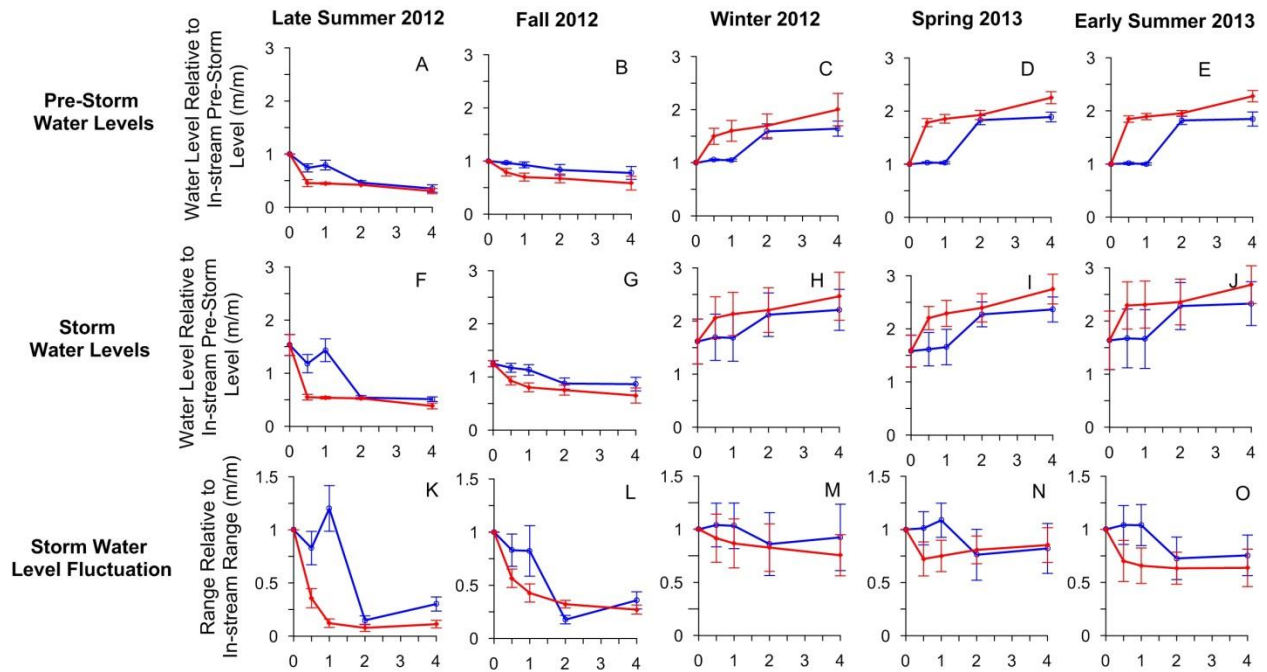


Figure 4-11. Average pre-storm water levels, average stormflow water levels, and ranges of storm water level fluctuations experienced over seasons in wells at the macropore (BLUE) and non-macropore (RED) transect. Values are averaged over all storm and non-storm data points for each season. Error bars show 1 standard deviation about the mean.

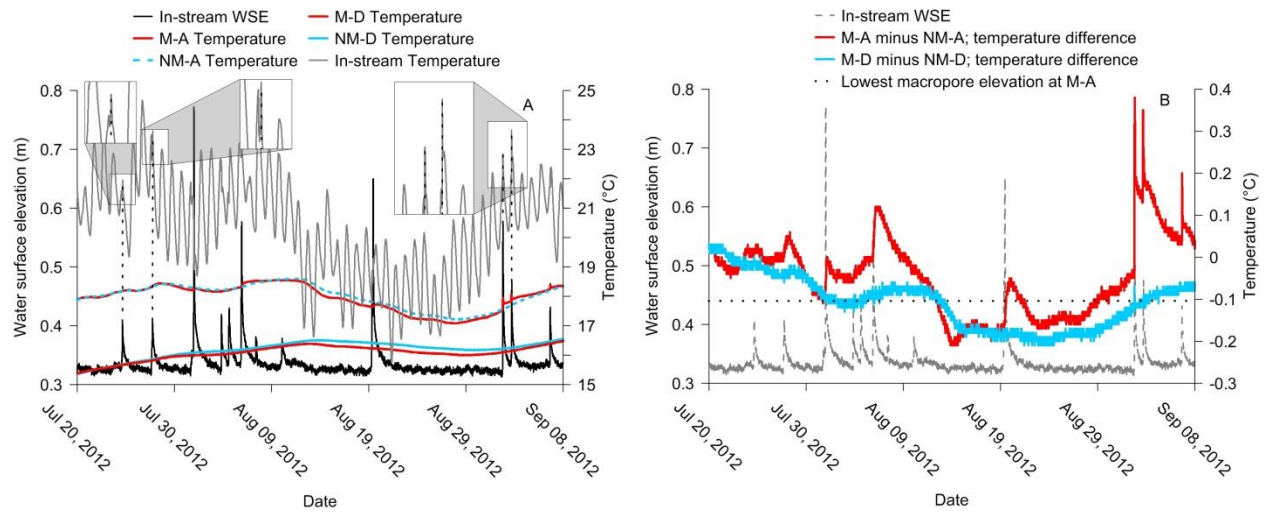


Figure 4-12. Panel A shows temperatures experienced in channel and in wells over 1.5 months during summer. “WSE” is water surface elevation. Panel B shows differences in temperature between the macropore and non-macropore transect at the 1st row (RED) and 4th row (BLUE) of wells for a series of storm events.

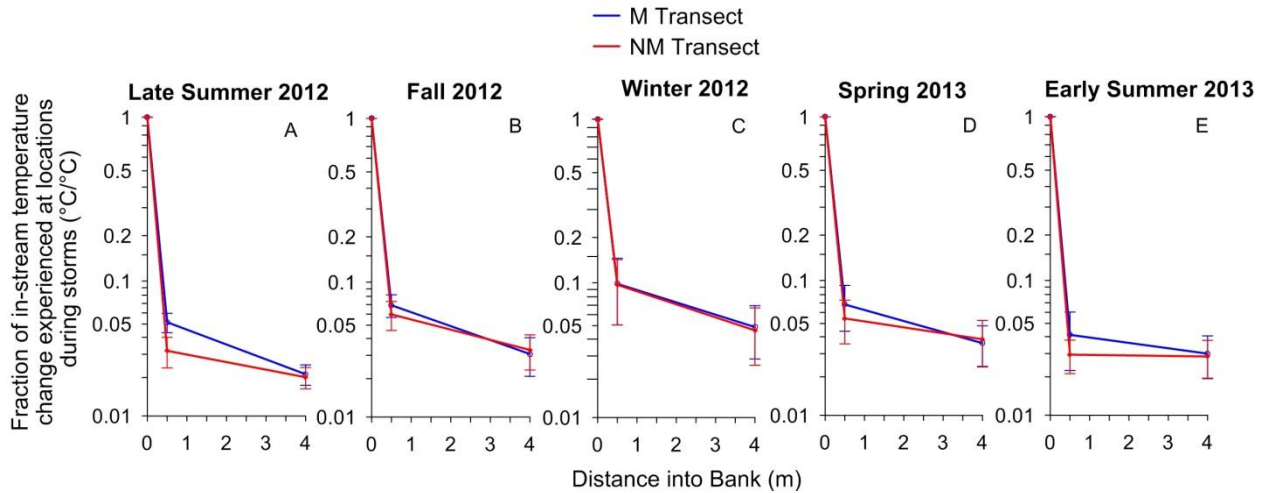


Figure 4-13. Water temperature ranges during storms at the 1st row, and at the 4th row of wells for the macropore and non-macropore transect. Ranges are calculated for each storm event in the year and averaged seasonally. Summer is split into 2012 and 2013 because background hydrologic conditions were different (i.e., losing in 2012, gaining in 2013). M-B and NM-B (at X=1 m) as well as M-C and NM-C (at X=2m) are not included because those locations had Hobos which have poorer accuracy temperature sensors.

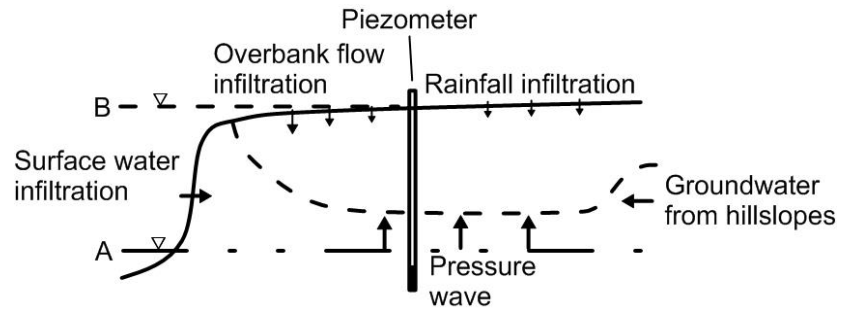


Figure 4-14. Conceptual model of potential hydrologic processes influencing near-channel groundwater levels during neutral baseflow conditions (case A) and storm flow conditions (case B).

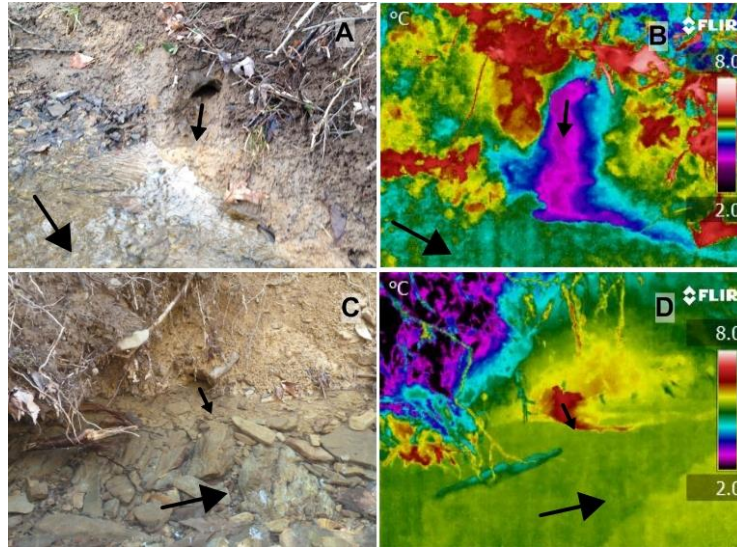


Figure 4-15. Thermal discharges from macropores during winter. Panel A shows macropore opening that is 4 cm tall by 3.5 cm wide discharging water into Slate Branch. Panel B shows a Forward Looking Infrared (FLIR) image of the same macropore, discharging water that is 1.7°C colder than stream flow. Panel C shows 3 cm tall by 5 cm wide macropore opening at Poverty Creek with no observable flow coming out of it. Panel D shows FLIR image of same macropore actively discharging water 1.6°C warmer than stream flow. Flow directions shown by arrows.

CHAPTER 5: *Conclusions*

Chapters 2-4 of this dissertation provide new insights into how the variability and heterogeneity of hydraulic conductivity (K) affects hyporheic exchange hydraulics and hyporheic zone functions in streams. The following sections summarize the major findings in the chapters, synthesize the results, provide context between chapters, discuss engineering significance of the work, and lastly discuss future research directions.

5.1 *OBJECTIVES AND FINDINGS*

The findings from Chapters 2-4 are discussed below in reference to the objectives presented in Chapter 1.

Chapter 1. The objective was to investigate the effect of variation of K on hyporheic hydraulics and stream temperature dynamics near in-stream structures by creating a fully-coupled surface water-groundwater CFD hydraulics model and a groundwater CFD temperature model. Major findings were:

- Residence time and hyporheic discharge exhibited countervailing trends with K .
- Fundamental shifts in weir-induced hyporheic hydraulics and temperature dynamics occurred at threshold K 's.
- Beyond a threshold K of 10^{-3} m/s, surface water stopped flowing over the weir and surface water markedly began sinking into the bed. This caused a decrease in the surface water head gradients across the weir and decreased hyporheic gradients. These gradient shifts caused the hyporheic flow cell size to decrease.
- Also above a threshold K 's of 10^{-3} m/s, inertial forces triggered deviation from Darcy's Law, such that using Darcy's Law caused up to a 10.1% overprediction of hyporheic discharges. Steep hydraulic gradients and high velocities near the weir locally increased inertial forces and the importance of non-Darcy flow.
- Cooling and buffering along hyporheic flow paths decreased as K was increased, particularly above thresholds of $K=10^{-5}$ and 10^{-4} m/s, respectively. However, these decreases were outweighed by increased hyporheic discharges, causing net increases to hyporheic heat advection and net cooling. Net downstream surface

water cooling from weir induced exchange during summer was maximized by maximizing hyporheic flow rates.

- Subsurface thermal heterogeneity increased with K up to $\sim 3^{\circ}\text{C}$, particularly for K above 10^{-5} m/s, which is important because it can influence habitat availability and diversity as well as influence biogeochemical reactions.

Chapter 2. The objective was to quantify the impact of macropores on hyporheic hydraulics and solute transport through meander bends using electrical resistivity imaging, falling head tests, and tracer injection experiments. Major findings were:

- Macropores exerted a strong control on hyporheic hydraulics and solute transport through meander bends.
- Individual macropores in a meander bend locally increased K by 29 to 550 times above nearby sediments. Transport velocities, hydraulic head gradients through the meander bend, and solute transport rates all were increased because of the macropore.
- Using electrical resistivity imaging along with conventional hydraulics methods (e.g., falling head tests, tracer tests) in tandem to detect preferential flow paths allowed quantification of variation of hyporheic hydraulics in space and time. Future studies can utilize these methods to more accurately characterize heterogeneity in the subsurface (e.g., paleochannels) and better predict subsurface transport.
- Strong connectivity of macropores to other naturally existing preferential flow paths increased hyporheic transport and dictated solute transport.

Chapter 3. Characterize the spatial characteristics of surface-connected macropores along streams in the Appalachian Mountains of southwestern Virginia and quantify their impact on bank storage by conducting reach scale field surveys, hydroperiod analyses, and monitoring riparian groundwater level and temperature fluctuations during storms. Major findings were:

- Macropores are common geomorphic features in the Appalachian province of southwestern Virginia. Macropore dimensions were up to a cross sectional width of 30.0 cm, a cross sectional height of 27.5, a length to first bend of 120.5 cm.

- The majority of macropores were active during large storm events in a one-year period, suggesting their greatest value may be in bank storage.
- Water level and temperatures fluctuations in groundwater wells suggest that macropores increase bank storage during storm events. Because macropores increase bank storage, they can decrease the in-stream peak discharge during storms and can increase groundwater recharge in riparian zones.
- Lastly, increased solute transport between the channel and groundwater zones suggests macropores can influence rates of biogeochemical cycling, pollutant attenuation, and increase the size of the hyporheic zone (thus creating hyporheic habitat).

5.2 MAJOR THEMES AND CONTEXT

Surface-connected macropores along stream channels, the focus of Chapters 3 and 4, demonstrate that small scale heterogeneities in K are common and influence bank storage and transport through meander bends. Because macropores can act as preferential flow paths, hyporheic zones with fine sediments can achieve significantly higher flow rates than would otherwise be expected, with corresponding implications for solute transport and hyporheic functions. Macropores may be important to these processes in a wide range of conditions and across landscapes, and may therefore broaden the portion of the landscape in which hyporheic exchange is important.

It is speculated that macropore occurrence, importance, and function could vary with gradients such as elevation, geomorphic regime, geomorphic structure, and urbanization. Macropores in steep sloping mountain streams, for example cascading or step-pool geomorphologies, may exist from fractured rock and scour. Because these streambeds generally consist of coarse sediments, macropores may have a small effect on net hyporheic exchange and functions. Macropores in lower gradient streams, such as dune-ripple geomorphologies, can exist from mechanisms such as bioturbation [Mermillod-Blondin and Rosenberg, 2006; Mermillod-Blondin et al., 2003] micro-erosion, and soil piping [Fox and Wilson, 2010]. Because these streambeds would have finer sediments than the higher gradient streams, macropores may comparatively be more important in augmenting hyporheic flow rates.

With urbanization, colmation due to fine sediments from construction can decrease the hydraulic conductivity of the streambed [Brunke, 1999]. However, macropores can re-establish

hyporheic exchange in these settings and influence biogeochemical cycling or pollutant attenuation. For example, in urban streams with nitrogen pollution (e.g., as nitrate) and where colmation has decreased streambed K , macropores may become the dominant pathways for nitrogen transport into anoxic zones where denitrification can occur. Similarly, macropores may reconnect the stream channel with paleochannels where biogeochemical reactions or pollutant attenuation can occur, depending availability of organic carbon and electron acceptors.

Lastly, macropores existing in the backwater of in-stream structures may control hyporheic hydraulics. In Chapter 2, the subsurface for the hydraulics and temperature model was idealized as homogenous, but the inclusion of macropores would have strongly influence hydraulics and temperature dynamics. Macropores would shift the observed hydraulics and temperature threshold K 's from Chapter 2. For example, macropores would increase flow rates through the hyporheic zone, causing non-Darcy flow and surface water to stop flowing over the weir at lower K values than modeled. These increased flow rates would decrease residence times and the associated cooling and buffering along those flow paths. Macropores would increase thermal heterogeneity within the subsurface, with flow paths near macropores having the highest thermal heterogeneity.

5.3 ENGINEERING SIGNIFICANCE

5.3.1 Implications for Stream Restoration

The goal of stream restoration is to improve the structure and function of streams. Three common practices with linkages to this dissertation are installing in-stream structures, introducing coarser sediments, and reintroducing meander bends by channel reconfiguration. These techniques can increase hyporheic exchange, but will be most effective when background groundwater levels do not heavily constrain hyporheic flow paths. Stream restoration practitioners can utilize findings in this work to assess stream functions incurred by hyporheic exchange.

Although weir-induced hyporheic exchange was specifically studied in Chapter 2, the results are pertinent to other commonly used in-stream structures, such as cross-vanes and j-hooks [Buchanan *et al.*, 2012; Radspinner *et al.*, 2010]. For structure-induced hyporheic exchange, downstream surface water cooling and subsurface thermal heterogeneity are flow-limited (limited by hyporheic flow rate) hyporheic functions. Although the net impact on downstream surface water cooling was small, this effect could be increased by installing multiple

structures. Ultimately, the largest thermal impact of in-stream structures will be increased thermal heterogeneity, which can increase habitat availability and diversity as well as influence the presence and rates biogeochemical reactions.

In-stream structures are commonly used in stream restoration design to control flow, reduce erosion, and create habitat [Buchanan *et al.*, 2012; Radspinner *et al.*, 2010]. In-stream structures that direct surface flow, such as cross vanes, are often placed on the upstream side of meander bend to protect the outside of the bend [Buchanan *et al.*, 2012]. The backwater created by the structures increases the head gradient through the meander bend, thereby increasing hyporheic exchange. Additionally, macropores are common geomorphic features that can be present in meander bends (i.e., Chapters 3 and 4). Therefore, in-stream structures placed on the upstream side of meanders can both increase the head gradient driving hyporheic exchange and inundate macropores in the meander bend to further increase hyporheic flow rates. However, the potential for hyporheic exchange to occur through meanders depends on background groundwater levels, which can limit hyporheic flow paths. In strongly gaining streams, flow through meanders will be cut off, but in strongly losing streams, flow through meanders will never return to the stream. Therefore, we expect the greatest increase in hyporheic exchange from in-stream structures on the upstream side of meanders will come for slightly gaining conditions, where flow paths eventually return to the stream, but the hyporheic zone is not constrained.

Coarse grained sediments can be added to or replace finer grained sediments to achieve significant hyporheic exchange [Kasahara and Hill, 2007]. Similarly, subsurface structure heterogeneity could be designed and built to perform particular hyporheic functions [Vaux, 1968; Ward *et al.*, 2011]. Simple investigations of K could allow identification of paleochannels or other flow paths with which reconnection of the surface stream with could provide biogeochemical cycling or pollutant attenuation [Lawrence *et al.*, 2013]. Because surface-connected macropores are common geomorphic features, they may provide pathways to paleochannels and preferential flow paths. Furthermore, the presence of preferential flow paths such as macropores increase hyporheic exchange in finer sediments and can enhance functions of hyporheic exchange that are flow-limited (e.g., thermal heterogeneity and downstream surface water cooling in Chapter 2). Macropores occurring along stream channels can also influence rates of local biogeochemical reactions or provide unique habitat for aquatic organisms. The

impact of macropores on water quality and stream functions will depend on hydrologic conditions, spatial characteristics of macropores, and physiochemical properties of surface water and groundwater. Ultimately, in order to quantify the potential functions of hyporheic exchange, it is important to first identify K and heterogeneity in the field.

5.3.2 When and where will restoring hyporheic exchange matter?

Hyporheic zone flow paths can be divided loosely into two categories known as the “gill” and “lung” models, respectively [Sawyer et al., 2009]. In the gill model, flow directions are similar during low flow and high flow conditions because of relatively stable background groundwater gradients, whereas in the lung model, flow directions have notable reversals due to relatively rapid variations in river water levels. The potential for hyporheic zone restoration depends on the setting in which hyporheic exchange (lung versus gill model) occurs. Restoring the gill model of hyporheic exchange (Chapter 2) will generally have a small effect on solute transport downstream in surface water, except in very coarse sediments, and the greatest effect will be at baseflow. Restoring the lung model of hyporheic exchange would have the greatest effect on downstream solute transport at higher flows. However, the lung model is based on streams whose hydrology is influenced by dam release. Additionally, urban streams with flashy hydrographs (i.e., from high runoff rates) will fit the lung model. Because the factors driving the hydrology which promotes the lung model are actually impacts (e.g., dams or urban environments), an important question is if the lung model can be achieved in restoration.

The ideal hyporheic restoration setting would have sufficiently long residence times for rate-limited functions to occur, but also would have a high percentage of total stream flow passing through the hyporheic zone at baseflow and elevated flow conditions. This ideal hyporheic setting may be difficult to achieve in restoration, because it would require significant flow reversals without elevated flow conditions. Yet such conditions may already occur in streams dominated by effluent in urban environments during dry months with very low flows [Lawrence et al., 2013]. Identifying and quantifying the conditions where this ideal hyporheic restoration setting exists is important to maximizing beneficial functions of hyporheic exchange.

5.4 FUTURE RESEARCH

The spatial characteristics (e.g., frequency, geometry, size, inter-connectivity) of macropores are important in determining flow rates through macropores [Matthai and Belayneh, 2004]. Accurately quantifying the full spatial characteristics of macropores is key in determining

their hydrologic value. A major future need is new field methods to detect macropores and characterize macropore geometry. While electrical resistivity imaging [Menichino *et al.*, 2012], ground penetrating radar [Gormally *et al.*, 2011; Holden, 2005], and liquid latex [Abou Najm *et al.*, 2010] offer promise in detecting and mapping macropore geometries, they each have disadvantages and limitations that make characterizing hyporheic zone macropores difficult. For example, electrical resistivity imaging and ground penetrating radar require training to perform and post-process the results, and liquid latex cannot be used in saturated settings. Because macropore structure, elevation along the channel, connectivity with other flow paths, and dimensions are likely unique, it may be useful to select the detection or mapping methods based on the individual macropore. Accurately mapping of macropore geometries will likely indicate that macropore impact on hyporheic flow and solute transport varies highly in space and between macropores. With more information about the spatial characteristics about macropores, modeling studies may be performed to quantify the hydrologic value of macropores (e.g., flow contributions) relative to the flow within the surface channel.

The hydraulics and temperature dynamics models in Chapter 2 have important implications for modeling hyporheic exchange and assessing stream functions. The models identified the presence of distinct thresholds where hyporheic hydraulics (e.g., advent of non-Darcy flows) and temperature dynamics (e.g., significant thermal heterogeneity) fundamentally shift. While the specific value of these thresholds may change with hydrologic conditions and geologic setting, thresholds should still be present. Future research should explore how these thresholds change in streams across gradients of elevation, land use, geomorphology, climate, and geology. Additionally, future research utilizing hydraulics and temperature models could include macropores as subsurface heterogeneities and explore the corresponding effects on subsurface flow dynamics and heat transport.

Flow-limited hyporheic functions, such as in-stream peak discharge reduction, groundwater recharge, or comparatively rate-limited functions, such as pollutant attenuation by denitrification are of interest because of their potential to improve water quality and stream health [Hester and Gooseff, 2010; 2011; Lawrence *et al.*, 2013]. Using fully-coupled CFD to model hyporheic exchange may be necessary when (1) non-Darcy flows decrease subsurface velocities and correspondingly increase residence time and (2) turbulent diffusion and hydrodynamic processes increase hyporheic flow rate. Therefore, accurate prediction of flow-

limited and rate-limited functions may require consideration of these hydraulic processes. For example, such processes will be important in predicting hyporheic hydraulics when K or hydraulic gradient are high, such as step-pool sequences or steep, coarse-bedded streams. Similarly, macropores increase K and can influence hyporheic functions that are rate-limited or flow-limited. For example, macropores in meanders may increase nutrient cycling by quickly supplying the hyporheic zone with dissolved oxygen and nutrients. However it is commonly assumed in hyporheic studies that the subsurface is homogenous [Cardenas and Wilson, 2007; Endreny *et al.*, 2011; Sawyer *et al.*, 2012]. Therefore, future hyporheic zone models should consider the addition of macropores, or other naturally occurring preferential flow paths (e.g., paleochannels [Poole *et al.*, 2006]), to better predict hyporheic hydraulics, particularly when solute transport or hyporheic functions are of interest [Fox *et al.*, 2009; Fox *et al.*, 2010; Sawyer *et al.*, 2012].

The countervailing between residence times and flow rates over a range of K suggests the control of K on hyporheic functions that are limited by flow rate or residence time. Future work is needed to identify the net downstream benefits from such exchange, targeting functions such as denitrification. For example, meander flow, bank storage, exchange within streambeds, and flow through gravel bars can promote denitrification [Boano *et al.*, 2010; Gu *et al.*, 2012; Gu *et al.*, 2007; Zarnetske *et al.*, 2011]. However, denitrification occurs along hyporheic flow paths when residence times are great enough that the hyporheic zone is anoxic, denitrifying microbes are present, and organic carbon is available [Zarnetske *et al.*, 2011]. The supply and delivery of organic carbon, oxygen, and nitrate to the hyporheic zone depends on the hyporheic flow rate. Additionally, availability of water quality constituents (e.g., dissolved oxygen or carbon) along flow paths depends on uptake or reactions, which can be tied to residence times along flow paths. Because K determines the net flow through the hyporheic zone as well as influences the presence of denitrification, there theoretically could a maximum downstream benefit at a particular K . Future work is needed to identify this K and how it varies with hydrologic conditions and setting.

5.5 REFERENCES

Abou Najm, M. R., J. D. Jabro, W. M. Iversen, R. H. Mohtar, and R. G. Evans (2010), New method for the characterization of three-dimensional preferential flow paths in the field, *Water Resour Res*, 46, W02503.

- Boano, F., A. Demaria, R. Revelli, and L. Ridolfi (2010), Biogeochemical zonation due to intrameander hyporheic flow, *Water Resour Res*, 46, W02511.
- Brunke, M. (1999), Colmation and depth filtration within streambeds: Retention of particles in hyporheic interstices, *Int Rev Hydrobiol*, 84(2), 99-117.
- Buchanan, B. P., M. T. Walter, G. N. Nagle, and R. L. Schneider (2012), Monitoring and assessment of a river restoration project in central New York, *River Res Appl*, 28(2), 216-233.
- Cardenas, M. B., and J. L. Wilson (2007a), Thermal regime of dune-covered sediments under gaining and losing water bodies, *J Geophys Res-Bioge*, 112, G04013.
- Endreny, T., L. Lautz, and D. I. Siegel (2011), Hyporheic flow path response to hydraulic jumps at river steps: Flume and hydrodynamic models, *Water Resour Res*, 47, W02517.
- Fox, G. A., and G. V. Wilson (2010), The Role of Subsurface Flow in Hillslope and Stream Bank Erosion: A Review, *Soil Sci Soc Am J*, 74(3), 717-733.
- Fox, G. A., J. W. Fuchs, D. E. Storm, C. J. Penn, and G. O. Brown (2009), Subsurface transport of phosphorus in riparian floodplains: influence of preferential flow paths, *J Environ Qual*, 38(2), 473-484.
- Fox, G. A., D. M. Heeren, R. B. Miller, D. E. Storm, T. Halihan, and C. J. Penn (2010), Preferential flow effects on subsurface contaminant transport in alluvial floodplains, *T ASABE*, 53(1), 127-136.
- Gormally, K. H., M. S. McIntosh, A. N. Mucciardi, and G. W. McCarty (2011), Ground penetrating radar detection and three-dimensional mapping of lateral macropores: II. riparian application, *Soil Sci Soc Am J*, 75(4), 1236-1243.
- Gu, C. H., W. Anderson, and F. Maggi (2012), Riparian biogeochemical hot moments induced by stream fluctuations, *Water Resour Res*, 48(9).
- Gu, C. H., G. M. Hornberger, A. L. Mills, J. S. Herman, and S. A. Flewelling (2007), Nitrate reduction in streambed sediments: Effects of flow and biogeochemical kinetics, *Water Resour Res*, 43, W12413.
- Hester, E. T., and M. N. Gooseff (2010), Moving beyond the banks: hyporheic restoration is fundamental to restoring ecological services and functions of streams, *Environ Sci Technol*, 44(5), 1521-1525.

- Hester, E. T., and M. N. Gooseff (2011), Hyporheic Restoration in Streams and Rivers, in *Stream Restoration in Dynamic Fluvial Systems: Scientific Approaches, Analyses, and Tools*, edited, pp. 167-187, AGU, Washington, DC.
- Holden, J. (2005), Controls of soil pipe frequency in upland blanket peat, *J Geophys Res-Earth*, *110*, F01002.
- Kasahara, T., and A. R. Hill (2007), Lateral hyporheic zone chemistry in an artificially constructed gravel bar and a re-meandered stream channel, southern Ontario, Canada, *J Am Water Resour As*, *43*(5), 1257-1269.
- Lawrence, J. E., M. E. Skold, F. A. Hussain, D. R. Silverman, V. H. Resh, D. L. Sedlak, R. G. Luthy, and J. E. McCray (2013), Hyporheic Zone in Urban Streams: A Review and Opportunities for Enhancing Water Quality and Improving Aquatic Habitat by Active Management, *Environ Eng Sci*, *30*(8), 480-501.
- Matthai, S. K., and M. Belayneh (2004), Fluid flow partitioning between fractures and a permeable rock matrix, *Geophys Res Lett*, *31*, L07602.
- Menichino, G. T., A. S. Ward, and E. T. Hester (2012), Macropores as preferential flow paths in meander bends, *Hydrol Process*, Published online 16 Nov 2012. DOI: 10.1002/hyp.9573.
- Mermillod-Blondin, F., and R. Rosenberg (2006), Ecosystem engineering: the impact of bioturbation on biogeochemical processes in marine and freshwater benthic habitats, *Aquat Sci*, *68*(4), 434-442.
- Mermillod-Blondin, F., J. P. Gaudet, M. Gerino, G. Desrosiers, and M. C. des Chatelliers (2003), Influence of macroinvertebrates on physico-chemical and microbial processes in hyporheic sediments, *Hydrol Process*, *17*(4), 779-794.
- Poole, G. C., J. A. Stanford, S. W. Running, and C. A. Frissell (2006), Multiscale geomorphic drivers of groundwater flow paths: subsurface hydrologic dynamics and hyporheic habitat diversity, *J N Am Benthol Soc*, *25*(2), 288-303.
- Radspinner, R., P. Diplas, A. Lightbody, and F. Sotiropoulos (2010), River Training and Ecological Enhancement Potential Using In-Stream Structures, *J Hydraul Eng*, *136*(12), 967-980.
- Sawyer, A. H., M. B. Cardenas, and J. Buttles (2012), Hyporheic temperature dynamics and heat exchange near channel-spanning logs, *Water Resour Res*, *48*, W01529.

- Sawyer, A. H., M. B. Cardenas, A. Bomar, and M. Mackey (2009), Impact of dam operations on hyporheic exchange in the riparian zone of a regulated river, *Hydrol Process*, 23(15), 2129-2137.
- Vaux, W. (1968), Intragravel flow and interchange of water in a streambed, *NOAA*, 66(3), 479-489.
- Ward, A. S., M. N. Gooseff, and P. A. Johnson (2011), How can subsurface modifications to hydraulic conductivity be designed as stream restoration structures? Analysis of Vaux's conceptual models to enhance hyporheic exchange, *Water Resour Res*, 47, W08512.
- Zarnetske, J. P., R. Haggerty, S. M. Wondzell, and M. A. Baker (2011), Dynamics of nitrate production and removal as a function of residence time in the hyporheic zone, *J Geophys Res-Biogeophys*, 116, G01025.

APPENDIX A: *Supplementary Material to the Hydraulics Model in Chapter 2*

Hyporheic Exchange Hydraulics Modeling

Computational fluid dynamics (CFD) software (e.g., COMSOL, Fluent, CFX, Flow3d) use the full Navier-Stokes equations to simulate dynamics of surface water or groundwater in three dimensions [Wendt, 2008]. For example, CFX has been used to predict complex flows around in-stream structures in surface water [Shen and Diplas, 2008] and non-Darcy flow at the particle scale [Cheng et al., 2008]. However, most hyporheic CFD applications divide the flow domain into separate surface water and groundwater models. Prior hyporheic models have fallen into 3 categories with respect to use of CFD:

(1) Surface water and groundwater domains that are both non-CFD [Endreny et al., 2011b; Hester and Doyle, 2008; Spanoudaki et al., 2009].

(2) Surface and groundwater domains that are both CFD but separated by a no-slip wall at the sediment interface [Cardenas and Wilson, 2006; 2007a; b; c; d; Cardenas et al., 2008a].

(3) Surface and groundwater domains that are both CFD and integrated as part of a single model, linked at the sediment interface to allow conservative momentum and mass transfer between the domains [Crispell and Endreny, 2009; Endreny et al., 2011a].

Approaches (1) and (2) do not directly simulate momentum and turbulence transfer (e.g., velocity distributions) near and across the surface water-groundwater interface. By comparison, approach (3) does simulate these processes, and is therefore the most accurate for evaluating hyporheic hydraulics and function, yet is not often selected due to challenges of steep learning curves, inadequate computer resources, or high run times.

Hyporheic Exchange Hydraulics with CFD: Governing Equations

We modeled the hydraulics of surface water-groundwater exchange near a single in-stream structure (weir representing a debris dam, log dam, boulder weir, cross vane, etc.) using the three-dimensional, finite volume method CFD software, ANSYS CFX. The continuity equation used is

$$\frac{\partial \rho}{\partial t} + \nabla \cdot (\rho \mathbf{v}) = 0 \quad (1)$$

where \mathbf{v} is the superficial (i.e., linear) velocity vector (m/s), ρ is the density of water (kg/m³), and t is time (s). We used the Navier-Stokes equation for conservation of momentum [ANSYS, 2011a],

$$\frac{\delta(\rho \mathbf{v})}{\delta t} + \nabla \cdot (\rho \mathbf{v} \times \mathbf{v}) = -\nabla p + \nabla \cdot \boldsymbol{\tau} + f + S_m \quad (2)$$

where p is the pressure (pa), f represents body forces (i.e., gravity), S_m is any momentum sources, and $\boldsymbol{\tau}$ is the viscous stress tensor (kg/m·s²) which is related to strain rate by,

$$\boldsymbol{\tau} = \mu(\nabla \mathbf{v} + (\nabla \mathbf{v})^T) - \frac{2}{3} \delta \nabla \cdot \mathbf{v} \quad (3)$$

where δ is the unit tensor, μ is the fluid dynamic viscosity (kg/m·s).

For groundwater flow, we employed a full porous media model, which includes porosity in every term in Equations 1 and 2. The porous region is defined as a pressure drop in the momentum equation, and represented by isotropic loss model with a linear component for viscous losses and a quadratic term for inertial losses,

$$\frac{dp}{dx} = -\frac{\mu}{k} v - \beta \rho v^2 \quad (4)$$

where k is the permeability (m²) and β is the inertial loss coefficient (1/m), also known as the non-Darcy flow coefficient or Forchheimer Coefficient. We assumed that the sediment permeability field is homogenous and isotropic, as has been done in hyporheic CFD models [Cardenas and Wilson, 2007a; Endreny et al., 2011a]. The viscous losses term uses the permeability of the media to model Darcy flow while the inertial losses term accounts for non-Darcy flow through β .

The Forchheimer extension (last term in Eq. 4) accounts for inertial losses from form drag around particles, where smaller media have more particles and higher inertial losses. The Forchheimer extension locally decreases the pressure drop within the momentum equation in the presence of non-Darcy flows. The Forchheimer extension has been tested and validated experimentally [Macini et al., 2011; Sobieski and Trykozko, 2011] and computationally [Ahmadi et al., 2010; Papathanasiou et al., 2001; Thauvin and Mohanty, 1998]. The success of the Forchheimer extension in characterizing non-Darcy flow is dependent on β . There exists a wide

range of equations proposed for calculating the β , which makes selection often case-dependent [Sobieski and Trykozko, 2011; Thauvin and Mohanty, 1998].

β has been empirically calculated under a variety of conditions and can depend on permeability, pore structure, porosity, and tortuosity [Li and Engler, 2001; Macini et al., 2011; Sobieski and Trykozko, 2011]. We calculated β from the one of the commonly used approaches, the Ergun equation,

$$\beta = \frac{a}{b^{0.5} * k^{0.5} * n^{3/2}} \quad (5)$$

where n is the porosity, k is the permeability, specifically in cm^2 , $a=1.75$, and $b=150$ [Li and Engler, 2001; Nield and Bejan, 2006]. This equation is valid for flow through porous beds of spherical particles with a wide range of inertial resistances [Andersson, 2012].

We modeled surface water using the mass and momentum conservation equations (Eq. 1 and 2). We used Reynolds Averaging of the Navier-Stokes equations for turbulence modeling, and we achieved turbulence closure with the Shear Stress Transport (SST) model in ANSYS CFX. SST combines the $\kappa\text{-}\omega$ model in the near-wall region with the $\kappa\text{-}\epsilon$ model in the free stream [Menter, 1994]. A blending function is used to determine which model is active, making the SST model accurate and reliable for a wide range of flow conditions. Additionally, the SST model includes a formulated transport equation for intermittency, which can be used to trigger the regional transition of turbulence to and from laminar [ANSYS, 2011b; Menter et al., 2006]. We used intermittency to identify the porous media as a laminar flow region and checked this assumption with Re during post-processing (discussed later). We used the Volume of Fluid (VOF) method in ANSYS CFX to model the free surface boundary of surface water. In CFX, VOF computes the volume fraction of air and water in each cell utilizing a separate equation to modify μ and ρ based on the volume fraction of air and water [ANSYS, 2011a].

Hydraulics Model Calibration

Hydraulic conductivity (K) measured at the field site using falling head tests in the bed and floodplain ranged from $9.2 \cdot 10^{-4}$ to $1.8 \cdot 10^{-5}$ m/s, with a geometric mean K of $4.5 \cdot 10^{-5}$ m/s [Hester et al., 2009]. To calibrate, we first ran the hydraulics model multiple times with K ranging from 10^{-7} to 10^{-3} m/s and used ANSYS DesignXplorer to create a response surface (i.e., function with minimum root mean square error) with respect to K for the pressures at points 1-7. We next used a goal-driven optimization function in DesignXplorer to change (i.e., calibrate) K

until the modeled pressures at the 7 points on the response surface best matched that observed on average from June 8, 2007 through June 12, 2007 from *Hester et al.* Calibration points 1-6. The geometric mean of the calibrated values is $K=6.7 \cdot 10^{-5}$ m/s, which is close to the geometric mean of $4.5 \cdot 10^{-5}$ m/s observed by *Hester et al.* [2009]. After calibration, the hydraulics model was run to steady state for a range of sediment types (silt to gravel), with K 's from 10^{-7} to 10^{-2} m/s for both Darcy-only and Darcy-Forchheimer versions. We selected $K=10^{-2}$ m/s as the upper end-member case because it (along with even higher values) can be frequently found in previous field studies of naturally occurring sediments, laboratory flume studies, and modeling studies of hyporheic exchange (e.g., *Calver* [2001], *Hester and Doyle* [2008], *Sawyer et al.* [2011], *Packman et al.* [2004]).

We have summarized the modeling scenarios in Table A-1 to aid comprehension of our research design and methods.

Table A-1. Summary of modeling scenarios.

| | Hydraulics Model | Temperature Dynamics Model |
|---------------------|--|--|
| Domains | Surface water and groundwater | Groundwater |
| Timescale | Steady state during summer baseflow | Transient - 4 days during summer baseflow |
| Equations | Hydraulics: Navier-Stokes with linear (Darcian) and quadratic (non-Darcian) momentum losses in media | Hydraulics: Navier-Stokes with linear (Darcian) momentum losses in media Temperature: Heat transport in water and sediment [ANSYS, 2011a] |
| Boundary Conditions | Hydraulics: Observed surface water flow rate, groundwater levels | Hydraulics: Bed pressures from hydraulics model, observed groundwater levels. Temperature: Observed stream and subsurface temperatures |
| K 's tested (m/s) | $10^{-7}, 10^{-6}, 10^{-5}, 10^{-4}, 10^{-3}, 10^{-2}$ | $10^{-7}, 10^{-6}, 10^{-5}, 10^{-4}, 10^{-3}$ |
| Calibration | Observed hyporheic pressures | Observed hyporheic temperatures |

Hydraulics Model Results: Hyporheic Flow Cell

Figure A-1 shows flow directions and paths for the Darcy flow model for $K=1 \cdot 10^{-5}$ m/s. A hyporheic flow cell is visible with surface water downwelling upstream of the weir and then upwelling on the downstream side of the weir. Down-valley background groundwater head gradients produced flow diagonally across the 3D domain (arrowheads in Figure A-1). This

caused the upwelling hyporheic flow paths to be deflected, with some longer/deeper downwelling flow paths originating from surface water far upstream of the weir to exit through the GW Left/GW DS outlets instead of returning to the channel. In other words, this section of stream, in addition to being hydrologically gaining, was also somewhat hydrologically flow-through.

We delineated the hyporheic flow cell by filtering hyporheic flow paths during post processing for a range of K (Figure A-1 shows basecase). Flow paths 0.01 m into the subsurface are ~0.05 m long whereas flow paths 0.5 m deeper are ~2.0 m long (i.e. ~40 times longer, Figure A-2). As K increased from 10^{-7} to 10^{-2} m/s, the length of the hyporheic flow cell longitudinally along the channel decreased from 2.02 to 1.63 m and its depth into the channel bed decreased from 0.83 to 0.62 m. Similarly, the mean hyporheic flow path length decreased from 1.50 to 1.08 m over this range of K . A threshold exists at $K=10^{-3}$ m/s, above which the most significant decreases in hyporheic zone geometry and flow path lengths occur. The mean residence time, calculated from averaging along all hyporheic flow paths in the post-processor, decreased from 14500 to 0.115 hrs as K increased from 10^{-7} to 10^{-2} m/s. Mean residence time and hyporheic discharge exhibited countervailing trends. As K increased, residence times decreased and hyporheic flow rates increased through the entire flow cell.

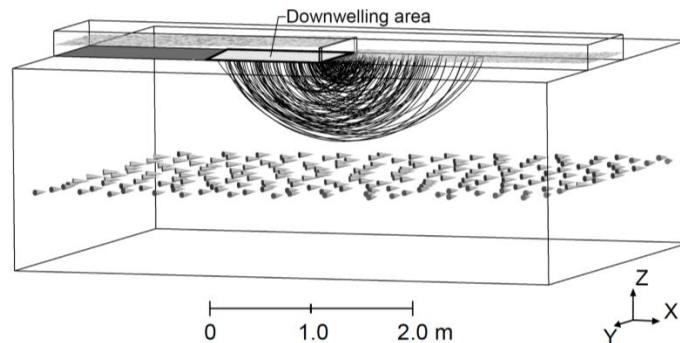


Figure A-1. Hyporheic flow cell and groundwater flow directions for Darcy-only model for the basecase. Flow paths shown originate from the downwelling area, which extends upstream of the weir and spans the width of the channel (light gray). Water surface is shown as transparent gray. Groundwater vector field is located on a profile 1.25 m below the sediment interface. Channel flow is from left to right.

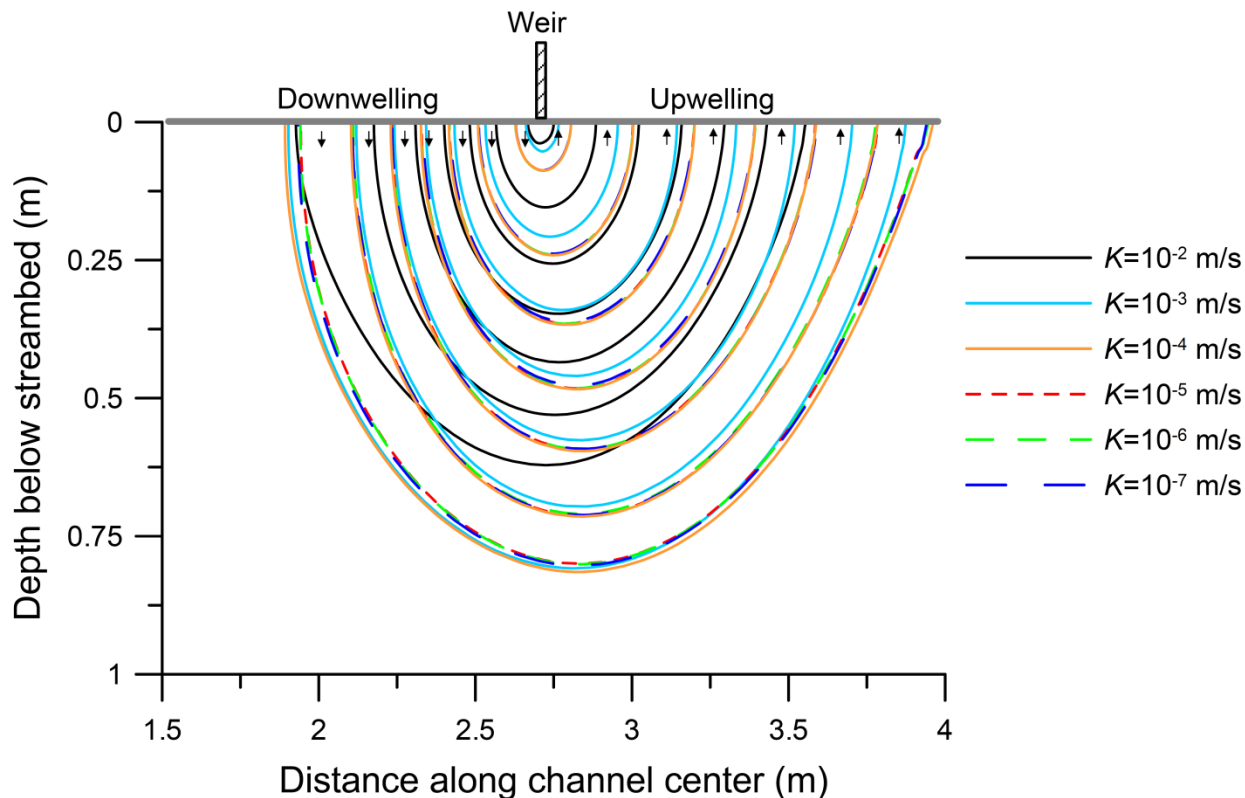


Figure A-2. Flow paths originating from downwelling area upstream of the weir for a range of K . Channel flow is from left to right. The sediment interface is at 0 m.

Hydraulics Model Results: Velocity Vector Fields

Vector fields on a vertical profile along the channel center are shown for the basecase (i.e., $K=6.7 \cdot 10^{-5}$ m/s) in Figure A-3 (left). Surface water flows exhibited velocities orders of magnitude higher than those in groundwater. For example, basecase surface velocities were 2 to 6 orders of magnitude higher than groundwater. The fastest surface velocities were water falling over the weir and near the free surface, with velocity stratification visible, particularly upstream of the weir (Figure A-3, left). Turbulent eddies can be seen in Figure A-3 just upstream of the weir in the surface water. The fastest groundwater velocities were directly beneath the weir, where the highest head gradients occurred. Nevertheless, even these high groundwater velocities were lower than most surface water velocities. As K increased, the discrepancy between surface water and groundwater diminished (Figure A-3, right).

Similar vector fields for K ranging from 10^{-2} to 10^{-7} m/s are summarized in Figure A-4. Groundwater velocities were taken directly under the weir at 0.01 m depth ($V_{-0.01m}$ in Figure A-

3) and 0.5 m depth ($V_{-0.5m}$ in Figure A-3), corresponding to shallow and deeper hyporheic flow. Surface water velocities (V_{sw} in Figure A-3) were averaged between 0.25 m upstream and downstream of the weir at 60% depth (average in log-law velocity profile). Over the range of K , $V_{-0.01m}$ was roughly 27 times higher than $V_{-0.5m}$. As K was increased, $V_{-0.01m}$ approached V_{sw} , exceeding it by 71.6% for $K=10^{-2}$ m/s. When a nappe was present ($K \leq 10^{-2}$ m/s), velocities there exceeded all other locations by several orders of magnitude.

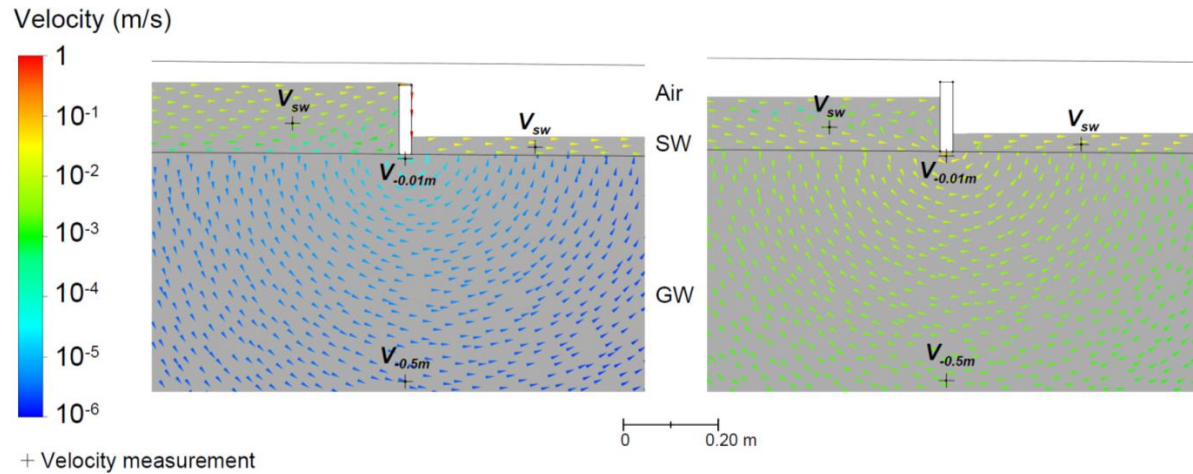


Figure A-3. Velocity vector fields on vertical profile along channel center. The left panel is the basecase, $K=6.7 \cdot 10^{-5}$ m/s. The right panel is $K=10^{-2}$ m/s. Groundwater domain of figure is cropped.

Hydraulics Model Results: Non-Darcy Flows and Criteria

We also calculated Fo for a vertical profile along the center of the groundwater domain for $K=10^{-2}$ to 10^{-4} m/s. Existing literature suggests the onset of non-Darcy flow is when $Fo > 0.005$ to 0.2 [Zeng and Grigg, 2006]. We utilized a threshold at the center of this range ($Fo=0.01$). Results of the Fo analysis (not shown) were very similar to Re analysis results, but indicated less area of non-Darcy flow, likely because of the slightly more stringent requirement for non-Darcy flow. For $K=10^{-3}$ m/s, Fo numbers exceeded 0.01 near the weir, roughly 0.05 m in the downstream direction and 0.03 m deep. For $K=10^{-2}$ m/s, Fo numbers were above 0.01 for a larger portion of the hyporheic zone, extending roughly 0.80 m in the downstream direction and 0.40 m into the bed. Ultimately, the same conclusions about the spatial occurrence of non-Darcy flow can be reached from Re analysis as by Fo analysis.

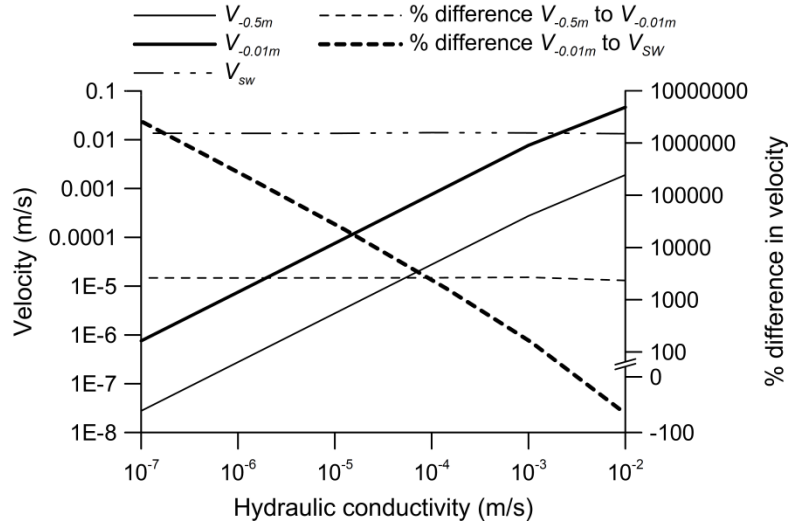


Figure A-4. Velocities near the weir versus K . Groundwater velocities are from 0.01 m ($V_{-0.01m}$) and 1 m (V_{-1m}) beneath the weir (Figure A-3). Surface water velocities (V_{sw}) are an average of two locations (one upstream and one downstream of the weir), each at 0.6 times the surface depth (Figure A-3).

We determined the effect (i.e., “value added”) of simulating of non-Darcy flow by calculating groundwater velocity differentials between the Darcy and Darcy-Forchheimer models. This difference is greatest at highest K , thus we plotted contours of this difference for $K=10^{-2}$ and 10^{-3} m/s for a longitudinal vertical section of the groundwater domain (Figure A-5). The maximum difference between the Darcy and Darcy-Forchheimer model was 0.0256 m/s and 0.00058 m/s for $K=10^{-2}$ and 10^{-3} m/s, respectively, and occurred directly under the weir where the hydraulic gradient was strongest. In relative terms, the Darcy-Forchheimer velocities at this location were 32.7% and 4.37% less than Darcy. Average velocity differences within the hyporheic flow cell were smaller than right by the weir at $5.01 \cdot 10^{-4}$ m/s and $5.38 \cdot 10^{-6}$ m/s for $K=10^{-2}$ and 10^{-3} m/s, respectively. This corresponded to Darcy-Forchheimer velocities 5.83% and 0.40% less than Darcy, respectively. As depth below the weir increased, the flow models approached the same velocities. We also calculated hyporheic bed fluxes along the channel centerline (from hydraulic gradient and K) for varying K . Hyporheic fluxes increased with both K and proximity to the weir (highest i), similar to Re and velocity differences (Figure A-5).

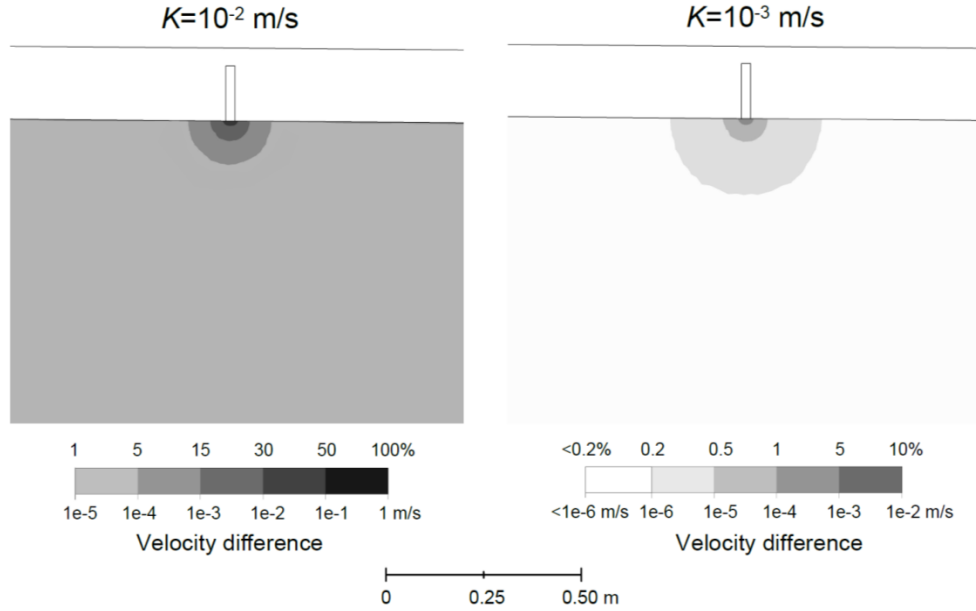


Figure A-5. Differences in groundwater velocities calculated by Darcy and Darcy-Forchheimer (Ergun) models for $K=10^{-2}$ m/s (left) and $K=10^{-3}$ m/s (right) for a vertical profile aligned with channel center. K 's below 10^{-3} m/s show no difference between the two models. Velocity scales are different for left and right panels. Groundwater domain of figure is cropped.

We calculated the particle Reynolds number (Re_p) within the groundwater domain over a vertical profile along the channel centerline as

$$Re_p = \frac{\rho D_p v}{\mu} \quad (7)$$

where D_p is the characteristic length taken to be the mean pore diameter (m). For our analyses of Darcy versus non-Darcy flow, we applied commonly used Re cutoffs (e.g., from $1 < Re < 100$ flow is non-Darcian [Freeze and Cherry, 1979]). While some of our modeled scenarios contained non-Darcy flow (see Results), none contained turbulent flow in the groundwater domain as determined by Re always < 100 . This validated the intermittency portion of our turbulence model (i.e., subsurface was laminar) discussed earlier. As another criterion for the presence of non-Darcy flow, we similarly calculated the Forchheimer Number (Fo) as

$$Fo = \frac{k\beta\rho v}{\mu} \quad (8)$$

where Fo is a form of Re_p in which the characteristic length has been changed from D_p to $k\beta$ [Zeng and Grigg, 2006]. The empirical formula of Sichardt [1928] relates the K to a maximum

Darcian velocity. *Sichardt* [1928] is commonly applied to the hydraulics of pumping wells [Beek, 2012] and the equation still can be used to calculate critical values of i at the non-Darcy threshold. The equation used is,

$$v_{md} = \frac{1}{15} * \sqrt{K} \quad (9)$$

where v_{md} is the maximum Darcy velocity and is the product of critical i and K .

These results can be summarized in a plot of K versus i (Figure A-6, panel A) which shows three different thresholds for non-Darcy flow (Re , Fo , and *Sichardt's* formula) based on observed model values. We include i 's up to 10 m/m, so that readers can compare our results to a wide range of conditions. The *Sichardt* [1928] formula is the most stringent, followed by Fo and then Re , which predict increasing parameter space of non-Darcy flow.

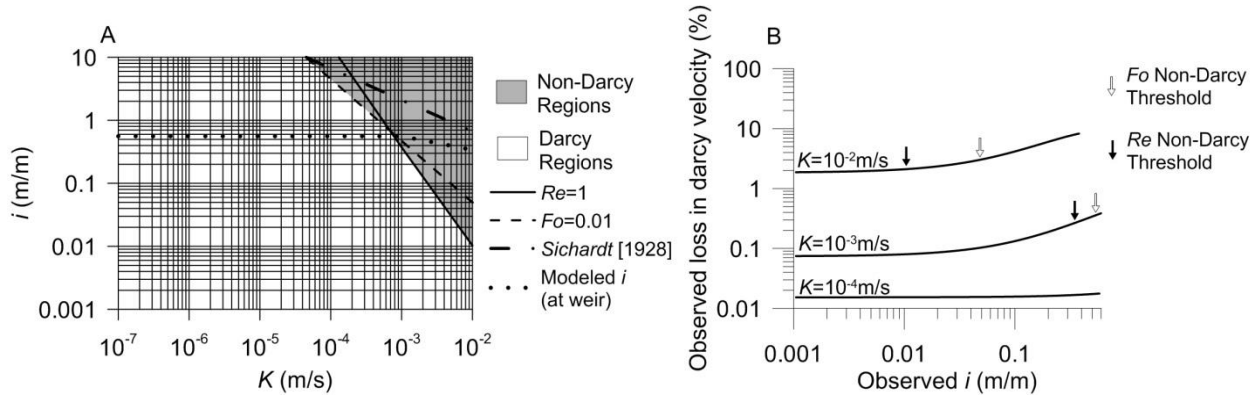


Figure A-6. Panel A shows criteria based thresholds of non-Darcy flow according to Re , Fo , and the empirical formula of *Sichardt* [1928]. Over 3000 locations with unique combinations of K and i were tested over the range shown (i.e., 1 combination is a data point). Plotted lines represent K and i combinations that equal non-Darcy threshold criteria. Dotted line shows the modeled i at the weir. Panel B shows differences in groundwater velocities calculated by Darcy and Darcy-Forchheimer (Ergun) models for $K=10^{-2}$ m/s (left) and $K=10^{-3}$ m/s (right) for 10 cm within the bed along channel center. Hydraulic gradients are shown as absolute values.

In this study we explored the applicability of several threshold criteria in predicting non-Darcy flow, including Re , Fo , and the empirical formula by *Sichardt* [1928]. We evaluated these criteria based on the allowed percent decrease in Darcy velocity before being considered non-Darcy. For example, for $K=10^{-2}$ m/s Re , Fo , and *Sichardt* [1928] predict non-Darcy flow at i 's of

0.01, 0.05, and 0.68 m/m, respectively. These thresholds for Re and Fo correspond to percent decreases in Darcy velocity of 2.05 and 3.05. For $K=10^{-3}$ m/s, Re and Fo criteria predict the onset of non-Darcy flow at about 0.3% decrease in Darcy velocity. For both $K=10^{-2}$ and 10^{-3} m/s, according to *Sichardt* [1928], the onset of non-Darcy flow was at a threshold beyond any K and i combination that we model. We can extrapolate our data (Figure A-6, panel B) to predict non-Darcy flow using *Sichardt* [1928], and find the thresholds at 8.81% and 0.42% loss in Darcy velocity for 10^{-2} m/s and 10^{-3} m/s, respectively. We therefore conclude that for $K>10^{-3}$ m/s, *Sichardt* [1928] inadequately predicts the onset of non-Darcy flows in comparison to Re or Fo . The selection of threshold criteria to indicate when non-Darcy flow is important would depend on the particular application and acceptable levels of error. Re is the best criterion to most conservatively predict the onset of non-Darcy flow, and therefore when inertial losses decrease subsurface transport rates. For instance, using Re as a criterion may be necessary as a conservative estimate of determining down-gradient transport when analyzing subsurface transport of volatile organic compounds.

Hydraulics Model Results: Hyporheic Flow Rate

Percent hyporheic flow (Q_h) increased with K until the stream became completely hyporheic (i.e. no flow over the weir, Figure A-7). Q_h was 1% at $K=6.2\cdot 10^{-5}$ m/s and 100% at $K=8.0\cdot 10^{-3}$ m/s. The effects of inertial losses associated with non-Darcy flow on Q_h were negligible (i.e. strictly Darcy flow) below $K=10^{-3}$ m/s and caused an increasing deviation from Darcy's Law above $K=10^{-3}$ m/s. At $K=2.5\cdot 10^{-3}$ m/s, the Darcy and Darcy-Forchheimer models predicted 39.8% and 37.7% hyporheic flow, respectively, indicating 5.3% less flow predicted by the Darcy-Forchheimer model. At $K=5\cdot 10^{-3}$ m/s, Darcy and Darcy-Forchheimer models predicted 79.6% and 69.6% hyporheic flow, respectively, indicating 12.6% less flow predicted by the Darcy-Forchheimer model.

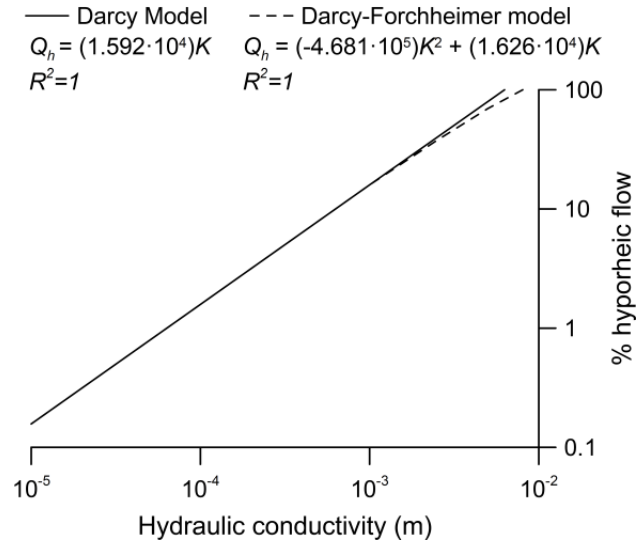


Figure A-7. Percent hyporheic flow versus K from Darcy and Darcy-Forchheimer models. The Darcy-Forchheimer model fit (dashed line) applies to $K \geq 10^{-3}$ m/s. For $K < 10^{-3}$ m/s, the Darcy model fit (solid line) applies to both Darcy and Darcy-Forchheimer flow.

Hydraulics Model Results: Sweetspot Concept and Broader Impacts

We propose the “hyporheic sweetspot concept”, where an intermediate K may exist that maximizes hyporheic zone functions and net effects of exchange (Figure A-8). Whether a sweetspot exists for a particular hyporheic function, and where along the K axis it exists, would depend on the nature of the relationship between the function (e.g., reaction rate) and residence time. Sweetspots would therefore likely be function or compound specific. The potential presence of hyporheic zone sweetspots has been suggested by previous studies, for example, a maximum denitrification potential was identified in marine sediments for high nitrate conditions and intermediate K [Cardenas *et al.*, 2008b], and similarly by the importance of both solute fluxes and residence times in determining denitrification in dune stream beds [Bardini *et al.*, 2012], but to our knowledge the balance between residence times and hyporheic flow rates has not been explored. Individual sweetspots may be influenced by flow conditions, channel geometry, and K heterogeneity. In some cases, hyporheic zone functions will be only limited by hyporheic flow rate, meaning that benefits would be maximized by maximizing flow rate, and a sweetspot will not exist. Biological studies suggest that sweetspots exist for water quality aspects of hyporheic habitat. The composition of hyporheic ecology is dependent on both flow rates and residence times, which influence interstitial velocities, organic matter content,

dissolved oxygen concentration, and temperature [Boulton, 2007; Doleolivier and Marmonier, 1992; Strayer *et al.*, 1997]. For example, fish embryos prefer cooler upwelling water that is not fully de-oxygenated but still nutrient laden [Baxter and Hauer, 2000; Curry and Noakes, 1995; Nielsen *et al.*, 1994].

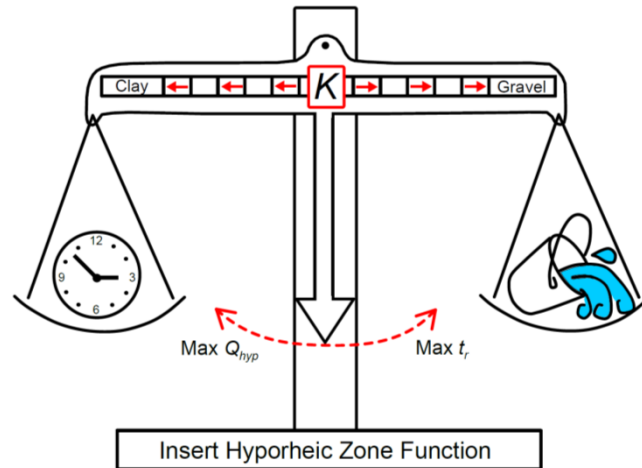


Figure A-8. Sweetspot concept for hyporheic zone functions. Hyporheic residence times (t_r , clock) and hyporheic flow rate (Q_{hyp} , water bucket) exhibit countervailing trends as K is varied. K acts as a weight in the center of the balance that is moved to the left or right depending on the sediment type.

Weirs promote heterogeneous subsurface flow path lengths and velocities, creating a range of hyporheic residence times. Deeper flow paths have slower velocities, longer lengths, and larger residence times compared to shallower paths (Figure A-3), with successive flow paths potentially having unique physiochemical properties and function (e.g., rates of biogeochemical reactions or microbial activity). For example, buffering and lagging from weir-induced hyporheic exchange may occur along deep flow paths with high residence time but not shallow flow paths with low residence time [Sawyer *et al.*, 2012]. As a result, the hyporheic flow cell should be considered as a series of streamtubes (as in Figure A-2) layered on top of each other, or as layers of an onion in three dimensions, each with different velocities and residence times. While the majority of hyporheic velocities observed in the subsurface were low compared to surface stream velocities (Figure A-3), flow paths directly under the weir in some cases reached the same order of magnitude as surface flow (Figure A-3, $K > 10^{-3}$ m/s). This suggests that the hyporheic sweetspot concept discussed earlier can be applied at the scale of individual flow paths

within the hyporheic zone. Particular hyporheic zone functions may occur along one flow path but not in an adjacent flow path because of differences in hyporheic velocities or residence times. The diversity of hyporheic flow paths enhances the chances that a sweetspot exists somewhere within a given flow cell. This agrees with previous research that found the presence of denitrification to be highly heterogeneous in the hyporheic zone and dependent on residence times [Bardini *et al.*, 2012; Marzadri *et al.*, 2011; Pinay *et al.*, 2009; Zarnetske *et al.*, 2011; Zarnetske *et al.*, 2012].

The results of this study have several implications for stream restoration. We proposed the existence of hyporheic function sweetspots, in which a particular K balances t_r and Q_{hyp} such that a hyporheic function is maximized. Stream planners or restoration designers can apply this concept to target and promote particular functions. This can be accomplished by placing structures at locations where the sweetspot K exists, or by changing K . Additionally, multiple structures may be placed so that hyporheic flow rates and hyporheic functions are additive. Structure sequencing will linearly increase cumulative hyporheic flow rates per relationships such as equations 11 and 12. By contrast, structure-sequencing impact on water quality is not likely to be linear because downstream conditions may offset hyporheic functions (e.g., ambient temperatures, dilution, contaminant reintroduction). More research is needed to characterize whether and where hyporheic sweetspots occur for various water quality functions.

REFERENCES

- Ahmadi, A., A. Arani, and D. Lasseux (2010), Numerical simulation of two-phase inertial flow in heterogeneous porous media, *Transport Porous Med*, 84(1), 177-200.
- Andersson, B. (2012), *Computational Fluid Dynamics for Engineers*, xi, 189 p. pp., Cambridge University Press, Cambridge ; New York.
- ANSYS, Inc. (2011a), Ansys CFX-Solver Theory Guide, edited, ANSYS, Inc., PA.
- ANSYS, Inc. (2011b), Ansys CFX-Solver Modeling Guide, edited, ANSYS, Inc., PA.
- Bardini, L., F. Boano, M. B. Cardenas, R. Revelli, and L. Ridolfi (2012), Nutrient cycling in bedform induced hyporheic zones, *Geochim Cosmochim Ac*, 84, 47-61.
- Baxter, C. V., and F. R. Hauer (2000), Geomorphology, hyporheic exchange, and selection of spawning habitat by bull trout (*Salvelinus confluentus*), *Can J Fish Aquat Sci*, 57(7), 1470-1481.

- Beek, C. G. (2012), *Cause and prevention of clogging of wells abstracting groundwater from unconsolidated aquifers*, xiv, 153 p., IWA, London.
- Boulton, A. J. (2007), Hyporheic rehabilitation in rivers: restoring vertical connectivity, *Freshwater Biol*, 52(4), 632-650.
- Calver, A. (2001), Riverbed permeabilities: Information from pooled data, *Ground Water*, 39(4), 546-553.
- Cardenas, M. B., and J. L. Wilson (2006), The influence of ambient groundwater discharge on exchange zones induced by current-bedform interactions, *J Hydrol*, 331(1-2), 103-109.
- Cardenas, M. B., and J. L. Wilson (2007a), Thermal regime of dune-covered sediments under gaining and losing water bodies, *J Geophys Res-Biogeophys*, 112, G04013.
- Cardenas, M. B., and J. L. Wilson (2007c), Effects of current-bed form induced fluid flow on the thermal regime of sediments, *Water Resour Res*, 43, W08431.
- Cardenas, M. B., and J. L. Wilson (2007c), Exchange across a sediment-water interface with ambient groundwater discharge, *J Hydrol*, 346(3-4), 69-80.
- Cardenas, M. B., and J. L. Wilson (2007b), Dunes, turbulent eddies, and interfacial exchange with permeable sediments, *Water Resour Res*, 43, W08412.
- Cardenas, M. B., J. L. Wilson, and R. Haggerty (2008a), Residence time of bedform-driven hyporheic exchange, *Adv Water Resour*, 31(10), 1382-1386.
- Cardenas, M. B., P. L. M. Cook, H. S. Jiang, and P. Traykovski (2008b), Constraining denitrification in permeable wave-influenced marine sediment using linked hydrodynamic and biogeochemical modeling, *Earth Planet Sc Lett*, 275(1-2), 127-137.
- Cheng, N. S., Z. Y. Hao, and S. K. Tan (2008), Comparison of quadratic and power law for nonlinear flow through porous media, *Exp Therm Fluid Sci*, 32(8), 1538-1547.
- Crispell, J. K., and T. A. Endreny (2009), Hyporheic exchange flow around constructed in channel structures and implications for restoration design, *Hydrol Process*, 23(8), 1158-1168.
- Curry, R. A., and D. L. G. Noakes (1995), Groundwater and the Selection of Spawning Sites by Brook Trout (*Salvelinus-Fontinalis*), *Can J Fish Aquat Sci*, 52(8), 1733-1740.
- Doleolivier, M. J., and P. Marmonier (1992), Patch Distribution of Interstitial Communities-Prevailing Factors, *Freshwater Biol*, 27(2), 177-191.

- Endreny, T., L. Lautz, and D. Siegel (2011a), Hyporheic flow path response to hydraulic jumps at river steps: Hydrostatic model simulations, *Water Resour Res*, 47, W02518.
- Endreny, T., L. Lautz, and D. I. Siegel (2011b), Hyporheic flow path response to hydraulic jumps at river steps: Flume and hydrodynamic models, *Water Resour Res*, 47, W02517.
- Freeze, R. A., and J. A. Cherry (1979), *Groundwater*. Englewood Cliffs, N.J., Prentice-Hall.
- Hester, E. T., and M. W. Doyle (2008), In-stream geomorphic structures as drivers of hyporheic exchange, *Water Resour Res*, 44, W03417.
- Hester, E. T., M. W. Doyle, and G. C. Poole (2009), The influence of in-stream structures on summer water temperatures via induced hyporheic exchange, *Limnol Oceanogr*, 54(1), 355-367.
- Li, D., and T. Engler (2001), Literature Review on Correlations of the Non-Darcy Coefficient, paper presented at SPE Permian Basin Oil and Gas Recovery Conference, Society of Petroleum Engineers, Midland, Texas, 15-17 May 2001.
- Macini, P., E. Mesini, and R. Viola (2011), Laboratory measurements of non-Darcy flow coefficients in natural and artificial unconsolidated porous media, *J Petrol Sci Eng*, 77(3-4), 365-374.
- Marzadri, A., D. Tonina, and A. Bellin (2011), A semianalytical three-dimensional process based model for hyporheic nitrogen dynamics in gravel bed rivers, *Water Resour Res*, 47.
- Menter, F. R. (1994), 2-Equation Eddy-Viscosity Turbulence Models for Engineering Applications, *Aiaa J*, 32(8), 1598-1605.
- Menter, F. R., R. Langtry, and S. Volker (2006), Transition modelling for general purpose CFD codes, *Flow Turbul Combust*, 77(1-4), 277-303.
- Nield, D. A., and A. Bejan (2006), *Convection in porous media*. Springer, New York.
- Nielsen, J. L., T. E. Lisle, and V. Ozaki (1994), Thermally stratified pools and their use by steelhead in northern California streams, *T Am Fish Soc*, 123(4), 613-626.
- Packman, A. I., M. Salehin, and M. Zaramella (2004), Hyporheic Exchange with Gravel Beds: Basic Hydrodynamic Interactions and Bedform-Induced Advective Flows, *Journal of Hydraulic Engineering*, 130(7), 647-656.
- Papathanasiou, T. D., B. Markicevic, and E. D. Dendy (2001), A computational evaluation of the Ergun and Forchheimer equations for fibrous porous media, *Phys Fluids*, 13(10), 2795-2804.

- Pinay, G., T. C. O'Keefe, R. T. Edwards, and R. J. Naiman (2009), Nitrate removal in the hyporheic zone of a salmon river in Alaska, *River Res Appl*, 25(4), 367-375.
- Sawyer, A. H., M. B. Cardenas, and J. Buttles (2011), Hyporheic exchange due to channel-spanning logs, *Water Resour Res*, 47, W08502.
- Sawyer, A. H., M. B. Cardenas, and J. Buttles (2012), Hyporheic temperature dynamics and heat exchange near channel-spanning logs, *Water Resour Res*, 48, W01529.
- Shen, Y., and P. Diplas (2008), Application of two- and three-dimensional computational fluid dynamics models to complex ecological stream flows, *J Hydrol*, 348(1-2), 195-214.
- Sichardt, W. (1928), *Das Fassungsvermögen Von Rohrbrunnen und Seine Bedeutung Für Die Grundwasser-absenkung Insbesondere Für Grössere Absenkungstiefen*, Springer, Dordrecht, The Netherlands.
- Sobieski, W., and A. Trykozko (2011), Sensitivity Aspects of Forchheimer's Approximation, *Transport Porous Med*, 89(2), 155-164.
- Spanoudaki, K., A. I. Stamou, and A. Nanou-Giannarou (2009), Development and verification of a 3-D integrated surface water-groundwater model, *J Hydrol*, 375(3-4), 410-427.
- Strayer, D. L., S. E. May, P. Nielsen, W. Wollheim, and S. Hausam (1997), Oxygen, organic matter, and sediment granulometry as controls on hyporheic animal communities, *Arch Hydrobiol*, 140(1), 131-144.
- Thauvin, F., and K. K. Mohanty (1998), Network modeling of non-Darcy flow through porous media, *Transport Porous Med*, 31(1), 19-37.
- Wendt, J. F. (2008), *Computational Fluid Dynamics: An Introduction*, Springer, Dordrecht, The Netherlands.
- Zarnetske, J. P., R. Haggerty, S. M. Wondzell, and M. A. Baker (2011), Dynamics of nitrate production and removal as a function of residence time in the hyporheic zone, *J Geophys Res-Bioge*, 116.
- Zarnetske, J. P., R. Haggerty, S. M. Wondzell, V. A. Bokil, and R. Gonzalez-Pinzon (2012), Coupled transport and reaction kinetics control the nitrate source-sink function of hyporheic zones, *Water Resour Res*, 48, W11508.
- Zeng, Z. W., and R. Grigg (2006), A criterion for non-Darcy flow in porous media, *Transport Porous Med*, 63(1), 57-69.

APPENDIX B: *Supplementary Material to the Temperature Model in Chapter 2*

Temperature Dynamics Model: Background and Governing Equations

Because the flow of water was rapid for some (i.e., high K) model runs, we used the NLTE heat transport model in ANSYS CFX. The NLTE model uses two separate heat transport equations, Eq. 1 for the fluid (i.e., water), and Eq. 2 for the solid (i.e., sediment).

$$\begin{aligned} \frac{\partial}{\partial t}(n\rho_f E_f) + \nabla \cdot \mathbf{v}(\rho_f E_f + P) \\ = \nabla \cdot \left(n\lambda_f \nabla T_f - \left(\sum_i h_i J_i \right) + (\bar{\tau} \cdot \mathbf{v}) \right) + h \frac{da_{fs}}{dV_f} (T_s - T_f) + S_f^h \end{aligned} \quad (1)$$

$$\frac{\partial(\rho_s C_s T_s)}{\partial t} = \nabla \cdot [\lambda_s \cdot \nabla T_s] - h \frac{da_{fs}}{dV_s} (T_s - T_f) \quad (2)$$

In all equations, subscript f refers to the fluid (i.e., water), s refers to the solid (i.e., sediment). C is the specific heat capacity (j/kg \cdot °C), h is the heat transfer coefficient (w/m 2 \cdot °C), V is the volume (m 3), T is the temperature (°C), E is total energy (j), λ is the thermal conductivity (w/m \cdot °C), n is the porosity, J is the heat flux (j/s). Porosity was set to 0.3. Density and viscosities of water were held constant [Sawyer *et al.*, 2012].

The interfacial area density (a_{fs}) between the water and sediment phases (1/m) and h are used to calculate heat transfer between pore water and sediment grains [ANSYS, 2011a; Nield and Bejan, 2006; Vafai, 2005]. Formulations have been proposed by Dixon and Cresswell [1979] and are shown in Nield and Bejan [2006] as,

$$h = a_{fs} h^* \quad (3)$$

where h^* (w/m \cdot °C) relates the interfacial area density to the heat transfer coefficient and,

$$a_{fs} = \frac{6(1-n)}{d_p} \quad (4)$$

where d_p is the particle diameter (m). a_{fs} is based upon the volume fraction of water and sediment and sediment diameter. h^* can be computed,

$$\frac{1}{h^*} = \frac{d_p}{Nu_{fs}\lambda_f} + \frac{d_p}{B\lambda_s} \quad (5)$$

where Nu_{fs} is the Nusselt number between the fluid and solid phases, λ is the thermal conductivity for the fluid (λ_f) and solid (λ_s) phases, $B=10$ for spherical particles. The Nusselt number is a ratio of convective to conductive heat transport. For low values of Re_p (i.e., $Re_p < 100$) Nu_{fs} is in the range of 0.1 to 12.4 [Miyauchi *et al.*, 1976; Nield and Bejan, 2006; Wakao *et al.*, 1976; Wakao *et al.*, 1979]. For laminar flow past a spherical particle, the Nu_{fs} is suggested as 2 [ANSYS, 2011a]. Because the hydraulics model showed that flow throughout the porous media is laminar for the range of K 's modeled in the current study (i.e., $K=10^{-3}$ to 10^{-7} m/s), the assumption of $Nu=2$ for the NLTE model is valid. Comparatively, the LTE model combines Eqs. 1 and 2 into a single equation with effective thermal properties (i.e., thermal conductivity) between the sediment and water.

Temperature Dynamics Model: Calibration

Our calibration (Table B-1) and subsequent thermal analyses were therefore confined to the final 96 hours, or 0:00 June 9, 2007 through 0:00 June 13, 2007. We calibrated the model to observed temperatures in wells at 19 hyporheic zone locations in Hester *et al.* [2009]. The columns of calibration points 1-18 are spaced on average 0.5 m longitudinally near channel center. The shallowest calibration points are located on average 0.15 m below the top of the sediment, with vertical spacing of 0.15 to 0.25 m beneath that. Point 19 was offset 1 m to the right of the stream center, 0.6 m below the channel bed.

Table B-1. Calibration of K to hyporheic temperatures. Observed values from Hester *et al.* [2009].

| Groundwater flow model | Calibrated K (m/s) | <i>Hester et al.</i> [2009] | |
|------------------------------------|----------------------|-----------------------------|---------------------|
| | | Observed | K (m/s) |
| 16:00 on 6-10-2007 | $4.0 \cdot 10^{-5}$ | Min | $1.4 \cdot 10^{-5}$ |
| 7:00 on 6-11-2007 | $2.1 \cdot 10^{-5}$ | Max | $7.6 \cdot 10^{-4}$ |
| 0:00 on 6-12-2007 | $2.8 \cdot 10^{-5}$ | Geometric Mean | $4.5 \cdot 10^{-5}$ |
| Geometric mean (Modeling basecase) | $2.9 \cdot 10^{-5}$ | | |

We used goal-driven least-squares optimization for K (Table B-1) until the modeled temperature at the 19 points best matched that observed from Hester *et al.* [2009]. Calibration was done separately at three different times, including 16:00 on June 10, 2007, 7:00 on June 11,

2006, and 0:00 on June 12, 2012, corresponding to the afternoon, morning, and midnight on three consecutive days. We used the geometric mean K of the calibrated values ($2.9 \cdot 10^{-5}$ m/s) as the basecase for heat transport modeling, which is the same order magnitude as the geometric mean ($4.5 \cdot 10^{-5}$ m/s) observed by *Hester et al.* [2009].

Temperature Dynamics Model: Thermal Dispersion

Hydrodynamic dispersion, including mechanical dispersion, can affect heat transfer within the hyporheic zone and is important relative to conduction when the thermal-mechanical Peclet number (Pe_T) is 0.1 or greater [*Cardenas and Wilson, 2007b*]. We calculated Pe_T as,

$$Pe_T = Re \cdot Pr = \frac{nvlc_w}{\lambda_{fs}} \quad (6)$$

where l is the length scale, taken to be the longitudinal dispersivity and set to 0.01 m [*Cardenas and Wilson, 2007b*].

Pe_T was calculated via Eq. 6 for the highest K model (10^{-3} m/s) to determine if mechanical dispersion was important to heat transport in the models. Figure B-1 shows Pe_T for a vertical profile along channel center in the groundwater domain. For $K=10^{-3}$ m/s, the maximum Pe_T was $2.6 \cdot 10^{-2}$ and is localized in a region < 5 cm beneath the weir. For $K=10^{-3}$ m/s, the average Pe_T was $9.6 \cdot 10^{-4}$ and is representative of the majority of the groundwater domain (Figure B-1). In our model, all Pe_T for the highest K were an order of magnitude or more below 0.1. As a result, mechanical dispersion was not explicitly included in the models (i.e., dispersivity was set to 0).

Temperature Dynamics Model: Non-Local Thermal Equilibrium

When there is rapid heat advection through porous media, local thermal equilibrium (LTE) may not be achieved between the water and sediment phases at the pore scale [*Haji-Sheikh and Minkowycz, 2008*]. In such a non-local thermal equilibrium (NLTE) case, water and sediment are at different temperatures, and the heat transport equation must be explicitly solved for both sediment and water. There are 3 conditions which can facilitate rapid heat advection and may require the use of NLTE in hyporheic zone temperature models: (1) rapid surface water temperature fluctuations, (2) high hydraulic gradients (e.g., caused by proximity to in-stream structures), and (3) high K . Condition 1 may potentially be caused by human impacts such as thermal temperature surge in urban environments [*Hester and Bauman, 2013; Nelson and*

Palmer, 2007]. Conditions 2 and 3 increase fluid velocities in the porous media, which previous research has shown requires an NLTE model [Amiri and Vafai, 1994; Vafai and Sozen, 1990]. Some studies have evaluated the effect of variations in K on hyporheic temperature dynamics [Cardenas and Wilson, 2007b; Sawyer et al., 2012]. However, we are unaware of studies that couple surface water-groundwater hydraulics with an NLTE energy model in order to test the limits of LTE applicability.

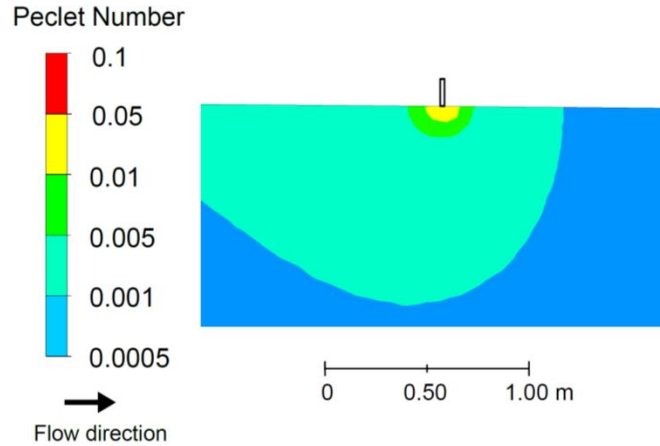


Figure B-1. Thermal Peclet number (Pe_T) contour map for $K=10^{-3}$ m/s for a vertical profile along channel center in the groundwater domain. The maximum Pe_T is $2.6 \cdot 10^{-2}$, located <5 cm beneath the weir. Most of the groundwater domain is a Pe_T value of $9.6 \cdot 10^{-4}$ (blue).

Groundwater domain is cropped.

We compared sediment and water temperatures between the NLTE model and LTE model results both spatially for $K=10^{-3}$ m/s (Figure B-2) and temporally for various K 's (Figure B-3). We chose 10^{-3} m/s because advection was greatest and therefore deviation from LTE would be greatest. For $K < 10^{-4}$ m/s, the temperature differences were mostly undetectable. Figure B-3 shows the temporal variation of the difference between water temperature and sediment temperature at point 6 (see Chapter 2 of dissertation) in the subsurface. Point 6 was selected to analyze downwelling temperatures instead of point E, because it is in the shallow subsurface rather than on the Upstream boundary. Downwelling water temperatures were warmer than sediment temperatures during the day and colder than sediment temperatures at night. The time of peak difference for downwelling temperatures appeared to shift later in the day as K decreased from 10^{-3} to 10^{-4} m/s. The maximum observed difference between the water and sediment temperatures was 0.000030°C for $K=10^{-3}$ m/s near the time of daily peak surface

water temperatures (6/10/07 at 12:00). Upwelling temperature differences showed similar trends to downwelling temperature differences, although they were not as widespread within upwelling flow cell.

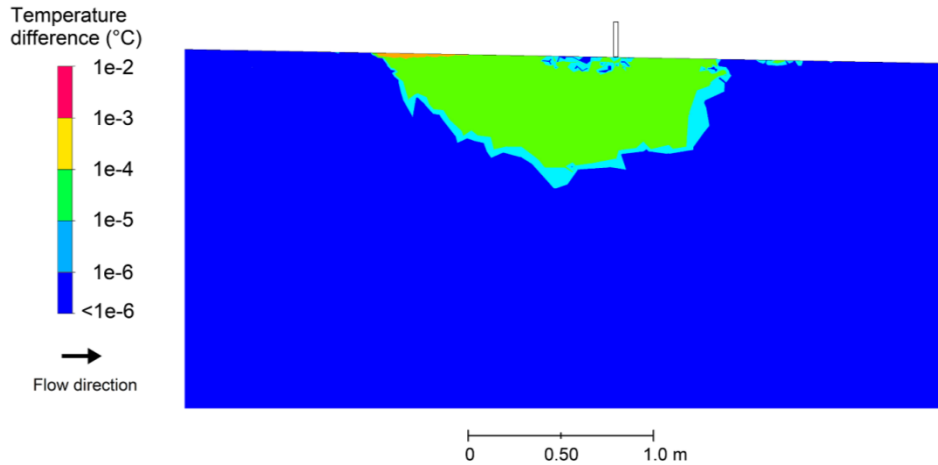


Figure B-2. Spatial distribution of temperature difference between water and sediment for vertical profile along channel center for $K=10^{-3}$ m/s on 6/10/07 at 11:00. Surface flow is from left to right with weir location shown.

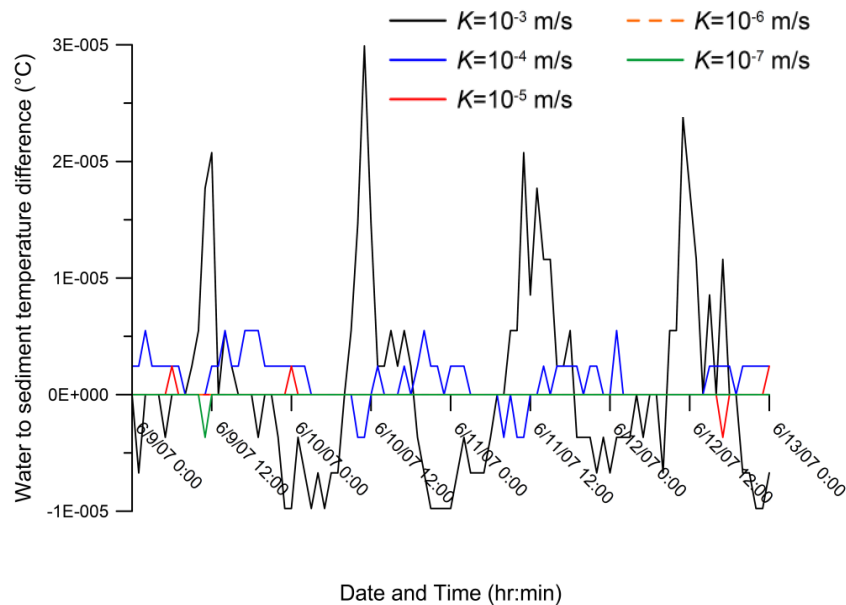


Figure B-3. Hourly temperature difference between water and sediment for the downwelling location (point 6) versus time. Positive values indicate pore water is warmer than sediment, and vice-versa.

REFERENCES

- Amiri, A., and K. Vafai (1994), Analysis of Dispersion Effects and Nonthermal Equilibrium, Non-Darcian, Variable Porosity Incompressible-Flow through Porous-Media, *Int J Heat Mass Tran*, 37(6), 939-954.
- ANSYS, Inc. (2011), Ansys CFX-Solver Theory Guide, ANSYS, Inc., PA.
- Cardenas, M. B., and J. L. Wilson (2007c), Effects of current-bed form induced fluid flow on the thermal regime of sediments, *Water Resour Res*, 43, W08431.
- Dixon, A. G., and D. L. Cresswell (1979), Theoretical prediction of effective heat-transfer parameters in packed-beds, *Aiche J*, 25(4), 663-676.
- Haji-Sheikh, A., and W. J. Minkowycz (2008), Heat transfer analysis under local thermal non-equilibrium conditions, *Emerging topics in Heat and Mass Transfer in Porous Media*, pp. 39-62, Springer Netherlands.
- Hester, E. T., and K. S. Bauman (2013), Stream and retention pond thermal response to heated summer runoff from urban impervious surfaces, *JAWRA J Am Water Res Assoc*, 49, 328-342.
- Hester, E. T., M. W. Doyle, and G. C. Poole (2009), The influence of in-stream structures on summer water temperatures via induced hyporheic exchange, *Limnol Oceanogr*, 54(1), 355-367.
- Miyauchi, T., H. Kataoka, and T. Kikuchi (1976), Gas film coefficient of mass-transfer in low peplet number region for sphere packed-beds, *Chem Eng Sci*, 31(1), 9-13.
- Nelson, K. C., and M. A. Palmer (2007), Stream temperature surges under urbanization and climate change: data, models, and responses, *JAWRA Journal of the American Water Resources Association*, 43(2), 440-452.
- Nield, D. A., and A. Bejan (2006), *Convection in porous media*. Springer, New York.
- Sawyer, A. H., M. B. Cardenas, and J. Buttles (2012), Hyporheic temperature dynamics and heat exchange near channel-spanning logs, *Water Resour Res*, 48, W01529.
- Vafai, K. (2005), *Handbook of porous media*. Taylor & Francis, Boca Raton.
- Vafai, K., and M. Sozen (1990), Analysis of Energy and Momentum Transport for Fluid-Flow through a Porous Bed, *J Heat Trans-T Asme*, 112(3), 690-699.

Wakao, N., K. Tanaka, and H. Nagai (1976), Measurements of particle-to-gas mass-transfer coefficients from chromatographic adsorption experiments, *Chem Eng Sci*, 31(12), 1109-1113.

Wakao, N., S. Kaguei, and T. Funazkri (1979), Effect of fluid dispersion coefficients on particle-to-fluid heat-transfer coefficients in packed-beds - correlation of nusselt numbers, *Chem Eng Sci*, 34(3), 325-336.

APPENDIX C: *Testing Ground Penetrating Radar to Characterize Macropores*

OBJECTIVE

To test and critique the ability of Ground Penetrating Radar (GPR) to detect and describe macropores within the shallow subsurface and in the hyporheic zone.

BACKGROUND

GPR is a geophysical mapping technique that transmits electromagnetic pulses into the subsurface and monitors the reflection of these waves back to the surface. The reflection off of objects with different electrical permittivities allows identification of different soil types, moisture content, and void spaces. A few studies have shown that low frequency GPR can be used to map macropores or soil pipes [*Gormally et al.*, 2011a; *Gormally et al.*, 2011b; *Holden*, 2005]. However, we wanted to test the ability of a 200 MHz antenna with GPR to rapidly characterize macropores within the hyporheic zone near streams.

METHODS

We tested the ability of GPR to pick up two 1 3/4 " polyvinyl chloride (PVC) pipes (0.5 m long) that we buried in an open field, representing natural macropores. We then filled one with salt water to change the electric permittivity, while leaving one filled with air, to see if we could get a better signal from GPR. In an open grassy field we buried the salt water-containing pipe and the air-containing pipe approximately 40 to 50 cm below ground surface at 12.5 m and 5 m respectively along the "position" axis (Figure C-1). We ran a Pulse EKKO 100 system with 200 MHz antennas 14m longitudinally along the PVC pipes. After collecting and processing the data with EKKO_View software, we created GPR tomograms and looked for reflections which would indicate the location of the macropores. The reflections showed up as upside down parabolas and discontinuities in the tomograms. Secondly, using the same methods, we attempted to detect naturally-occurring macropores in a stream bank by running the same GPR over a 10m transect along the bank of Stroubles Creek.

Grass Field

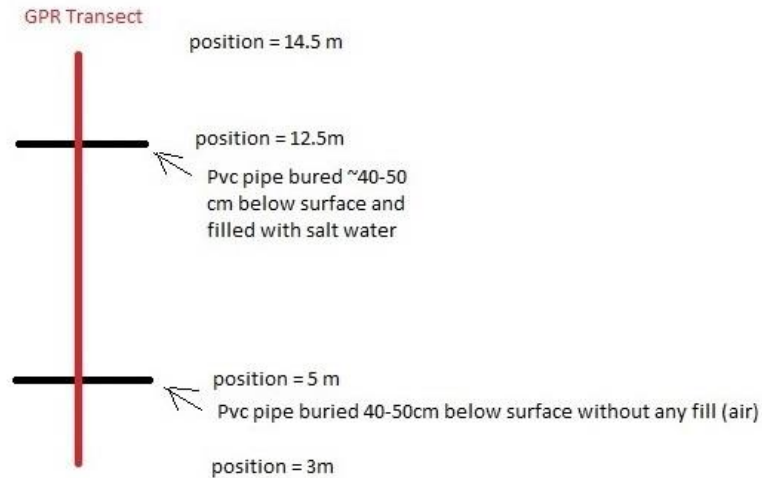


Figure C-1. Site plan view schematic for macropore detection with GPR in grass field.

RESULTS AND DISCUSSION

Figure C-1 shows a site schematic including orientation of GPR transect and macropores; Figures C-2, C-3, and C-4 show GPR tomograms and results. In Figures C-2, C-3, and C-4, PVC pipe containing salt water was at position = 12.5 m and depth ~ 0.50 m. PVC pipe containing air was at position = 5 m and depth ~ 0.50 m. The PVC pipes (representing macropores) show up as parabolas (upside down "u"). These parabolas are most visible when inspecting the colored tomograms. The maximum points on the parabolas are not shown because they cut into the shallow subsurface (<1 m), where the 200 MHz antenna experienced noise/error. However the contrast between the PVC pipes, holding air or saltwater, versus in situ soil is strong enough to detect their presence on the tomogram. The elevation of the PVC pipe can be estimated by following the arms on the parabola to the maximum point where they cross.

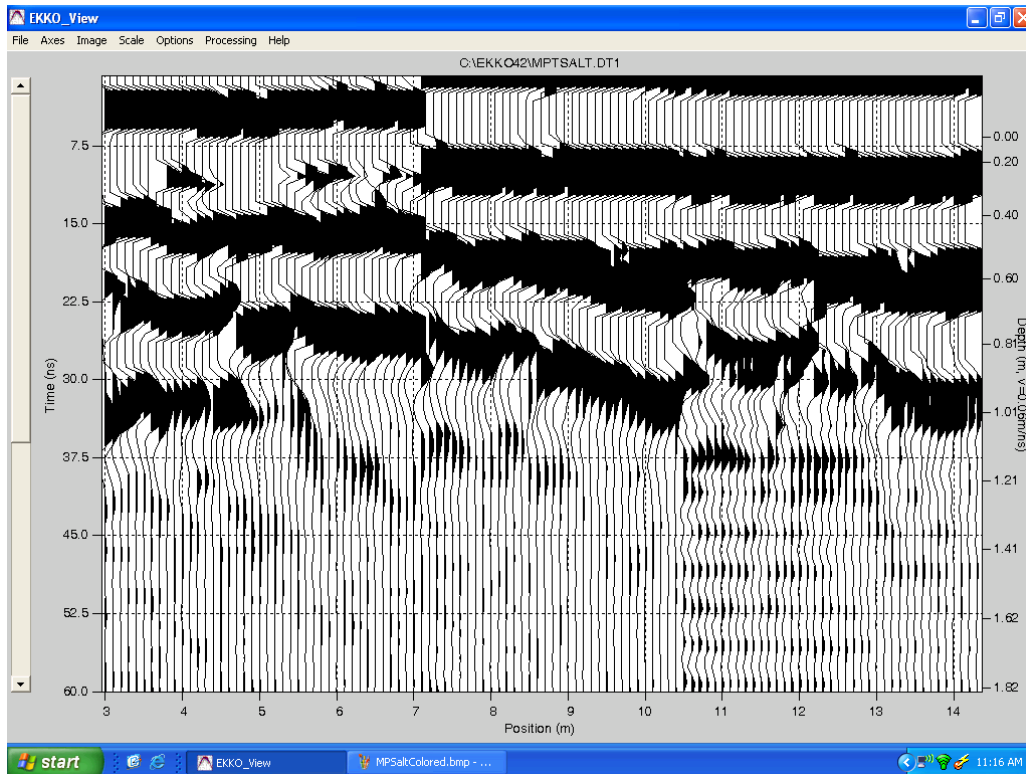


Figure C-2. Example output from post-processor from grass field experiment.

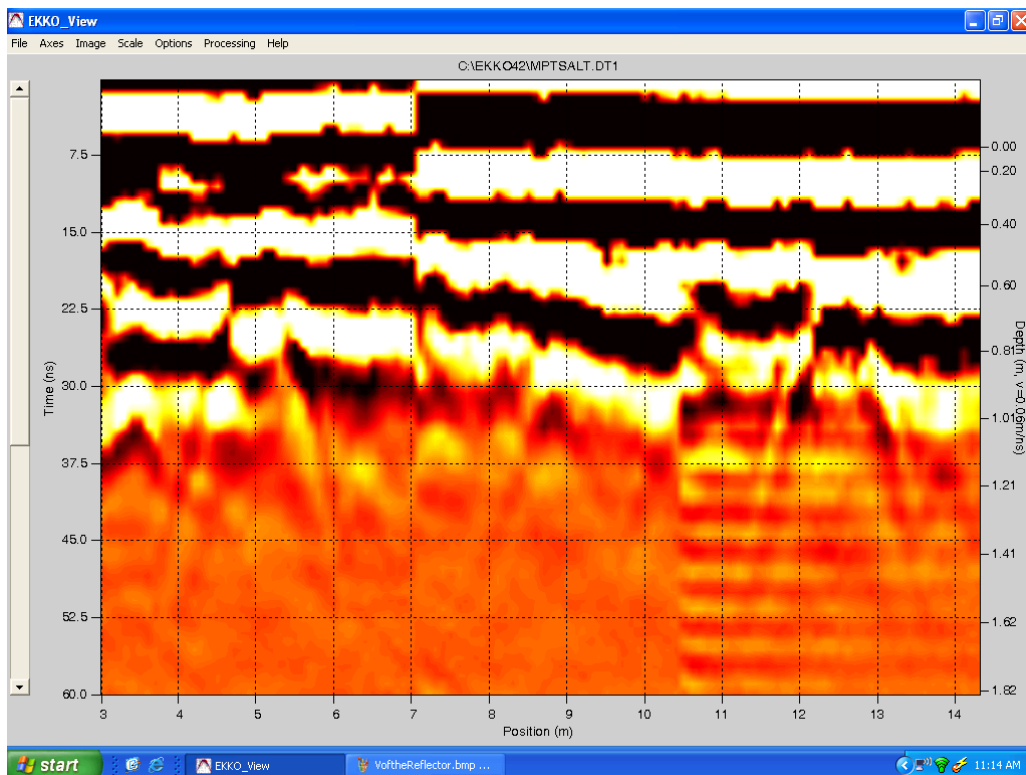


Figure C-3. Colored tomogram with macropores in grassy field experiment.

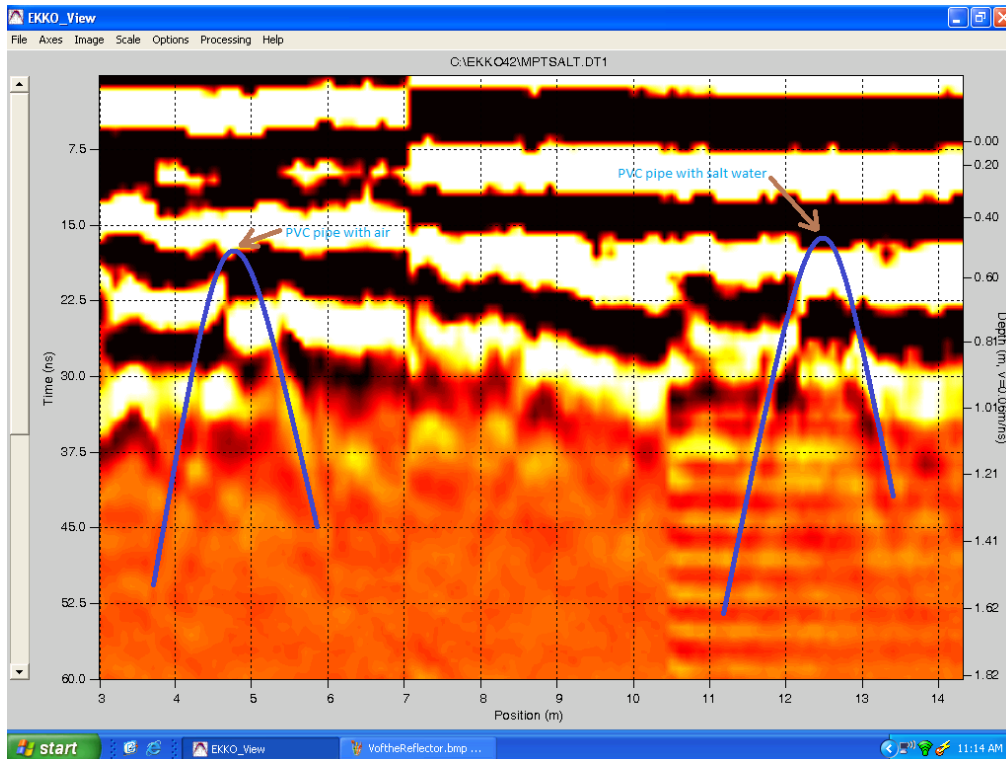


Figure C-4. Colored tomogram with macropore locations identified in grassy field experiment.

The tomograms show PVC pipes (representing macropores). However, when we tried to detect the presence of a naturally occurring macropore that went into the banks of Stroubles, the analysis became difficult. The biggest problem was heterogeneity near the stream, because GPR is sensitive to sediment type changes as well as subsurface features (roots and large rocks). We were not able to confidently tell the difference between the macropore signature on the GPR tomograms from all of the other signatures within the tomogram. To remedy this we suggest (1) having an exhaustive series of controlled experiments to determine all the different signatures of macropores on GPR, (2) Ground truthing (e.g., excavating with hydraulic cement) several macropores after detecting them with GPR to determine their signatures, (3) performing GPR in areas without thick riparian zones with large trees or on banks without much heterogeneity.

GPR transmits electromagnetic pulses from antennas into the ground and measures the time elapsed between the pulses being sent and received back at the surface. The velocity of the radar pulses changes as they travel through materials of different physical and chemical properties. When the travel time is measured and the ground velocity is known/estimated, the depth into the ground can be calculated. Determining the ground velocity requires some knowledge of soil conditions apriori, or collection of soil cores. The depth scale in Figures C-2,

C-3, and C-4 is based on radar velocity in clay (0.06 m/ns). Figures C-3 and C-4 have no filtering applied, they have only been "gained" (i.e., increased contrast) or had color added. The black bars near the top are noise and errors resulting from using a 200 MHz antenna (low frequency) and trying to get readings so close to the ground surface. A higher frequency antenna, such as 400 or 900 MHz, may be better able to collect data in the shallow subsurface.

REFERENCES

- Gormally, K. H., M. S. McIntosh, and A. N. Mucciardi (2011a), Ground-Penetrating Radar detection and three-dimensional mapping of lateral macropores: I. calibration, *Soil Sci Soc Am J*, 75(4), 1226-1235.
- Gormally, K. H., M. S. McIntosh, A. N. Mucciardi, and G. W. McCarty (2011b), Ground penetrating radar detection and three-dimensional mapping of lateral macropores: II. riparian application, *Soil Sci Soc Am J*, 75(4), 1236-1243.
- Holden, J. (2005), Controls of soil pipe frequency in upland blanket peat, *J Geophys Res-Earth*, 110, F01002.

APPENDIX D: *Testing Concrete to Cast Molds of Macropores along Stream Channels*

OBJECTIVE

Test the use of hydraulic concrete to create molds of naturally occurring macropores. Concrete molds would allow accurate quantification of macropore dimensions over its depth, tortuosity, and potentially connections with other macropores. Previous methods (e.g., liquid latex, geophysical methods) are problematic because they require unsaturated conditions, long completion times, or specialized equipment and experience with the method.

METHODS

- A 1.5 m long 2” diameter PVC pipe was cut into roughly 40 cm and 110 cm lengths. The pipes were connected at a 90-degree bend using a 90-degree PVC elbow and a rubber clamp. This was the apparatus which delivered hydraulic concrete by gravity into the macropore. The ends of the pipes were wrapped with duct tape to allow a tight seal at the macropore opening.
- Several more apparatuses were made with different diameter pipes, so that we could test different diameter macropores (Figure D-1). We made 7 total apparatuses that had diameters of 1.27, 1.91, 2.54, 3.81, 5.08, 7.62, 10.16 cm.
- We created an experimental macropore that was 4 cm in diameter and 50 cm deep (Figure D-2).
- We hammered in two wooden stakes at an angle to form an “X”. This served as the base for the apparatus (Figure D-2).
- We inserted the 3.81 inch diameter apparatus into the macropore, such that the end was sitting on the wooden stakes (Figure D-3).
- We patched the outside rim of the apparatus and bank face with clay and poured hydraulic concrete into the apparatus (Figure D-4).
- Gravity and head build up in the apparatus forced hydraulic concrete into the macropore. We allowed the hydraulic concrete to harden for 3 minutes then removed the apparatus from the macropore (Figure D-5).
- After 15 minutes we carefully excavated the soil around the concrete mold of the macropore (Figure D-6).



Figure D-1. Apparatuses to inject concrete into macropores. Ruler shows 0.5 m distance.



Figure D-2. Experimental macropore that extends 0.5 m into the bank.



Figure D-3. Apparatus inside macropore.



Figure D-4. The bank face is patched around apparatus and concrete is poured into the apparatus.

RESULTS AND DISCUSSION

After curing for only a few minutes, the hydraulic concrete was strong enough to remain in the macropore and hold its shape once the apparatus was removed (Figure D-5). Partial excavation after 15 minutes showed that the hydraulic concrete was able to keep the shape (Figure D-6). Therefore, we successfully created a mold of a macropore using hydraulic concrete. We believe the key to success is the concrete mixture. The ideal hydraulic concrete mixture that has high slump so that it fills in the macropore, quickly sets and cures, and has only small aggregates (e.g., a mortar or a cement/sand mixture). We used a Type III Portland cement with gravel. Our success was limited because gravel in our concrete mix began to clog our PVC pipe. However, the gravel was an important constituent in the mix because it provided strength. Future work needs to explore the use of hydraulic concrete while substituting gravel for other constituents (e.g., sand) to add strength to the mold of the macropore. Nevertheless, our results suggest that creating molds of naturally macropores using hydraulic concrete is possible, does not require long curing times, and can be done in inundated or unsaturated macropores. This is an attractive alternative to several other mapping methods because. For example, liquid latex requires unsaturated conditions and requires days to dry. Geophysical methods require background experience with the methodologies, long completion times, data processing, and post-processing of the results.



Figure D-5. Apparatus removed and macropore remains filled with hydraulic concrete.



Figure D-6. The partially excavated macropore mold after 15 minutes.

APPENDIX E: *Testing the Hydrologic Connectivity of Macropores to other Preferential Flow Paths and Measuring the Hydraulic Conductivity of Macropores*

OBJECTIVE

To determine a method of performing falling head tests in macropores to determine their hydrologic significance and connectivity with other preferential flow paths.

METHODS

- We used the apparatuses shown in Appendix D to perform falling head tests and rhodamine tracer tests. See Appendix D for description of apparatuses
- We went to the tributary to Tom's Creek and tested several macropores of varying sizes
- We hammered in two wooden stakes at an angle to form an "X". This served as the base for the apparatus
- We selected and inserted an apparatus that fit snugly into the macropore, and patched the opening around the apparatus with clay
- Hydrologic connectivity test. We poured a small amount of diluted rhodamine tracer into the apparatus and visually observed the transport of tracer out of adjacent macropores
- Falling head test
 - We used an Onset LevelTroll700 with 1 second logging intervals and placed the probe inside the apparatus
 - We performed a falling head test by filling the apparatus to the rim with stream water and then let the water level decrease
 - We downloaded the data and determined hydraulic conductivity using Hvorslev's method [*Freeze and Cherry, 1979*]

RESULTS

- Hydrologic connectivity tests. We tested several macropores and found that the direction and magnitude of tracer transport was variable. In general we found 3 responses from the rhodamine tests
 - Several macropores tests transported the rhodamine back to the surface stream a short distance away from the injection macropore (Figure E-1). The longest distance rhodamine was transported before it was resurfaced at the stream through another macropore was 60 cm.
 - A few macropores we tested did not return any rhodamine to the surface stream. As we added rhodamine to the apparatus, it quickly drained the apparatus and was

transported through the macropore. Even after waiting 5 minutes, no tracer re-emerged from the banks

- Some macropores we tested held the rhodamine until the apparatus was removed, at which point rhodamine spilled back into the stream



Figure E-1. Top panel shows tracer transport 10 seconds after rhodamine addition to apparatus installed in macropore. Bottom panel shows 30 seconds after initial addition of rhodamine.

- Falling head tests. We tested several macropores with limited success. We attribute this to the pressure exerted on the banks by the falling head test. In general we observed three results.
 1. The bank face where we patched the base of the apparatus and bank face would seep water or completely fail. A falling head test could not be performed in these regions after bank failure.

2. Several macropores we tested existed in very low permeability sediments and the water level during the falling head test decreased very slowly.
3. A few macropores quickly drained the water we added during the falling head test. However it was difficult to determine if the water was being re-routed to the surface stream via other macropores or transported off into the floodplain.



Figure E-2. Top panel shows apparatus set up inside macropore with a Leveltroll700 pressure transducer inside. Bottom panel shows the addition of water for a falling head test.

DISCUSSION

- Hydrologic connectivity tests
 - The injection of rhodamine tracer into macropores using the apparatus we created worked well. We observed three types of responses from the experiments, indicating that (1) macropores can transport solute further off into the floodplain (away from the channel, (2) macropores can transport solute back to the channel (over distances up to 60 cm, or (3) macropores will act as surface storage features instead of preferential flow paths. These results suggest that the hydrologic significance of macropores is highly variable and dependent on connection with other flow paths.
 - Future studies should consider tracking salt tracers with conductivity probes through the floodplain or subsurface to quantify tracer transport through different macropores.
- Falling head tests
 - Although the column of water we placed in the apparatus to drive the falling head test was short, some bank faces collapsed during the falling head test, indicating the water pressure was too great. This result was problematic because it caused a failure of the falling head test and destruction of the bank face. Furthermore this event raised the question for those falling head tests that did work, if the macropore we tested was actively scoured during the test. This would suggest that we increased the hydraulic conductivity by performing the falling head test. We suggest that future studies explore and consider the maximum water column height that can be used before scour or failure occurs.
 - The macropores that exhibited very high hydraulic conductivity could be caused by a strong connection with other macropores that connect back to the surface stream or out into the floodplain or deeper groundwater zones
- Combination of connectivity tests and falling head tests
 - While each test has its strengths and weaknesses, the best result is when these two tests are performed in tandem. From the hydrologic connectivity test we can qualitatively determine what type of connection the macropore has to other

preferential flow paths. From the falling head tests we can quantify the hydrologic significance of a particular macropore and its connections.

- We suggest that the connectivity tests are performed first, to avoid scouring macropores or breaking the bank face

REFERENCES

Freeze, R. A., and J. A. Cherry (1979), *Groundwater*. Englewood Cliffs, N.J., Prentice-Hall.

APPENDIX F: *The Effect of Macropores on Transient Storage during Baseflow*

OBJECTIVE

To quantify the effect of macropores on baseflow transient storage using tracer injection experiments.

METHODS

We assessed the importance of macropores on transient storage at baseflow by performing two tracer injection experiments, one without macropores (non-macropore [NM]) and one with artificially created macropores (macropore [M]). We performed a transient storage experiment on the NM and M scenarios, injecting a conservative tracer at the upstream part of the reach and monitoring the arrival of the tracer downstream [Aumen, 1990; Bencala and Walters, 1983]. The transient storage experiments were performed at a tributary to Stroubles Creek in Blacksburg, Virginia (Figure F-1). The experimental reach was 35 m long, with bed and banks comprised of sand, silt, and clay. Stream slope was 0.005 m/m, and channel dimensions ranged from 30 to 40 cm wide and 6 to 10 cm deep. In-stream discharge was calculated using dilution gauging [Moore, 2004] and varied little between the two experiments, averaging 3.3 L/s. We injected a sodium chloride tracer at the upstream end of the reach and monitored conductivity 10 m upstream (background), 5 m downstream, and 35 m downstream using an In-Situ AquaTroll-100s. We used a 45 minute constant rate drip of 120 mL/min for each experiment, increasing the in-stream specific conductance up to 378 $\mu\text{s}/\text{cm}$ (58.3% increase) and 401 $\mu\text{s}/\text{cm}$ (57.7% increase) from background.

The first injection experiment was performed on the NM scenario. Because some macropores existed in the channel naturally, we closed those macropores that existed below the waterline by collapsing them at their connection to the surface stream or plugging them with clay. The second injection experiment was performed after we created artificial macropores (M treatment). These macropores were created by drilling a 2.54 cm diameter auger bit on average 30 cm into the bed and banks within the saturated zone (i.e. below the channel water line, Figure F-2). The resultant artificial macropores ranged from 3 to 5 cm in opening diameter. Macropores were drilled such that orientation was perpendicular to streamwise direction or angled slightly upstream (consistent with observation of natural macropores during field surveys). A total of 100 macropores were drilled within the 35 m reach and were approximately evenly spaced along the reach (~3 macropores per meter, Figure F-3). The total macropore volume for the M treatment was 0.0377 m^3 . Several meters of the reach could not retain

macropores due to low bank height and sandy soil texture; we clustered macropores upstream or downstream of these areas.

We estimate the transient storage parameters (TSPs) using the One Dimensional Transport with Inflow and Storage model (OTIS) [Runkel, 1998]. OTIS is a one-dimensional finite difference model that solves the one-dimensional advection-dispersion equation for stream channels with inflowing groundwater (gaining from catchment) and exchange with a non-flowing transient storage zone (Eq. 1 and 2).

$$\frac{\partial C}{\partial t} = -\frac{Q}{A} \frac{\partial C}{\partial x} + \frac{1}{A} \frac{\partial}{\partial x} \left[AD \frac{\partial C}{\partial x} \right] + \frac{Q_L}{A} (C_L - C) + \alpha (C_s - C) \quad (1)$$

$$\frac{\partial C_s}{\partial t} = -\alpha \frac{A}{A_s} (C_s - C) \quad (2)$$

The transient storage zone can represent either surface water dead zones or the hyporheic zone. C , C_L , C_s , are the solute concentration in the stream, groundwater, and storage zone, respectively. Q and Q_L are the discharge of the stream and lateral groundwater inflow (L/s), respectively. The time since drip start is t (s), x is distance, A is the channel cross sectional area, A_s is the storage zone area (m²), D is the dispersion coefficient (m²/s), α is the exchange coefficient with the storage zone (1/s). We used the parameterization component of OTIS (OTIS-P) to fit observed data to the model and estimate transient storage parameters (TSPs), α , A , A_s , and D , for the NM and M treatments. Because our reach was short (35 m) and the banks had low permeability sediments, we assumed lateral inflow of groundwater was negligible. This assumption was validated by the steady plateau value observed. Optimization was initially performed by allowing all parameters (α , A , A_s , and D) to change. Holding particular parameters constant and re-running the model did not change model results. Q was determined from dilution gauging and we report concentration as relative concentration (RC [L/L]) [Moore, 2004]. Average surface water channel dimensions from OTIS-P indicated wetted-channel volume was 0.651 m³, which agreed with cross sectional surveys. F_{med} is a transient storage metric describing the fraction of travel time spent in the transient storage zone [Runkel, 2002]. We calculated F_{med} from Runkel [2002],

$$F_{med} = \frac{T_{med} - T_{med}^m}{T_{med}} \quad (3)$$

where T_{med} is the time (s) required to reach 50% of the plateau concentration, and T_{med}^m is the time (s) required to get to 50% of the plateau concentration in the main channel (i.e., with $\alpha=0$). T_{med} and T_{med}^m come from modeling with OTIS.

The Damkohler number (DaI) is the ratio of the average in-stream transport time and the transient storage zone interaction timescale (Eq. 4) [Bahr and Rubin, 1987; Harvey and Wagner, 2000; Wagner and Harvey, 1997].

$$DaI = \alpha \left(1 + \frac{A}{A_s} \right) * \frac{L}{v} \quad (4)$$

We determined the mean transport velocity (v) by dividing the length of the stream reach ($L=35$ m) by the time to reach 50% of the plateau concentration (mean arrival time). Accepted DaI values to minimize uncertainty in TSPs range from 0.1 to 10 [Jin and Ward, 2005; Stofleth et al., 2008; Wondzell, 2006]. Similar to DaI , the parameter sensitivity ratio (PSR) is the ratio of the estimated TSP and the standard deviation. TSP estimates are valid when PSR is greater than 2 [Jin and Ward, 2005]. We also report the 95% confidence interval limits from OTIS-P for each estimated parameter and the residual sum of squares from the fit of all the parameters together.



Figure F-1. Left panel shows injection setup and beginning of reach (0m to 5m). Right panel shows middle of reach (5m to 25m).



Figure F-2. Construction of macropores.



Figure F-3. Left panel shows post-macropore creation conditions on outside bend. Right panel shows non-macropore conditions.

RESULTS

We determined the TSPs for the reach with macropores (M) and without macropores (NM) to determine if macropores contributed to transient storage. A_s , α , and F_{med} were all higher (16.6%, 20.1%, and 31.5%, respectively) with macropores present than without (Table F-1). We note that the 95% confidence intervals for the two treatments overlap somewhat for α , suggesting that the difference is not significant at the 5% significance level for that particular parameter. Overall, these results indicate a modest but measurable effect of the artificially created macropores. The discharge decreased slightly between treatments, from 3.4 L/s to 3.2 L/s. D and A varied less than 3% between the two treatments, consistent with minimal changes

to the channel geometry and discharge. Despite the decrease in discharge, DaI values between the two runs were similar: 4.65 and 5.29 for NM and M, respectively.

Observed and modeled breakthrough tracer curves are shown in Figure F-4. To determine whether adding transient storage parameters A_s and α improved model fit, we ran OTIS with these parameters turned off (Figure F-4A, F-4B, blue lines) and on (Figure F-4A, F-4B, red lines). Including A_s and α clearly improved the fit of the model to observed data in both treatments, in particular at the rising limb before plateau and the tail of the breakthrough tracer curves (e.g., for the NM treatment the residual sum of squares (RSS) is 27.3 without transient storage and 0.216 with transient storage)

We used several statistical measures to quantify the uncertainty of our results. The DaI for the NM and M treatments were 4.65 and 5.29, respectively. $DaI = 1$ is ideal to ensure reliability of A_s and α [Harvey and Wagner, 2000; Wagner and Harvey, 1997]; however, is difficult to achieve given that it is highly dependent on reach length and channel discharge. In existing literature, a range of $0.1 < DaI < 10$ is commonly accepted [Becker *et al.*, 2013; Jin and Ward, 2005; Wondzell, 2006]. Therefore, based on DaI , our A_s and α estimates are reliable. Another commonly used metric of certainty is PSR. In our analyses the PSR is greater than 2 for all cases, suggesting good certainty in parameter estimates [Jin and Ward, 2005]. Wondzell [2006] reported acceptable TSPs when coefficients of variation (inverse of PSR) were less than 0.1; our coefficients of variation were less than 0.11. However, the fitted α for the NM treatment is within the 95% confidence interval for the M treatment. We therefore conclude that macropores in our study increased A_s and F_{med} , but not α .

Table F-1. Stream and Transient Storage Parameters for the treatment scenarios.

| | Q (L/s) from dilution gauging | v (m/s) from BTC | Transient Storage Parameters and Analysis | | | | | | |
|-----------------------------------|--|--------------------------|---|-----------------------|-------------------------|-----------------|----------------|---------------|--------------|
| | | | D (m ² /s) | A (m ²) | A_s (m ²) | α (1/s) | Reach DaI | F_{med} | A_s/A |
| No Macropores (NM) | 3.38 | 0.182 | 4.45e-02 | 1.85e-02 | 2.83e-03 | 3.21e-03 | 4.65 | 0.0588 | 0.153 |
| PSR: TSP/ σ | | | 14.8 | 157.1 | 27.5 | 11.7 | | | |
| 95% lower confidence limit | | | 3.86e-02 | 1.83e-02 | 2.62e-03 | 2.67e-03 | | | |
| 95% upper confidence limit | | | 5.05e-02 | 1.88e-02 | 3.03e-03 | 3.75e-03 | | | |
| Macropores (M) | 3.20 | 0.171 | 4.58e-02 | 1.87e-02 | 3.30e-03 | 3.88e-03 | 5.29 | 0.0773 | 0.176 |
| PSR: TSP/ σ | | | 10.9 | 97.8 | 20.0 | 8.8 | | | |
| 95% lower confidence limit | | | 3.75e-02 | 1.83e-02 | 2.98e-03 | 3.00e-03 | | | |
| 95% upper confidence limit | | | 5.41e-02 | 1.90e-02 | 3.63e-03 | 4.75e-03 | | | |
| % change | -5.6 | -6.0 | 2.9 | 1.1 | 16.6 | 20.9 | | 31.5 | 15.0 |

Notes: PSR= Parameter Sensivity Ratio. TSP = Transient Storage Parameter. Mean velocity (v) calculated from arrival of 50% of plateau concentration.

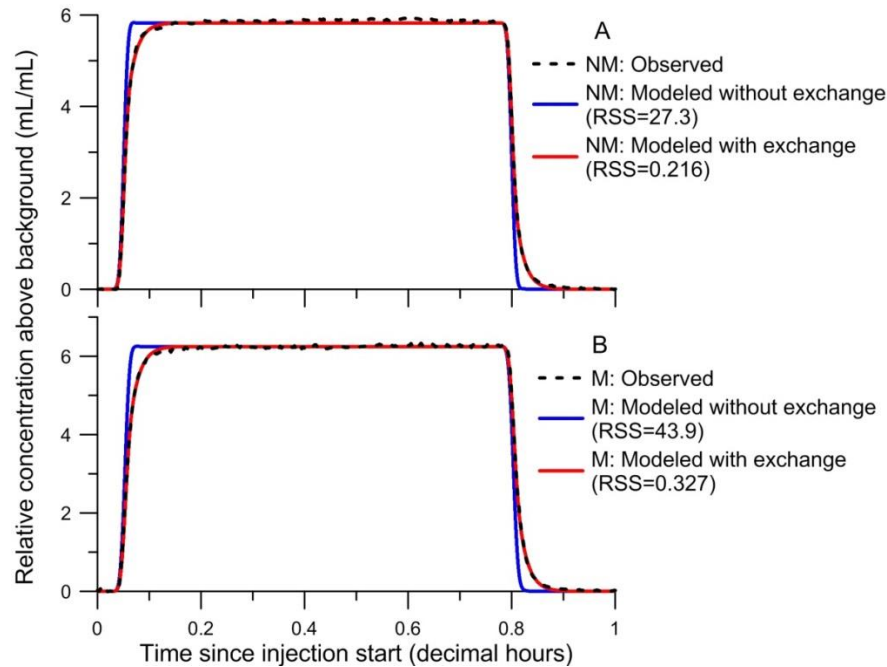


Figure F-4. Breakthrough tracer curves (BTCs). Panels A and B show the observed BTC, the modeled BTC with exchange, and the modeled BTC without exchange at 35 m downstream for NM and M treatments, respectively.

DISCUSSION

We studied a reach within a small stream, with bed and banks comprised of sand, silt, and clay, and an average travel time of 3 to 4 minutes. As a result, pre-existing hyporheic exchange and transient storage are limited. In fact, A_s for the NM treatment is 0.00283 m^2 , which is at the low end of a naturally observed range of 0.001 to 1 m^2 from 136 different studies [Stofleth *et al.*, 2008]. However, NM α is $0.00321/\text{s}$, is within the upper half of the range natural observed, 10^{-5} to 0.01 1/s [Stofleth *et al.*, 2008], which we attribute to exchange with existing surface storage zones. Previous studies have shown that exchange rates with surface transient storage zones can be more than an order of magnitude higher than exchange rates with hyporheic transient storage zones [Briggs *et al.*, 2009; Briggs *et al.*, 2010]. We attribute such surface transient storage to exchange with small surface storage zones on the outside of meanders with eddying of water. Average D ($0.0452 \text{ m}^2/\text{s}$) is within an accepted range [Jin and Ward, 2005; Stofleth *et al.*, 2008; Wondzell, 2006]. The average A (0.0186 m^2) makes sense given our measured channel dimensions.

We attribute the observed increases in A_s/A after adding artificial macropores (Table F-1) to those macropores serving as both unobstructed pathways for transport to the subsurface and as surface storage zones. The simultaneous increase in F_{med} suggests that macropores increased the fraction of stream travel time spent in the transient storage zone. However, A_s was low even post-macropore creation, suggesting that the net effect of macropores on hyporheic exchange was limited by low permeability silts and clays lining the macropores. Therefore, macropores may have larger impact on the hyporheic portion of transient storage when sediments are coarser, particularly where macropores penetrate lower permeability surface layers to reach other preferential flow paths (e.g., paleochannel, other macropores).

We increased the surface volume of this small stream by 5.8% by creating 100 macropores along 35 meters. This means that we added, on average, a macropore every 0.35 m. Comparatively, our survey data across five streams indicate an average macropore interspacing of 1.12 m. Therefore, we added 320% (or 3.2 times) more macropores than the average we observe in the field. Nevertheless, macropores are often clustered, as we saw a median interspacing of macropores of 0.38 m in our survey of five streams, which is very close to our construction interspacing of 0.35 m. We therefore conclude that clusters of macropores may

cause impacts to transient storage in natural systems similar to what we observed, but over short reaches.

REFERENCES

- Aumen, N. G. (1990), Concepts and methods for assessing solute dynamics in stream ecosystems, *J N Am Benthol Soc*, 9(2), 95-119.
- Bahr, J. M., and J. Rubin (1987), Direct comparison of kinetic and local equilibrium formulations for solute transport affected by surface reactions, *Water Resour Res*, 23(3), 438-452.
- Becker, J. F., T. A. Endreny, and J. D. Robinson (2013), Natural channel design impacts on reach-scale transient storage, *Ecol Eng*, 57, 380-392.
- Bencala, K. E., and R. A. Walters (1983), Simulation of solute transport in a mountain pool and riffle stream - a transient storage model, *Water Resour Res*, 19(3), 718-724.
- Harvey, J. W., and B. Wagner (2000), Quantifying hydrologic interactions between streams and their subsurface hyporheic zones, *Streams and Ground Waters*, 344.
- Jin, H. S., and G. M. Ward (2005), Hydraulic characteristics of a small coastal plain stream of the southeastern United States: effects of hydrology and season, *Hydrol Process*, 19(20), 4147-4160.
- Moore, R. (2004), Introduction to salt dilution gauging for streamflow measurement: Part 1, *Streamline Watershed Management Bulletin* 7 (4): 20, 23.
- Runkel, R. L. (1998), *One-dimensional transport with inflow and storage (OTIS) : a solute transport model for streams and rivers*, U.S. Dept. of the Interior, Denver, CO.
- Runkel, R. L. (2002), A new metric for determining the importance of transient storage, *J N Am Benthol Soc*, 21(4), 529-543.
- Stofleth, J. M., F. D. Shields, and G. A. Fox (2008), Hyporheic and total transient storage in small, sand-bed streams, *Hydrol Process*, 22(12), 1885-1894.
- Wagner, B. J., and J. W. Harvey (1997), Experimental design for estimating parameters of rate limited mass transfer: Analysis of stream tracer studies, *Water Resour Res*, 33(7), 1731-1741.
- Wondzell, S. M. (2006), Effect of morphology and discharge on hyporheic exchange flows in two small streams in the Cascade Mountains of Oregon, USA, *Hydrol Process*, 20(2), 267-287.

APPENDIX G: *Stream Gauge Locations and Rating Curve Data*

Stream gauges for the study in Chapter 3 were installed in 5 streams near Blacksburg, VA to monitor the variation in stream stage over a one year period. Table G-1 lists the streams and the Global Positioning System (GPS) coordinates for the gauges. Figure G-1 shows the locations of the stream gauges on an aerial photograph.

Table G-1. Stream gauges and GPS coordinates.

| Stream Gauge | GPS Coordinates |
|----------------------|-----------------------|
| Stroubles Creek | 37.215801, -80.437161 |
| Toms Creek Tributary | 37.242217, -80.457917 |
| Poverty Creek | 37.279548, -80.473227 |
| Craig Creek | 37.314729, -80.399967 |
| Slate Branch | 37.189163, -80.423381 |

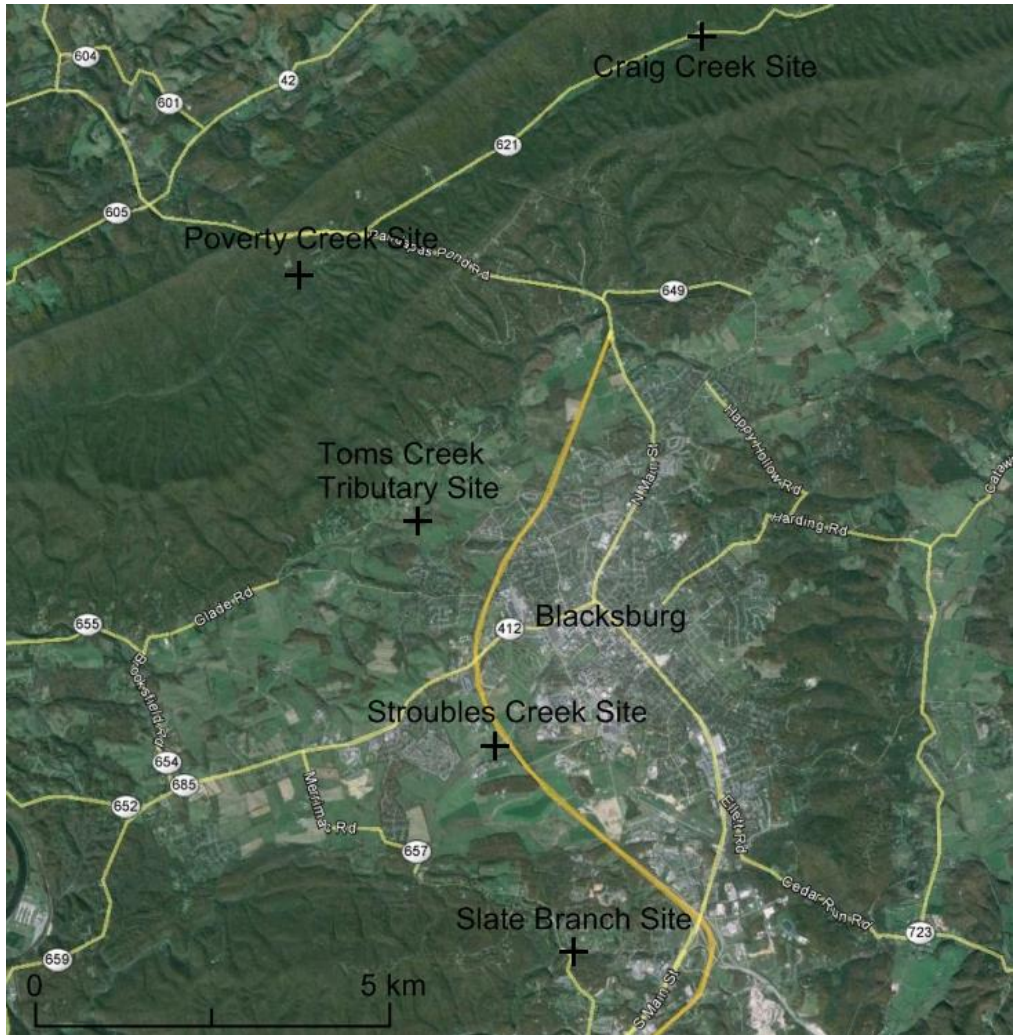


Figure G-1. Stream gauge site locations near Blacksburg, VA. Aerial photo retrieved from Google maps.

For each stream gauge site, rating curves were created by measuring discharge using the velocity-area method for several storm events [Hersch, 1993]. Listed in Table G-2 are the discharges measured and the corresponding water levels for several storms.

Table G-2. Data for rating curves at sites.

| Stream Gauge | Water Level (m) | Discharge (m ³ /s) |
|---------------|-----------------|-------------------------------|
| Craig Creek | 0.053 | 0.026 |
| | 0.099 | 0.059 |
| | 0.159 | 0.105 |
| | 0.309 | 0.353 |
| | 0.563 | 1.031 |
| | 0.691 | 2.015 |
| Poverty Creek | 0.057 | 0.008 |
| | 0.128 | 0.062 |
| | 0.131 | 0.043 |
| | 0.193 | 0.134 |
| | 0.238 | 0.318 |
| | 0.260 | 0.502 |
| Slate Branch | 0.022 | 0.019 |
| | 0.096 | 0.057 |
| | 0.127 | 0.127 |
| | 0.135 | 0.141 |
| | 0.148 | 0.175 |
| | 0.152 | 0.203 |
| | 0.164 | 0.261 |
| | 0.212 | 0.446 |

| | | |
|----------------------|-------|-------|
| Stroubles Creek | 0.041 | 0.097 |
| | 0.072 | 0.178 |
| | 0.093 | 0.270 |
| | 0.105 | 0.237 |
| | 0.132 | 0.390 |
| | 0.246 | 1.204 |
| Toms Creek Tributary | 0.060 | 0.005 |
| | 0.100 | 0.010 |
| | 0.175 | 0.033 |
| | 0.202 | 0.060 |
| | 0.249 | 0.081 |

REFERENCES

Herschy, R. (1993), The velocity-area method, flow measurement and instrumentation, 4(1), 7-10.